Freie Universität Berlin

Femtosecond XUV Photoelectron Spectroscopy of Organic Molecules in Aqueous Solution

Johan Hummert

im Fachbereich Physik der Freien Universität Berlin eingereichte Dissertation

Berlin 2017

Diese Arbeit wurde zwischen März 2014 und November 2017 am Max-Born-Institut fur nichtlineare Optik und Kurzzeitspektroskopie im Forschungsverbund Berlin e.V. angefertigt. Die Promotion wurde betreut von Prof. Dr. Marc Vrakking und Dr. Oleg Kornilov.

1. Gutachter: Prof. Dr. Marc J.J. Vrakking

2. Gutachter: Prof. Dr. Karsten Heyne

Disputation: 19.4.2018

Contents

1 Introduction

Interaction of light with organic molecules is a fundamental research topic at the intersection of physics, chemistry, and biology. Absorption of sunlight by organic molecules is by far the most important energy source on the earth, supplying the energy for plant life and subsequently for animal and human life. On the other hand light absorption also has destructive power, as seen in the damaging of DNA by ultraviolet radiation, ultimately leading to harmful mutations.

Responsible for the absorption of light in these biological processes are certain photoactive molecules, typically called chromophores. The functions of chromophores cover a tremendous range, from providing the initial energy for photosynthesis, to triggering human vision. Investigation of the initial relaxation of these molecules after light absorption is essential to understand the various functions.

Additionally there is a technological motivation to investigate the function of photoactive organic molecules. Light-activated molecular switches are promising for electronics [1] and medicine [2]. Other promising areas of application are, for example, dye sensitized solar-cells and organic light-emitting diodes. Future applications, for example on greenhouses, could benefit from the ability to tailor the absorption spectrum of these solar cells [3].

First changes in molecules after absorption of a photon take place on the timescale of femtoseconds [4]. To investigate such fast dynamics, researchers rely on ultrafast laser spectroscopy methods. With advances in short pulse laser technology the relaxation dynamics of molecules on the picosecond and femtosecond timescales have become accessible [5]. Time-resolved absorption and fluorescence spectroscopy methods helped to unravel the ultrafast electronic relaxation pathways of countless organic molecules [6].

But all-optical methods have limitations. They only access transition energies and not the absolute binding energies of the electronic states. Additionally optically forbidden transitions are inaccessible and thus the role of so-called dark states cannot be investigated directly. These limitations are overcome in pump-probe photoelectron spectroscopy using ultrashort laser pulses, a technique capable of resolving molecular dynamics on all excited state potential energy surfaces [7].

The power of time-resolved photoelectron spectroscopy can be even greater with probe pulses in the extreme ultraviolet (XUV) regime, which are capable of resolving dynamics even in the ground electronic state of the molecule. Table-top sources of ultrashort XUV pulses are available since the discovery of high harmonic generation [8], leading to time-resolved XUV photoelectron spectroscopy studies of many atomic and molecular systems in the gas phase [7].

There are, however, strong limitations to XUV photoelectron spectroscopy when it comes to the investigation of large organic molecules, since the method demands high

vacuum conditions. Bringing organic molecules into the gas phase without damaging them is not a trivial task. Additionally, a gas phase experiment may not necessarily yield a result relevant for the biological function of the molecule, due to the importance of the interaction between the molecule and its environment.
In all-optical techniques organic molecules are routinely studied in solution, i.e. in their natural environment. Therefore the interaction of the molecule with the surrounding solvent is intrinsically included and can be investigated by changing solvent parameters like polarity, viscosity, or affinity to hydrogen bonding. The influence of the environment is found to be essential for the function of organic chromophores. For example, the efficiency of the light-induced isomerization of retinal, the chromophore of human vision, strongly depends on the environment of the molecule [9].
The importance of the environment, and developments in ultrafast photoelectron spectroscopy in recent years, have sparked increasing interest in XUV photoelectron spectroscopy of solvated molecules [10]. The most successful way of bringing photoelectron spectroscopy to liquid samples is the liquid jet technique, perfected by Faubel and coworkers [11]. The liquid jet is a micrometer thin liquid filament, which is injected into the vacuum under high pressure. This provides a clean, continuously refreshed liquid surface in a high vacuum environment. The technique has been applied in multiple XUV and X-ray studies, exploring the electronic structure of liquid water [12–14]. However, liquid jet photoelectron spectroscopy of organic molecules has so far been limited to either time-resolved spectroscopy with UV laser pulses [15] or steady-state spectroscopy with XUV radiation at synchrotron facilities [16].
In this thesis I present the implementation of time-resolved XUV photoelectron spectroscopy of organic molecules in solution using the liquid jet technique. The newly implemented method combines the advantages of XUV photoelectron spectroscopy with the possibility to investigate the influence of the surrounding solvent. To this end a liquid jet endstation is implemented at an existing XUV monochromator setup based on high harmonic generation [17].
Since time-resolved XUV photoelectron spectroscopy on liquid targets is a very recent technique, a part of this thesis is dedicated to the implementation of the liquid jet endstation on the monochromator setup. The liquid jet delivery system is a commercial product (*Microliquids*). Within the scope of this thesis it is substantially modified, to improve its stability and the precision of the alignment. The photoelectron detection from the liquid target is accomplished with a magnetic bottle time-of-flight spectrometer [18], which provides the high collection efficiency necessary for experiments with dilute samples of solvated molecules. The implemented setup has the capability to reproduce very recent results, for example the observation of the laser-assisted photoelectric effect in liquid water [19].
The commissioned experimental setup is used for investigation of molecular systems. The first sample is a sulfonated yellow dye, Quinoline Yellow WS. This molecule is chosen for a proof-of-principle experiment due to its favorable photochemical characteristics. In

the experiment, static and time-resolved photoelectron signals are successfully measured at a concentration of 10 mM of Quinoline Yellow in an aqueous solution. The relaxation dynamics observed in the pump-probe experiment are consistent with a recent proposal of an excited state intramolecular proton transfer process in the unsulfonated form of the dye [20].
After the successful proof-of-principle experiment, the technique is used to investigate functional photoactive molecules. As synthetic functional molecules, azobenzene derivatives are investigated. Azobenzene derivatives isomerize upon irradiation with visible light, which makes them promising candidates for application as molecular switches [21]. In this thesis the light-induced isomerization of two amino-azobenzene dyes, Methyl Orange and Metanil Yellow, is investigated with time-resolved XUV photoelectron spectroscopy in aqueous solution. In the experiment ground and excited state photoelectron spectra are obtained together with isomerization timescales for both molecules. The measured isomerization timescale for Methyl Orange is in good agreement with previous all-optical studies [22]. The isomerization of Metanil Yellow is found to be significantly slower. This can be linked to the larger rotational moment of inertia, and therefore supports the hypothesis of a mainly rotational isomerization of amino-azobenzene derivatives [23].
As an example for a biologically relevant molecule, the amino acid Tryptophan is investigated. The ionization energy of aqueous Tryptophan is an important parameter in biochemistry, since ionization of Tryptophan is a precursor for oxidation and damage of proteins [24]. The ionization energy of aqueous Tryptophan is directly measured with liquid jet XUV photoelectron spectroscopy, which provides an accurate estimate of the phase transition shift, i.e. the difference between the ionization potentials in the gas phase and in solution. The steady-state experiment performed in this thesis is the first step towards a time-resolved photoelectron experiment, which could be helpful to understand the complex relaxation dynamics of Tryptophan [25].
The thesis is structured as follows: In the second chapter the necessary fundamentals of molecular physics and time-resolved photoelectron spectroscopy are briefly reviewed. Additionally, this chapter covers the computational methods, which are applied to calculate ground state ionization energies of solvated molecules. The third chapter discusses the implementation of liquid phase pump-probe photoelectron spectroscopy, covering the experimental setup. Steady-state and time-resolved photoelectron measurements on water and other solvents are presented in this chapter. These measurements are essential to test and characterize the experimental setup. In chapter 4, the results from the static and time-resolved photoelectron spectroscopy of Quinoline Yellow WS in aqueous solution are presented. Chapter 5 covers the results on the light-induced isomerization of the two amino-azobenzene dyes Methyl Orange and Metanil Yellow. In chapter 6, the XUV-only photoelectron spectroscopy of aqueous Tryptophan is presented. Chapter 7 provides summary and outlook.

2 Time-resolved Photoelectron Spectroscopy

Photoelectron spectroscopy was first introduced as a method to precisely measure absolute values of atomic binding energies [26]. Since then X-ray photoelectron spectroscopy has been applied to countless molecular and solid state targets and has become a standard tool in physical chemistry. The ability to access binding energies of the whole manifold of populated electronic states makes it the most important source of information on the electronic structure of matter [27]. Since the method can be used to obtain information on populated electronic states, it can also access excited states if these have previously been populated.

To populate an excited state with an ultrashort laser pulse and probe the ensuing reaction with a second pulse after a variable time-delay, is the central idea of pump-probe spectroscopy. Molecular pump-probe spectroscopy enables us to watch chemical reactions in real time, which is the essence of the novel fields of femtochemistry [5] and femtobiology [6]. The foundation for this was the groundbreaking work of Ahmed H. Zewail on pump-probe spectroscopy [5]. With femtosecond spectroscopy the excited state dynamics in photoreactions can be directly observed, including transient states that are inaccessible with static techniques. The observables are often optical signals. For example in transient absorption spectroscopy the observable is the change in probe pulse absorption, induced by the pump pulse.

If the photon energy of the probe pulse is sufficient to eject electrons from the sample, the transient photoelectron spectrum becomes accessible. Thus femtosecond pump-probe spectroscopy is combined with photoelectron spectroscopy. The resulting method is capable of resolving electronic and vibrational dynamics in molecules. The photoelectron probe gives direct access to binding energies, which often yields a much more intuitive physical picture [7].

In this chapter I will provide a brief overview of time-resolved photoelectron spectroscopy. I will review the concepts of molecular physics and photochemistry, which are relevant to the presented work, and give an overview of the theory of molecular electronic states and molecular orbital theory. This review is largely based on Demtröder's textbook on molecular physics [28] and Carlson's review of photoelectron spectroscopy [27]. Additionally I will introduce the computational methods, used in this thesis to calculate ionization energies of molecules. The brief review of density functional theory in section 2.2 is based on Lewars' 2016 textbook on computational chemistry [29]. Whenever examples are useful to illustrate the discussed concepts, I will use the water molecule, since its electronic configuration is important in later chapters of this thesis.

2.1 Molecular Electronic Structure

The properties of a molecular system are governed by the Schrödinger equation. In a complete quantum mechanical description, the Hamiltonian depends on the degrees of freedom of all nuclei and electrons. Additionally, the degrees of freedom are coupled by the electron-electron repulsion, the inter-nuclear repulsion, and the attraction of electrons and nuclei.
Already for the simplest molecule, the hydrogen ion consisting of two protons and a single electron, the Schrödinger equation cannot be solved analytically. Therefore any description of the electronic states of complex molecules has to rely on approximations, the first of which is typically the Born-Oppenheimer approximation. It exploits the fact that the electrons are orders of magnitude lighter than the nuclei and can respond almost instantly to any change of the position of the nuclei. Therefore one can consider the electrons as moving in the potential of the fixed nuclei. In a system with fixed nuclei the kinetic energy of the nuclei can be neglected and the inter-nuclear repulsion can be treated as constant.
With this powerful approximation the nuclear and electronic degrees of freedom are decoupled. Then eigenfunctions $\phi_n(\mathbf{r})$ of the purely electronic Hamiltonian $\hat{H}_0$ with eigenvalues E_n exist for any fixed nuclear geometry $\mathbf{R}$. The electronic part of the Schrödinger equation becomes

$$\hat{H}_0\phi_n(\mathbf{r}) = E_n(\mathbf{r};\mathbf{R})\phi_n(\mathbf{r}) \tag{2.1}$$

with n as the principal quantum number of the electronic states. The energy eigenvalues E_n still depend parametrically on the nuclear geometry, therefore the energy of each electronic state can be seen as multidimensional surface in the space of the nuclear coordinates. By reintroducing the kinetic energy of the nuclei $\hat{T}_N$, the nuclear part of the Schrödinger equation becomes

$$\left[\hat{T}_N + E_n(\mathbf{R})\right]\chi_{n,\nu}(\mathbf{R}) = E_{n,\nu}\chi_{n,\nu}(\mathbf{R}) \tag{2.2}$$

with ν as the quantum number of the nuclear wavefunctions $\chi_{n,\nu}$. In this equation the energy E_n acts as a potential, which is why $E_n(\mathbf{R})$ can be seen as a potential energy surface on which the nuclei move. The nuclear wavefunctions $\chi_{n,\nu}$ describe the rotational and vibrational states of the corresponding electronic state.
While this is already a great simplification, the electronic Hamiltonian at a fixed geometry still contains the full electron-electron interaction. For large molecular systems with many electrons this makes a solution of the electronic part of the Schrödinger equation nearly impossible, even for a fixed nuclear geometry. The next step towards a solution is the independent particle approximation, which considers a single electron in the potential of the nuclei and in the averaged potential of all other electrons. The

result is an electronic wavefunction $\phi_i(\mathbf{r}_i)$ for each electron which depends only on the coordinates of that electron. This one-electron spatial wavefunction is called an orbital. In atoms every orbital is characterized by the principal quantum number n, the angular momentum quantum number l, and the magnetic quantum number m, analogous to the wavefunctions of the hydrogen-atom. For a given principal quantum number n the other quantum numbers have the ranges $l = 0 \,..\, n-1$ and $m = -l \,..\, l$. Atomic orbitals with $l = 0, 1, 2, ...$ are designated as $s, p, d, ...$-orbitals. The hydrogen atom is the only system for which the atomic orbitals can be calculated analytically. For other atoms the orbitals can be approximated, for example, by the hydrogen wavefunctions.
According to the Pauli exclusion principle every orbital can contain two electrons with opposite spins. The electronic ground state of a system with N electrons is the configuration, where the $N/2$ orbitals with the lowest energies are occupied. In many cases N is even, meaning that the total spin is zero and the ground state is a singlet state. Doublet states are states with a total spin of 1/2, i.e. an odd number of electrons. Triplet states have a total spin of one, i.e. two electrons with parallel spins.

2.1.1 Molecular Orbitals

The usual approach to obtain approximate solutions for molecular orbitals is by means of a linear combination of atomic orbitals (LCAO). Figure 2.1 illustrates this, using the water molecule as an example. The hydrogen atoms each only have one electron in an s-orbital, so the wavefunction of H_2 can be symmetric (σ) or anti-symmetric (σ^*). The oxygen atom has 8 electrons in the configuration $1s^2 2s^2 2p^4$, where the $2p$-orbital is split into three contributions, due to three possible values of the magnetic quantum number.
The linear combination of the atomic orbitals can now form molecular orbitals with lower or higher energy than the initial atomic orbitals as shown in figure 2.1. Orbitals with a lower energy than the atomic orbitals are bonding while orbitals with a higher energy are anti-bonding. Orbitals which maintain the shape and energy of the atomic orbital are non-bonding, like the $1b_1$ orbital of the water molecule which maintains the shape of the oxygen $2p_x$-orbital.
The molecular orbitals of water are no longer labeled according to quantum numbers, but rather according to the symmetry of the molecular orbital. The water molecule belongs to the C_{2v} point group, meaning that the molecular orbitals can be labeled as a_1, a_2, b_1 and b_2 according to their symmetry. In the photon energy range covered in the experimental part of this thesis, the highest three occupied orbitals are relevant. These are, from higher to lower binding energy, the O-H-bonding, $2p$-like $1b_2$ orbital, the slightly-bonding mixed O($2p$)O($2s$)H($1s$) $3a_1$ orbital, and the non-bonding, out-of-plane lone-pair $1b_1$ orbital [13]. The shapes of the orbitals from a density functional calculation are also shown in figure 2.1 (details of the computational method are given in section 2.2).

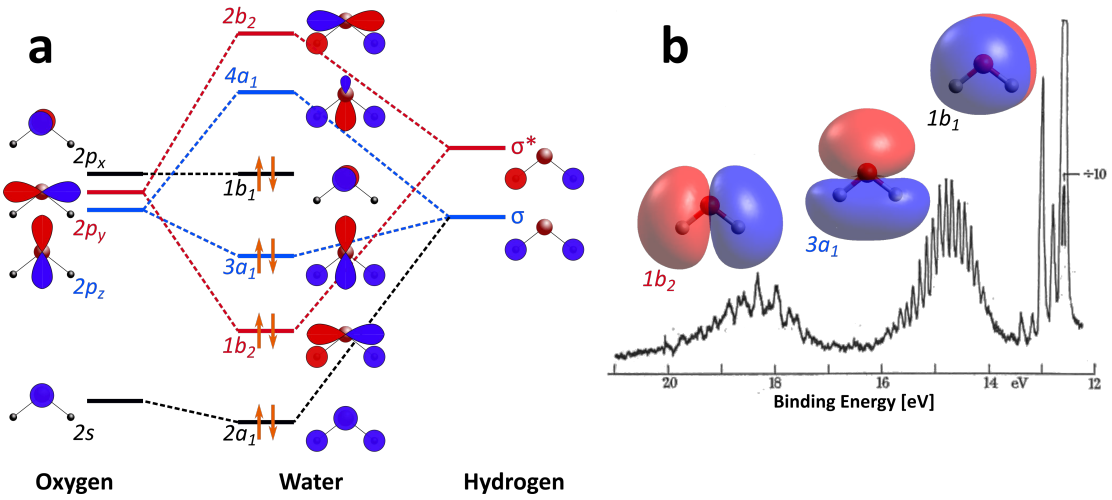

Fig. 2.1: **a)** Water orbitals arising from a linear combination of oxygen and hydrogen orbitals. **b)** High resolution photoelectron spectrum of gas-phase water (adapted from ref. [30]). The orbital shapes from density functional theory (see section 2.2) are shown at the corresponding photoelectron peaks.

Large organic molecules often have no symmetry and thus their orbitals cannot be categorized relying on the symmetry of the entire molecule. In this case it is useful to further categorize the interaction of the atomic orbitals by their symmetry with respect to the bond connecting the atoms. Orbitals which are symmetric with respect to rotation around the bond axis are designated with σ. Bonding σ-orbitals have no nodal plane between the nuclei, while anti-bonding σ^*-orbitals have a nodal plane perpendicular to the bond axis. σ-orbitals are the result of overlapping s-orbitals or p-orbitals in the direction of the bond axis.

p-orbitals perpendicular to the bond axis form bonding π- and anti-bonding π^*-orbitals depending on their relative phases. The π-orbitals in conjugated systems are often delocalized and span large parts of the molecule. In most photoactive organic molecules these extended π-systems are responsible for large absorption cross-sections and thus for the photophysical and photochemical properties of the molecule.

p-orbitals which do not form π- or σ-bonds largely maintain the shape of the atomic orbitals. These non-bonding n-orbitals are also called lone-pair orbitals due to their weak interaction. Non-bonding orbitals, for example on groups containing nitrogen atoms, have a strong influence on the photochemistry of organic molecules, as will become apparent in the study of the amino-azobenzene dyes (chapter 5).

2.1.2 Photoelectron Spectroscopy

Photoelectron spectroscopy is the most direct method to obtain information about the energies of molecular orbitals. In the technique, electrons are promoted from an occupied molecular orbital into the continuum, usually with a single high energy XUV or X-ray photon. The observable is the kinetic energy of the ejected photoelectron E_{kin}. This kinetic energy is the difference between the photon energy and the ionization energy, i.e. the energy necessary to eject the electron. Therefore the ionization energy for a known photon energy $h\nu$ is directly given by

$$IE = h\nu - E_{kin} \tag{2.3}$$

Koopman's theorem states that this measured ionization energy for a molecular orbital is equal to the binding energy of the electron in its orbital, while all other molecular orbitals are not influenced by the ionization. This treats the ionization as instantaneous and neglects any influence of electronic relaxation of the ion on the photoelectron energy. In this approximation the photoelectron spectrum directly maps the energies of the orbitals. If the ion however relaxes on the timescale of the photoemission, reacting to the change in electronic states due to the missing electron, this relaxation energy can be transmitted to the electron. In that case the measured kinetic energy is higher than the binding energy of the molecular orbital.
Additionally the ion will not necessarily be left in the ground vibrational state after photoionization. In the framework of the Born-Oppenheimer approximation the transition probability in photoionization depends on the overlap between the initial vibrational state and the vibrational levels of the ionic state. This is known as the Franck-Condon principle. For ionic states with a different potential energy surface $E_n(R)^{(ion)}$ the overlap can be largest between the zero vibrational level of the neutral state and a higher vibrational level of the ionic state.
In this context it is important to differentiate between the adiabatic binding energy and the vertical binding energy. The adiabatic binding energy is the energy difference between the neutral molecule and the completely relaxed molecular ion. In contrast, the vertical binding energy is associated with the maximum of the measured photoelectron band, which is the transition energy to the ionic vibrational level with the highest transition probability.
These concepts are schematically illustrated for a system with two molecular orbitals in figure 2.2. The ionic ground state $E_1(R)^{(ion)}$ corresponds to removing an electron from the highest occupied molecular orbital (HOMO) in figure 2.2. The potential energy surface of $E_1(R)^{(ion)}$ has its minimum at a nuclear geometry, which is similar to the minimum geometry of the neutral ground state. Therefore the transition probability is highest for the ground vibrational level and the adiabatic and vertical binding energies are similar.

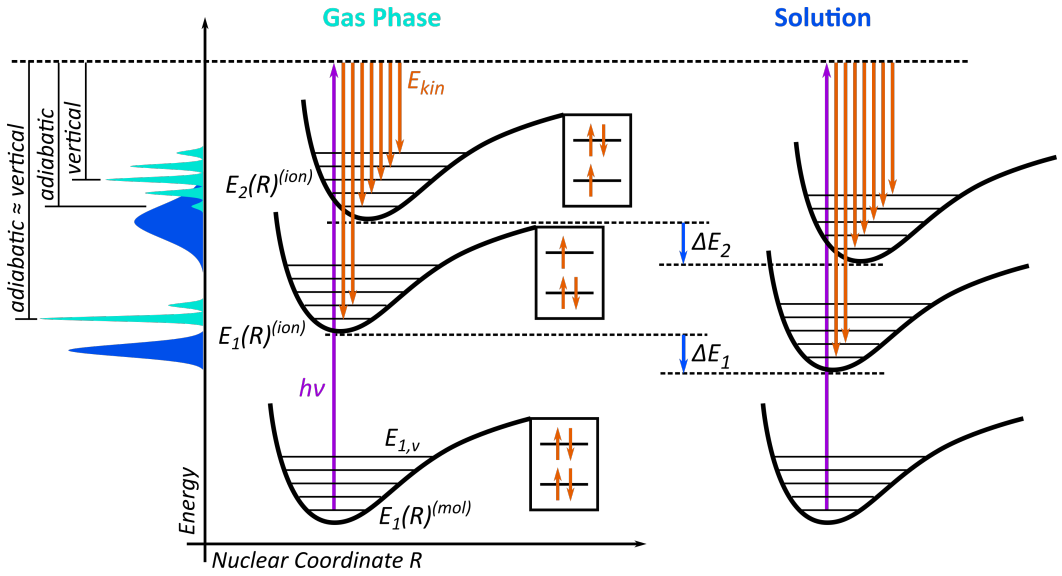

Fig. 2.2: Principle of photoelectron spectroscopy in the gas phase and in solution for a system with two orbitals. Schematic photoelectron spectra are shown on the left, illustrating the difference between adiabatic and vertical binding energies (see text). The phase transition shift of the ground state is not shown, the shifts of the first and second ionic state are ΔE_1 and ΔE_2.

The second ionic state $E_2(R)^{(ion)}$, corresponding to removal of an electron from the lower-lying orbital, has a different equilibrium geometry. Thus the schematic photoelectron spectrum shows more peaks from vibrational transitions and the difference between the adiabatic and vertical binding energy is substantial.

Usually ionic states with the electron removed from a non-bonding orbital have a similar equilibrium geometry and therefore high cross-sections for ionization to the ground vibrational level of the ionic state. The change in equilibrium geometry caused by the removal of bonding electrons is larger, therefore the transition to the ground vibrational level will often not have the highest cross-section. This effect is clear in the photoelectron spectrum of gas-phase water, where only few vibrational peaks are observed for the non-bonding $1b_1$-orbital, while there is a long vibrational progression on the peak assigned to ionization from the bonding $3a_1$ orbital (fig. 2.1b).

So far the discussion considers an isolated molecule. For a molecule in solution the influence of the solvent has to be included, which changes the measured binding energy. The polarization of the dielectric around the ion decreases the energy of the ionic states relative to the vacuum level significantly. In general there is also a shift of the ground state energy, but it is small in comparison.

The photoionization process is usually too fast for solvent reorganization to play a role, therefore the measured binding energy is the energy difference of the solvated

molecule and the ion in the polarized environment without its reorganization. This decreases the molecule-ion energy gap and therefore yields lower binding energies (fig. 2.2). The difference in binding energy is known as phase transition shift, which is the same for all orbitals if only the polarization effect is considered. In this polarization model the influence of the individual molecular orientation is neglected. However in liquid water hydrogen bonding has a large impact on the orbital energies. Sophisticated computational methods are needed to accurately predict the effect of the condensed phase on individual molecular orbitals [13, 31, 32].

2.2 Calculation of Ionization Energies with Density Functional Theory

Most computational chemistry methods rely on the linear combination of atomic orbitals as a basis. Thus accurate representations of the atomic orbitals are a prerequisite. Hydrogen-like wavefunctions have radial nodes and are therefore not particularly suitable for computational treatment. Therefore modern computational methods rely on approximation of the atomic wavefunctions with Gaussian functions. In this approach an atomic wavefunction is approximated by a linear combination of Gaussian functions, usually centered on the nucleus. In computational chemistry such an approximate wavefunction is called a basis function and a finite set of basis functions constitutes a basis set.

The complexity of the basis set is determined by both the number of Gaussian functions used for the fitting of a single atomic orbital and by the number of atomic orbitals included in the calculation for a particular element. For example the so-called "minimal" basis set STO-3G uses three Gaussian functions to approximate a single atomic orbital. For a hydrogen atom STO-3G then includes a single basis function for the $1s$-orbital. For elements from ${}_3$Li to ${}_{10}$Ne the $1s$, $2s$, and $2p$ orbitals are included. This group includes for example oxygen, so for the water molecule this basis set would include all atomic orbitals depicted in figure 2.1.

Calculations using the minimal basis set often fail to accurately reproduce experimentally determined molecular properties. One reason for this is that the spreading of an atomic orbital into the molecule is not described well with a single basis function. The single basis function falls off too quickly with the distance from the nucleus. This can be overcome by splitting the basis function for each atomic orbital into two contributions, one for the inner shell and one for the outer shell. The outer shell function falls of more slowly and thus provides the flexibility to adjust the spreading of the atomic orbital. The basis sets with split basis functions are called double-zeta if each function is split into two contributions, triple-zeta if it is split into three contributions, and so forth.

Another improvement of basis sets is based on the inclusion of higher-lying, unoccupied atomic orbitals. The basis functions of these higher-lying orbitals are in this context

known as polarization functions, since they allow the electron distribution to be displaced along a specific coordinate, i.e. polarized. Such a basis set would for example include the unoccupied $3d$-orbitals for an oxygen atom.

2.2.1 Density Functional Theory

There are many computational methods that aim to solve the Schrödinger equation. In these wavefunction-based, so-called *ab initio* techniques, the accuracy of the calculation is determined by the necessary approximations and the quality of the basis set. Density functional theory (DFT) follows a fundamentally different approach. The main idea is to describe molecular properties using the electron density function $\rho(\mathbf{r})$. The advantage of this approach is a far lower computational cost compared to *ab initio* methods, while the results are in many cases comparable. Another advantage of this approach is that the electron density is an actual physical observable, that can be measured for example in X-ray diffraction experiments.
The central theorem of DFT, first published by Hohenberg and Kohn [33], states that molecular properties are functionals of the electron density. This means that there is, for example, a functional $E[\rho(\mathbf{r})]$, which returns the correct ground state energy of the system. The theorem however merely proves the existence of this functional and does not give a method for constructing it, which is the central problem of DFT. Additionally the electron density is also unknown. The most successful way to deal with this problem is the method devised by Kohn and Sham. The first step is to express the total ground state energy as

$$E[\rho] = T[\rho] + \int \rho(\mathbf{r}) v(\mathbf{r}) \mathrm{d}\mathbf{r} + V_{ee}[\rho_0] \tag{2.4}$$

where T is the kinetic energy of the system. The integral term is the classical energy of the electrons in the electrostatic potential $v(\mathbf{r})$ of the nuclei. V_{ee} is the electron repulsion potential energy. The next step is to introduce a fictitious reference system, in which electrons do not interact, but which has exactly the same unknown ground state electron density ρ as the real system. With this the kinetic energy can be expressed as

$$T[\rho] = T_{ref}[\rho] + \Delta T[\rho] \tag{2.5}$$

where $\Delta T[\rho]$ is the difference between the real and the reference kinetic energy. The electron repulsion term can be rewritten by integrating over the repulsion between infinitesimal volume elements

$$V_{ee}[\rho] = \frac{1}{2} \int\int \frac{\rho(\mathbf{r})\rho(\mathbf{r}')}{|\mathbf{r} - \mathbf{r}'|} \mathrm{d}\mathbf{r}\mathrm{d}\mathbf{r}' + \Delta V_{ee}[\rho] \tag{2.6}$$

with a correction term $\Delta V_{ee}[\rho]$.

The correction term mainly needs to mediate the problem that in a charge density description an electron will repel itself, which is obviously unphysical. The ground state energy can then be written as

$$E[\rho] = T_{ref}[\rho] + \int \rho(\mathbf{r}) v(\mathbf{r}) \mathrm{d}\mathbf{r} + \frac{1}{2} \int\int \frac{\rho(\mathbf{r})\rho(\mathbf{r}')}{|\mathbf{r} - \mathbf{r}'|} \mathrm{d}\mathbf{r}\mathrm{d}\mathbf{r}' + E_{xc} \tag{2.7}$$

with both correction terms comprised in the exchange-correlation energy E_{xc}. The exchange correlation energy is now the only term including the elusive energy functional. The kinetic energy of the non-interacting reference system can be rewritten introducing the Kohn-Sham (KS) spatial wavefunctions

$$T[\rho] = -\frac{1}{2} \sum_{i=1}^{2n} \langle \psi_i^{KS} | \nabla_i^2 | \psi_i^{KS} \rangle \tag{2.8}$$

Substituting this kinetic energy into equation (2.7) and employing a variational approach leads to the KS-equations

$$\left[-\frac{1}{2} \nabla_i^2 + v(\mathbf{r}) + \int \frac{\rho(\mathbf{r}')}{|\mathbf{r} - \mathbf{r}'|} + v_{xc} \right] \psi_i^{KS} = \epsilon_i^{KS} \psi_i^{KS} \tag{2.9}$$

where v_{xc} is the exchange correlation potential, which is a functional derivative of the exchange correlation energy. The part in brackets is also known as the KS-operator $\hat{h}^{KS}$. The DFT algorithm for the solution of the Kohn-Sham equations is:

1. The initial guess for the electron density is calculated from a superposition of the basis functions $\{\phi\}$.

2. Using the electron density, an initial guess for v_{xc} is calculated. In this step the approximate exchange correlation functional E_{xc} is needed.

3. With the initial guesses for the density and the potential an approximate KS-operator $\hat{h}^{KS}$ is calculated.

4. The KS-matrix elements are calculated on the basis set, i.e. $K_{l,m} = \langle \phi_l | \hat{h}^{KS} | \phi_m \rangle$.

5. Diagonalizing the KS-matrix yields the first approximation of the energy eigenvalues ϵ_i^{KS} and the wavefunctions ψ_i^{KS}, expanded on the basis set.

6. The first iteration of the KS-orbitals is used to calculate an improved electron density ρ.

The steps 2-6 are then repeated until a specified convergence in reached. The quality of the result then obviously depends largely on the specific exchange correlation functional.

The number of developed DFT functionals is tremendous, and it is out of the scope of this thesis to provide an overview. It should be noted that all functionals employed in the calculations for this thesis use the meta-generalized gradient approximation (meta-GGA). Within this approximation the functional locally depends on the electron density as well as its first and second spatial derivatives. Additionally some hybrid functionals are used. In hybrid functionals the energy functional includes a certain percentage of the so-called Hartree-Fock exchange energy. This is a correction of the classical Coulomb repulsion term by reintroducing "Pauli repulsion".
It should be noted that molecular orbitals are intrinsically not included in DFT, but are reintroduced as the KS-wavefunctions. These KS-orbitals are similar in shape and symmetry to the orbitals obtained with wavefunction-based methods. Therefore they provide a good basis at least for a qualitative discussion of orbital properties [34].

2.2.2 Calculation of Ionization Energies in Solution

Before ionization energies can be calculated the equilibrium geometry of the molecule in question has to be determined, since DFT operates on fixed nuclear coordinates. The equilibrium geometry is characterized by a minimum in total energy, thus finding it with DFT is quite straightforward. Starting at an approximate geometry the spatial derivatives of the total energy can be used to find the minimum on the potential energy surface.
In principle the Kohn-Sham DFT calculation provides molecular orbitals ψ_i^{KS} and orbital energies ϵ_i^{KS}. According to Koopmann's theorem these orbital energies should directly correspond to the vertical ionization energies of the molecule, and no further calculation would be necessary. Since the KS-orbitals are not true wavefunctions, this simple approach is not sufficient. While the shape and ordering of DFT orbitals is correct in many cases, the orbital energies are often poor approximations for the vertical ionization energies.
The energy for ionization from the highest occupied molecular orbital (HOMO) can be found using a different approach. A separate DFT calculation of the ionized molecule, i.e. with one electron removed, gives the ground state energy of the ion. The difference between the ground state energies of neutral and ionized molecule then provides a better value for the HOMO ionization energy. Because ionization is considered too fast for structural rearrangement, both calculations are performed on the optimized geometry of the neutral molecule to obtain the vertical ionization energy.
This method is used for the calculations of vertical binding energies in this thesis, but it obviously only works for ionization from the HOMO. Binding energies of lower-lying orbitals are obtained under the assumption that the spacing between the KS-orbitals corresponds to the spacing between the real molecular orbitals. Thus all orbitals are corrected by the same energy shift, which is the energy difference between the KS-energy of the HOMO and the HOMO binding energy calculated with a DFT calculation of

the ion. There is some justification for this assumption, since DFT often produces quite accurate values for the gap between the highest occupied and lowest unoccupied molecular orbitals. This way the full photoelectron spectrum can be calculated at least qualitatively.
The DFT described so far considers an isolated molecule. There are two basic methods of including the solvent in quantum chemistry calculations, explicit and implicit solvation. For explicit solvation, solvent molecules are placed around the solute molecule. Since it is usually too costly to include the solvent molecules in a full quantum-mechanical calculation, explicit solvation is often treated with molecular mechanics (MM) or mixed methods of quantum and molecular mechanics (QM/MM).
The option used in this thesis is implicit solvation, which places the solute in a cavity within a continuous dielectric medium. A key problem in this so-called conductor-like polarizable continuum model (CPCM) is the shape of the cavity. Spherical cavities are rather crude models for most molecules. A more sophisticated model is that of the exposed surface of overlapping spheres placed at each nucleus. The radius of the spheres is determined by the van-der-Waals radius. In recent implementations, the surface is then smoothed by projecting a large number of polygons onto it [35].
The CPCM includes three contributions to the solute-solvent interaction energy. The cavitation energy is the energy needed to create the cavity. The dispersion energy accounts for attractive or repulsive van der Waals forces. The electrostatic energy accounts for the electrostatic interaction between solute and solvent. The cavitation and the dispersion energy are calculated using empirical values and only depend on the cavity surface area. The electrostatic energy is evaluated by placing polarization charges on the cavity surface and calculating the electrostatic interaction between the molecular charges and the polarization charges [29].
As mentioned before the choice of the appropriate functional and basis set for a particular problem is a highly complex topic. For this thesis the choice is based mainly on a recent publication by Isegawa and coworkers [36]. In this publication various computational methods, including several DFT functionals, were benchmarked for the calculation of ionization energies of organic molecules [36]. HOMO ionization energies were calculated both in vacuum and in aqueous solution using the CPCM.
For geometry optimization Isegawa and coworkers [36] chose the meta-GGA functional TPSS [37] and the def2-TZVP basis set [38]. Therefore this method of geometry optimization was chosen also for the calculations in this thesis. Of the density functionals tested in ref. [36], the Minnesota hybrid functional M06-2x [39] produced the best results regarding ionization energies. Therefore this functional, together with the def2-TZVP basis set, is used for the DFT calculation of ionization energies. All DFT calculations presented in this thesis are performed using version 4.0.1 of the *ORCA* program system [40].
As an example, I will consider again the water molecule. The geometry optimization is performed with the TPSS functional on the def2-TZVP basis set. A vacuum

DFT calculation at the M06-2x/def2-TZVP level of theory yields values of 10.77 eV, 12.78 eV, and 16.43 eV for the KS-energies of the highest occupied molecular orbitals. This is far from the experimental values of 12.6 eV, 14.8 eV, and 18.6 eV [41]. The correction energy extracted from the DFT calculation of the ion is 1.90 eV. Therefore the corrected ionization energies are 12.67 eV, 14.68 eV, and 18.33 eV and thus much closer to experimental values.

2.3 Molecular Dynamics upon Electronic Excitation

So far only occupied molecular orbitals have been considered. But absorption of a photon can transfer an electron into an unoccupied molecular orbital. The system is left in an electronically excited state, with a hole in one of the former occupied orbitals and an electron in a previously unoccupied orbital. The system relaxes and dissipates the energy, for which multiple mechanisms are available after excitation.
To discuss the possible relaxation dynamics, it is important to take into account that the minimum of the excited state potential energy surface is not necessarily at the same nuclear geometry as the minimum of the ground state potential energy surface. Excitation, similar to ionization, occurs vertically, i.e. without a change in the geometry. The transition probability is proportional to the overlap of the initial and final wavefunctions, therefore electronic excitation is often combined with vibrational excitation. Especially ultrashort laser pulses can excite many vibrational modes coherently, due to their large spectral bandwidth.
Since the excitation leads to a non-equilibrium geometry, electronic relaxation is usually accompanied by changes in the molecular geometry. Conical intersections are points in the nuclear geometry landscape where two potential energy surfaces cross. At these points the system can pass from one electronic state into another. This radiationless transition between electronic states is called internal conversion. An internal conversion accompanied by a spin-flip is defined as intersystem crossing, meaning, for example, the transition from an excited singlet state to an excited triplet state. While internal conversion typically occurs on timescales from femtoseconds to a few picoseconds, intersystem crossing is typically associated with timescales of hundreds of picoseconds. The ground state potential energy surface can have multiple energy minima, corresponding to multiple stable or meta-stable ground state geometries, also known as isomers. Radiationless relaxation pathways can leave the molecule in a different isomer. To simplify the description of isomerization pathways, the change in geometry is often considered to occur along a single reaction coordinate, for example a rotation around a specific bond.
Complementary to the radiationless pathways, molecules can also undergo relaxation to the ground state by emission of radiation, i.e. fluorescence. Fluorescence typically occurs on nanosecond timescales. Since internal conversion timescales are orders of magnitude faster, it is usually assumed that fluorescence occurs after internal conversion

to the lowest excited singlet state. The energy difference between the absorbed photon and the emitted photon is known as the Stokes-shift.
After the relaxation to the electronic groundstate, remaining vibrational energy can be dissipated as heat. In solution vibrational energy can also be transferred to the solvent. The ground state vibrational relaxation in solution is usually associated to timescales of around ten picoseconds.
Pump-probe photoelectron spectroscopy aims to follow the dynamics after excitation on all involved potential energy surfaces. The simplest scheme of pump-probe spectroscopy uses two short laser pulses with a tunable delay between them. The first pulse excites the sample, initiating the dynamics which are then probed with the second short laser pulse after a delay time Δt. In all-optical techniques the observable is often the change in probe pulse absorption caused by the pump pulse. This technique can observe molecular dynamics after excitation through observables like the bleach of ground state absorption, the rise and decay of excited state absorption, and stimulated emission. A rigorous analysis of various detection schemes and the expected signals can be found in [42].

2.3.1 Visible-Pump, XUV-Probe Photoelectron Spectroscopy

In time-resolved XUV photoelectron spectroscopy the probe is the ionization by a single high energy photon and the observable is the photoelectron kinetic energy as discussed in the previous section. As a simple example I will consider a system with two excited states and a single ionic state. For such a system the potential energy curves along a generic reaction coordinate are schematically shown in figure 2.3.
For simplicity I will assume that the visible pump pulse excites the molecules exclusively into the second excited state. In the simplified model the second excited state only relaxes to the first excited state with a rate constant k_2. From the first excited state the molecules relax exclusively to the ground state with a rate constant k_1. For this system the rate equations are

$$\begin{aligned} \frac{\mathrm{d}N_0}{\mathrm{d}t} &= -P_{pump}(t)N_0(t) + k_1 N_1(t) \\ \frac{\mathrm{d}N_1}{\mathrm{d}t} &= k_2 N_2(t) - k_1 N_1(t) \\ \frac{\mathrm{d}N_2}{\mathrm{d}t} &= P_{pump}(t)N_0(t) - k_2 N_2(t) \end{aligned} \tag{2.10}$$

with the populations of the ground state N_0, the first excited state N_1, and the second excited state N_2. The function P_{pump} is the time-dependent transition probability from the ground state to the second excited state, which is proportional to the envelope of the pump pulse. Usually pulses with Gaussian envelopes are assumed both for the pump- and the probe pulse. The system of rate equations can be solved numerically to obtain the time-dependent populations of all states.

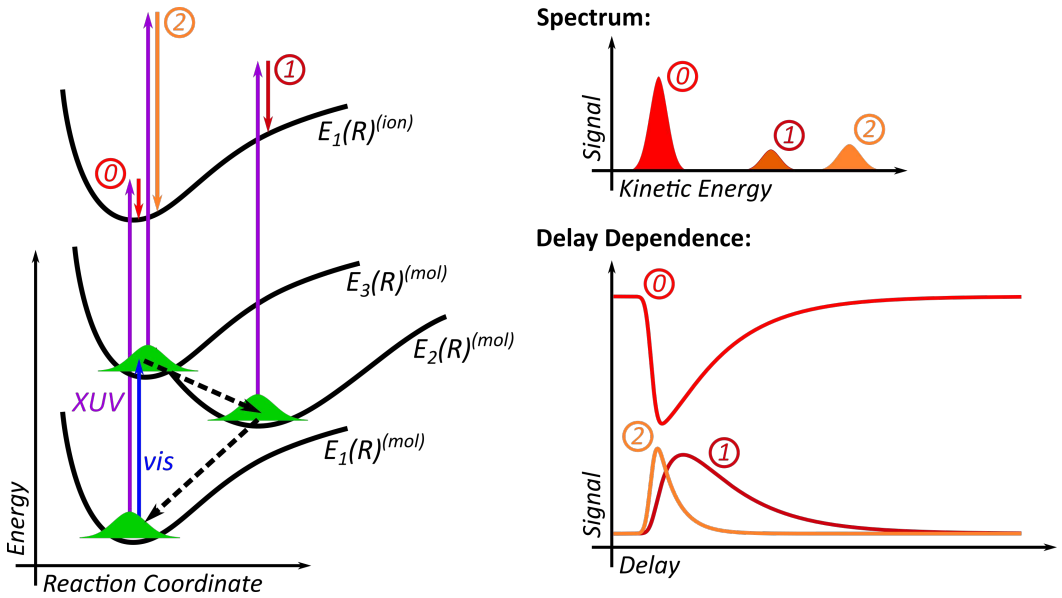

Fig. 2.3: Principle of visible-pump XUV-probe photoelectron spectroscopy for a system with two excited states and a single ionic state. If the XUV pulse arrives before the pump pulse, only the ground state peak is detected (0). For short positive delays one expects an excited state peak (2) together with a depletion of the ground state signal. For longer delays the signal of the intermediate state rises (1). The delay dependence of the expected signals is also shown for a sequential decay (see text).

At a delay Δt after the pump pulse the probe pulse ionizes the sample and ejects electrons with a kinetic energy, linked directly to the energy of the states. The model assumes that ionization only goes to a single ionic state and that the ionization cross-section is the same for all states. Under this assumption the delay-dependent signals are proportional to the populations of the states, convoluted with the Gaussian envelope of the probe pulse.

The expected signals for this model system are shown in figure 2.3, based on the numerical solution of the rate equations (2.10). The second excited state in the example is populated by the Gaussian pump pulse and decays with a single time constant $\tau = 1/k_2$. As shown in ref. [42], its signal can then be expressed with the analytical function

$$S(\Delta t) = \frac{A}{2} \exp\left[\frac{\sigma_{cc}^2}{2\tau^2} - \frac{\Delta t}{\tau}\right] \times \left(1 + \mathrm{erf}\left[\frac{\Delta \mathrm{t}}{\sqrt{2}\sigma_{\mathrm{cc}}} - \frac{\sigma_{\mathrm{cc}}}{\sqrt{2}\tau}\right]\right) \tag{2.11}$$

where σ_{cc} is the width-parameter of the cross-correlation of the pump- and probe pulse. This function will be used in this thesis as a model function to retrieve decay constants from the measured signals.

In cases where a single decay constant is not sufficient to model the measured signal, biexponential decays will be modeled with a sum of two exponentially decaying signals. This served as a good approximation for cases where signals from two excited states overlap.
The model of well-separated signals with exponential decay constants is idealized. It is apparent from figure 2.3 that the geometry of the potential energy surfaces of the excited states and the ionic state will influence the signals. The photoelectron spectrum of a single excited state can shift to lower kinetic energy when the system relaxes to a minimum on the potential energy surface. Also the possibility of ionization to multiple ionic states has to be considered. Therefore accurate simulation of pump-probe photoelectron data demands knowledge of all involved potential energy surfaces, including the ionic states.
However, pump-probe photoelectron spectroscopy has some significant advantages over optical pump-probe techniques like transient absorption spectroscopy. If the photon energy of the probe pulse is high enough, the electronic ground state can be ionized and ground state dynamics can be observed. The transient signals from excited states and the ground state are clearly separated in energy and can therefore be distinguished without ambiguity. Additionally, while ionization cross-sections may vary, photoionization knows no true "dark" states as they exist in absorption. Any populated molecular state can be ionized and therefore observed [7].

3 Time-Resolved Photoelectron Spectroscopy of Liquids

The application of time-resolved photoelectron spectroscopy to liquids has a fundamental problem. Photoelectron spectroscopy relies on the transfer of electrons to a detector without scattering, but evaporation from a liquid surface leads to a higher pressure and hence scattering probability. Since liquids are volatile samples with a high vapor pressure, the pressures that can be reached in the presence of a free liquid surface are incompatible with transferring electrons to a detector without scattering. On the other hand any pressure below the vapor pressure will turn a free liquid surface into ice via evaporation and subsequent freezing caused by the energy loss.
These difficulties were first overcome in the work of Hans and Kai Siegbahn where a free-flowing jet of formamide was used to obtain the first photoelectron spectra of a liquid [43]. The jet delivers a clean, constantly refreshed liquid surface into the vacuum and is small enough to maintain the necessary vacuum conditions. Liquid filaments of water, and various alcohols, were first introduced by Faubel and coworkers [11]. Since then the technique was used for multiple studies of liquid water [10, 12, 13] and solvated electrons [44–47]. Liquid jet studies using XUV pulses are still mainly performed at synchrotron facilities, but recently light sources based on high harmonic generation have been implemented for studies on liquids and solvated molecules [48–50].
This chapter discusses the implementation of femtosecond XUV photoelectron spectroscopy on such a liquid jet. The XUV pulses are generated via high harmonic generation. A time-delay-compensating XUV monochromator is used to select a single harmonic from the high harmonic spectrum. The chapter starts with a brief discussion of the monochromator setup, but since the monochromator was designed and implemented for a previous PhD-thesis, I refer to the thesis of Martin Eckstein [17] for more details. Section 3.2 covers the liquid jet setup. The liquid jet assembly is described, focusing on the modifications that were made to improve the commercial *Microliquids* system. Photoelectron spectra are acquired with a magnetic bottle time-of-flight spectrometer [18], the calibration and performance of which is described.
Once operational, the photoelectron spectrometer can be used to collect photoelectron spectra of water and other solvents. The results from photoelectron spectroscopy of liquid water are presented in detail in section 3.3. The binding energies of water in the gas phase as well as in the liquid phase are measured in good agreement with literature values. Further experimental challenges are discussed in this context related to electrostatic, electrokinetic, and light-induced space charge effects.
Section 3.4 discusses XUV-only photoelectron spectroscopy of other solvents. These measurements are the first step towards extending the technique to solvents other than water, which is challenging due to differences for example in vapor pressure and viscosity.

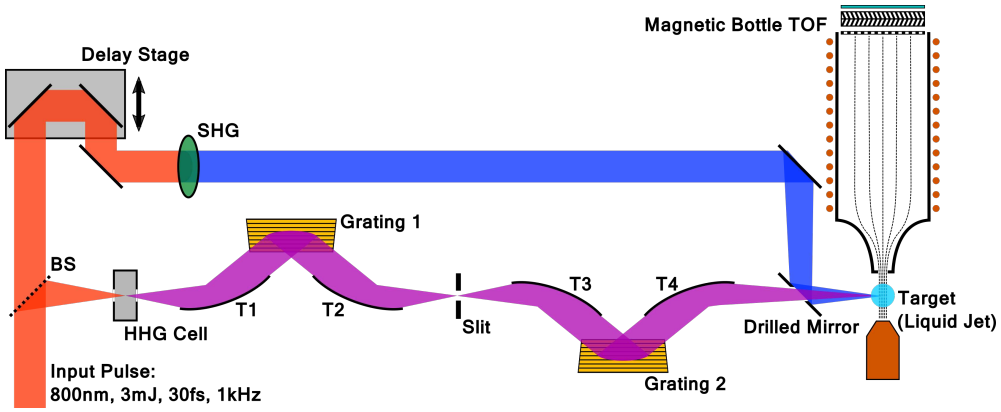

Fig. 3.1: Simplified schematic of the experimental setup. A beamsplitter (BS) splits the laser pulse into two pulses, one for high harmonic generation (HHG) and one for second harmonic generation (SHG). The wavelength selection stage of the XUV monochromator consists of two toroidal mirrors T1 and T2 and the first grating. The toroidals T3 and T4 and the second grating constitute the recompression stage. The XUV and second harmonic foci overlap on the liquid jet.

Furthermore pump-probe photoelectron measurements of water are presented in section 3.5, using both 800 nm and 400 nm pump pulses. Multiphoton ionization of water by the pump light is observed. To be able to distinguish water signals from molecular signals, a careful characterization of the intensity dependence of these single-color spectra, and of pump-probe signals from water, is essential. The only pump-probe signal found in water is the so-called laser-assisted photoelectric effect in liquid and gas phase water, which is observed both with 800 nm and, although two orders of magnitude weaker, with 400 nm pump light.

3.1 Optical Setup

A schematic of the experimental setup is shown in figure 3.1. A commercial titanium sapphire amplifier system (*Aurora, Amplitude Technologies*) provides ultrashort laser pulses with a pulse energy of up to 20 mJ at a repetition rate of 1 kHz. Typically pulse durations of 20-30 fs can be achieved at a central wavelength of 795 nm. The pointing of the laser output beam is actively stabilized with a commercial system (*TEM Aligna*), thus allowing for stable operation for days. Only part of the pulse energy (3-5 mJ) is used for the monochromator setup described in this section. The pulse is split into a pump pulse, used for second harmonic generation, and a probe pulse, used to generate the XUV pulse.
In the pump arm the beam diameter is reduced with a telescope from 3 cm to 1.5 cm. Approximately 1 mJ of pulse energy is used for second harmonic generation (SHG).

The SHG setup consists of an 800 nm half wave plate and a 50 μm thick BBO-crystal [51]. No additional focusing optics are used, so the 400 nm light is generated from a collimated beam. This reduces the conversion efficiency to around 15%, i.e. a maximum output pulse energy of ca. 150 μJ. Due to the high density of the liquid jet target and the absorption cross-section of the investigated molecules this was found to be sufficient, which justifies the simplified SHG scheme.

3.1.1 High Harmonic Generation

In the XUV arm, a telescope reduces the beam diameter to 1 cm. The separate telescopes for the pump and probe beams allow for independent adjustment of the divergence in both arms. This proved highly useful to match the positions of the pump- and probe-beam foci along the propagation direction. The probe pulse (2-3 mJ) is then used for high harmonic generation.
Phase-matched high order harmonic generation was discovered in 1987, when Ferray and coworkers observed the emission of XUV radiation upon focusing a high intensity pulsed laser beam into a rare gas target [8]. The spectrum of the emitted radiation showed peaks at odd multiples of the laser frequency. Furthermore the harmonic intensity did not exhibit the expected decrease with harmonic order but showed a plateau of practically constant intensity up to a sharp cut-off frequency.
A deeper understanding of the high harmonic spectrum came with the introduction of a quasi-static model [52, 53] separating the process into three steps, namely ionization, acceleration, and recombination. The ionization step is treated in the tunneling regime, i.e. quantum mechanically. After ionization, the electron is described as a free electron in the laser field, neglecting the field of the ion. For linearly polarized light it can be shown that half the electrons return to the ion within the first laser period after ionization. The returning electron can recombine with the ion, which is accompanied by the emission of radiation. In a multicycle laser pulse the radiation emitted from multiple cycles interferes constructively for odd multiples of the driver frequency and destructively for even multiples, leading to a high harmonic spectrum with peaks at odd harmonics. The high harmonic structure in the spectrum means that the high harmonic radiation is also periodic in the time-domain, leading to a attosecond pulse train [52].
Although high order harmonic generation has been observed in a variety of gas-phase and solid state materials since its discovery, most applications rely on noble gases as generation medium. In the experiments for this thesis mainly argon and krypton are used. The 800 nm laser pulse with a typical energy of 2-3 mJ is focused into a gas cell with a dielectric focusing mirror (focusing length 62.5 cm, not shown in fig. 3.1). The pressure in the 6 mm long gas cell is actively stabilized with a commercial control system (*MKS Systems*). Typical pressures in the cell are 20 mbar for krypton and 40 mbar for argon.

3.1.2 Time Delay Compensating XUV Monochromator Setup

The full harmonic spectrum, while very useful for transient absorption spectroscopy [54] and the generation of attosecond pulse trains or isolated attosecond pulses [55], is not ideal for photoelectron spectroscopy, where a defined photon energy is required. This issue can be overcome by selecting a single harmonic using diffractive optics. The result is a femtosecond XUV pulse with a duration similar to that of the IR input pulse. This is achieved by the time-delay compensating monochromator.

The optical layout of the time-delay compensating monochromator is based on conical diffraction and was first introduced by Poletto and coworkers [56]. Due to the low conversion efficiency of high harmonic generation [57], a crucial parameter in XUV optical systems is the transmission efficiency. In a conical diffraction configuration and with an appropriate blaze angle, efficiencies in the first diffraction order of up to 70% of the reflectivity of the grating material can be reached [58]. Other methods to spectrally filter XUV light are for example multilayer mirrors [59], transmission zone plates [60] or reflection zone plates [61]. Although the time-delay-compensating monochromator is the most complicated of the schemes listed above in terms of optical setup, it offers the highest degree of wavelength tunability, a feature especially important for experiments using the XUV as pump pulse [62].

In the monochromator setup used in this thesis an aluminum foil (100 nm, *Lebow*) is inserted after the high harmonic generation, transmitting a large part of the generated XUV light but blocking the co-propagating IR. It is used when the XUV light is transmitted in zero order, for example to measure the XUV spectrum. When the gratings are in the position to transmit the first diffraction order to the target, the filter can however be removed since the IR and XUV are separated after the first grating. This increases the XUV transmission by a factor of 2-5 depending on harmonic order and the age of the aluminum filter, whose transmission decreases when it is oxidized.

The first stage of the monochromator consists of a toroidal mirror collimating the XUV light (T1), a grating in conical diffraction configuration, and a second toroidal mirror (T2), focusing the beam onto a slit, all under grazing incidence. At this point the wavelength selection is complete and one could refocus the XUV beam after the slit directly onto the target.

However the diffraction on the first grating leads to a phase front tilt, which significantly affects the pulse duration of the XUV pulse. Since this is a purely geometrical effect it can be compensated by a second monochromator stage, which is an exact mirror image copy of the first stage. It has been shown that the compression stage shortens the duration of the XUV pulse significantly and that the entire setup can reach a time resolution close to the duration of the initial 800 nm pulse [17].

The XUV monochromator that is implemented at the Max Born Institute features three sets of gratings with grating constants of 150, 300, and 600 lines/mm and blaze angles of 3.4°, 4.3°, and 7.0° respectively, optimized for different energy ranges. The

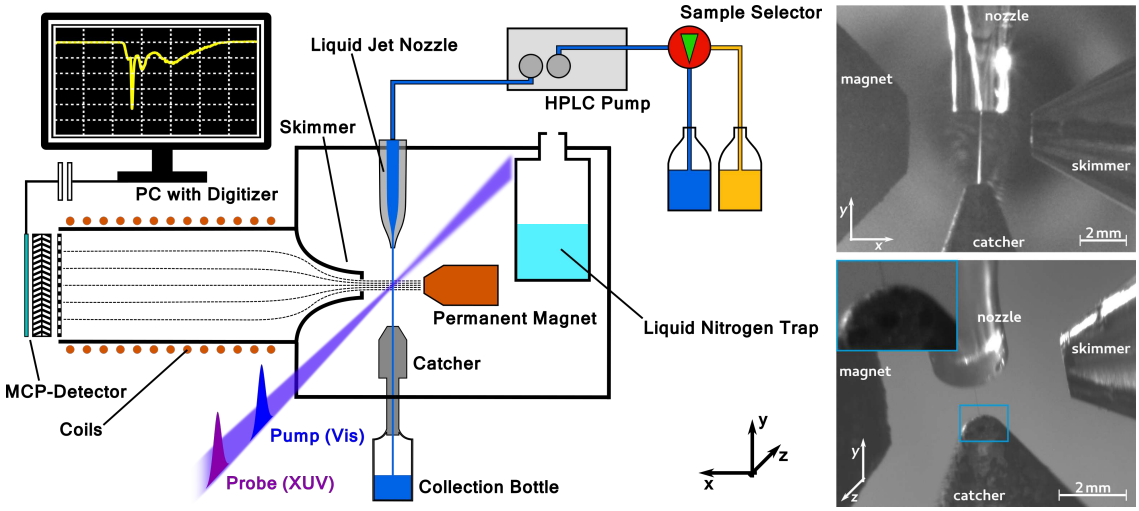

Fig. 3.2: Schematic of the liquid jet endstation. The chamber housing the liquid jet is directly attached to the monochromator vacuum system. The pump- and probe-beam foci are overlapped with the liquid jet in the interaction region of the magnetic bottle time-of-flight electron spectrometer.

transmission and spectral resolution of all gratings were extensively characterized in gas-phase experiments using a velocity map imaging spectrometer. Unless otherwise specified the data for this thesis was acquired using the 150 lines/mm grating, mainly for its higher transmission of the lower harmonics (i.e. harmonics 11-17). In typical operation the XUV bandwidth is approximately 0.5 eV, the XUV flux is around $5{\cdot}10^6$ photons per pulse, and the pump-probe cross-correlation is 40-50 fs [17].

3.2 Liquid Jet Endstation

Figure 3.2 shows a schematic of the liquid jet endstation. The main vacuum chamber, housing the liquid jet, is directly attached to the chamber of the monochromator vacuum system, which houses the compression stage. An aluminum tube with an inner diameter of 7 mm connects the last chamber of the monochromator to the main liquid jet chamber. This scheme, similar to a differential pumping stage, helps to maintain pressures below 10^{-6} mbar in the monochromator chamber with the liquid jet in operation. Since the output beam of the monochromator is fixed in space, it cannot be aligned to the liquid jet. Therefore the entire liquid jet setup is designed such that it can be moved with sub-millimeter precision in all three dimensions.
In figure 3.2 the laser pulses propagate in the positive z-direction, the liquid jet flows from the nozzle to the catcher in the negative y-direction, and the photoelectrons are guided into the spectrometer in the positive x-direction. The pump and probe beams enter the chamber non-collinearly under an angle of approximately 0.5°. They

are overlapped with the liquid jet in the focus of the magnetic bottle time-of-flight spectrometer. The two photographs in figure 3.2 show the interaction region. The top photograph shows it from the point where the laser beam exits the liquid jet chamber, in a typical alignment of the liquid jet. The second camera (bottom photograph) views the catcher from an angle in the y, z-plane and is used to align the liquid jet into the catcher.

3.2.1 Liquid Jet Assembly

The first version of the liquid jet assembly used for the experiments presented in this thesis is a commercial product from *Microliquids GmbH* [63]. A commercial high pressure liquid chromatography (HPLC) pump is used to pump the sample from the sample bottles to the nozzle, where the liquid filament is formed. Before the HPLC pump the sample can be selected with a polyether ether ketone (PEEK) selector valve, allowing switching between up to eight samples during a running measurement. The HPLC pump has the advantage that a set flowspeed is maintained with an accuracy of 5%. The pump adjusts the piston speed, and therefore the pressure in the tubing after the pump, accordingly.
Going from capillaries with smaller diameter to capillaries with larger diameter can help to reduce pressure oscillations caused by the piston movement. In the system presented here an approximately 1.5 m long capillary with an inner diameter of 0.127 mm is used directly after the pump, followed by an approximately 20 cm long capillary with an inner diameter of 0.762 mm. Inlet filters in the sample bottles and two inline filters in the HPLC pump and before the feedthrough to the vacuum system prevent dust from entering and blocking the nozzle channel.
The fused silica liquid jet nozzle is held in place by a stainless steel nut on a polytetrafluoroethylene (PTFE) seal. The nozzle has an inner diameter of typically 18 μm at the tip leading to a liquid filament of approximately 15 μm in diameter [64]. Typically a flowspeed of 0.5 ml/min is set at the pump. This yields pressures in the range of 20-30 bar, measured with the pressure sensor of the HPLC pump, and a streaming velocity of about 30 m/s.
In vacuum the liquid filament starts breaking apart into droplets after a decay time t_{lj}, which depends on the density ρ, the surface tension σ, and the dynamic viscosity η of the solvent used. According to ref. [65], the decay time is given by

$$t_{lj} = 12 \left(\sqrt{\frac{\rho d_{lj}^3}{\sigma}} + \frac{3\eta d_{lj}}{\sigma} \right) \tag{3.1}$$

for a jet with diameter d_{lj}. For the streaming velocity and the diameter given above this means that a water jet will remain intact for approximately 3.5 mm. In the arrangement presented here the liquid jet travels a distance of 4-5 mm through the main vacuum

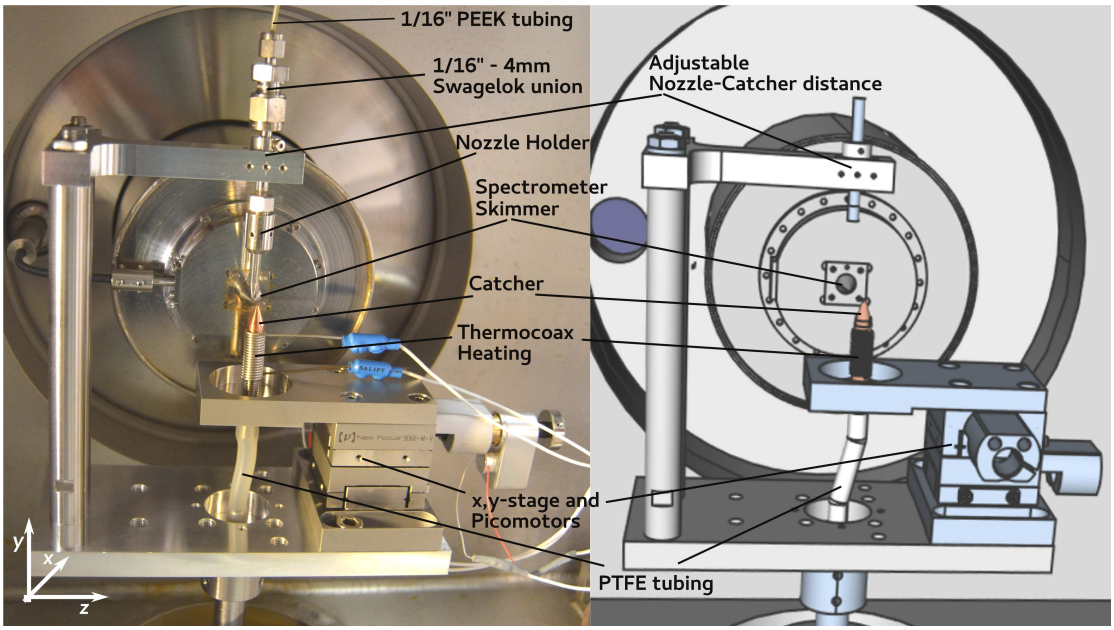

Fig. 3.3: Photograph and 3D construction drawing of the new design of the liquid jet assembly, that was developed as part of this thesis. The nozzle holder and the fused silica nozzle are the only parts from the *Microliquids* assembly still in use. The entire assembly is held on a single 12.7 mm stainless steel tube, which can be moved manually in the x, y and z directions with manipulators outside the vacuum chamber (not shown).

chamber after which it exits the high vacuum through the 200 μm orifice of a heated copper catcher. This decreases the pressure in the interaction region further, since the full break up of the jet takes place inside the catcher. Additionally a cold trap filled with liquid nitrogen is used to further reduce the pressure by freezing the solvent evaporated from the liquid jet. With this approach a pressure below 10^{-4} mbar can be maintained in the liquid jet chamber when operating the liquid jet with water.
The liquid is collected below the catcher in an evacuated bottle, cooled with an ice water mixture to keep the collected liquid below its room temperature vapor pressure. It was found that the sample collection is only feasible with water. For more volatile solvents like ethanol, cooling of the collection bottle to temperatures below the respective boiling point at the pressure of the collection bottle would have to be implemented.
In the *Microliquids* setup the liquid jet assembly is mounted on a three axis manipulator used to manually align it to the XUV beam and the photoelectron spectrometer. The catcher is mounted on a separate equivalent manipulator. This constitutes the main weakness of the original construction. Any alignment of the liquid jet to the laser beam or the spectrometer focus region has to be made with both manipulators simultaneously, which inherently carries the risk of the jet missing the catcher orifice. When the

jet misses the catcher orifice, the result is a sharp rise in chamber pressure due to evaporation and often a complete interruption of the experiment caused by freezing of the jet. In the worst cases also freezing of the liquid inside the nozzle is observed, damaging the nozzle and halting operation for several hours. Furthermore separate mounting of the liquid jet and the catcher reduces the mechanical stability of the jet relative to the catcher, also increasing the risk of missing the catcher orifice.
As part of this thesis a new liquid jet assembly was designed, aiming to correct the weakness of the original design. Figure 3.3 shows a 3D construction drawing and a photograph of the newly designed liquid jet catcher assembly in the vacuum chamber. In the new design the liquid jet and the catcher are mounted together on a single 12.7 mm stainless steel tube, which also connects the catcher and the collection bottle. The entire assembly can be moved in all three dimensions with manipulators outside the vacuum. The liquid is supplied by a flexible peek capillary connected to a fixed vacuum feedthrough. The redesigned catcher is mounted on a stainless steel tube heated by Thermocoax wire wound around it. It can be aligned to the liquid jet via a *Newport* x,y translation stage using two picomotors with a travel range of 10 mm. Flexible PTFE tubing connects the catcher tube (6 mm OD) to the tube guiding the liquid to the collection bottle.
With the improved design, the alignment of the liquid jet to the laser beam and the photoelectron spectrometer is independent of the jet-catcher alignment. This improves not only the alignment and stability in long measurements, but also makes it possible to change the liquid jet position during measurements to investigate the liquid and gas phase contributions separately, as will be discussed in detail in section 3.3. In the new design the distance between the nozzle and the catcher cannot be adjusted in vacuum anymore. This adjustment is however only necessary when switching solvents and therefore having to perform it in air is not a significant disadvantage.

3.2.2 Magnetic Bottle Time-Of-Flight Spectrometer

The magnetic bottle time-of-flight (TOF) spectrometer was invented by Kruit and Read [18]. A strongly divergent magnetic field is used to parallelize photoelectron trajectories into a small divergence beam, ideally with an acceptance angle of 2π. If the high magnetic field region, in which the electron trajectories are parallelized, is sufficiently short, the device is suitable for TOF measurements. In this case the dependence of the TOF on the emission angle is negligible and the TOF is proportional to $1/\sqrt{E_{kin}}$. The large acceptance angle leads to a much higher collection efficiency than can be achieved in field-free TOF spectrometers [66].
The magnetic bottle spectrometer used in the experiments presented here is similar to the designs published elsewhere [64, 66]. The magnetic field "bottle" is induced by a permanent magnet and copper coils wound around the flight tube. The permanent magnet with a soft iron pole generates a strong magnetic field (approx. 0.5 T) in the

interaction zone. The copper coils induce a weak homogeneous magnetic field, which leads to the diverging field to parallelize the electron trajectories. Typically a current of 0.9 A was applied to the coils. The flight tube is approximately 0.76 m long. It is separated from the main liquid jet chamber by a skimmer with a diameter of 0.5 mm. The skimmer and the outer tube, surrounding the coils, are made of μ-metal, thus shielding the flight tube from external magnetic fields.
A grounded gold mesh electrically terminates the flight tube before the photoelectron detector. The electrons are detected with a chevron-type microchannel plate (MCP) detector. The front of the MCP is held on a positive acceleration potential of approximately 300 V with respect to ground, to increase the detection efficiency. Typically a voltage of 2100 V is applied to the back of the MCP, meaning that the amplification potential is 1800 V. A phosphor screen behind the MCP is held on a constant voltage of 3000 V and used as anode for electron detection.
The electronic signal on the phosphor screen is coupled out over a highpass filter, consisting of a 2.2 nF capacitor and a 50 kΩ resistance. The signal is amplified by a factor 10 using a fast amplifier (*Philips 6954-B-10*), and detected on a 1 MHz PCI digitizer card (*Acqiris AP 240*). The trigger signal for the digitizer is supplied by a photodiode, detecting the 800 nm input laser pulse. This way the electron arrival time relative to the laser pulse can be obtained.
The initial detection scheme yielded a FWHM of over 10 ns for single electron signals, which would limit the resolution for higher kinetic energies. This response was found to be caused by the capacitances between the phosphor screen and the MCP. The single electron pulse FWHM could be improved to 4-5 ns by increasing the distance between the MCP and the phosphor screen from initially 1 mm to 4 mm and fitting the assembly with insulating screws to decrease the capacitance.
To align the electron spectrometer to the fixed focus position of the monochromator, the entire liquid jet chamber can be adjusted in all three dimensions. Additionally the magnet position can be adjusted with three stepper motors to align it to the flight tube entrance. In other setups employing a magnetic bottle spectrometer to study photoemission from liquids with UV ionization, the magnetic bottle is adjusted by using it as a spatial imaging device and obtaining a focused image of the liquid jet in the interaction region [64]. This is however not necessary when XUV pulses are used, since the XUV pulse ionizes diffuse gas phase targets and the magnetic bottle can be adjusted by optimizing the resolution, i.e. minimizing the peak width for a given gas phase photoemission line. The initial measurements for alignment and calibration of the magnetic bottle spectrometer were carried out with nitrogen, argon, and helium gas targets, injected into the vacuum chamber through the same liquid jet nozzle.
Figure 3.4a shows TOF photoelectron spectra of gas phase molecular nitrogen, obtained using the 13th harmonic (20.3 eV). The digitizer signal is acquired for each laser shot and averaged to obtain what is referred to as "averaging mode" spectra. Simultaneously the arrival times of single electron hits surpassing a certain threshold (usually 6 mV)

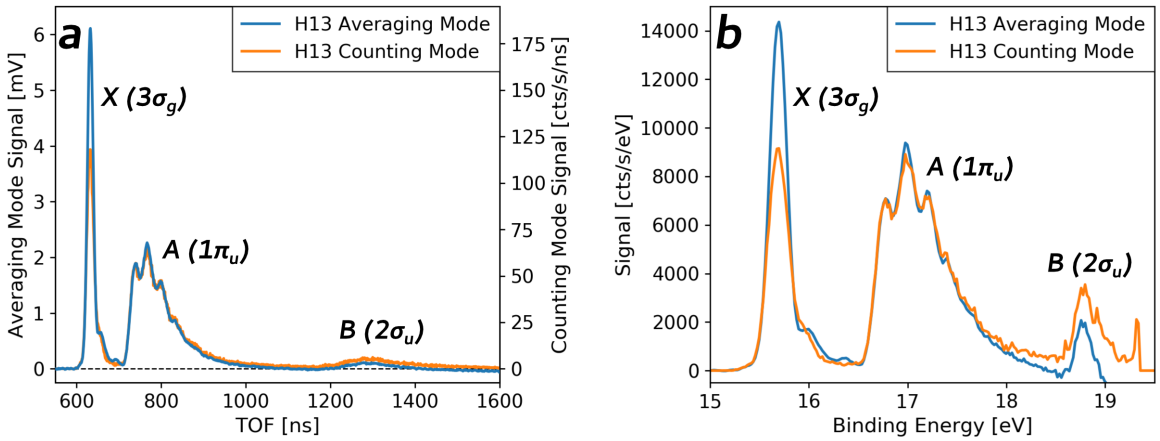

Fig. 3.4: Photoelectron spectra of nitrogen obtained with the harmonic 13 (20.3 eV). **a)** The TOF trace shows that the counting mode saturates at approximately 120 cts/s at the repetition rate of 1 kHz. **b)** After calibration and conversion to binding energy (see text) the photoelectron spectrum is consistent with ref. [67]. The sharp peak at a binding energy of 19.3 eV probably corresponds to electrons reflected from the magnet, which arrive at long TOF.

are detected in the acquisition software. The sum of the detected hits over their arrival time gives the "counting mode" spectra. In TOF ranges where the electron signal is sufficiently weak to distinguish individual electrons, the counting mode suppresses the analog noise, for example from the digitizer, and increases the signal-to-noise ratio efficiently.

The averaging and counting mode spectra in figure 3.4a are scaled to overlap for the photoelectron bands associated to the A- and B-state at longer TOF. In the high energy (i.e. short time of flight) band associated to the X-state the counting mode signal is significantly lower than the averaging mode signal. This is caused by the saturation of the counting mode, which sets in when the signal exceeds approximately 120 counts per second in a single channel (1 ns). With the laser repetition rate of 1 kHz this corresponds to an average of 0.12 counts per laser shot.

The cause of the saturation is the probability of overlapping electron peaks in the single shot signal, which cannot be distinguished as individual counts. Assuming that electron peaks falling into the same 6 ns range cannot be separated, the decrease in signal due to overlapping peaks can be estimated with the Poisson distribution function. Under this assumption a signal of 0.18 cts/shot would be decreased by approximately 30% and a signal of 0.06 cts/shot would still be detected as 5% weaker in the counting mode. This estimate agrees well with the measured saturation, a small decrease in the A-state photoelectron peak at 70 cts/s is also visible in figure 3.4.

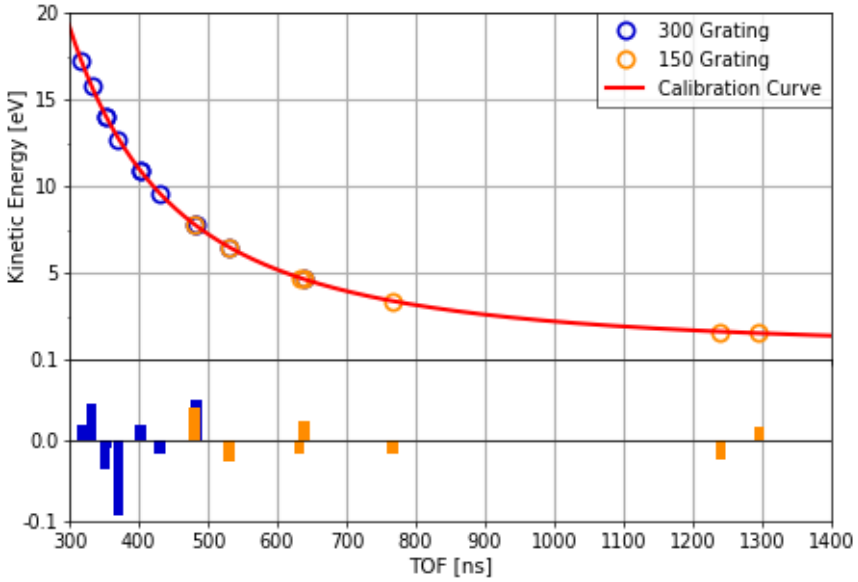

Fig. 3.5: Calibration curve measured with the harmonics 11-21 using the vertical binding energies of the X, A, and B ionic states of molecular nitrogen [67]. The residuals show that the error in the energy calibration is below 0.1 eV. The extracted calibration parameters are: t_0 =0.7±2.2 ns, s_0 =76.8±0.6 cm and E_0 =0.51±0.03 eV.

From the scaling factor a conversion factor between averaging mode and counting mode signals can be extracted which is approximately 30 cts/s/mV. This means, in good agreement with measured single-shot spectra, that the average area of a single count is 30 pVs.

Another effect observed in the TOF traces is that the averaging mode signal drops to negative values for long time-of-flight values, an effect that is strongly reduced in the counting mode. The effect increases with higher count rates, and is therefore probably linked to the response of the detection electronics to higher currents. This distortion of the low kinetic energy part of the photoelectron spectrum is however irrelevant for this setup, since the signals of interest are at the high energy end of the spectrum.

The three bands in the photoelectron spectrum of figure 3.4 correspond to ionization from the $3\sigma_g$, $2\pi_u$, and $2\sigma_u$ orbitals, which are labeled as the X, A, and B ionic states respectively. In a He II photoelectron spectroscopy study Baltzer and coworkers reported vertical binding energies of 15.58 eV, 16.93 eV, and 18.75 eV for these ionic states [67].

The known vertical binding energies yield three TOF values with a known electron kinetic energy, which can be used for calibration of the electron spectrometer. The photoelectron spectrum of nitrogen is measured for several harmonics to obtain calibration points covering a wide range of kinetic energies. The calibration function of

the photoelectron spectrometer is given by

$$E_{kin} = \frac{m_e}{2}\left(\frac{s_0}{t - t_0}\right)^2 - E_0 \tag{3.2}$$

where m_e is the electron mass. The calibration parameters are the flight-time offset t_0, the travel distance s_0, and an energy offset E_0 [64]. Figure 3.5 shows the calibration curve obtained with nitrogen and several harmonics using two of the monochromator grating sets. The calibration measurement spans an energy range of 15 eV and the deviation from the calibration curve for all points is below 100 meV. With this calibration curve, any TOF spectrum $S(t)$ can be converted to a kinetic energy spectrum

$$S(E_{kin}) = S(t)\frac{(t - t_0)^3}{m_e s_0^2} \tag{3.3}$$

The result of this conversion is shown in figure 3.4b, where the integrated peak area, now in cts/s/eV, is the same as before in cts/s/ns. The converted spectrum agrees remarkably well with the spectrum measured with He II radiation [67], which demonstrates the high signal-to-noise ratio and resolution of the magnetic bottle spectrometer.
The peaks associated with the vibrational progression of the A-state have a width of approximately 0.3 eV, meaning that the resolution is limited by the monochromator rather than the electron spectrometer [17]. For higher kinetic energies the resolution decreases due to the width of single electron signals. For example, the peak of the X-state obtained with the harmonic 21 has a width of approximately 0.7 eV. At a kinetic energy of approximately 17 eV and factoring in the resolution of the monochromator of approximately 0.5 eV this corresponds to a TOF spectrometer resolution of approximately 3%.

3.2.3 Electrostatic Charging

The fused silica liquid jet nozzle is insulating and can therefore charge up during measurements. The generated electric field influences the photoelectron trajectories on the way to the spectrometer entrance (fig. 3.6). The influence amounts to an energy shift observed in the photoelectron spectra which depends on the position of the nozzle. Figure 3.6 shows the energy shift measured for the positions of the X, A, and B bands of nitrogen with harmonic 15 (23.5 eV) upon moving the nozzle up (y-direction).
To model the charging effect, the field is assumed to be that of a point charge with charge Q at the nozzle tip $(0, y)$. The x-component of the field is then given by

$$\mathcal{E}_x = \frac{Q}{4\pi\epsilon_0}\frac{x}{\sqrt{x^2 + y^2}} \tag{3.4}$$

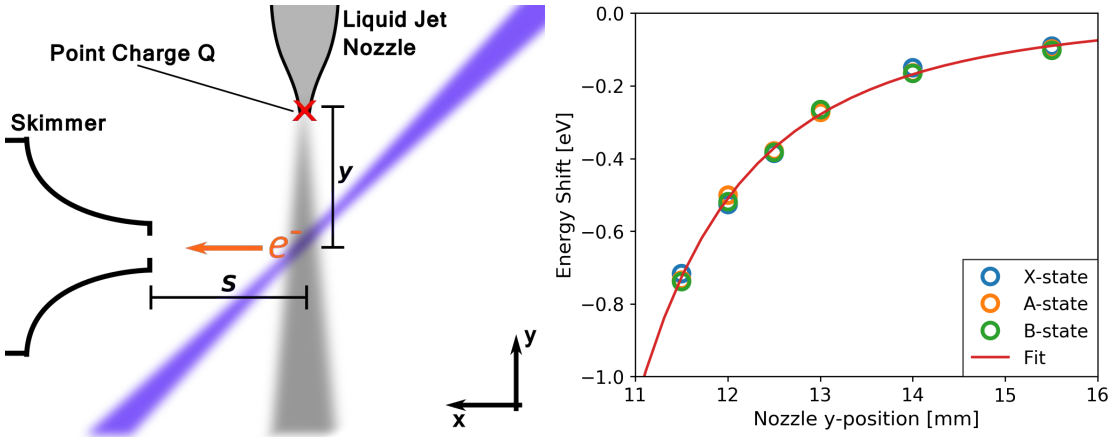

Fig. 3.6: The insulating liquid jet nozzle can charge up in experiments, which leads to a shift of photoelectron peaks when the nozzle is moved up (y-direction). The field of the charged nozzle is modeled with the field of a point charge (see text). The fit with equation (3.5) yields a total charge of 160±20 pC and a zero position of 7.6±2 mm, where the zero position is the y-position, where the nozzle tip would be in the laser beam.

and the energy difference accumulated by the electrons traveling to the skimmer in x-direction is

$$\Delta E = \int_0^s \mathcal{E}_x \, \mathrm{d}x = -\frac{Qe}{4\pi\epsilon_0}\left(\frac{1}{\sqrt{s^2+y^2}} - \frac{1}{y^2}\right) \tag{3.5}$$

with the distance s from the interaction region to the spectrometer entrance. For the vertical movement this model can be fit to the measured energy shift, giving a y-position of approximately 4 mm for the lowest measured point and a total charge of approximately 160 pC. From camera images the lowest measured position can however be estimated to be 1-2 mm. Additionally charging-induced shifts above 1 eV are never observed in the liquid jet experiments. The simple point charge model seems to overestimate the charge and underestimate the distance, which is expected since the charge is distributed vertically.

The electrostatic charging can be removed by coating the nozzle surface with graphite spray [14, 64]. In gas phase tests this was found to remove the effect entirely. The graphite spray is however slightly water soluble and very well soluble in ethanol. Thus coating the nozzle causes problems in liquid jet measurements, especially when working with solvents other than water. As evident from figure 3.6, the shift is the same for electrons originating from different molecular orbitals. This means that the shift is independent of the electron kinetic energy. Therefore by acquiring daily calibration curves using the photoelectron spectrum of water, a procedure discussed in the next section, the shift can be corrected and the graphite spray is not needed.

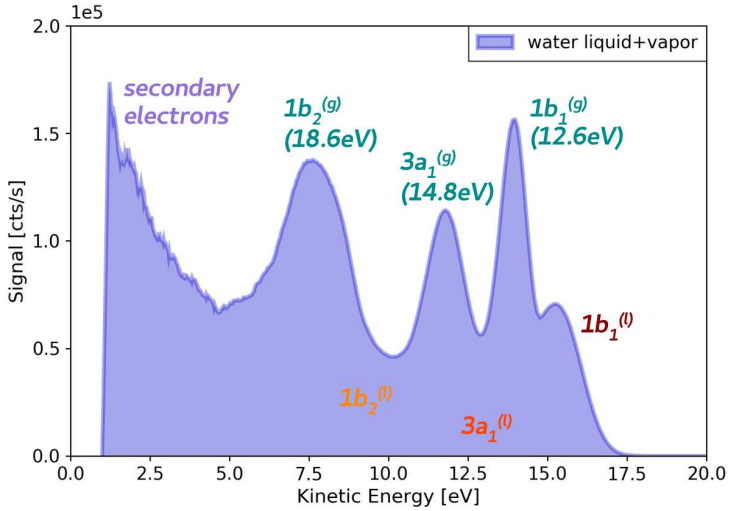

Fig. 3.7: Photoelectron spectrum obtained with harmonic 17 (26.5 eV) incident on the liquid jet running with water. The spectrum consists of contributions from water vapor, liquid water, and secondary electrons.

3.3 Photoelectron Spectroscopy of Water

The photoelectron spectrum obtained with harmonic 17 (26.5 eV) incident on the liquid jet is shown in figure 3.7. The spectrum consists of three contributions, namely photoelectrons from water vapor, from liquid water, and so-called secondary electrons. Since the liquid jet has a diameter of approximately 15 μm and the XUV focus diameter is around 100 μm, a strong contribution of electrons of gas phase water, evaporated from the jet, is to be expected. The gas phase water spectrum consists of the three peaks labeled as $1b_1^{(g)}$, $3a_1^{(g)}$, and $1b_2^{(g)}$, according to the highest three occupied water orbitals introduced in section 2.1. The binding energies of the valence orbitals of gas phase water are well-known from photoelectron spectroscopy and are 12.6 eV, 14.8 eV, and 18.6 eV for the $1b_1$, $3a_1$, and $1b_2$ orbitals respectively [41].
The clearest liquid water signal in the spectrum in figure 3.7 is the peak with the highest kinetic energy labeled $1b_1^{(l)}$. The peaks from the liquid $3a_1$ and $1b_2$ orbitals overlap with the gas phase water signals. The first measurement of the ionization potential of liquid water orbitals was carried out in 1997 [11]. Since then several studies [12–14] have refined not only the values of the vertical binding energies but also improved the understanding of the effects leading to the differences between the gas phase and liquid phase photoelectron spectra. The main observation is a phase transition shift of all photoelectron peaks to lower binding energies and a broadening of the liquid peaks with respect to the gas phase measurements. The $3a_1$ peak is strongly broadened and a splitting of the orbital, as it is observed in ice, is suggested [13, 14].
The peak at low kinetic energy is attributed to secondary electrons, which have lost

kinetic energy by scattering on water molecules inside the liquid jet. The kinetic energy of the secondary electron peak is independent of the harmonic order, i.e. the photon energy [11]. It can therefore be easily identified by measuring spectra with various harmonic orders.

3.3.1 Charging Effects and Energy Calibration

In photoelectron spectroscopy with femtosecond laser pulses large numbers of electrons are ejected from the sample by every single laser pulse. Especially for solid state targets this can lead to high electron densities in proximity to the sample and a subsequent distortion of the spectrum by the Coulomb repulsion between the electrons. In photoelectron spectra this mainly results in broadening of the peaks [68, 69]. The liquid jet is a high density target and the source region is small, so effects of the space charge have to be considered.
A simple test for light-induced spectral distortions can be performed by varying the XUV intensity. This can be accomplished for example by inserting the aluminum filter or using different slit widths, which changes the XUV photon flux. For a variation in count rates by an order of magnitude, no spectral broadening of the water peaks is observed. The peak broadening seems to be well below the intrinsic resolution of the XUV monochromator or the natural peak width of water photoelectron peaks.
While the light-induced charging is hence negligible, another charging effect is caused by the interplay of the aqueous solution and the fused silica surface inside the nozzle channel. Upon contact with water the silica surface becomes hydrated, meaning that silanol groups (SiOH) dissociate to form SiO^--groups on the surface and H_3O^+ ions in the aqueous solution. This leads to a negative surface charge [70]. In a static situation a layer of positive counterions is subsequently formed on the negatively charged silica surface [70, 71].
In the nozzle channel the fast flow of the liquid can carry away ions from the layer of counterions, meaning that the liquid jet itself carries excess positive charges [72]. Simultaneously negative charges diffuse in the opposite direction on the silica surface, which becomes conductive upon hydration [73]. The streaming current is usually defined as the current flowing with the liquid jet, i.e as positive when the liquid carries excess positive charges. That this effect, known as electrokinetic charging in the liquid jet community, can produce a constant streaming current, is also supported by measurements in silica nanochannels [74].
In the first liquid jet experiments with metallic nozzles it was already discovered that electrokinetic charging of the jet constitutes a problem [75]. The charged liquid surface generates an electric potential with respect to the grounded spectrometer entrance. This so called streaming potential can, depending on its sign, accelerate or decelerate photoelectrons generated close to the surface. The measured electron kinetic energies are then offset by the energy difference acquired in the potential of the charged liquid

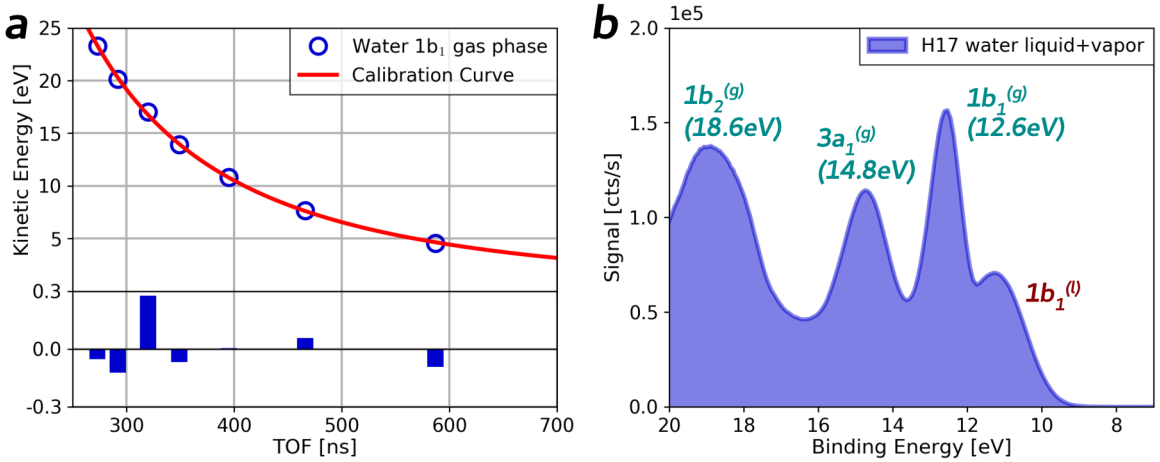

Fig. 3.8: **a)** TOF calibration using the peak of the $1b_1$ orbital of gas phase water and the harmonics 11-23. The obtained calibration parameters are t_0=7 ns (fixed), s_0=76.7±0.3 cm, and E_0=0.3±0.1 eV. **b)** Calibrated photoelectron spectrum of water obtained with the 17th harmonic.

surface. Faubel and coworkers [75] investigated the electrokinetic charging in metal nozzles and found that addition of salt to the aqueous solution can suppress the electrokinetic charging.

Systematic investigations on electrokinetic charging in fused silica nozzles and its effect on photoelectron spectra were conducted by Preissler and coworkers [72] and Kurahashi and coworkers [14]. For pure water a positive streaming current on the order of tens of nA is measured, depending on the flowspeed. The sign of the effect is well established [14, 72], but the magnitude of the energy shifts observed in photoelectron spectroscopy is so far inconsistent with the measured streaming currents. In both studies [14, 72] a decrease of the streaming current with increasing salt concentration is found. A salt concentration of 30-100 mM, depending on flowspeed, yields a streaming current of zero and accurate photoelectron energies [14, 72].

In the experiments presented in this thesis a concentration of 60 mM NaCl, dissolved in demineralized water, is used to remove electrokinetic charging. There can however still be energy shifts of photoelectron peaks on the order of several 100 meV caused by residual electrokinetic charging as well as electrostatic charging. Therefore day-to-day changes in the energy calibration need to be monitored and corrected. This is easily implemented using the liquid jet signal itself and the well-known energy of the $1b_1$ peak from ionization of gas phase water.

Figure 3.8a shows a calibration curve obtained by measuring water photoelectron spectra with the harmonics 11-23. In liquid jet experiments the electron spectrometer also detects XUV light, scattered on the liquid jet. This photon peak, which is absent in gas phase measurements, can be used to fix the TOF-offset t_0 in the calibration. The

photoelectron spectrum of water after calibration (figure 3.8b) agrees with photoelectron spectra measured at synchrotron facilities [12], factoring in the lower energy resolution of the XUV monochromator.

3.3.2 Decomposition of Liquid Jet Photoelectron Spectra

After calibration the spectrum can be decomposed into the three contributions discussed earlier, i.e. a gas phase water signal, a liquid water signal, and a secondary electron signal. The decomposition yields the possibility for a quantitative comparison of the acquired liquid water spectra with existing synchrotron data. Additionally the total count rates from liquid and gas phase water can be extracted.
To obtain spectra of only the gas phase contribution, the liquid jet can be moved out of the XUV beam. Relative to the calibration which is valid for the liquid spectrum, the acquired pure gas phase spectra are shifted in energy. This shift is caused by electrostatic and residual electrokinetic charging. To model the gas phase contribution of the complete liquid jet spectrum, the measured gas phase spectrum is therefore shifted by an energy ΔE and scaled to account for the lower vapor density further from the liquid surface.
To model the liquid water contribution of the spectrum one has to first consider the condensed phase effects on the photoelectron spectrum in more detail. The effects which are considered as reasons for the changes in the photoelectron spectrum are electronic polarization, surface dipoles, and hydrogen bonding.
Electronic polarization means the screening of the molecular ion by the polarizable dielectric solvent, as discussed in section 2.1. This screening effect causes a shift of all photoelectron peaks to lower binding energies. This is the dominating effect with an estimated shift of 1.4 eV, a value which alone already reproduces the experimentally observed shifts [12]. The effect of orientation of water molecules on the surface (i.e. surface dipoles) is estimated to be 100 times weaker and is therefore negligible [12].
While the first two effects are equal for all orbitals, the impact of hydrogen bonding can influence all orbitals differently. The theoretically predicted effect is a splitting of the electronic levels, which mainly affects the $3a_1$ orbital. This splitting, while visible in the spectrum of ice, where the hydrogen bonding structure is more homogeneous, is assumed to be smeared out by the larger disorder in liquid water [12, 13].
To extract vertical binding energies for the orbitals of liquid water, the peaks associated with the $1b_1$ and $1b_2$ orbitals are usually modeled with single Gaussian peaks with a width, which is increased compared to the gas phase [12]. The assignment of binding energies to the two contributions of the liquid $3a_1$ photoelectron peak, for example in ref. [14], relies on fitting with two Gaussian peaks, under the assumption that the two contributions have the same intensity and width.
This amounts to a total of 4 Gaussian peaks to model the liquid water spectrum. Due to the strong gas phase contribution it proved not feasible to fit the measured spectrum

to obtain the vertical binding energies of the overlapping $3a_1$ and $1b_2$ orbitals. The binding energies and widths of these peaks are therefore fixed to the most recent values from Kurahashi and coworkers [14]. Only the $1b_1$ peak is modeled with a Gaussian peak with free parameters for the vertical binding energy and the width.
The secondary electron distribution can be described as

$$I_{secondary}(E) = I_0\sqrt{\frac{\pi\sigma^2}{2}}\exp\left(\frac{\sigma^2}{2\tau^2}+\frac{E_0-E}{\tau}\right)\left[1+\mathrm{erf}\left(\frac{E-E_0}{\sqrt{2}\sigma}-\frac{\sigma}{\sqrt{2}\tau}\right)\right] \quad (3.6)$$

with the intensity I_0, the peak energy E_0 and width σ of the distribution before scattering, and the exponential damping factor τ [11]. Due to the negative signal at long time-of-flight, visible at low kinetic energies (see fig. 3.7), the parameters of the secondary electron function cannot be reliably extracted. Apart from the intensity the parameters are therefore fixed to the values from ref. [11], i.e. $E_0 = 0.94\,eV$, $\sigma = 0.74\,eV$, and $\tau = 2.11\,eV$.
To summarize, the following contributions and parameters are used to model the liquid jet photoelectron spectra:

Gas phase peaks:
: The measured gas phase spectra are separately fitted with three Gaussian peaks to retrieve their relative energies, widths, and amplitudes. To model the vapor contribution in the gas+liquid-spectrum only two parameters are used to adjust the measured gas phase spectrum: an energy shift ΔE and a scaling factor.

Liquid phase peaks:
: The $1b_1^{(l)}$ peak is well-resolved and can be fitted with a Gaussian function retrieving peak position, width and amplitude. For the $3a_1^{(l)}$ and $1b_2^{(l)}$ peaks the only free parameters are the two amplitudes, while the peak positions and widths are fixed to the values from ref. [14].

Secondary electrons:
: The secondary electron peak is modeled using the formula from equation (3.6). The only free parameter is the intensity, all other parameters are fixed to the values from ref. [11] as given above.

The photoelectron spectra measured from the liquid jet are modeled using a sum of these three contributions yielding a total of eight fit parameters. The peak positions and the signal of the gas phase and liquid phase contributions, retrieved from the fit, are shown in table 3.1. The fits for harmonics 15 and 19 are shown in figure 3.9.
Overall the binding energies obtained for the valence orbitals of water vapor in table 3.1 agree well with literature values [12, 41]. Whenever the binding energies deviate by more than 0.1 eV from the reference values, for example for the harmonic 19, the

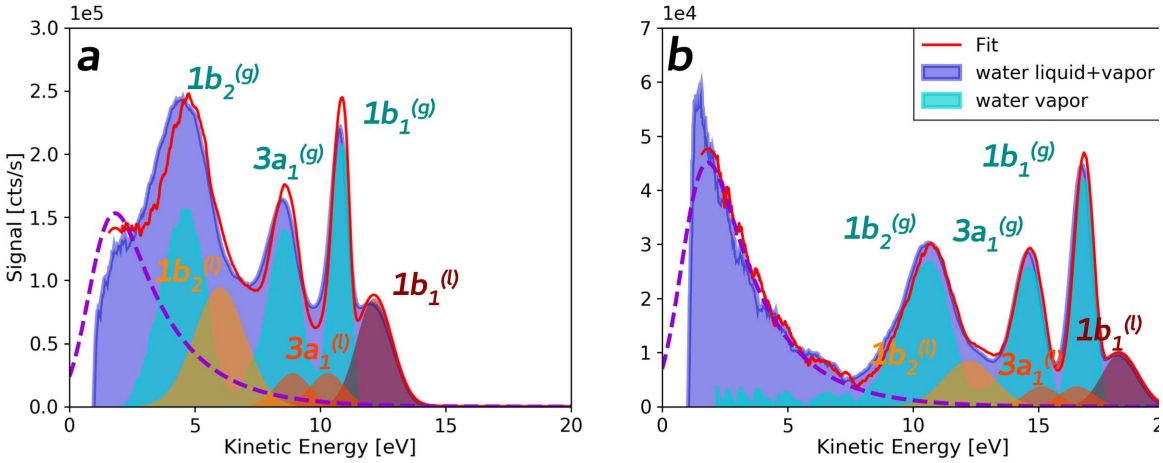

Fig. 3.9: Photoelectron spectra of liquid and gas phase water obtained with the 15th harmonic (a) and the 19th harmonic (b) are modeled with the fitting procedure described in the text. The model function contains the measured gas phase spectrum, which leads to the noise visible on the fit (red curve). All extracted fit parameters are listed in table 3.1.

deviation is consistent over the whole spectrum. It is probably caused by residual charging and can be corrected by shifting the entire spectrum in energy.
The measured peak widths for gas phase water are larger than the peak widths reported by Winter and coworkers [12]. This is however consistent with the larger energy bandwidth of the XUV pulses obtained from the XUV monochromator. The total signal of the individual peaks shows no strong photon energy dependence and changes in count-rate are mainly caused by changes in XUV intensity. For example with the harmonic 15, a total count rate of approximately 700 electrons per laser shot from gas phase water is observed.
The variance of the liquid water $1b_1$ orbital binding energy is larger than that of the gas phase binding energies. Averaged over several harmonics and corrected for the shifts, extracted from the gas phase measurements, the mean vertical binding energy is 11.18 eV. This agrees with the value reported in ref. [12] rather than with the value in ref. [14]. The total liquid water signal, for example measured with the harmonic 15, amounts to approximately 500 electrons per pulse.

3.3.3 Probing Depth and Signal Estimates

A recurring question in the liquid jet community is the depth from which electrons can be extracted out of liquid water, i.e. the mean free path (MFP) of electrons in water. The mean free path of electrons depending on the electron kinetic energy can be approximately described by the so-called universal curve [76]. This universal curve,

Table 3.1: The photoelectron spectra of liquid and gas phase water, measured with several harmonics, are modeled with the procedure described in the text. Binding energies and widths are extracted for all gas phase peaks and compared to literature values. The binding energy of the $1b_1$ orbital is used for calibration. For the liquid phase spectra the binding energy and FWHM is extracted only for the $1b_1$-peak, while the position and width of the other peaks is fixed to the values reported in ref. [14]. For the harmonic 21 the gas phase water spectrum was not measured, therefore the spectrum obtained with the harmonic 23 was used, shifted accordingly.

gas phase									
	$1b_1$			$3a_1$			$1b_2$		
	IP [eV]	FWHM [eV]	cts/shot	IP [eV]	FWHM	cts/shot	IP [eV]	FWHM [eV]	cts/shot
Ref. [12]	12.60	0.30		14.84	1.18		18.78	1.75	
H13	12.67 (+0.07)	0.68	186	14.90 (+0.06)	1.50	240	-	-	-
H15	12.60 (+0.00)	0.75	168	14.86 (+0.02)	1.60	226	18.86 (+0.08)	1.95	320
H17	12.55 (-0.05)	0.79	126	14.79 (-0.05)	1.51	162	18.89 (+0.11)	2.15	242
H19	12.83 (+0.23)	0.85	38	15.06 (+0.22)	1.37	37	19.15 (+0.27)	2.29	62
H21	12.41 (-0.19)	-	121	14.70 (-0.14)	-	107	18.62 (-0.16)	-	149
H23	12.61 (+0.01)	1.18	65	14.89 (+0.05)	1.45	57	18.82 (+0.04)	2.15	79
Liquid Phase									
Ref. [14]	11.31	1.45		13.09/14.48	1.63		17.41	2.41	
H13	11.47 (+0.16)	1.74	167			417			-
H15	11.24 (-0.05)	1.66	152			91			242
H17	11.19 (-0.12)	1.73	136			71			123
H19	11.38 (+0.07)	1.71	18			13			22
H21	10.88 (-0.43)	1.69	46			30			58
H23	11.06 (-0.25)	1.67	22			5			25

validated as an approximation by measurements on a multitude of materials, has a minimum around 30 eV and rises towards lower electron energies. According to this a MFP of 0.5 to 1 nm is to be expected for the energy range important in this experiment (approx. 10-25 eV). However it is established that a material dependence cannot be ignored completely [77]. Recent experimental [78–80] and theoretical [81] results show that the concept of a universal curve is not sufficient for the probing depth in liquid water.

Most studies show that the MFP curve in the energy range covered here is relatively flat, with more recent studies [79, 80] giving a value of approximately 2 nm. Therefore photoelectron spectroscopy of aqueous solution with XUV light cannot strictly be called surface-sensitive. On the other hand it is also somewhat questionable to speak of bulk solvation for large, nanometer-scale molecules. The topic of surface versus bulk molecular concentration will be treated in more detail in section 4.2.

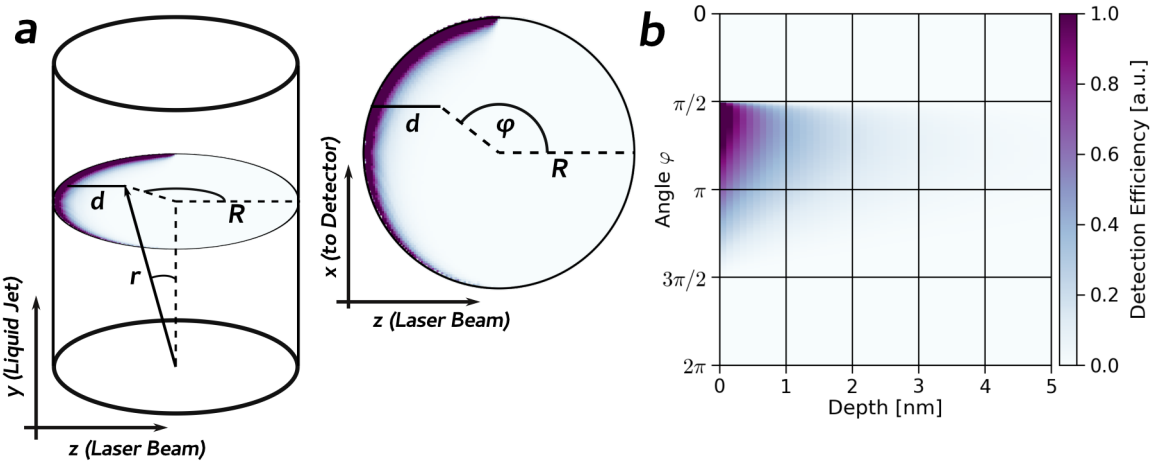

Fig. 3.10: **a)** The origin of photoelectrons from the jet. The density of incoming photons is assumed to be homogeneous, therefore one can consider a horizontal cut through the jet. The detection efficiency depends on the point of origin $\mathbf{r} = (x, y, z)$ and the direction of electron emission (θ, ϕ). **b)** Calculated origin of photoelectrons in polar coordinates from a horizontal cut (see text).

In the case of XUV photoionization the mean free path is not the only significant parameter. The absorption cross-section of gas phase water in the relevant wavelength range is approximately 20 Mb [82, 83]. In liquid water a similar absorption cross-section can be assumed for photon energies above 20 eV [84]. Under this assumption the XUV intensity is decreased to less than 0.2% after a travel distance of 100 nm in liquid water. Therefore the photon density in the liquid jet has to be considered as well to estimate the probing depth and the expected photoelectron signals.

The geometry used to calculate the estimated signals and probing depths is shown in figure 3.10a. In Cartesian coordinates the laser travels in the direction of the z-axis, the liquid jet is oriented in the y-direction and the spectrometer entrance is in the positive x-direction.

For a cylindrical liquid jet segment of radius R and length ω_0 a uniform density of incoming photons $n_0 = N_0/(2R\omega_0)$ in the y, z-plane is assumed. With this the photon density at any point inside the jet is

$$n_{ph}(x, z) = n_0 e^{-\sigma c d} \tag{3.7}$$

where $d = z + \sqrt{R^2 - x^2}$ is the distance traveled inside the jet, σ is the absorption cross-section of water and c is the number density. In the XUV photon energy range covered here the absorption cross-section of water is essentially equal to the ionization cross-section.

Therefore the density of electrons detected from a point within the liquid jet is equal to the density of absorbed photons multiplied by the detection probability $P(x, z)$.

$$n_e(x, z) = c\sigma n_{ph}(x, z)P(x, z) \tag{3.8}$$

The detection probability depends on the distance l the electron has to travel to reach the jet surface. For an electron originating at a point (x, z) and emitted in the direction (θ, ϕ) this distance is

$$l(x, z, \theta, \phi) = \frac{1}{\sin\theta}\Big(- x\cos\phi - z\sin\phi + \sqrt{(-x\cos\phi - z\sin\phi)^2 + R^2 - x^2 - z^2}\Big) \tag{3.9}$$

where θ is the azimutal angle from the y-axis and ϕ is the angle in the (x, z)-plane (see fig. 3.10a). The probability p for an electron to reach the surface without scattering is then given by

$$p(x, z, \theta, \phi) = e^{-l(x,z,\theta,phi)/l_e} \tag{3.10}$$

where l_e is the mean free path of an electron in liquid water. For the total detection probability $P(x, z)$, equation (3.10) needs to be integrated over the solid angle

$$P(x, z) = \frac{1}{4\pi}\int_0^\pi \mathrm{d}\theta \int_0^\pi \mathrm{d}\phi \sin\theta e^{-l(x,z,\theta,\phi)/l_e} \tag{3.11}$$

where the integration over ϕ is limited to a half circle, such that only electrons with a nonzero component of their velocity pointing towards the skimmer are considered. This integral can be evaluated numerically via a simple Monte-Carlo integration with uniform sampling to obtain $P(x, z)$. The density of detected photoelectrons can then be obtained by multiplication with the photon density according to equation (3.8).
The resulting electron density for a mean free path of 2 nm and an ionization cross-section of $20{\cdot}10^{-18}\,\mathrm{cm}^2$ is shown in polar coordinates in figure 3.10b. Evidently most electrons (over 75%) originate from the quadrant $[\pi/2, \pi]$ of the liquid jet, which is pointing towards the spectrometer and the incoming XUV pulse.
From the calculated detection probability one can obtain an average probing depth of approximately 1 nm. Furthermore an exit efficiency of 2.6% can be estimated, meaning that 2.6% of the generated electrons exit the liquid jet without scattering and traveling towards the spectrometer. Calculation of both parameters for liquid jet diameters from 10 to 20 μm show no significant dependence on the radius.
For a typical monochromator output flux of $5 \cdot 10^6$ photons per pulse, of which approximately 10% are incident on the liquid jet, approximately 10000 electrons exit the jet without scattering. In the previous section, however, count rates from liquid water of approximately 500 were measured. The reason for this discrepancy is probably

Table 3.2: Characteristics of a few common organic solvents. The density, the vapor pressure, and the polarity are taken from ref. [85]. The viscosity and the surface tension are from ref. [86]. The gas phase ionization potentials are extracted from ref. [87].

Solvent	Formula	Density [g/ml] (25°)	Vapor Pressure [mbar] (20°)	Surface Tension dyn/cm (25°)	Viscosity [cP] (25°)	Polarity (relative)	Ionization Potential [eV] (gas phase)
Water	H_2O	0.998	17.5	72.7	0.89	1.000	12.6
Ethanol	C_2H_6O	0.789	59	22.0	1.07	0.654	10.6
Acetonitrile	C_2H_3N	0.786	97	28.7	0.37	0.460	12.2
Heptane	C_7H_16	0.684	48	19.8	0.39	0.012	9.9
Cyclohexane	C_6H_12	0.779	104	24.7	0.89	0.006	9.9
Dimethylsulfoxide	C_2H_6OS	1.092	0.6	42.9	1.99	0.444	9.1
Toluene	C_7H_8	0.867	29	27.9	0.56	0.099	8.8

that the estimate assumes a solid collection angle of 2π for the magnetic bottle. In a similar magnetic bottle configuration and for the same photon energy range considered here (20-50 eV), Kothe and coworkers [66] measured collection efficiencies ranging from 5-8% rather than 50%. The decreased collection angle is caused by the small skimmer aperture, which is the same in the setup implemented for this thesis. The lower collection efficiency gives a ten times lower estimate of 1000 electrons per pulse. Additionally the transmission of the grid in front of the photoelectron detector and the detection efficiency of the MCP detector itself are not included in the estimate. With this in mind, the measured signals from the previous section agree quite well with the estimated electron yield.

3.4 Photoelectron Spectroscopy of Organic Solvents

One goal of liquid phase photoelectron spectroscopy is to investigate the influence of the surrounding solvent on organic molecules. In steady-state and time-resolved optical spectroscopy this is often accomplished by studying the influence of solvent parameters like polarity or viscosity, i.e. by performing the same experiment in multiple solvents. To gain this ability it is essential to extend photoelectron spectroscopy to solvents other than water.

It is, however, no coincidence that published studies employing the liquid jet technique almost exclusively investigate water. Water is one of the solvents with the lowest vapor pressure, and the higher vapor pressure of other solvents usually complicates liquid jet operation. Table 3.2 shows characteristics of a few commonly used solvents. Higher vapor pressure for example leads to a higher vapor density close to the liquid jet and to a higher pressure in the vacuum chamber.

Lower viscosity, lower density or higher surface tension cause a faster break-up of the liquid jet. The travel distance of the intact liquid jet can be calculated using equation

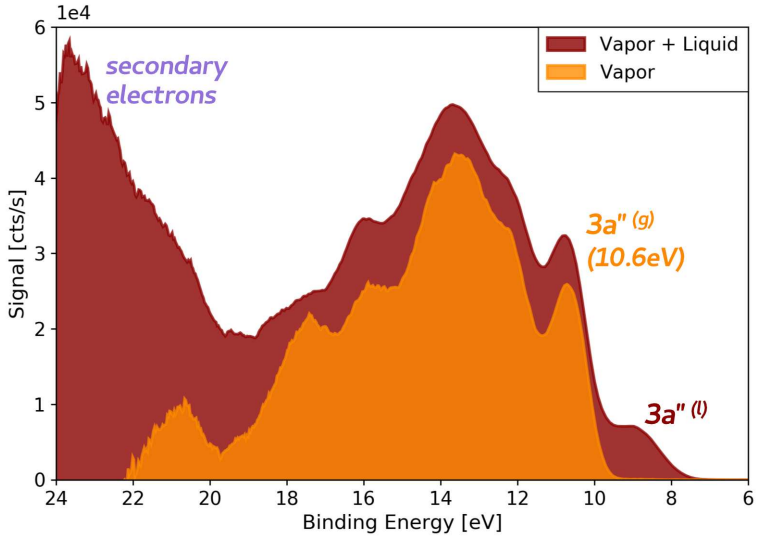

Fig. 3.11: Photoelectron spectra of gaseous and liquid ethanol obtained with the harmonic 17 (26.5 eV). The gas phase spectrum is acquired by moving the liquid jet out of the XUV focus.

(3.1) and the parameters in table 3.2. For a flowspeed of 30 m/s a water jet stays intact for a distance of approximately 3.5 mm, while an ethanol jet would be expected to stay intact for about 6.2 mm.
But these solvent parameters are not the only ones to consider. The detection of solute photoelectron signals relies heavily on the lower ionization potential of the solute compared to the solvent, as will be discussed in detail in the next chapter. While, for example, dimethylsulfoxide has favorable characteristics regarding vapor pressure and viscosity, its low ionization potential would make experiments on solvated molecules almost impossible. Of the low polarity solvents heptane, cyclohexane, and toluene, heptane would probably be the most useful, since cyclohexane has a much higher vapor pressure and toluene a lower ionization potential.
To show that experiments with other solvents than water are feasible in the liquid jet setup presented here, XUV-only measurements with ethanol and acetonitrile are performed. These solvents were selected for their relatively high ionization potentials, which makes them the most promising for photoelectron spectroscopy of solutes.

3.4.1 Ethanol

To measure photoelectron spectra of liquid ethanol the liquid jet flow was reduced to 0.4 ml/min, which resulted in the same pressure inside the liquid jet HPLC pump as for water. During measurements with ethanol the pressure in the liquid jet chamber was approximately $5 \cdot 10^{-5}$ mbar, increased compared to water operation because of the

higher vapor pressure. To keep the pressure in the detector chamber below 10^{-5} mbar, the distance of the liquid jet to the skimmer had to be increased. Additionally the collection bottle had to be evacuated continuously, leading to the evaporation of the ethanol in the catcher tube. Ethanol sample solutions can therefore not be recycled.
Figure 3.11 shows the photoelectron spectrum recorded with the 17th harmonic incident on the ethanol jet. The ethanol contains 10 mM NaBr to suppress electrokinetic charging. The gas phase spectrum is acquired by moving the liquid jet out of the XUV beam. The peak at a binding energy of 10.6 eV corresponds to ionization from the $3a''$-orbital [88]. The known binding energy of the $3a''$-orbital is also used for calibration of the ethanol spectra.
The gas phase photoelectron spectrum agrees well with the gas phase spectrum measured by Faubel and coworkers [11]. When the liquid jet is in the XUV-focus an additional peak appears at lower binding energy, which can be assigned to ionization from the $3a''$-orbital of liquid ethanol.
To extract the binding energy of the liquid phase $3a''$-orbital, the photoelectron peaks associated with the liquid phase and gas phase $3a''$ ionization are modeled with two Gaussian peaks. This yields a vertical binding energy of the liquid phase $3a''$-orbital of 9.1 eV. This is significantly lower than the 9.66 eV measured by Faubel and coworkers [11], but agrees reasonably well with the 9.3 eV vertical binding energy reported in ref. [50].
The count rates extracted from the Gaussian fit are 103 and 26 counts per laser shot for the gas phase and the liquid phase peaks respectively. The ratio of liquid phase to gas phase signal is approximately 1:4, compared to 1:1 in the case of water. This is probably related to the higher vapor pressure of ethanol. Expectedly the photoelectron spectrum of ethanol extends to lower binding energies than that of water. Nevertheless it could be feasible to collect photoelectron spectra of organic molecules with an ionization potential below 7 eV. At this binding energy the count rates from liquid ethanol are comparable with the count rates from water at 9 eV, which is the approximate threshold for detection of solute signals in liquid water, as will be discussed in the next chapter.

3.4.2 Acetonitrile

For measurements with acetonitrile the flow at the HPLC-pump had to be increased to 0.7 ml/min to reach similar pressures as in the operation with water. While the operation with ethanol was relatively straightforward, the operation with acetonitrile proved more challenging, probably due to the even higher vapor pressure. For a stable acetonitrile jet the distance between jet and catcher was decreased. Additionally the collection bottle was continuously evacuated also in the case of acetonitrile.
The photoelectron spectra obtained with harmonic 15 and the acetonitrile jet in and out of the XUV focus are shown in figure 3.12. The acetonitrile contains 10 mM NaI to suppress electrokinetic charging.

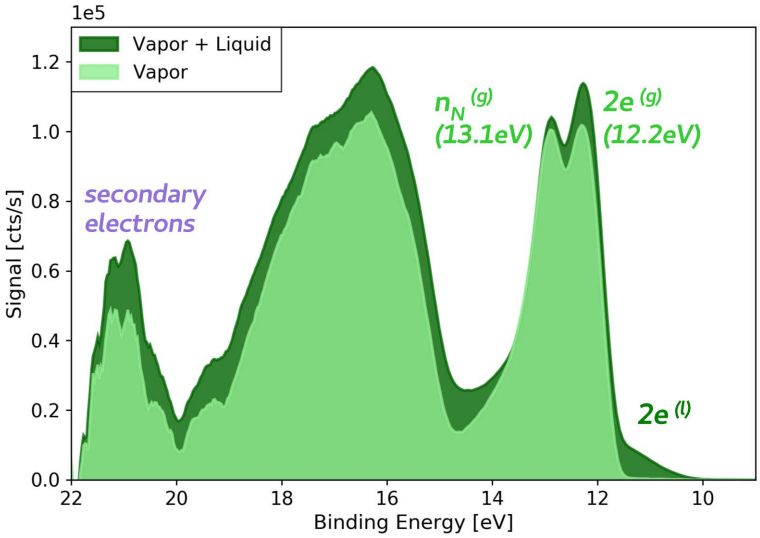

Fig. 3.12: Photoelectron spectra of liquid and gas phase acetonitrile acquired with the harmonic 15 (23.4 eV). The gas phase spectrum is obtained by moving the liquid jet out of the XUV focus.

The gas phase spectrum agrees well with the spectrum obtained by Gochel-Dupuis and coworkers [89], factoring in the energy bandwidth of the XUV-monochromator. The two overlapping bands at low binding energy can be assigned to the $2e$-orbital and the n_N-orbital as labeled in figure 3.12.

The $2e$ orbital is related to the C=N bonding π-system and has a vertical binding energy of 12.2 eV [89]. The corresponding peak is also used for calibration of the acetonitrile photoelectron spectra. For the non-bonding nitrogen lone pair orbital n_N a binding energy of 13.1 eV is reported [89], which is reproduced accurately in the experiment.

With the liquid jet in the XUV focus a band at lower binding energy appears, which can probably be assigned to ionization from the $2e$-orbital of liquid acetonitrile. This assignment remains however tentative, since no photoelectron spectrum of liquid acetonitrile has been published so far. The binding energy of the liquid phase feature is 11.2 eV, extracted by a Gaussian fit of the liquid phase band and the two overlapping gas phase contributions.

The count rates extracted for the ionization of the gas phase and liquid phase $2e$-orbital are 76 and 7 counts per laser shot respectively. Thus the ratio of liquid phase to gas phase signal is approximately 10:1, compared to 1:1 for water. So while the higher ionization energy of acetonitrile would facilitate the measurement of solute photoelectron spectra, the weak liquid phase signal is a considerable complication.

3.5 Time-resolved Photoelectron Spectroscopy of Water

The pump-probe photoelectron experiments presented in this section serve the purpose of further characterizing the experimental setup. In molecular measurements in solution, transient signals from the sample can be mixed with transient signals from the solvent. Hence a well characterized pump-probe response of liquid water is important to distinguish it from molecular pump-probe signals. To this end time-resolved photoelectron experiments were conducted using both 800 nm and 400 nm pump pulses. In both cases the laser-assisted photoelectric effect from liquid water can be observed.
The laser assisted photoelectric effect is well-known from pump-probe photoelectron experiments on gas-phase [90, 91] and solid state targets [92]. In liquid water it was observed for the first time recently [19]. In the overlap of an ionizing XUV or X-ray pulse and a strong visible or IR pulse, electrons, ejected by the XUV pulse, can exchange energy with the IR field. In the photoelectron spectrum the effect manifests itself as sideband peaks, corresponding to absorption or stimulated emission of photons from the IR laser field. The kinetic energy of the electrons from the sidebands of an unperturbed energy level with binding energy E_0 is therefore given as

$$E_{kin}^{\pm n} = \hbar\omega_{xuv} - E_0 \pm n\hbar\omega \tag{3.12}$$

where $\hbar\omega$ is the photon energy of the laser field. The effect can be understood in terms of a so-called dressing of the free electron wave function, meaning the evolution of the electron in a state driven by the laser field. In a simple two-step model, similar to the three-step model in high harmonic generation, the unperturbed XUV photoemission is considered as the first step. Because the tightly bound ground states are less affected by the IR laser field, this approximation is justified. The second step is the evolution of the electron wave function in the laser field, neglecting the influence of the ion potential [93].
According to ref. [94], in this regime the angular differential cross-section of the nth sideband can be expressed as

$$\mathrm{d}\sigma_n \propto J_n^2\left(\alpha_0 k_n \cos\theta\right) \frac{\mathrm{d}\sigma^{(0)}}{\mathrm{d}\Omega} \sin\theta \mathrm{d}\theta \mathrm{d}\phi \tag{3.13}$$

where J_n is a Bessel function of the first kind with order n, α_0 is the norm of the classical excursion vector for an electron in the laser field, and k_n is the norm of the wave vector.
$\frac{\mathrm{d}\sigma^{(0)}}{\mathrm{d}\Omega}$ is the angular cross-section of the electrons from unperturbed XUV ionization, i.e. the photoline. Using the asymmetry parameter β, the angular cross-section for linearly polarized light is

$$\frac{\mathrm{d}\sigma^{(0)}}{\mathrm{d}\Omega} = \frac{\sigma_{tot}}{4\pi}\left(1 + \frac{\beta}{2}(3\cos^2\theta - 1)\right) \tag{3.14}$$

where σ_{tot} is the total cross-section of the unperturbed photoemission from the corresponding bound state [95].
With this, equation (3.13) can be integrated over the solid angle to obtain the total cross-sections of the photoline and the first sideband. For the first sideband the Bessel function $J_1(x)$ can be approximated by $x/2$, which is valid for small arguments x.
The laser polarization is oriented parallel to the liquid jet and therefore perpendicular to the spectrometer. This polarization is determined by the maximum transmission of the XUV monochromator. The total cross-sections for the first sideband and the photoline are then

$$\begin{aligned} \sigma^{(1)} &\propto \frac{\alpha_0^2 k_1^2 \sigma_{tot}}{16\pi} \int_{-\Delta\vartheta}^{\Delta\vartheta} \mathrm{d}\phi \int_{\pi/2-\Delta\vartheta}^{\pi/2+\Delta\vartheta} \mathrm{d}\theta \sin\theta \cos^2\theta \left(1 + \frac{\beta}{2}(3\cos^2\theta - 1)\right) \\ \text{and} \quad \sigma^{(0)} &\propto \frac{\sigma_{tot}}{4\pi} \int_{-\Delta\vartheta}^{\Delta\vartheta} \mathrm{d}\phi \int_{\pi/2-\Delta\vartheta}^{\pi/2+\Delta\vartheta} \mathrm{d}\theta \sin\theta \left(1 + \frac{\beta}{2}(3\cos^2\theta - 1)\right) \end{aligned} \tag{3.15}$$

with $\Delta\vartheta$ as the acceptance angle of the magnetic bottle, defined as half the opening angle of the cone towards the spectrometer. The proportionality constant is the same for the photoline and the first sideband. With the integrals evaluated, the relative signal of the photoline and the sideband becomes

$$\frac{\sigma^{(1)}}{\sigma^{(0)}} = \frac{\alpha_0^2 k_1^2}{4} \frac{10\cos^2(\pi + \Delta\vartheta) + 9\beta\cos^4(\pi + \Delta\vartheta) - 5\beta\cos^2(\pi + \Delta\vartheta)}{30 + 15\beta\cos^2(\pi + \Delta\vartheta) - 15\beta} \tag{3.16}$$

This can be further simplified by using the identity $\cos(\pi/2 + x) = \sin(x)$. Transforming to SI units, according to ref. [92], yields

$$\frac{\sigma^{(1)}}{\sigma^{(0)}} = \frac{4\pi\alpha I E_{kin}}{m_e \hbar\omega^4} \frac{10\sin^2\Delta\vartheta + 9\beta\sin^4\Delta\vartheta - 5\beta\sin^2\Delta\vartheta}{30 + 15\beta\sin^2\Delta\vartheta - 15\beta} \tag{3.17}$$

with the laser intensity I and the fine structure constant α. This formula can be used to estimate the dressing field intensity from the relative amplitude of the photoline and the first-order sideband.
The peak of the first-order sideband is only present in the time overlap of the pump and probe pulse and its amplitude depends linearly on the laser intensity (see eq. 3.17). Therefore the sideband signal can be used for a direct measurement of the experimental cross-correlation. This way the time-resolution and the exact zero delay can be determined independently of measured transient signals.

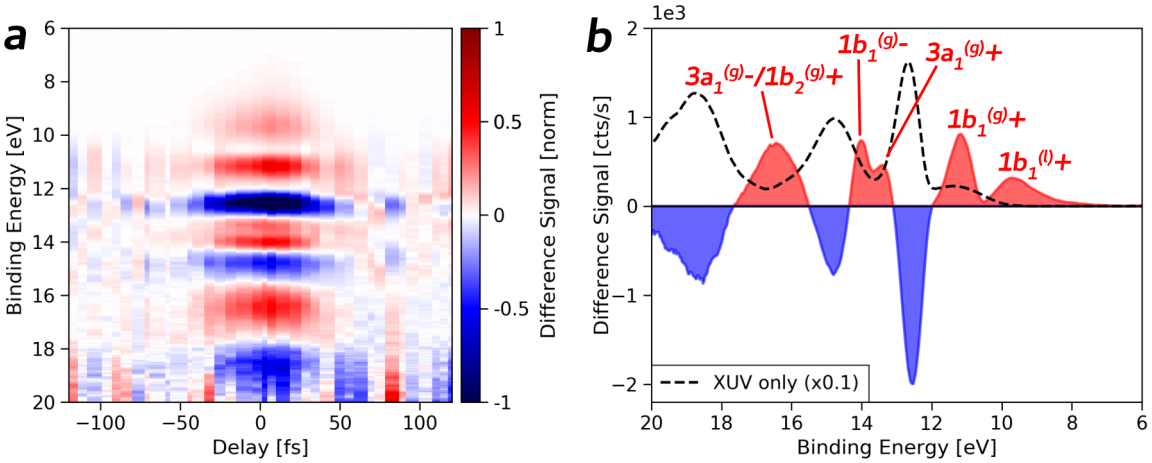

Fig. 3.13: Liquid and gas phase water sidebands generated at the overlap of 800 nm pump pulses and 17th harmonic probe pulses. **a)** False color map of the pump probe signal around the zero delay. The map shows the normalized difference signal, obtained by subtracting the spectrum at negative delays, where no pump probe signal is observed. The relative magnitude of the difference signal can be gauged in panel **b**, where the averaged difference spectrum around time-overlap (-5 to 5 fs) is compared to the XUV-only photoelectron spectrum.

3.5.1 800 nm Pump Pulses

The pump probe data is recorded by scanning the delay between the 800 nm pump pulse and the XUV probe pulse, while acquiring photoelectron spectra for each delay. Figure 3.13 shows the difference pump-probe photoelectron spectrum as a function of the delay between the 800 nm pulse and the 17th harmonic pulse (26.5 eV). The difference signal is obtained by subtracting the spectrum at negative delays, where no pump-probe signal is observed. The temporal profile of all pump-probe features can be modeled with Gaussian functions, which yields a FWHM of the cross-correlation of approximately 50 fs.

Upon comparing the difference spectrum at time overlap with the XUV-only photoelectron spectrum the features can clearly be related to sideband generation (fig. 3.13b). A depletion of the three gas-phase water peaks is observed. The positive signals can be attributed to the first-order sidebands of the gas-phase peaks labeled as $1b_1^{(g)}\pm$, $3a_1^{(g)}\pm$, and $1b_2^{(g)}\pm$ as well as the positive sideband of the liquid-phase $1b_1$ peak.

The total signal of the XUV-only liquid and gas phase $1b_1$ peaks can be extracted by modeling the photoelectron spectrum in the range from 8 to 13 eV with two Gaussian peaks. To extract the sideband count rates, the difference spectrum is modeled in the binding energy range from 6 to 11.8 eV, where the depletion of $1b_1^{(g)}$ is not relevant.

The model function includes three contributions, two positive Gaussian peaks for the positive sidebands $1b_1^{(g)}+$ and $1b_1^{(l)}+$ and a negative Gaussian for the depletion of $1b_1^{(l)}$. The retrieved ratio of sideband signal to the photoline signal is 8.1% for the gas phase $1b_1$ peak and 12.8% for the liquid phase $1b_1$ peak.
From the signal ratios the 800 nm intensity can be retrieved using equation 3.17. The asymmetry parameters of water were recently measured in a liquid jet photoelectron spectroscopy experiment [96]. Nishitani and coworkers obtained values of β_g =1.3 in the gas-phase and β_l=0.27 in the liquid-phase for the asymmetry parameter of the $1b_1$-orbital. A conical collection angle of 20° was measured for a magnetic bottle spectrometer in a similar configuration [66], so this value is used for the estimate. This yields IR intensities of 2.4 TW/cm^2 for the gas phase and 4.0 TW/cm^2 for the liquid phase. The higher IR intensity obtained from the liquid water sideband signal could be explained by the influence of focal volume averaging. The liquid jet diameter is smaller than the focus diameter, therefore the average IR intensity incident on the liquid water is higher than the overall average intensity. On the other hand also the influence of the origin of photoelectrons from inside the liquid jet (see sec. 3.3.3) was not considered in the calculation. The change in detection efficiency depending on the emission angle could lead to a different apparent asymmetry parameter.
For comparison the IR intensity can also be retrieved from a power measurement. The measured averaged power of the 800 nm laser beam is 20 mW, corresponding to a pulse energy of 20 μJ. Assuming a pulse duration of 45 fs and a focus diameter of 100 μm, this yields a peak intensity of 5.7 TW/cm^2. Considering the estimated parameters used in the calculation of the IR intensity from the power measurement and from the sideband intensity, the agreement is quite good. The higher intensity calculated from the power measurement could indicate a larger than estimated focus diameter.

3.5.2 400 nm Pump Pulses

400 nm pump light is used in all molecular pump-probe measurements that are presented in this thesis, so a more thorough characterization of the pure water signals is needed. The pump pulse wavelength of 400 nm was chosen for several reasons. Many biologically relevant systems have a high absorption cross-section around 400 nm, for example all-trans retinal and carotenes [97]. Additionally the absorbance of water, even though it is already weak across the visible spectrum, has a clear minimum at 400 nm [98, 99]. This makes it very unlikely to observe pump-probe dynamics in pure liquid water. Lastly, 400 nm pulses are easily generated from the 800 nm laser pulse by second harmonic generation.
Figure 3.14a shows 400 nm only photoelectron spectra of water for a range of 400 nm intensities. With the liquid jet moved out of the laser focus no photoelectron signal could be detected, meaning that the entire 400 nm photoelectron signal originates from liquid water. At lower intensity the spectrum resembles the secondary electron

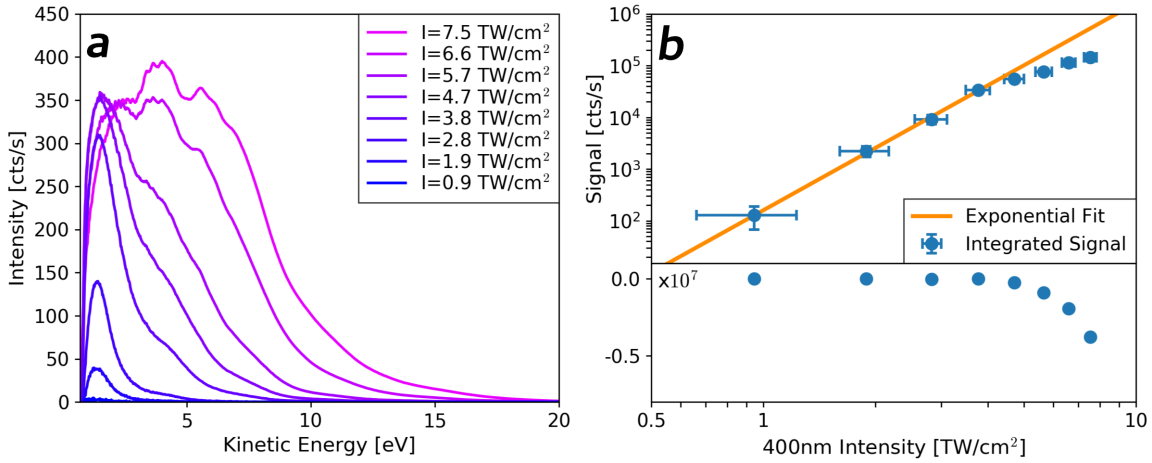

Fig. 3.14: **a)** Water jet photoelectron spectra obtained with 400 nm pulses. The intensities are estimated from a power measurement. **b)** Intensity dependence of the integrated 400 nm photoelectron signal. An exponential fit of the 4 points at the lowest intensity yields an exponent of 4.0±0.2.

signal, which points to a large fraction of secondary electrons. At higher intensities the spectrum becomes more structured. The new features are spaced by approximately 3 eV, which indicates above-threshold ionization, i.e. more photons than necessary being absorbed in the ionization process.

Since liquid water has an ionization potential of 11.3 eV it is expected that four 400 nm photons (3.1 eV) are necessary for photoionization. The dependence of the integrated photoelectron signal on the 400 nm intensity is shown in figure 3.14b. An exponential fit of the four points with the lowest intensity shows the expected four-photon dependence. At higher intensities, coinciding with the aforementioned changes in the photoelectron spectrum, the total signal deviates from the fitted four-photon intensity dependence function. This could be related to the negative signal, observed at long time-of-flight and high count rates.

Figure 3.15 shows a pump-probe measurement of water using the 17th harmonic and 400 nm pump light. The only pump-probe signal can be linked to the laser assisted photoelectric effect in liquid water. Similar to figure 3.13, the difference map is shown, but here the only distinguishable pump-probe signal is the first positive sideband of the liquid water $1b_1$ peak. The sideband signal is much weaker than for the 800 nm pump pulse, which is expected since the sideband amplitude is inversely proportional to the fourth power of the photon energy according to equation (3.17). The measurement was also performed at a lower pump pulse energy to match the pump pulse energy used in the molecular pump-probe experiments.

A Gaussian fit of the time profile of the $1b_1^{(l)}+$ sideband signal yields a value of 48 fs for the FWHM of the cross-correlation. The total signals of the photoline and the sideband

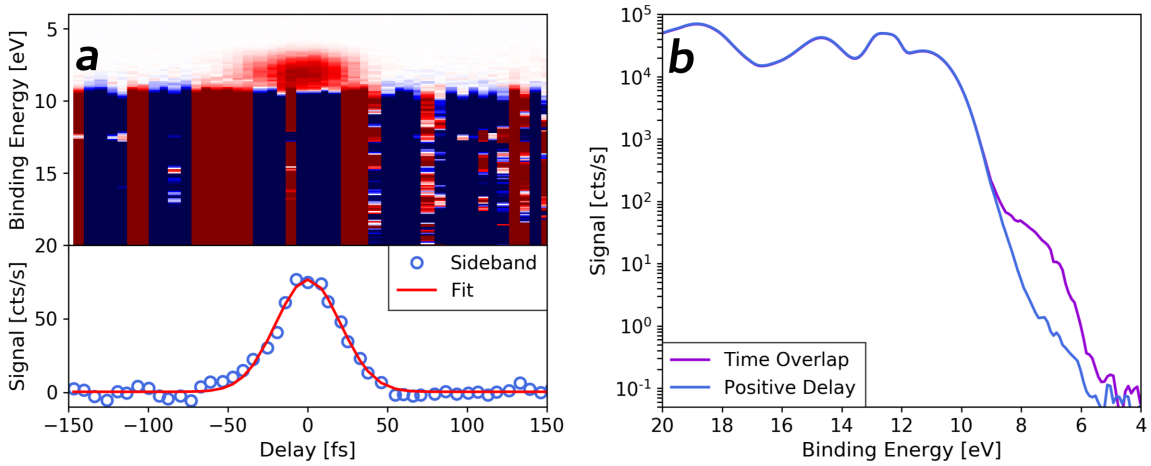

Fig. 3.15: **a)** Pump-probe difference map of the 400 nm pump, 17th harmonic probe data. A Gaussian fit of the sideband signal yields a cross-correlation of 48 fs. **b)** Integrated spectrum around time-overlap (-10 to 10 fs) and at positive delays (100 to 150 fs).

at time overlap can again be retrieved via a Gaussian fit of the spectrum. The ratio of the sideband signal to the photoline signal is 0.17%. Using the asymmetry parameter β_g=0.27 and the collection angle $\Delta\vartheta$=20° in equation (3.17), a 400 nm intensity of 0.7 TW/cm^2 is calculated.
The measured average power is 2 mW. Assuming a 100 μm focus diameter and a pulse duration of 45 fs, the intensity estimated from the power measurement is approximately 0.6 TW/cm^2. The two values are in excellent agreement, proving that the sideband signal provides a valid way to retrieve the pump pulse peak intensity.

3.6 Summary

In this chapter the implementation of time-resolved XUV photoelectron spectroscopy on liquid targets is presented. The implementation of the liquid jet endstation at the existing XUV monochromator is discussed. The liquid jet assembly, which was initially a commercial system, is redesigned. The implementation of the new design improves the stability of the liquid jet assembly against vibrations and facilitates alignment of the liquid jet to the output beam of the XUV monochromator. This is a prerequisite for the long acquisition times necessary in time-resolved experiments.
The performance of the magnetic bottle time-of-flight photoelectron spectrometer is also discussed in this chapter. In XUV photoelectron spectroscopy of gaseous nitrogen the accuracy of the energy calibration is determined to be better than 0.1 eV. The implemented counting mode efficiently eliminates the analog noise, which is important for the detection of the weak solute signals, as will be discussed in the next chapter.

The energy resolution of the photoelectron spectrometer is below the energy resolution of the monochromator at low kinetic energies, and approximately 3% at an electron energy of 15 eV. At higher electron energies the resolution is limited by the single electron response of the MCP-detector. This could be improved by replacing the current detector with a higher quality time-of-flight detector.
In XUV-only photoelectron experiments on the liquid jet, the photoelectron spectra of gaseous and liquid water are measured. The binding energies of the valence orbitals of water, extracted from the photoelectron spectra, are in good agreement with literature values. The liquid jet photoelectron signals are subject to energy shifts caused by electrostatic and electrokinetic charging effects. These effect lead to a higher inaccuracy of the energy calibration. Since the photoelectron spectrum of gas-phase water is however continuously measured also during time-resolved experiments, the shifts can be monitored in the experiment. This way an accuracy of the calibration below 0.2 eV can be achieved also in liquid-phase photoelectron spectroscopy.
Furthermore the XUV photoelectron spectra of ethanol and acetonitrile are measured to demonstrate the capability of the implemented setup to work with more volatile samples than water. This is the first step towards investigating the influence of solvent parameters on the electronic structure and relaxation of solute molecules.
Pump-probe photoelectron experiments are performed both with 800 nm and 400 nm pump pulses and XUV probe pulses. The laser-assisted photoelectric effect, which was first observed in water very recently [19], is observed both with 800 nm and with 400 nm pump pulses. A detailed analysis shows, that the sideband signals can be used to characterize not only the experimental cross-correlation, but also the pump pulse intensity. The capability to observe the extremely weak sideband signal with a 400 nm dressing field demonstrates the sensitivity of the implemented photoelectron detection.

4 Electronic Relaxation of Quinoline Yellow in Aqueous Solution

The main challenge of studying organic solutes in liquid jet photoelectron spectroscopy with XUV pulses is the ratio of the photoelectron signal originating from the sample and from the solvent. At a concentration of 10 mM, which is already considered a high concentration in most all-optical time-resolved techniques, the ratio of solvent to sample molecules in water is approximately 5500:1.
This is why there are few available photoelectron studies of organic molecules in solution. The published studies are conducted either at synchrotron facilities, obtaining only ground state ionization energies [16], or with UV ionization, lacking the sensitivity to the ground state [100]. The combination of the liquid jet technique with time-resolved XUV photoelectron spectroscopy was recently used to investigate a dense ferrocyanide ion solution [101], however at a concentration of 500 mM, which is not accessible for most large organic molecules.
In XUV photoelectron spectroscopy the detection of ground state solute signals relies on the fact, that the ionization energies of large molecules are usually lower than that of the solvent. If this difference in energy is sufficient, the sample photoelectron spectra can successfully be separated from the solvent signal. As discussed in section 3.4, this makes water the most promising solvent for a proof-of-principle experiment.
In this chapter a time-resolved XUV photoelectron measurement of a yellow dye, Quinoline Yellow WS, dissolved in water is presented. It is demonstrated that static and excited state photoelectron signals can be obtained at a concentration of a few millimolar.
In section 4.1 the choice of the dye molecule and its characteristics will be discussed. Since the molecules is sparsely documented, DFT geometry optimization calculations are performed to gain more information on the molecular structure in aqueous solution. XUV-only photoelectron spectra of Quinoline Yellow WS in aqueous solution are presented in section 4.2, investigating also the influence of the concentration and the photon energy on the photoelectron signal. The measured photoelectron spectra are in excellent agreement with the density functional calculations, which are performed for this thesis and also presented in that section.
Time-resolved photoelectron data after excitation with 400 nm pump pulses is presented in section 4.3. In this context a strong increase in the 400 nm only signal compared to neat water is observed, which causes a light-induced space charge effect similar to the effect observed in ref. [49]. A correction method for this space charge effect is proposed, using a simple analytical model and a fitting procedure.
Section 4.3 furthermore discusses the excited state dynamics of Quinoline Yellow WS, which are observed in a time-resolved photoelectron experiment. A shift of the excited state photoelectron signal to lower kinetic energies is observed with a timescale of

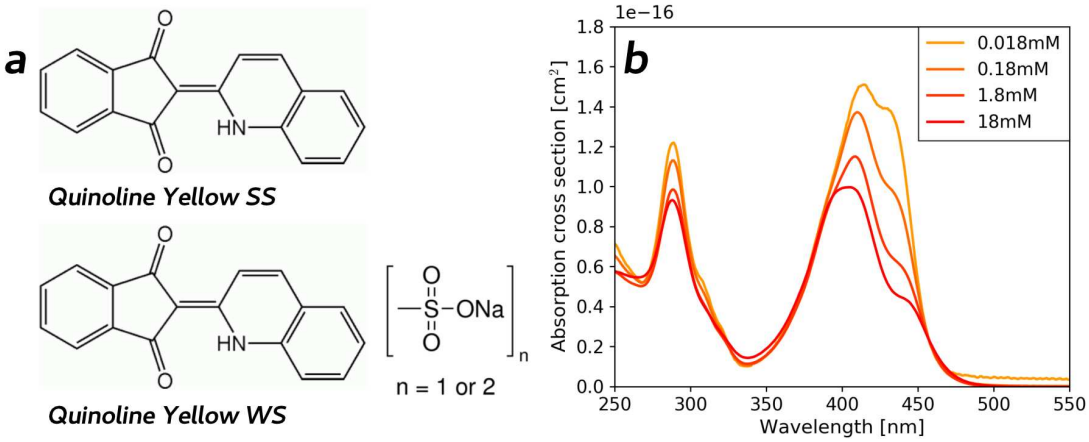

Fig. 4.1: **a)** Molecular structure of Quinoline Yellow SS (spirit-soluble) and Quinoline Yellow WS (water-soluble). **b)** Absorption Spectra of Quinoline Yellow WS in Water at different concentrations, measured using a commercial UV-vis spectrometer.

approximately 250 fs. This timescale can probably be attributed to the initial solvent rearrangement after excitation, a process that occurs on femtosecond timescales in water. After the initial spectral change, the excited state signal exhibits a biexponential decay with decay constants of 1.3 ps and 90 ps. The fast decay is compatible with a recently proposed excited state intramolecular proton transfer (ESIPT) in a similar molecule [20]. For the slow decay a possible interpretation is internal conversion to the ground state, likely via a rotational pathway.

4.1 Quinoline Yellow

Quinoline Yellow water-soluble (QYWS) is a food colorant, used as additive E104 in the European Union [102]. It is based on the dye Quinoline Yellow spirit-soluble (QYSS). The molecular structures of both are shown in figure 4.1a. The difference between the spirit-soluble and the water-soluble form are the sulfonic acid substituents (SO_3Na). Both QYSS and QYWS were purchased from *Sigma Aldrich* and used without modification, meaning that the water-soluble form is a mixture of mono- and disulfonic acids of Quinoline Yellow, according to the *Sigma Aldrich* documentation.

Most chemical suppliers (e.g. *MP Biomedicals*, *Alfa Chemistry*, *Chembase.cn*) give an average molar mass of 477 g/mol for QYWS, meaning that the disulfonic acid form dominates the mixture. For European suppliers this is also consistent with ref. [103], where the composition of QYWS from various suppliers was analyzed. The value of 477 g/mol is used to calculate the concentrations of all the solutions used for experiments in this thesis.

QYWS was chosen as a sample for a proof-of-principle experiment mainly for its high solubility of up to 270 mM in water (extracted from ref. [104]), its availability and its high absorption cross-section at the pump wavelength of 400 nm (see fig. 4.1b). The absorption spectra were measured using a commercial UV-vis spectrometer, as were all other absorption spectra presented in this thesis.
Figure 4.1b shows absorption spectra measured at various concentrations ranging from 18 μM to 18 mM. At a concentration of 18 μM, the, absorption spectrum has a peak at 405 nm with a shoulder at higher wavelength. The measured absorption cross-section of the peak decreases with increasing concentration. Additionally the main peak at 400 nm shifts to lower wavelengths. These changes in the absorption spectrum could indicate aggregation of the sample. The changes in the spectrum are already observed between concentrations of 18 and 180 μM, which is surprising for a reported solubility of up to 270 mM [104]. Apart from aggregation also a change in the tautomeric equilibrium could be a possible explanation, since QYWS can exist in two tautomeric forms (see below).

4.1.1 Molecular Structure

To discuss the characteristics of the water-soluble form QYWS, it is instructive to first consider the unsulfonated dye QYSS. QYSS, also known as Quinophthalone, consists of a Quinoline group (C_9H_7N) and a 1,3-Indandione group ($C_9H_6O_2$) connected by a C-C bridge bond. Two main tautomeric forms are considered for QYSS, which are shown in figure 4.2 [105]. In the keto-tautomer the bridge bond is a single bond and the equilibrium geometry is non-planar with an angle of approximately 90° between the planes of the Quinoline and the Indanione moiety. In the enol-tautomer the bridge bond is a double bond and the molecule is planar.
Although many suppliers, including *Sigma Aldrich*, give the molecular structure of the keto-tautomer in their documentation, it was found in IR-spectroscopy and NMR studies that QYSS assumes the planar enol-form in solution [105, 106]. The extended conjugated system in enol-QYSS is also thought to be responsible for the dye properties of the molecule [106]. In the ground state of enol-QYSS the hydrogen atom, that is bound to the nitrogen of Quinoline, forms a strong intramolecular hydrogen bond with the oxygen of 1,3-Indandione. This form is known as the enamino tautomer [20]. A competing structure, with the hydrogen atom bound to the oxygen of the 1,3-Indandione, is known as the ketoenol tautomer. In DFT investigations on similar molecules it is concluded that the enamino tautomer, i.e. with the hydrogen bound to the nitrogen, is favored [107].
The planar enol form is also considered to be more abundant in the water-soluble QYWS according to ref. [103]. The available literature is however inconsistent considering the sulfonation sites. While all structures of the disulfonic acid of QYSS found in ref. [103] have a single sulfonic acid group on both the Indandione and the Quinoline moiety,

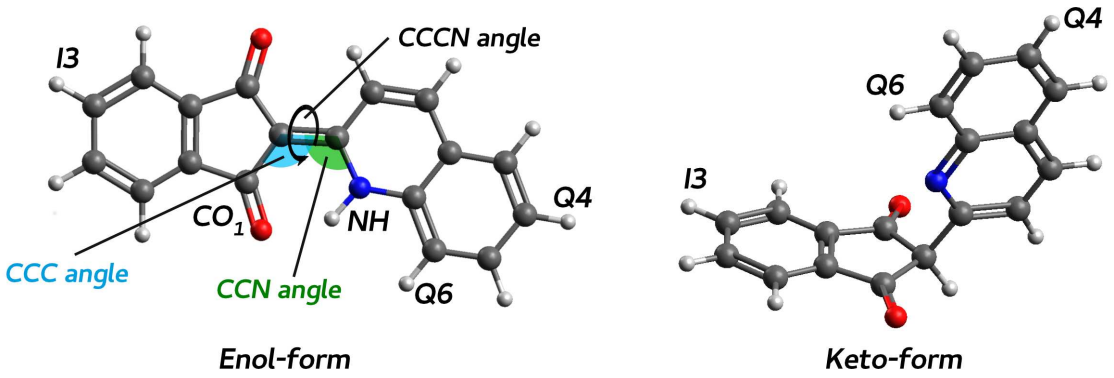

Fig. 4.2: DFT (TPSS/def2-TZVP) optimized geometries of the enol- and the keto-form of Quinoline Yellow SS. In the enol-form the angles are illustrated which are used in table 4.1 to describe the relative orientation of the Quinoline moiety relative to the Indandione. The positions labeled $I3$, $Q4$, and $Q6$ are the sulfonation sites considered for QYWS.

many chemical suppliers (*MP Biomedicals*, *Alfa Chemistry*, *Chembase.cn*) show a structure with both sulfonic acid groups attached to the Quinoline part of the molecule.

To gain more information on the molecular structure of both QYSS and QYWS, density functional calculations using the *ORCA* program system [40] were performed with the aim of obtaining the optimized geometries of the various molecular structures considered. For all calculations of the water soluble form the sulfonic acid groups (SO_3Na) are replaced with the protonated form (SO_3H). This approach was shown to yield the calculated properties closest to the experimental values for the hydrated form of sulfonated dye molecules [108]. The initial geometry for the vacuum geometry optimization is obtained via a force field optimization of the molecules in the software *Avogadro* (version 1.2.0) [109].

The geometry of the molecules is optimized with a density functional calculation using the TPSS functional [37] and the def2-TZVP basis set [38], as discussed in section 2.2. To simulate the influence of the aqueous solution a geometry optimization is performed, including solvent effects with the conductor-like continuum polarization model (CPCM) [35] implemented in the *ORCA* program. For the geometry optimization in solution the result of the vacuum geometry optimization is used as starting point. An overview of the optimized geometries in vacuum, and including the water solution, is shown in table 4.1. The optimized geometries in cartesian coordinates are listed in the appendix (A.2).

Considering at first the relative energy, it is apparent that the enol-form is lower in energy both for QYSS and all calculated forms of QYWS. The energy difference however ranges from 0.1 eV for QYWS Q6I3 to 1.1 eV for QYSS. In the enol-form the ketoenol tautomer was considered only for two configurations. For both the structure with the

hydrogen atom attached to the nitrogen, i.e. the enamino tautomer, is energetically favored. The energy difference between the enamino and the ketoenol tautomer is about 0.3 eV for QYSS in vacuum and 0.9 eV for QYWS Q4I3 in water.
The decrease in energy due to solvation is consistently above 1 eV for most molecular structures. The geometry changes within both the Indandione part and the Quinoline part of the molecule are small, even when going from the enol to the keto tautomer. There is only a consistent increase of the bridge bond length of 0.1 Å in the keto tautomer.
Three angles are used to describe the relative orientation of the Quinoline and the 1,3-Indandione, as shown in figure 4.2. The CCN and CCC angles give the angles of the groups relative to the bridge bond. The CCCN angle describes the out-of-plane rotation around the bridge bond. In the enol-tautomer there are only small deviations in the angles. The molecular structure appears to be rather independent of sulfonation and the molecule remains planar.
In the keto-tautomer, the rotation angle (CCCN) exhibits large fluctuations depending on sulfonation and solvation. Since the bridge bond is a single bond in this tautomer, it is expected that the rotational flexibility is larger than in the enol-tautomer. On the other hand it can not be excluded that there are several stable conformations both in the enol- and in the keto-tautomer. In that case the geometry optimization for any given sulfonation could converge to a different conformer, i.e. a local minimum in the ground state potential energy surface.

Table 4.1: Results of the DFT (TPSS/def2-TZVP) geometry optimization for QYSS and several structural isomers of QYWS (i.e. different sulfonation sites) both in the enol- and in the keto-form (fig. 4.2). For the bond lengths within the Quinoline and 1,3-Indanione groups only the mean unsigned error (MUE) and the maximum error (MaE) with respect to QYSS are listed. The angles are defined as shown in figure 4.2. The differences in final energy ΔE in vacuum are given relative to the isomer with the minimum energy, e.g. QYWS Q4I3 for all disulfonic acids of QYSS. For the geometries including the aqueous solution (calculated via CPCM) the difference in energy is given relative to the optimized geometry in vacuum.

enol-form

		bond lengths [Å]							I-Q angles [degree]			ΔE [eV]
		Indandione			Quinoline			Bridge				
		MUE	MaE	CO_1	MUE	MaE	NH		CCC	CCN	CCCN	
QYSS	vac.			1.25			1.04	1.40	123.0	117.6	0.3	min.
QYWS Q4	vac.	0.001	0.004	1.25	0.003	0.006	1.04	1.40	123.0	117.5	1.3	min.
QYWS Q4	H_2O	0.002	0.004	1.25	0.002	0.004	1.03	1.41	123.6	117.7	1.4	-0.83
QYWS Q4I3	vac.	0.001	0.003	1.25	0.002	0.004	1.04	1.40	122.9	117.4	1.5	min.
QYWS Q4I3	H_2O	0.002	0.007	1.25	0.003	0.004	1.03	1.41	123.5	117.6	1.3	-1.17
QYWS Q6I3	vac.	0.001	0.004	1.24	0.004	0.012	1.04	1.40	122.9	117.7	0.2	0.26
QYWS Q6I3	H_2O	0.002	0.008	1.25	0.004	0.012	1.04	1.41	123.3	117.4	0.2	-1.19
QYWS Q4Q6	vac.	0.003	0.008	1.24	0.006	0.015	1.05	1.39	123.1	117.9	2.4	0.30
QYWS Q4Q6	H_2O	0.002	0.005	1.25	0.005	0.014	1.04	1.40	123.4	117.6	2.7	-1.14

keto-form

		Indandione				Quinoline		Bridge	I-Q angles			ΔE [eV]
		MUE	MaE	CO	CH	MUE	MaE		CCC	CCN	CCCN	
QYSS	vac.			1.22	1.10			1.52	112.0	116.1	40.9	0.79
QYWS Q4	vac.	0.021	0.044	1.25	1.10	0.020	0.053	1.50	114.4	118.3	66.5	1.13
QYWS Q4	H_2O	0.002	0.007	1.22	1.10	0.002	0.005	1.51	115.3	116.2	48.7	-1.29
QYWS Q4I3	vac.	0.003	0.007	1.21	1.09	0.001	0.004	1.52	108.7	115.6	92.8	0.89
QYWS Q4I3	H_2O	0.003	0.011	1.22	1.09	0.002	0.004	1.49	109.9	115.7	87.1	-1.26
QYWS Q6I3	vac.	0.003	0.012	1.21	1.10	0.002	0.007	1.51	111.8	117.8	89.7	0.43
QYWS Q6I3	H_2O	0.004	0.009	1.22	1.10	0.006	0.015	1.49	118.9	119.6	29.1	-1.55
QYWS Q4Q6	vac.	0.003	0.009	1.21	1.09	0.004	0.013	1.51	111.0	115.7	44.9	0.63
QYWS Q4Q6	H_2O	0.002	0.008	1.22	1.09	0.004	0.012	1.51	111.7	115.2	45.8	-1.23

4.2 XUV Photoelectron Spectroscopy Results

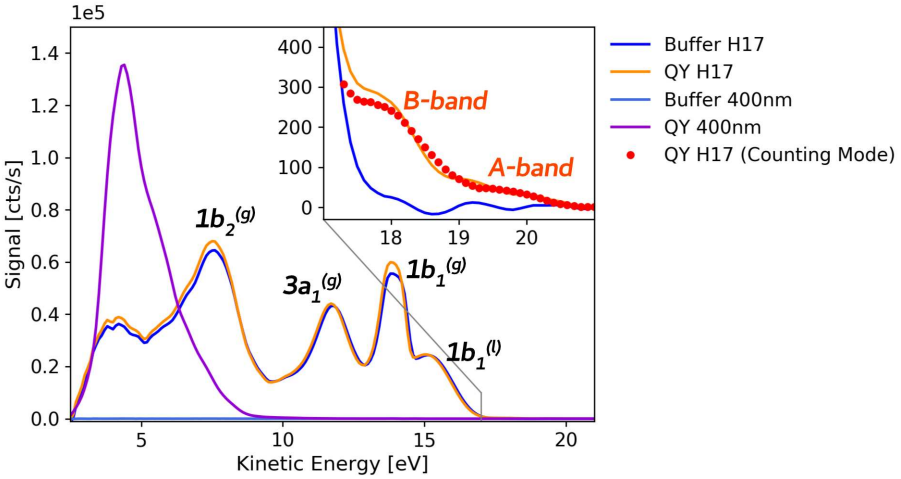

Fig. 4.3: Photoelectron spectra of 10 mM QY Solution and a reference NaCl solution (Buffer), acquired with the 17th harmonic (26.5 eV) and with the 400 nm pump pulse (3.1 eV). The XUV spectra are normalized using the $1b_1$ liquid water peak. On the high kinetic energy edge two photoelectron bands of QY, labeled *A*- and *B*-band, are visible.

As discussed above, the XUV pulses will ionize the solvent as well as the solute molecules. At a concentration of 10 mM the expected ratio of solvent to solute signal is 5500:1, assuming equal ionization cross-sections. To distinguish molecular signals in the XUV photoelectron spectra from the signals originating from water, a careful comparison of spectra with and without the solute is necessary. For this, a 60 mM NaCl reference solution is prepared. Part of this reference solution is then used to prepare a 10 mM Quinoline Yellow solution. Figure 4.3 shows the photoelectron spectra of both the reference solution (buffer) and the QY solution. Figure 4.3 also shows spectra obtained upon ionization of the NaCl solution and the QY solution by the 400 nm pump pulse. The XUV photoelectron spectra of water and the QY solution are normalized to the signal of the liquid water $1b_1$ peak. For the most part the spectra are the same. But on the high kinetic energy edge of the liquid water band, two additional peaks are visible in the spectrum of the QY solution. Because these peaks are absent in the spectrum of the reference solution, they can be attributed to ionization of the Quinoline Yellow molecules. The two QY photoelectron bands, corresponding to vertical binding energies of approximately 7 eV and 8.5 eV, are designated as the *A*- and *B*-band for future reference.

The integrated photoelectron signal of both molecular photoelectron bands is approximately 100 times weaker than the integrated signal of the liquid water $1b_1$ peak. This

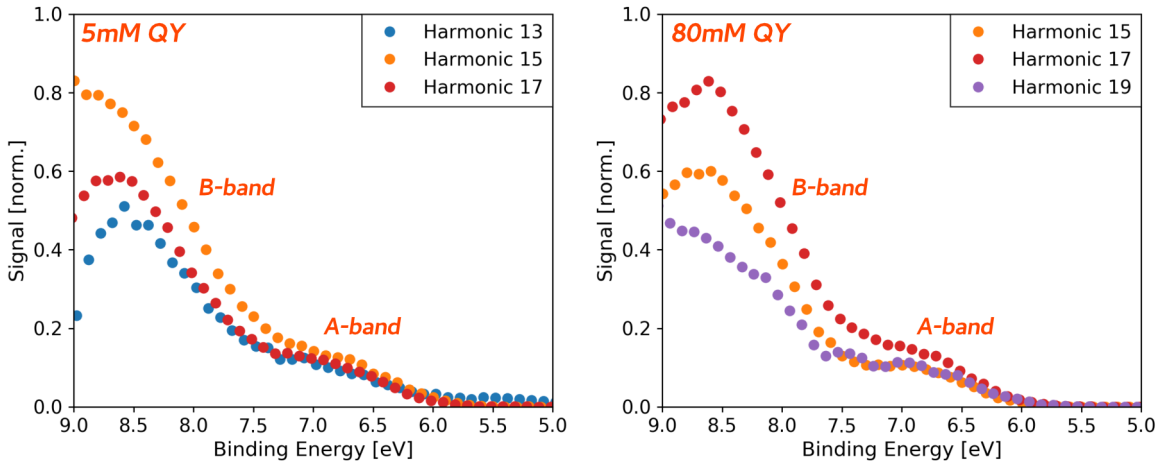

Fig. 4.4: QY photoelectron spectra (water spectrum subtracted) obtained with different harmonics and with QY concentrations of 5 mM and 80 mM. All spectra are normalized to the $1b_1$ peak of liquid water.

ratio is much higher then the ratio estimated before for equal ionization cross-sections. From the ratio one can estimate that the ionization cross-section of QY is larger than that of water by a factor of 50. In this context it should however be noted that only the low binding energy part of the photoelectron spectrum of QY is obtained. Any contributions from higher lying ionic states are hidden under the much stronger water signal, so that the total cross-section can be even higher.
The photoelectron spectra obtained upon ionization with the 400 nm pulse show a pronounced change upon switching from the reference solution to the QY solution. The pump pulse intensity is kept below 1 TW/cm^2 to avoid ionization of water by the pump pulse. Consequently, there is no detectable photoelectron signal from water. But there is a strong photoelectron signal at low kinetic energy when QY is present in the solution. This change in signal has multiple reasons. First of all the photoionization cross-section of QY is larger than that of water, as evident from the XUV photoelectron spectra. Second, the ionization potential of Quinoline Yellow is lower than that of liquid water, so two or three 400 nm photons are sufficient to ionize QY, while four 400 nm photons are necessary to ionize water. Third, the strong absorption of QY at 400 nm leads to resonance enhancement of the multiphoton ionization.

4.2.1 Influence of Photon Energy and Concentration

By subtracting the photoelectron spectrum of the reference NaCl solution from the spectrum of the QY solution, the spectrum of the QY molecules can be extracted. The spectra of aqueous QY obtained with several harmonics, and concentrations of 5 mM and 80 mM QY in the solution, are shown in figure 4.4. The spectra are normalized to

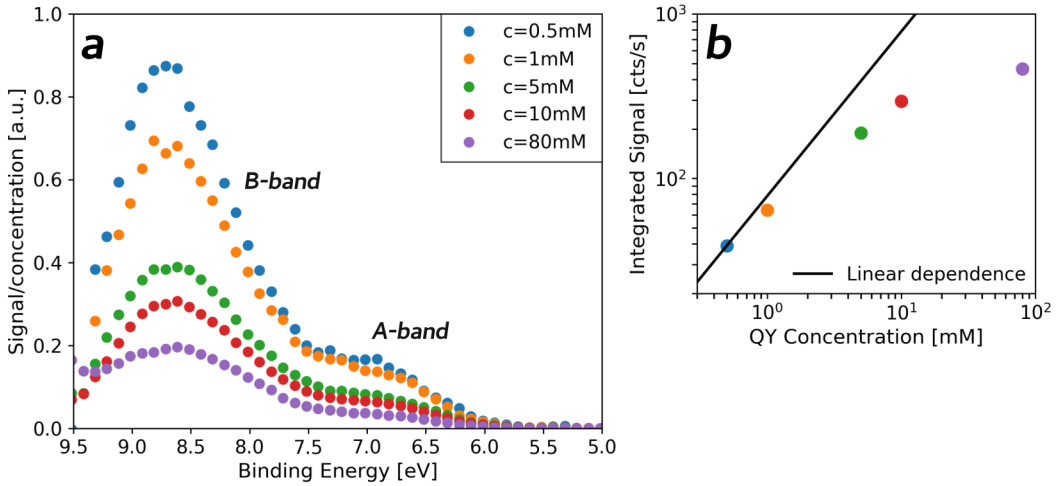

Fig. 4.5: **a)** Photoelectron spectra obtained with the 17th harmonic and different concentrations of QY. The spectra are normalized to the QY concentration. **b)** Concentration dependence of the total QY photoelectron signal. Already at a concentration of 5 mM the signal clearly deviates from a linear concentration dependence.

the signal of the $1b_1$ liquid water peak, to correct for fluctuations in the XUV intensity. This normalization can, however, introduce an error, since QY photoelectron signal of unknown magnitude overlaps with the liquid water peak in the spectrum of the QY solution. For binding energies below 9 eV the water signal is small and the error introduced by the normalization is negligible.

The spectra measured using different photon energies overlap quite well for the A-band. The magnitude of the B-band signal changes with photon energy, which indicates changes in the relative ionization cross-section. While there are no strong changes in the overall shape of the photoelectron spectrum, it is found that the photoelectron signal of QY does not increase linearly with the concentration. Therefore the concentration dependence of the total QY signal needs to be investigated in more detail. To this end spectra with the harmonic 17 are acquired at concentrations ranging from 0.5 to 80 mM. Each spectrum is averaged over an acquisition time of approximately 5 minutes, i.e. 300000 laser shots.

The photoelectron spectra at various concentrations of QY are shown in figure 4.5a. First of all the plot demonstrates that high quality photoelectron spectra of solvated molecules can be recorded in a relatively short acquisition time, even with a solute concentration below 1 mM. The spectra are normalized to the concentration. Thus one would expect them to overlap, if the signal depended linearly on the concentration. This is not the case, and already for the step going from 1 mM to 5 mM there is a clear saturation effect. Figure 4.5b clearly shows that the total signal deviates from a linear

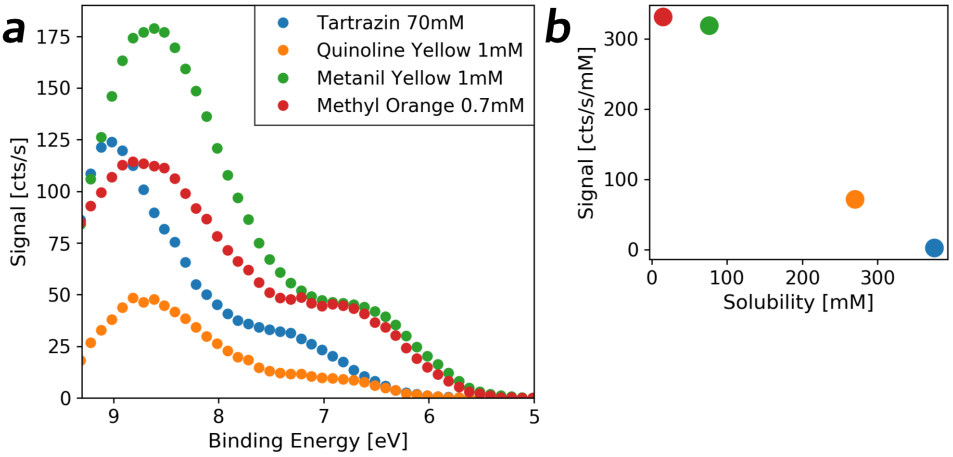

Fig. 4.6: **a)** Photoelectron spectra of several sulfonated dye molecules (molecular structures in Appendix A.1) in aqueous solution. **b)** The integrated photoelectron signal divided by the concentration shows a negative correlation with the dye solubility (solubilities extracted from ref. [104]).

dependence on the concentration. For example when going from a QY concentration of 10 mM to 80 mM, the signal increases by less than a factor of two.
One possible explanation for this saturation effect would be sample aggregation, since there was some evidence of aggregation of Quinoline Yellow in the absorption spectra (fig. 4.1). Usually one would however expect the aggregate to have an XUV photoionization cross-section similar to the summed up cross-sections of the individual molecules. Thus aggregation should not lead to a strong decrease in signal with increasing concentration. A more likely explanation for the saturation effect is that the concentration on the liquid jet surface saturates.
Since XUV photoelectron spectroscopy has a probing depth of less than 2 nm, only the surface concentration will be sampled. If the surface concentration saturates earlier than the bulk concentration, the photoelectron signal exhibits saturation before the concentration limit in the sample solution is reached. Thus the saturation of the photoelectron signal indicates that the dye concentration is higher on the surface.
The idea that molecules accumulate on the liquid jet surface can be supported with experiments on other dye molecules. In the experiments carried out for this thesis XUV photoelectron spectra of several sulfonated dye molecules were measured. Figure 4.6 shows the photoelectron spectra of four sulfonated dye molecules in aqueous solution. In the binding energy range where the dye signal can be extracted, the photoelectron spectra are similar, which justifies a direct comparison of the total signals. For most dyes the concentration in the solution was chosen to be approximately 1 mM, so the saturation effect discussed before should be negligible. Only for Tartrazin a significantly higher concentration had to be used to reach a comparable photoelectron signal.

Table 4.2: Vertical ionization energies of QYSS and various sulfonation species of QYWS from DFT calculations (M06-2x/def2-TZVP). The considered sulfonation sites are labeled according to figure 4.2. The ionization energies are calculated in vacuum and in water solution (using CPCM). Details of the calculation method are discussed in section 2.2.

		SS	WS Q4	WS Q4I3	WS Q6I3	WS Q4Q6
enol	vac.	7.62	8.00	8.32	8.11	8.12
	H_2O	-	6.30	6.45	6.43	6.47
keto	vac.	8.62	9.21	9.40	9.51	9.22
	H_2O	-	7.30	7.33	7.60	7.77

The inset in figure 4.6 shows the integrated photoelectron signal divided by the dye concentration, as a function of dye solubility. The plot clearly suggests a negative correlation between the solubility of the molecules and the total photoelectron signal. This can be intuitively understood by considering the link between the solubility and the surface excess of the solute molecules. The dyes used here are by themselves hydrophobic and are only made water-soluble by adding the sulfonic acid groups. It is therefore likely that they have a positive surface excess, meaning that they decrease the surface free energy of the solution and are therefore likely to collect close to the surface. This leads to a surface concentration that is higher than the bulk concentration [110]. In water solution, the surface excess is negatively correlated to the hydration free energy. Solubility, on the contrary, increases with the hydration free energy [110]. This explains why the less soluble sample molecules have a higher surface excess and therefore an increased surface concentration. This in turn leads to a higher photoelectron yield, since only the surface concentration is sampled in XUV photoelectron spectroscopy. Thus the solubility of the sample molecules in liquid jet photoelectron spectroscopy is not as limiting as expected.

4.2.2 DFT Ionization Energies

Assigning the two peaks in the XUV photoelectron spectrum of Quinoline Yellow is challenging, because of the large number of conformations and ionic states to consider. To obtain an estimate of how much the conformation influences the ionization energy, DFT calculations are performed based on the optimized geometries from the previous section. As discussed in section 2.2, the HOMO ionization energy is calculated as the difference in energy between the neutral molecule and the ion. All calculations are performed with the *ORCA* program system [40] at the M06-2x/def2-TZVP level of theory.

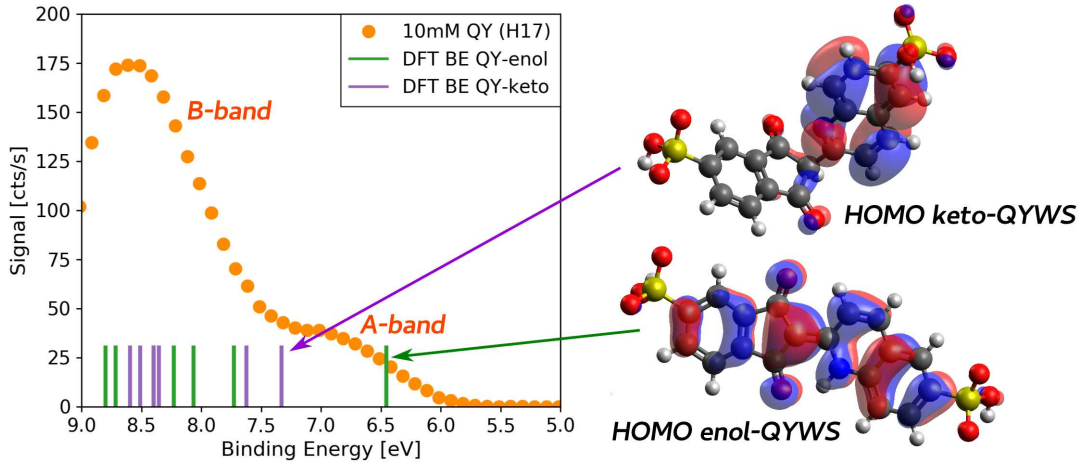

Fig. 4.7: Comparison of the QY photoelectron spectrum obtained using the 17th harmonic (26.5 eV), with the ionization energies from the DFT calculation (M06-2x/def2-TZVP). The highest occupied molecular orbitals of enol- and keto-QYWS are visualized, as obtained from the DFT calculation.

The DFT ionization energies for all considered sulfonation species of Quinoline Yellow in vacuum and in water are listed in table 4.2. One observation is that sulfonation increases the ionization energy both in the enol- and in the keto-form. The vertical ionization energy of the keto-form is consistently approximately 1 eV higher than that of the enol-form, indicating that the first band in the XUV photoelectron spectrum could consist purely of ionization of enol-QY, while the second band could contain signal from both tautomers. The phase transition shift, i.e. the difference in ionization energy between vacuum and solution, is similar for the enol- and keto form, and ranges from 1.5 to 2 eV.

The differences in ionization energy due to the different sulfonation sites in QYWS are small compared to the enol/keto difference and the phase transition shift. Although the geometry optimization of keto-QYWS showed large changes in geometry between the differently sulfonated forms, the ionization energies are similar. Within the error of the calculation, which can be expected to be up to 0.5 eV [36], the ionization energies of all sulfonation species are the same. Hence the influence of the sulfonation site and the conformation seems to be relatively small. The HOMO ionization energy is likely still determined by the π-electrons on the rings of both Indandione and Quinoline.

While the HOMO ionization energies of enol- and keto-QY in water solution obtained from the DFT calculation agree quite well with the onset of the two photoelectron bands, more ionic states have to be considered to model the full photoelectron spectrum. As discussed in section 2.2, approximate ionization energies of lower-lying orbitals can be obtained from the orbital energies given by the DFT calculation. To this end all orbital energies are corrected using the more accurate value of the HOMO ionization

energy (see section 2.2 for details). This approach, applied to the disulfonic acid form with the lowest single point energy after geometry optimization (QYWS Q4I3), yields the orbital ionization energies. The calculated ionization energies for both the enol- and the keto-form are shown together with the photoelectron spectrum in figure 4.7.
The QY photoelectron spectrum is clearly incompatible with the calculated ionization energies of keto-QY. The measured spectrum could be explained with an enol-keto equilibrium as it is suggested in ref. [106] or with only enol-QY in the solution as assumed by refs. [20, 105]. It appears that the *A*-band in the photoelectron spectrum can be attributed to ionization of the HOMO of enol-QY. The *B*-band is made up of ionization to multiple ionic states, and could also contain signal from ionization of keto-QY. The density of ionic states also explains the shape of the photoelectron spectrum.
The shape of the HOMO's of enol- and keto-QYWS sulfonated at I3 and Q4, as obtained from the DFT calculation, are also visualized in figure 4.7. The HOMO of enol-QYWS is a π-orbital delocalized over the entire molecule. In the non-planar keto-form this orbital does not exist, which explains the large difference in ionization energy between the tautomers. The HOMO-orbital of keto-QY is mainly localized on the Quinoline part of the molecule and has a higher ionization energy.
The error of DFT ionization energies, especially in combination with solvent calculations, are typically considered to be on the order of 0.3-0.5 eV [36]. Considering this, the agreement between the calculation and the experiment is remarkable. In conclusion the shape of the photoelectron spectrum is largely determined by the density of ionic states and not the influence of differently sulfonated dye molecules or conformers.

4.3 Time-Resolved Photoelectron Spectroscopy Results

For the time-resolved experiments a 10 mM QY solution is prepared based on the 60 mM NaCl reference solution, as described in section 4.2. Figure 4.8a shows the QY photoelectron spectra acquired for different delays between the 400 nm pump pulse and the 26.5 eV probe pulse as a false color map. The binding energy is calculated with respect to the XUV photon energy. At positive delays the XUV pulse arrives after the 400 nm pulse. The delay axis is linear only up to a delay of 200 fs and logarithmic for larger positive delays to better represent different decay channels. The false color maps in figure 4.8 are averaged over 8 separate delay scans, meaning that each individual spectrum is averaged over an acquisition time of 80 s (80000 laser shots).
Figure 4.8b shows a difference false color map, obtained by subtracting the spectrum at negative delays. The spectrum at negative delays is equivalent to the sum of the single color spectra except for intensity fluctuations. While XUV-induced dynamics both in water and QY are certainly possible, this kind of experiment would result in low kinetic energy photoelectrons. It is therefore safe to assume, that there is no pump-probe signal at negative delays in the electron energy range where molecular

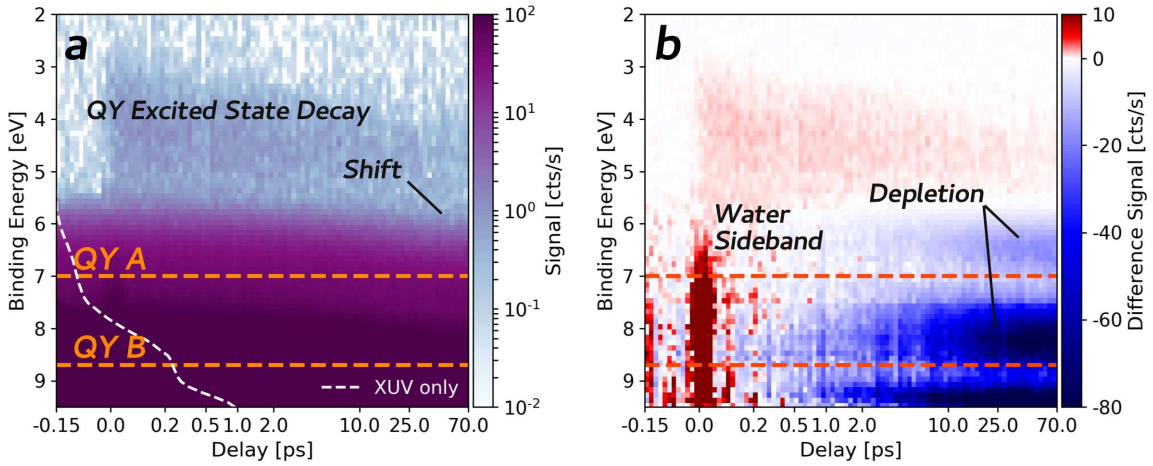

Fig. 4.8: **a)** Counting mode pump-probe photoelectron data of a 10 mM QY solution, acquired with a 400 nm UV pulse and a 26.5 eV XUV pulse. The binding energy is calculated with respect to the XUV photon energy. At positive delays, the XUV-pulse comes after the UV pulse. Note that the delay axis consists of a linear and a logarithmic part, to better represent the occurring fast and slow decays. **b)** Difference map of the UV-pump, XUV-probe signal, obtained by subtracting the signal at negative delays.

signals are observed. Thus red areas in the map (fig. 4.8b) correspond to increase of the XUV photoelectron signal by the UV pulse, while blue areas correspond to depletion of the photoelectron signal.

There are three distinct pump-probe features visible in the maps. The increase in photoelectron signal at time overlap, which is visible in the counting mode difference signal (fig. 4.8b), can be attributed to the first positive sideband of the liquid water $1b_1$ peak. This signal can be used to obtain accurate values for the zero delay and the cross-correlation, independent from molecular signals, as discussed in section 3.5.

In the unsubtracted map (fig. 4.8a) a shift of the spectrum to lower kinetic energies is observed, which was not observed in measurements of pure water with comparable 400 nm intensity. The shift is thus clearly caused by the presence of the QY molecules. This shift increases with increasing positive delay and causes the strong depletion features around binding energies of 6 eV and 8 eV in the difference map (fig. 4.8b). The origin of this signal is discussed in the next section.

The third pump-probe effect is an increase in signal between binding energies of 2 eV and 5 eV. As the shift, this signal is clearly caused by the molecular sample, since it was not observed in pure water measurements. It is visible in both maps in figure 4.8 as a broad photoelectron band, decaying with increasing positive delay. Regarding the energy and magnitude, this signal matches the expectations for an excited state signal. It can therefore be attributed to the QY excited state decay.

4.3.1 Light-Induced Space Charge Effect

Figure 4.9 shows QY solution photoelectron spectra, obtained at negative delays (XUV before 400 nm) and at positive delays, together with the XUV-only spectrum. Except for intensity fluctuations, the spectrum at negative delays is equivalent to the XUV-only spectrum, which validates the subtraction of the negative delay signal to obtain the difference signals. At positive delays, however, both the liquid water peak and the Quinoline Yellow peaks (see inset) are shifted to lower kinetic energies.
A similar effect was recently observed in pure water measurements by Al-Obaidi and coworkers [49]. In this publication the effect was attributed to a light-induced space charge effect caused by the intense pump pulse. The pump pulse generates a large number of electrons and ions in the liquid jet, which in turn generate an electric field. The photoelectrons ejected by the XUV probe pulse are then influenced by this electric field, leading to a delay-dependent change in their kinetic energy.
The shift seen in the time-resolved photoelectron experiments can be interpreted as the result of a similar space-charge effect. This effect is not directly related to the electronic structure of the QY molecules. It is however not observed in measurements with pure water and similar pump pulse intensity, since it is indirectly caused by the solute molecules. As discussed in section 4.2, the lower ionization potential of the solute molecules paired with a resonance enhancement effect leads to a much stronger electron yield from pump pulse ionization.
This also explains why the gas phase peaks are not affected by the energy shift. The UV-induced electrons originate only from the liquid jet itself, since the intensity of the UV pulse is not sufficient to ionize water, as seen in section 4.2. The electrons from ionization of water vapor by the XUV pulse on the other hand originate from a larger volume, forming a weak, homogeneous electron cloud. Thus most of the electrons from water vapor are generated far away from the liquid surface and are not influenced by the electric field generated by the UV pulse.
Overall the behavior seen here is consistent with the effect observed in ref. [49], except for one significant difference: In the experiment presented here, the observed shift is zero at time-overlap, while a strong shift to higher kinetic energies at time-overlap is reported in ref. [49]. Since Al-Obaidi and coworkers used longer 800 nm pump pulses and higher intensities, it is possible that they misinterpreted an increased sideband signal as a light-induced shift.
To model the light-induced shift, one has to describe the electric potential generated upon ionization by the pump pulse. In a first approximation the ion and the electron clouds can both be described by spherical shells with constant charges Q and $-Q$. The electron cloud expands rapidly, due to the kinetic energy of the electrons, while the ions move much slower. Although a movement of the ions on picosecond timescales was proposed before [49], it proved sufficient for the delays covered here to treat the positive charges as static.

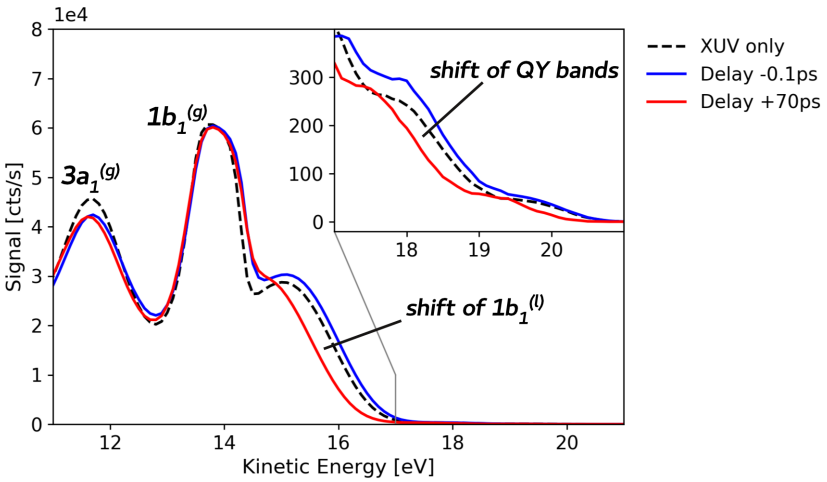

Fig. 4.9: Comparison of the photoelectron spectra obtained for QY solution at positive and negative UV-XUV delays with a measurement employing only the XUV pulse. At negative delays the spectrum is similar to the XUV-only spectrum, apart from intensity fluctuations. At large positive delays the liquid water peak and the QY peaks are clearly shifted to lower kinetic energies, while the gas-phase water peaks remain unshifted.

The model is illustrated in figure 4.10. At $t = 0$, the pump pulse generates a static ion sphere and an expanding electron sphere. At the delay time $t = \Delta t$, the XUV ionization generates electrons, which move in the potential of the charged spheres, usually with a higher kinetic energy than the UV-induced electrons. At the crossing time $t = t_x$, the XUV-induced electrons overtake the electron sphere.

The UV-induced photoelectrons are modeled by an expanding sphere with radius $R_{pump}(t) = r_{lj} + v_{pump}t$, where r_{lj} is the radius of the liquid jet and $v_{pump} = \sqrt{2E_{pump}/m_e}$ is the radial velocity of the UV-induced electrons with average kinetic energy E_{pump}. The potential of a charged spherical shell with radius R is given by

$$V(r) = \begin{cases} \frac{Q}{4\pi\epsilon_0}\frac{1}{R} & \text{for } r < R \\ \frac{Q}{4\pi\epsilon_0}\frac{1}{r} & \text{for } r > R \end{cases} \tag{4.1}$$

which means that the total potential induced by UV-ionization vanishes outside the sphere of the UV-induced electrons, and is equal to that of a positive point charge Q inside the sphere. Therefore the kinetic energy shift of the XUV-induced electron is the energy lost in the field of the ions up to the radius r_x, where the XUV-induced electrons overtake the UV-induced electrons.

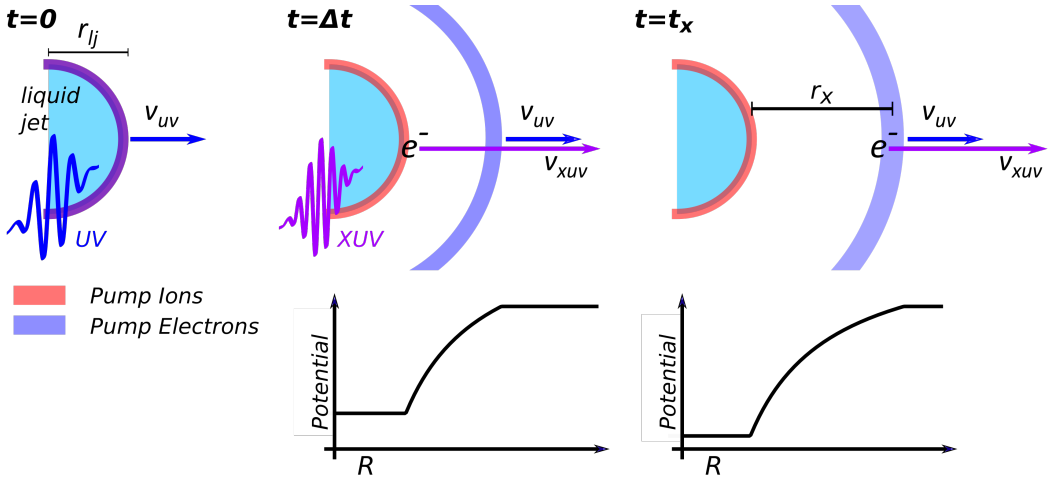

Fig. 4.10: Illustration of the light-induced shift, which is caused by the electric potential induced by the UV pump pulse. At $t = 0$ the UV ionization generates ions and electrons, which are described as a static ion sphere and an expanding electron sphere. At the delay time $t = \Delta t$ the XUV ionization generates electrons, which move in the potential of the charged spheres. At the crossing time $t = t_x$ the XUV-induced electrons overtake the sphere of the UV-induced electrons.

The classical movement of an electron in a Coulomb potential with zero angular momentum is governed by the differential equation

$$m\ddot{r} = -\frac{eQ}{4\pi\epsilon_0}\frac{1}{r^2} \tag{4.2}$$

which can be easily solved numerically for initial conditions

$$\begin{aligned} r(\Delta t) &= r_{lj} \\ \dot{r}(\Delta t) &= \sqrt{2E_{xuv}/m_e} \equiv v_{xuv} \end{aligned} \tag{4.3}$$

From the solution one can then extract the delay-dependent crossing time t_x, using the condition

$$r(t_x) = r_{lj} + v_{pump}(t_x) \tag{4.4}$$

The delay-dependent energy shift can then be extracted from the velocity of the XUV electron at the crossing time $\dot{r}(t_x)$.
If the electrons generated by the XUV pulse move much faster than the electrons generated by the pump pulse, the change in the velocity of the XUV-induced electrons is small compared to their absolute velocity. In this regime the calculation of the crossing distance can be simplified by approximating the trajectories of the XUV-induced

electrons with a uniform motion

$$r(t) = r_{lj} + v_{xuv}(t - \Delta t) \tag{4.5}$$

and neglecting the change of the potential during the travel time of the XUV-induced electrons. The energy shift is then simply determined by the energy lost in the potential of a point charge Q, up to the crossing distance r_x. If both the expansion of the UV-induced electron sphere and the movement of the XUV-induced electrons are described with a uniform motion, the crossing distance is

$$r_x = r_{LJ} + \frac{v_{pump} v_{xuv} \Delta t}{v_{xuv} - v_{pump}} \tag{4.6}$$

which leads to an energy shift

$$\Delta E = \frac{eQ}{4\pi\epsilon_0} \left(\frac{1}{r_{lj}} - \frac{1}{r_x} \right) \tag{4.7}$$

To test the limits of this approximation, energy shifts are calculated both by solving the differential equation (4.2) numerically and with the approximate equation (4.7). The values obtained for the energy shift are compared for various kinetic energies of the UV-induced electrons, charges Q, and delays. It is found, that the shift calculated with equation (4.7) deviates by less than 10 meV from the shift retrieved by solving the differential equation, for charges below 5000 $\bar{e}$ and initial kinetic energies of the XUV-induced electrons over 10 eV. In this kinetic energy range the dependence of the shift on the kinetic energy E_{xuv} is also found to be negligible for a fixed charge Q.
In the pump-probe experiments presented here the average kinetic energy of the electrons ejected by the pump pulse is usually around 1 eV. The kinetic energy of liquid water electrons ($1b_1$), ejected with a 23.4 eV XUV photon, is 12.1 eV. Thus the condition for the kinetic energy difference is satisfied for measurements with the harmonic order 15 or higher.
To retrieve the energy shift from the pump-probe data, the delay-dependent kinetic energy of the liquid water $1b_1$ electrons needs to be extracted. To this end the liquid $1b_1$ peak and the onset of the overlapping gas-phase $1b_1$ peak are modeled with two Gaussian peaks, as shown in figure 4.11b. Since the gas-phase peak does not shift in energy, its kinetic energy and width are fixed in the fit.
The Gaussian fit yields the kinetic energy of the liquid water $1b_1$ peak and thus the delay-dependent energy shift. The shift is then modeled using equation (4.7) as shown in figure 4.11a. The only two fitting parameters are the total charge of the UV-induced electrons per shot and the average energy of the UV-induced electrons. Both these parameters can be checked for consistency with the UV-only photoelectron spectrum, which is routinely acquired during pump-probe measurements. The fit shown in figure 4.11 gives the parameters $Q = 3430\bar{e}$ and $E_{pump} = 0.68$ eV. From the single-color 400 nm

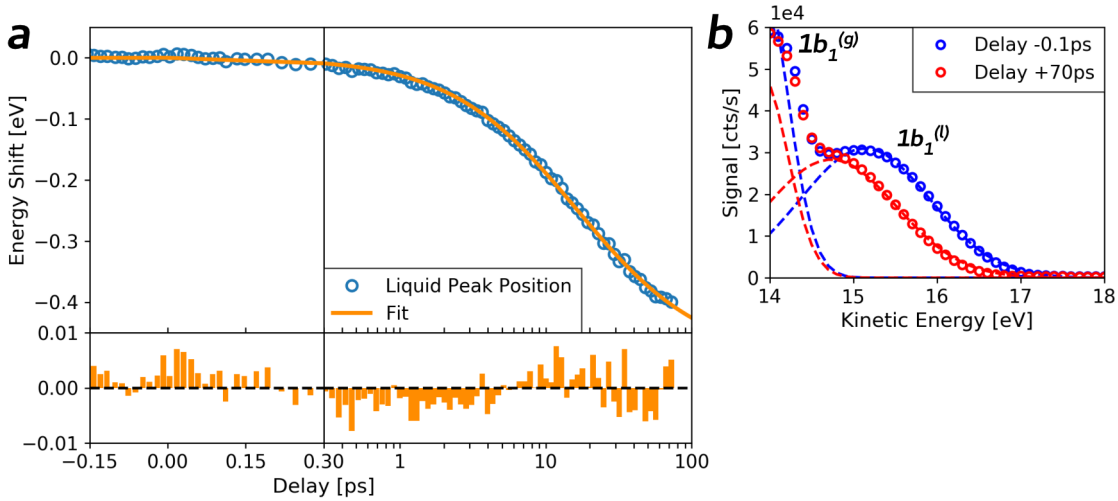

Fig. 4.11: In the time-resolved experiment the ionization by the UV pulse leads to a space charge effect, which causes a delay-dependent shift of the liquid phase photoelectron peaks. To retrieve the delay-dependent energy shift from the pump-probe data, the $1b_1^{(l)}$ peak and the onset of the $1b_1^{(g)}$ peak are fitted with two Gaussian peaks (panel b). The position of the $1b_1^{(g)}$ peak is fixed to 12.6 eV and its FWHM is only fitted once at negative delays and then fixed to that value. Panel a shows the retrieved delay-dependent energy shift of the $1b_1^{(l)}$, which is modeled with equation (4.7). The extracted fit parameters are $Q = 3430 \pm 20\,\bar{e}$ and $E_{pump} = 0.68 \pm 0.02$ eV.

spectrum a total count rate of 400-500 cts/shot is extracted. This agrees reasonably well with the fitted parameter considering the collection efficiency of the magnetic bottle, which is approximately 8% [66]. The average kinetic energy is less consistent with the single-color spectra and additionally the kinetic energy distribution of the UV-induced electrons is broad (see fig. 4.3), which means that the model is idealized. Nevertheless the model proves to be sufficient for the correction of the molecular pump probe signals.

With the fit a model function for the delay-dependent shift is extracted, based on the liquid water signal. This, in turn, can be used to correct the shift of the QY photoelectron signal. The correction is accomplished by shifting the data in kinetic energy for every delay-point according to equation (4.7) and interpolating the shifted data on the original energy grid. Additionally the amplitude of the $1b_1^{(l)}$ peak obtained from the fit for every delay point can be used to normalize the data to the liquid water signal and thus correct for XUV intensity fluctuations. This procedure is however only valid if there is no systematic delay-dependence of the $1b_1^{(l)}$-peak signal. In the presented time-resolved experiments, no pump-probe effect on the liquid water signal

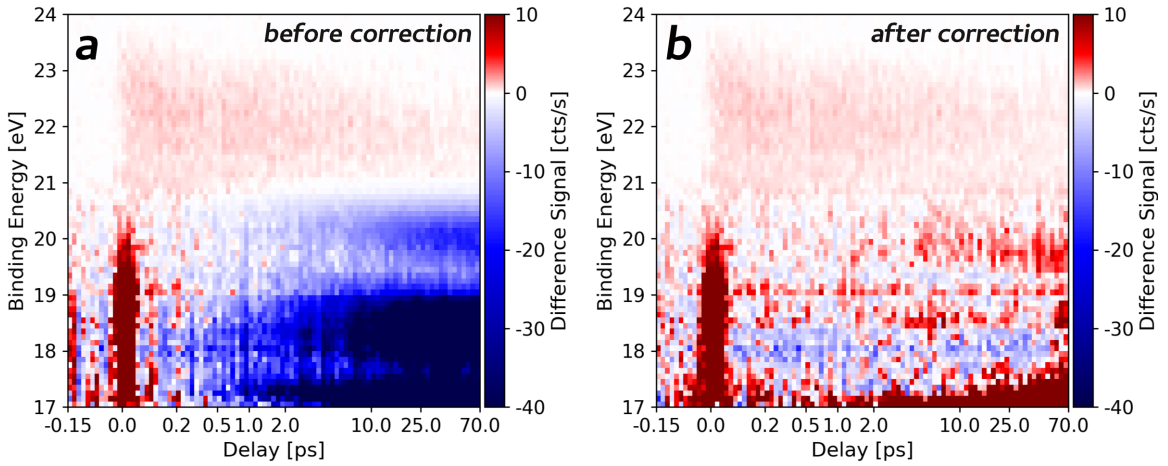

Fig. 4.12: QY solution photoelectron data before (a) and after (b) the procedure to correct for the shift caused by a light-induced space charge effect. To obtain the difference maps the spectrum at negative delays was subtracted as before. The depletion features associated with the light-induced shift are almost completely removed by the correction procedure described in the text.

is observed, therefore this normalization procedure can be applied to correct for signal fluctuations.

The result of the correction procedure including the aforementioned normalization is shown in figure 4.12. The shift to lower kinetic energies of the QY signal is successfully corrected. Thus, the influence of the space charge effect on the transient molecular signals is corrected, and any remaining pump-probe features can be interpreted in the context of the excited state relaxation of the QY molecules.

As figure 4.12 shows, the depletion features in the counting mode data are almost entirely removed by the correction procedure. It is noteworthy that the false color maps show only the counting mode signal, which is dominated by electrons originating from Quinoline Yellow. The correction procedure on the other hand relies entirely on the water signals and is completely independent of the molecular signals. That the correction nonetheless works for the molecular signals, is a clear indication that the observed effect is not a direct molecular effect, but affects the whole liquid-phase photoelectron signal equally.

Another important characteristic of the presented correction procedure is that the shift is negligible for small delays, which means that errors in the correction procedure will mainly affect dynamics on longer timescales. Any molecular pump probe effects observed within the first 0.5 ps will not be influenced by the correction procedure.

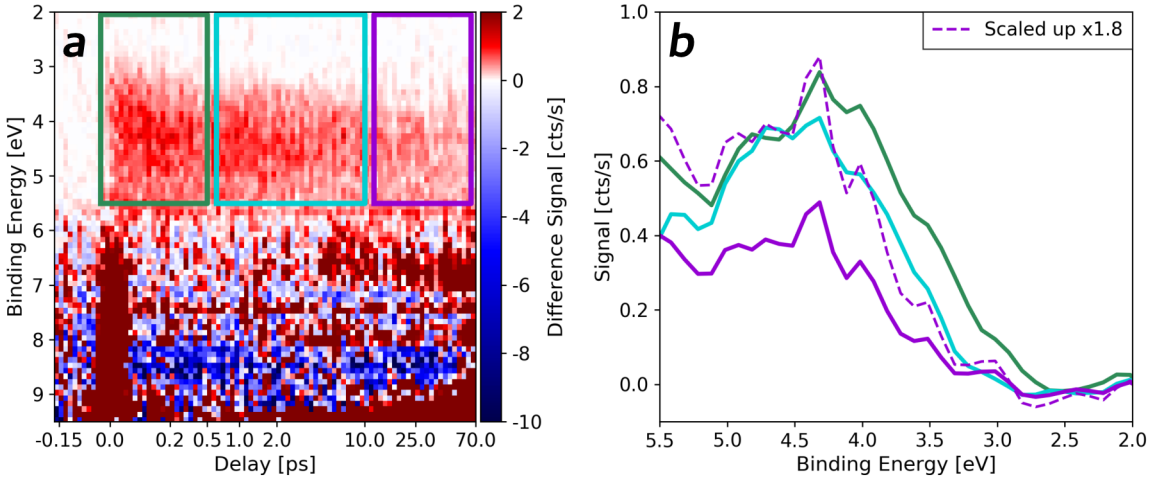

Fig. 4.13: **a)** Corrected and normalized map of the QY pump-probe photoelectron data with the signal at negative delays subtracted. **b)** Averaged QY excited state photoelectron spectrum around zero time delay (green, -0.03-0.5 ps), at short delays (turquoise, 0.6-10 ps), and at long delays (purple, 12-65 ps) as highlighted in the map.

4.3.2 Quinoline Yellow Excited State Decay

Figure 4.13a shows the time-dependent QY photoelectron spectrum as a false color map, after the shift correction. As discussed before, the spectrum at negative delays is subtracted to obtain the difference signal. In figure 4.13b the averaged difference spectra around zero time delay (green, -0.03-0.5 ps, at short positive delays (turquoise, 0.6-10 ps), and at long delays are shown (purple, 12-65 ps). The spectrum at long delays overlaps with the spectrum at short delays, if it is scaled appropriately (dashed line). The spectrum around zero time delay extends to higher kinetic energy, i.e. lower binding energy. The spectral change occurs in the first 500 fs, which is a first indication of sub-picosecond dynamics in the experiment.

The region where the spectral difference is observed is centered around 3.5 eV. In section 4.2 the static XUV photoelectron spectrum of Quinoline Yellow WS was compared to ionization energies from the DFT calculation. The conclusion was that the highest occupied molecular orbital of the enol-QY is located at a binding energy of approximately 6.5 eV with a large gap to the next occupied molecular orbital. Therefore the region where spectral change is observed matches the region where a change in the photoelectron spectrum is anticipated, when a single 400 nm photon (3.1 eV) is absorbed from the HOMO of enol-QY. This corresponds to the excitation from the delocalized π-orbital, which is a clear indication for the excitation of the enol-form of the dye by the pump pulse.

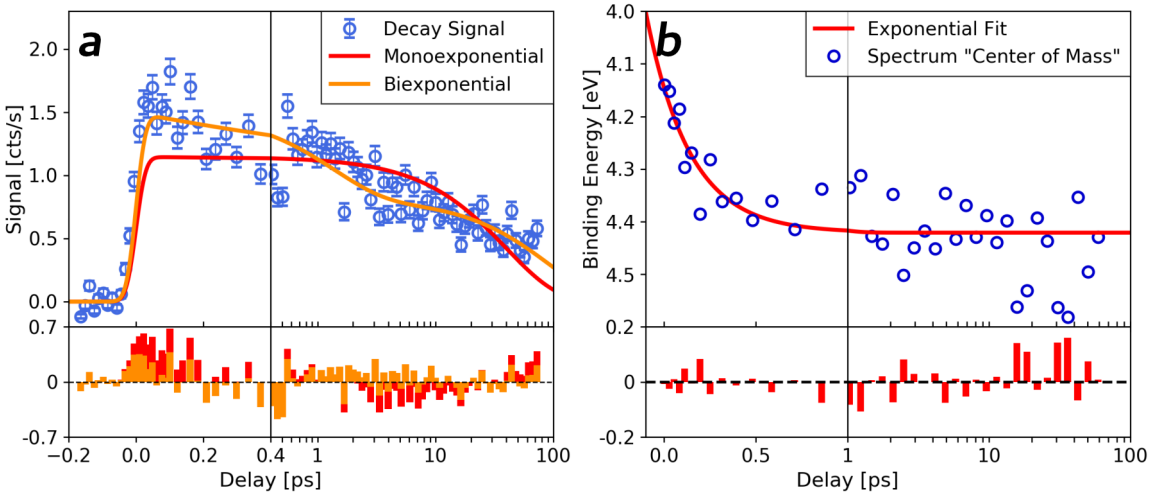

Fig. 4.14: **a)** Integrated excited state decay signal (Binding Energy 5.2-2.5 eV). The fit with a monoexponential decay function clearly fails to model the dynamics. The biexponential fit yields decay constants of 1.3±0.4 ps and 90±20 ps. **b)** Time-dependent "center of mass" of the excited state photoelectron spectrum. The spectral shift is modeled with an exponential function starting at the zero time delay. The fit yields a shift of 0.28±0.04 eV and a decay constant of 250±70 fs.

There is, however, no feature in the difference signal (fig. 4.13a) corresponding to the depletion and recovery of the HOMO ground state signal, which would be expected around a binding energy of 6.5 eV. The amplitude of a depletion signal should be equal to that of the excited state signal. The ground state transient signal would thus be on the order of one count per second and is probably not visible due to the higher background signal from single-color XUV photoionization in the region around 6.5 eV. The fluctuations in the background single-color signal are on the range of several counts per second and obscure the ground state transient signals.

To extract the excites state dynamics of Quinoline Yellow the excited state decay signal is integrated in the binding energy region from 5.2 eV to 2.5 eV. The time-dependence of the integrated signal is shown in figure 4.14a. The errorbars are obtained from the square root of the total count rate, assuming a Poisson distribution. The integrated signal can then be modeled with an exponential decay function, as discussed in section 2.3. From a Gaussian fit of the liquid water sideband signal the exact zero time delay and a cross correlation FWHM of 45 fs can be extracted, therefore these parameters are fixed in the fit of the excited state decay.

The excited state dynamics of Quinoline Yellow cannot be modeled with a single decay constant, as is apparent in figure 4.14a. Therefore the decay is modeled with a biexponential decay function, which yields decay constants of approximately 1.3 ps and

90 ps. These two timescales can however not explain the spectral change in the first 0.5 ps which is visible in the excited state spectrum (fig. 4.13).
To access the dynamics associated with the fast spectral change, the "center of mass" of the excited state spectrum is extracted, which is the average binding energy of the excited state photoelectron spectrum from 5.2 to 2.5 eV. To reduce the noise, the number of delay points is additionally reduced by binning delay points. The dynamics of the spectral "center of mass" are shown in figure 4.14b. As expected from the excited state spectra, the spectral shift occurs within the first 0.5 ps, after which no further spectral changes are observed. An exponential fit of the spectral dynamics yields a third time constant of approximately 250 fs. This time constant appears to be associated with a spectral shift rather than with a decay of the excited state signal.

4.3.3 Discussion

The fastest response that is observed in the time-resolved photoelectron experiment of Quinoline Yellow, is a shift of the excited state photoelectron spectrum with a timescale of approximately 250 fs. On this timescale no loss of excited state photoelectron counts is observed. It is therefore unlikely that this timescale is associated with an internal conversion process. A possible explanation for this effect is ultrafast solvent rearrangement after electronic excitation. Upon electronic excitation, the dipole moment of the molecule can change both in value and direction. This means that the solvent polarization adjusts to the new molecular dipole moment, stabilizing the excited state in energy. This effect is for example observed as a red-shift in time-resolved fluorescence spectroscopy [111].
In most solvents two timescales are found for the solvent rearrangement following excitation. A fast timescale, typically sub-picosecond, is linked to the inertial reorientation of the solvent molecules. A slower timescale is connected with diffusion-driven movement of solvent molecules. Water is the fastest reacting solvent, with a predicted timescale of the inertial rearrangement of approximately 20 fs [112]. Jimenez and coworkers [113] studied the rearrangement of water molecules after excitation of a coumarin dye in water solution. They found a shift of the fluorescence spectrum of approximately 0.2 eV and a timescale for the inertial rearrangement of under 100 fs [113].
The energy shift measured in the time-resolved photoelectron experiment is comparable to the energy shift reported in ref. [113]. The measured timescale is however significantly slower than the estimated timescale for the inertial rearrangement of water molecules. A possible explanation for this discrepancy could be the hydrogen bonding to the ionic sulfonic acid groups. It was reported before that solvation shells of anions are more rigid, which slows down solvent rearrangement [114].
After the initial spectral shift the excited state photoelectron spectrum exhibits a biexponential decay with decay constants of approximately 1.3 ps and 90 ps. These timescales are both linked to a decay of the excited state photoelectron signal rather

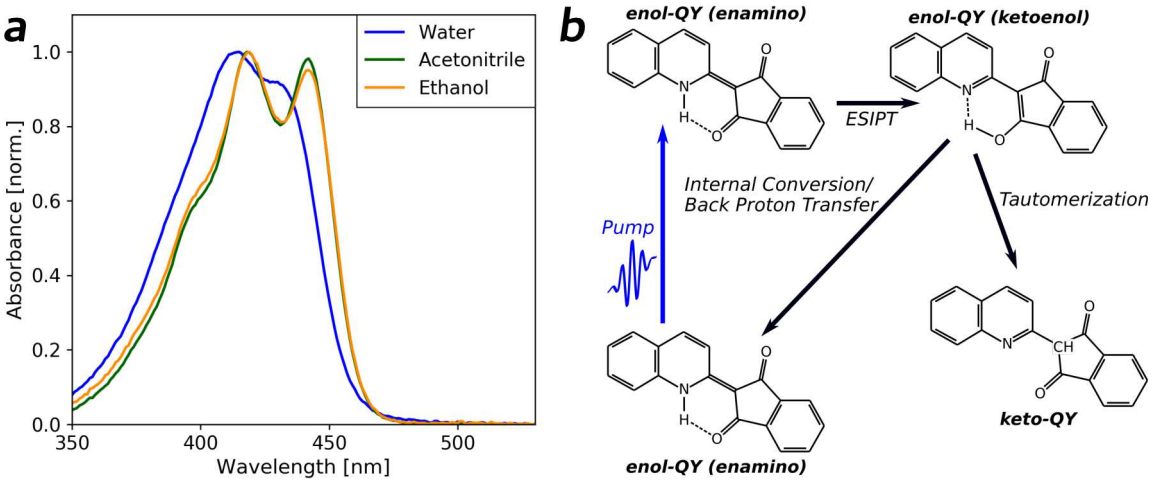

Fig. 4.15: **a)** Absorption spectra of QYWS in water, ethanol, and acetonitrile, measured at a concentration of approximately 2 μM. The spectra are normalized to the maximum absorbance. **b)** Some possible relaxation pathways for Quinoline Yellow. The first step could be an excited state intramolecular proton transfer (ESIPT) from nitrogen to oxygen.

than a change in the photoelectron spectrum. Thus they can probably be attributed to the electronic relaxation of the excited Quinoline Yellow molecules.

To aid in the interpretation of the pump-probe photoelectron data, the absorption spectra of QYWS in various solvents are measured. Figure 4.15a shows spectrally resolved absorption in water, ethanol, and acetonitrile. The absorption spectra in ethanol and acetonitrile have two clear peaks and a shoulder at lower wavelength indicative of a vibrational progression. The spacing between the peaks corresponds to a vibrational frequency of approximately 1300 cm^{-1}. The closest frequency found in Quinoline lies at 1314 cm^{-1} and is assigned to one of the C-N stretching modes [115]. In the structurally similar 2-phenyl-1,3-Indandione, which is 1,3-Indandione with a phenyl ring instead of Quinoline, the most prominent modes in this frequency region are found around 1230 cm^{-1} and 1330 cm^{-1} and are predominantly assigned to a mixed stretching and bending motion of the attached phenyl ring [116]. It therefore seems plausible that the vibrational structure visible in absorption and fluorescence is linked to a C-N stretching motion.

QY has a low fluorescence quantum yield, especially in polar solvents [20]. The timescales of 1.3 ps and 90 ps, observed in the photoelectron experiment, are orders of magnitude faster than typical fluorescence timescales and would therefore lead to fluorescence quenching. That the fluorescence in water is quenched by the ultrafast timescales observed in the time-resolved photoelectron experiment is further supported by the strongly washed-out structure in the absorption spectrum of QY in water.

A proposed mechanism for the electronic relaxation is illustrated in figure 4.15b. A possible explanation for the 1.3 ps timescale is an excited state intramolecular proton transfer (ESIPT) from the nitrogen on Quinoline to the oxygen on the 1,3-Indandione. This proposal is supported by a recent transient absorption study of the electronic relaxation of the unsulfonated form of Quinoline Yellow in cyclohexane [20]. After excitation with 400 nm pulses, Han and coworkers [20] found three relaxation timescales of 3.3 ps, 15 ps, and 84 ps. Upon replacing the hydrogen on the nitrogen of Quinoline with deuterium, they observed an increase of both the short and the long timescale. Together with time-dependent DFT (TDDFT) calculations the authors [20] attributed the timescale of 3.3 ps to the ESIPT process illustrated in figure 4.15b.
Excited state proton transfer from nitrogen to oxygen is an uncommon effect, since proton transfer between hetero-atoms is more often considered in reverse, i.e. from oxygen to nitrogen [117]. But proton transfer from nitrogen to oxygen is not unheard of, and is observed for example in indigo dyes [118]. In the case of QY, however, one has to consider that Quinoline is known as a photobase, meaning that it is less likely to donate a proton in the excited state [119]. Han and coworkers argue that photobasicity is a relative measure, meaning that ESIPT between photobases is possible if the relative basicity of the participating groups is sufficiently different [20].
A comparison between ref. [20] and the experiment presented here is not straightforward, since it is not entirely clear if the molecular structure with the intramolecular hydrogen bond (fig. 4.15b) is valid in aqueous solution. Water forms complex networks of hydrogen bonds and it is possible that both the nitrogen of Quinoline and the oxygen of 1,3-Indandione form hydrogen bonds with the solvent, instead of forming an intramolecular hydrogen bond. There are, however, several arguments supporting the planar, internally hydrogen-bonded structure also in water solution. First, the intramolecular hydrogen bond is reported to be strong [105], which could suggest that it is favored over bonding with the solvent. Second, the absorption spectra of Quinoline Yellow in weakly and strongly hydrogen bonding solvents are relatively similar (fig. 4.15a). This also supports the planar structure even in hydrogen bonding solvents, since the absorption is attributed mainly to the delocalized π-orbital of planar Quinoline Yellow. Third, the ionization energies obtained by DFT calculation of the enol-tautomer exhibit excellent agreement with the measured photoelectron spectrum (see section 4.2), although the continuum cavity model for the solvent does not include hydrogen bonding to the solvent.
Another possible explanation for the 1.3 ps timescale would be an internal conversion process to a lower-lying excited state. But this is incompatible with the DFT calculations in ref. [20], which showed that 400 nm light excites QY into the lowest-lying excited state. Therefore the proton transfer illustrated in figure 4.15b is most likely responsible for the dynamics observed in the photoelectron experiment. The measured timescale in water is 2-3 times faster than that observed in cyclohexane [20], which indicates a lowering of the barrier along the proton transfer coordinate in polar solvents.

The 90 ps timescale observed in the photoelectron measurement is in good agreement with the long timescale observed by Han and coworkers [20]. This could be linked to intersystem crossing to a triplet state. But a populated triplet state should be visible as a change in the excited state photoelectron spectrum, which is not observed. Additionally Han and coworkers [20] found no effect of nitrogen purging on the observed dynamics, which also speaks against an intersystem crossing.

The more likely explanation for the long timescale is an internal conversion back to the ground state. In their TDDFT calculations Han and coworkers [20] found no crossing between ground and excited state along the proton transfer coordinate. Hence the internal conversion to the ground state needs to include an additional change in geometry. In the DFT geometry optimization in section 4.1, large changes of the rotation angle around the bridge bond between differently sulfonated forms of QY. The changes in the rotation angle, although larger in the keto-tautomer, were also present in the enol-tautomer. This instability of the angle between the two parts of the molecule could suggest that a rotation around the bridge bond is a possible relaxation pathway for the molecule.

The rotation around the bridge bond would be aided by an initial excited state proton transfer to oxygen, since this removes electron density from the bridge bond and turns it into a single bond. One option is a pathway to the ground state, combining rotation with a back-proton-transfer. At least in water solution, an additional option would be a tautomerization pathway towards the keto-form of the molecule as illustrated in figure 4.15b. The keto-form has a hydrogen attached to the carbon atom on the Indandione end of the bridge bond, therefore the tautomerization pathway would require an additional proton transfer.

Due to the larger distance this second proton transfer process would likely involve the solvent. Proton transfer through water is a complicated process, since water forms large networks of hydrogen bonds. The hydrogen bond chains act as proton wires and can transport protons effectively over long distances [120, 121]. The timescale of 90 ps matches the expected timescale for a proton transfer mediated by water, since proton transfer through hydrogen bond chains of two water molecules was observed on similar timescales for example in 7-Hydroxyquinoline [122].

4.4 Summary

This chapter presents the first results of photoelectron spectroscopy of an organic molecule, Quinoline Yellow, in aqueous solution. The XUV photoelectron spectrum of the organic dye Quinoline Yellow WS in aqueous solution is measured at concentrations down to 0.5 mM. This concentration is ten times lower than concentrations used in previous liquid jet measurements even at synchrotron facilities [16], demonstrating the sensitivity of the implemented setup.

Due to the high sensitivity, the influence of the solute concentration and the XUV photon energy can be investigated in detail. The photoelectron spectra obtained with different XUV photon energies are consistent. Measurements at different concentrations of Quinoline Yellow in the solution show that the photoelectron signal does not increase linearly with increasing concentration. This indicates the importance of the surface concentration of solutes in liquid jet photoelectron spectroscopy, which can differ significantly from the bulk concentration due to accumulation of molecules on the liquid surface. In XUV photoelectron experiments with several sulfonated dyes a negative correlation between the solubility and the photoelectron yield is discovered. This negative correlation further supports the hypothesis of a surface excess of the solute molecules.
To support the interpretation of the photoelectron spectra, DFT calculations at the M06-2x/def2-TZVP level of theory were performed, where the solvent was simulated via the conductor-like polarizable continuum model (CPCM). The agreement between the measured photoelectron spectra and the ionization energies obtained via DFT calculations is remarkable. The comparison of measured spectra and DFT results leads to the conclusion that one of the measured photoelectron bands in the spectrum can clearly be assigned to the delocalized π-orbital, which is the highest occupied molecular orbital of the enol-tautomer of QY.
In the UV-pump, XUV-probe experiment of QY in aqueous solution a strong increase in the UV-only signal compared to neat water is observed, which causes a light-induced space charge effect similar to the effect observed in ref. [49]. A fitting procedure is devised, which can be used to correct the pump-probe electron data for this effect. The correction procedure relies entirely on the liquid water photoelectron signals and is thus independent of the molecular pump-probe effects of interest.
In the time-resolved experiment of QY in aqueous solution, the photoelectron spectrum and the dynamics of the electronically excited molecule are obtained. A shift of the excited state photoelectron spectrum on a 250 fs timescale is observed, which can be explained by the initial solvent rearrangement after excitation. Apart from the shift, the excited state signal exhibits a biexponential decay with decay constants of approximately 1.3 ps and 90 ps.
Following a recent study investigating the unsulfonated form of QY [20], the 1.3 ps decay is attributed to an intramolecular excited state proton transfer process. This turns the bridge bond of Quinoline Yellow into a single bond, decreasing the molecules rotational stability. Therefore a possible explanation for the 90 ps decay is an internal conversion to the ground state following a rotational pathway. Another possible interpretation of the slow decay would be a tautomerization pathway to the keto-tautomer of Quinoline Yellow.
Altogether the proof-of-principle experiment is clearly successful, dynamics of excited state decay can be observed using pump-probe photoelectron spectroscopy of solvated molecules at millimolar concentration. Further insight into the plausibility of

intramolecular proton transfer in aqueous solution could come from experiments with deuterated Quinoline Yellow. The molecule deuterates easily [20], therefore experiments with deuterated Quinoline Yellow should be performed in a solution of deuterated water. Additionally, a time-resolved photoelectron experiment in an aprotic solvent like acetonitrile could help with the interpretation of the 90 ps timescale. The tautomerization pathway would be inhibited in an aprotic environment, because it probably includes a proton transfer through the solvent.
Additional information could come from time-dependent DFT (TDDFT) calculations, as they were performed by Han and coworkers [20], but including various solvents. Future TDDFT calculations should not only include the proton transfer coordinate, but also the coordinate associated with rotation around the bridge bond.

5 Isomerization of Amino-Azobenzene Dyes in Aqueous Solution

Molecular switches are molecules that can reliably be transferred from one stable state into another. This switch is often triggered by photoabsorption, meaning that after photoexcitation the molecule relaxes, with a high quantum yield, to a product state. In most cases the product state is a conformational isomer. For example the retinal molecule is one of the most effective molecular switches in nature, responsible for the initial step in human vision. Embedded in the rhodopsin protein, retinal has a high isomerization quantum yield and isomerizes to one specific target state. In solution the photoisomerization lacks that selectivity, which illustrates that the function of molecular switches strongly depends on the environment [9].
One of the most common man-made molecular switches is azobenzene. It has two isomers, the stable trans-isomer and the metastable cis-isomer. The isomerization in either direction can be triggered by photoabsorption, with an efficiency depending on the excitation wavelength. This makes it one of the most versatile base molecules for molecular switches. Molecular switches based on azobenzene are promising candidates for application in electronics [1] and medicine [2]. Therefore the isomerization dynamics of azobenzene derivatives are a topic of high interest.
Additionally azobenzene exhibits an unusual dependence of the isomerization quantum yield on the excitation wavelength. This sparked major interest in the isomerization of azobenzene itself, since it indicates dynamics on several excited state potential energy surfaces. The isomerization mechanism is controversial even today [123, 124]. The study of amino-azobenzene derivatives could offer a complementary approach to disentangle the complex isomerization dynamics of azobenzene, since there is evidence for a different ordering of excited states [125].
In this chapter results of time-resolved photoelectron spectroscopy of two amino-azobenzene derivatives, Methyl Orange and Metanil Yellow, are presented. Both are mainly known for their use as industrial dyes and pH-indicators, but show a similar isomerization behavior as many azobenzene-based molecular switches. In the first section the literature concerning the isomerization of azobenzene and of the amino-azobenzene dyes is briefly reviewed.
In section 5.2 XUV-only photoelectron spectra of both dyes in solution are presented. The ground state photoelectron spectra are compared to DFT calculations of vertical ionization energies. The results of time-resolved photoelectron spectroscopy are presented in section 5.3. Excited state photoelectron spectra and isomerization timescales are retrieved for both dyes. The measured isomerization timescale for the better-studied dye Methyl Orange agrees with literature values, while Metanil Yellow exhibits slower isomerization. For Metanil Yellow the experiment reveals dynamics before isomerization, which could be linked to internal conversion.

5.1 Photochemistry of Azobenzene and Amino-Azobenzenes

The so-called azo dyes get their name from the double-bonded nitrogen group (azo-group), whose non-bonding lone pair orbital is responsible for their photochemical behavior. The absorption spectrum of azo dyes can be modified by adding substituents. This property makes them attractive for the use as dyes or pigments in industrial products ranging from clothing and food to paint and paper [126].
Whether the compounds are used as dyes, as molecular switches, or as indicators, determines the desired properties. For industrial dyes a high light-fastness is needed, meaning that isomerization to a stable product state, which changes the absorption spectrum, is an unwanted effect. Furthermore low reactivity is desired, meaning that absorbed light energy should be dissipated rapidly and without dissociation or charge transfer. In indicators or molecular switches on the other hand changes in structure after irradiation or depending on the environment are desired. Here high isomerization quantum yield and reversibility are key features. The photochemical characteristics, which determine possible applications, are directly linked to the electronic relaxation of the dye.

5.1.1 Isomerization of Azobenzene

To discuss the photochemistry of the azo dyes it is helpful to first review the well-documented characteristics of the parent molecule azobenzene. Azobenzene has been studied extensively with energy-domain and time-domain experimental techniques and with computational methods, both in the gas phase and in solution. This review does not cover the literature completely, but rather focuses on the established relevant facts and few recent works highlighting the existing interest in the isomerization of azobenzene molecules.
Figure 5.1a shows the molecular structure of azobenzene in the trans- and cis-isomer and the two main isomerization pathways discussed in the literature. The trans-isomer is considered to be planar. In the cis-isomer both phenyl-rings are twisted out of the plane by about 60° (NNCC angle) [127]. The two isomerization pathways are the rotation around the N=N double bond and the inversion of one of the nitrogen atoms [21].
The UV-vis absorption spectrum of trans-azobenzene (fig. 5.1b) shows two main electronic transitions. The strongest absorption band for trans-azobenzene is centered at around 320 nm (i.e. 3.9 eV) and is assigned to a symmetry-allowed $\pi\pi^*$ transition. The considerably weaker transition centered around 450 nm (i.e. 2.8 eV) is associated with a symmetry-forbidden $n\pi^*$ transition. Both the position and the strength of the transitions show weak solvent dependence, and even in gas-phase measurements a similar absorption spectrum is obtained [128]. In the absorption spectrum of the cis-isomer the $\pi\pi^*$ transition is shifted slightly to lower wavelengths and the absorbance

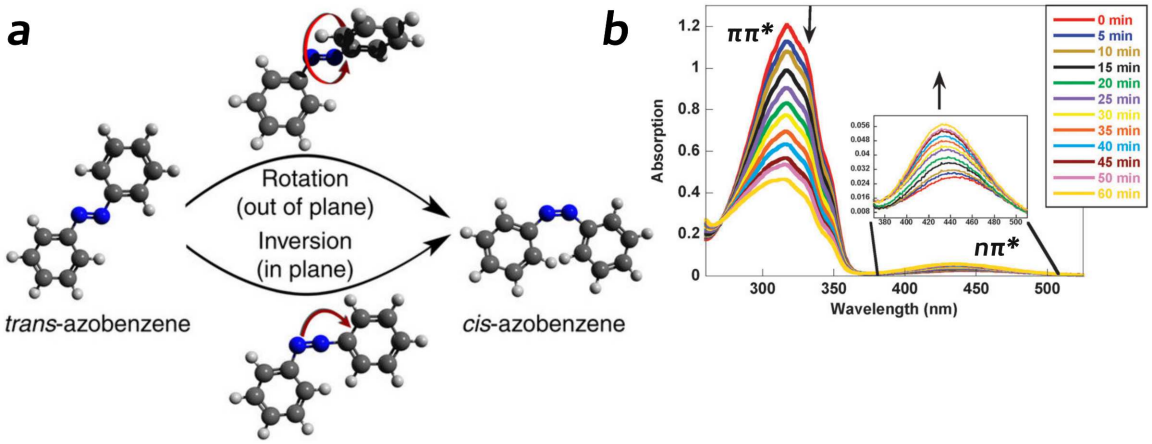

Fig. 5.1: **a)** Molecular structure of trans- and cis-azobenzene and the two main isomerization pathways suggested in the literature (from ref. [124]). **b)** Absorption spectrum of trans- azobenzene and its changes due to light-induced trans-cis isomerization (from ref. [21]).

of the $n\pi^*$ transition is substantially increased. Upon irradiaton and subsequent isomerization, the absorbance of the $n\pi^*$ transition increases, while the absorbance of the $\pi\pi^*$ transition decreases, as shown in figure 5.1b [21, 129].

Isomerization from trans- to cis-azobenzene and vice versa can be triggered by both S_1 ($n\pi^*$) or S_2 ($\pi\pi^*$) excitation. Additionally the cis-trans isomerization can occur thermally, with an activation energy of around 1.0 eV [129]. Quantum yields of the trans-cis isomerization show a relatively weak solvent dependence, but are sensitive to the initially excited state. Quantum yields of 23-35% after S_1 excitation and 5-15% after S_2 excitation are measured. Cis-trans isomerization on the other hand does not show such a clear dependence on excitation, and a quantum yield of 40-60% is observed depending on the solvent [21]. The different isomerization quantum yields of the molecule for the two excited states have sparked major interest in the isomerization and led to many studies employing time-resolved spectroscopy and quantum chemistry calculations to explore the isomerization dynamics.

The isomerization of gas-phase azobenzene after S_1 excitation was recently studied with high resolution spectroscopy [124] and perturbation theory [130]. Both studies come to the conclusion that isomerization after S_1 excitation occurs mainly via a rotational pathway. After excitation to S_2, the only significant pathway is the internal conversion to S_1 on a timescale of approximately 170 fs, according to Tan and coworkers [124]. A compatible explanation for the difference in isomerization quantum yield is the involvement of other excited states [131]. Another possible explanation is an internal conversion to a region on the S_1 potential energy surface which is inaccessible to direct S_1 excitation [123].

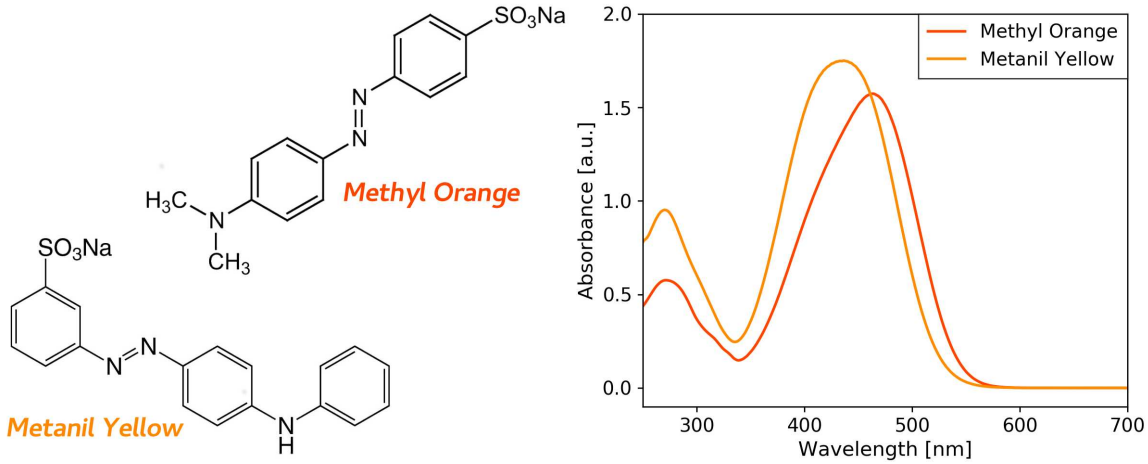

Fig. 5.2: Molecular structures (from *Carl Roth*) and absorption spectra of the two azo dyes, Methyl Orange and Metanil Yellow. The absorption spectra were measured in water solution at concentrations of approximately 1 mM.

In solution the situation is even more complicated. Most computational publications do not include the solvent, which complicates the comparison to liquid-phase experiments. An exception is a study [132] of the isomerization of azobenzene after S_1 excitation in various solvents, using a mixed quantum mechanical and molecular dynamics approach (QM/MD). Tiberio and coworkers [132] conclude, that a mixed inversion-rotation mechanism is most probable for azobenzene in solution. The contribution of inversion is found to increase with solvent viscosity [132]. In contrast, a recent transient absorption study [123] observed no viscosity dependence of the isomerization kinetics. In combination with perturbation theory calculations, Quick and coworkers [123] conclude that the so-called "hula-twist" is the most probable isomerization mechanism, which is a concerted motion of both the nitrogen atoms and the phenyl-rings.
In summary the model of pure rotation or pure inversion is clearly too simplified especially in solution. While a mainly torsional pathway seems to be well-established in vacuum, a multidimensional pathway has to be considered in solution.

5.1.2 Photochemistry of the Amino-Azobenzene Dyes

The molecular structures of the two azo dyes used in the experiments are shown in figure 5.2. Both have a sulfonic acid group on one of the phenyl-rings, attached to increase solubility in water and polar solvents. On the other phenyl-ring a hydrogen is substituted by nitrogen, to which two methyl groups are attached in the case of Methyl Orange and a third phenyl-ring in the case of Metanil Yellow. Due to the electronegative amino-group both molecules belong to the class of amino-azobenzenes, which exhibit several key differences with respect to azobenzene [21, 129].

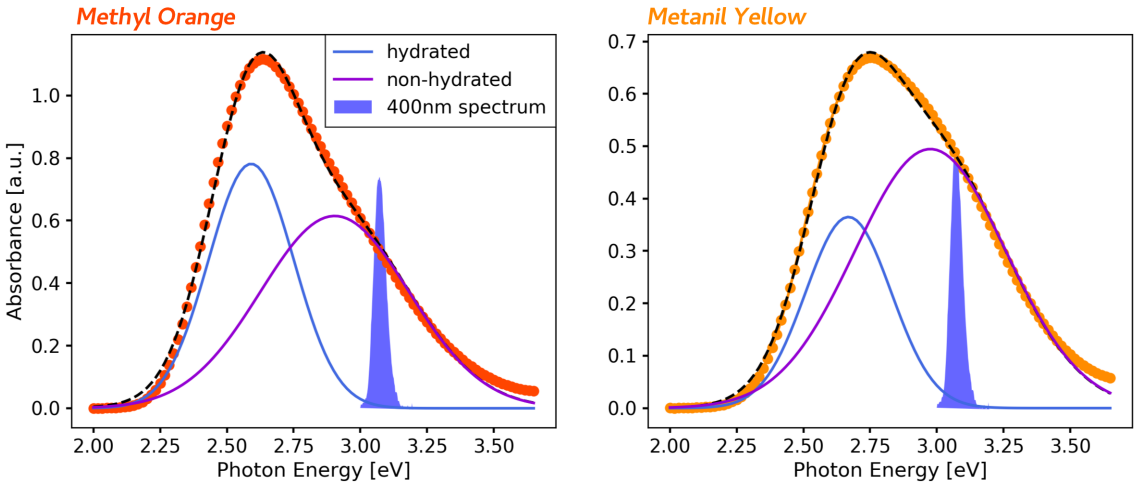

Fig. 5.3: Decomposition of the absorption spectra of Methyl Orange and Metanil Yellow. Gaussian peaks are used as opposed to the skewed functions used in ref. [136]. Nonetheless the decomposition of Methyl Orange is comparable to that shown in ref. [136].

The main difference, used also to define the group of amino-azobenzenes, is the shift of the $\pi\pi^*$ transition to lower energies, leading to the overlap of the $\pi\pi^*$ and $n\pi^*$ transitions. For the dyes used here, the overlap is so strong that only one absorption band can be distinguished in the visible range of the UV-vis absorption spectrum (fig. 5.2). Another general tendency for amino-azobenzenes is the rapid thermal cis-trans isomerization, which complicates measurements of the cis-isomer absorption spectrum and of the isomerization quantum yield [129].

While the photochemistry of Methyl Orange is relatively well documented, there is no literature available on the photochemistry of Metanil Yellow. Therefore the following literature review will mainly consider the characteristics of Methyl Orange and the related dye 4-(dimethylamino)azobenzene (DMAAB), which is the unsulfonated form of Methyl Orange.

The absorption spectrum of Methyl Orange and other amino-azobenzene dyes is strongly dependent on acidity of the solvent, leading to their application as pH-indicators [133]. In non-acidic media the solution is yellow, but with increasing acidity the color changes towards the red, indicating a shift of the absorption spectrum to lower wavelengths. This is caused by protonation of nitrogen atoms in the azo dye, with the most likely protonation site being the azo-nitrogen further away from the amino substituent [134]. The acid dissociation constant of Methyl Orange in Water is 3.4 [135], which in this context means the pH-value where there is an equilibrium of protonated and deprotonated dye. Therefore in a solution at neutral pH, as it is used here, only approximately 0.03% of the dye is protonated.

It was however discovered already in 1955 [137] that the absorption spectrum of DMAAB in ethanol changes drastically on addition of water to the solution even at neutral pH. The effect of hydration of the dye appears to be somewhat similar to the effect of protonation, with a second band appearing in the absorption spectrum at higher wavelengths. This effect was investigated systematically by Reeves and coworkers [136], who measured absorption spectra of Methyl Orange and several similar dyes in water, ethanol, and mixtures of the two solvents. They concluded that the principal absorption band consists of two overlapping bands, of which one is associated to the hydrated form of the dye. It is ruled out that the second band appearing at lower energy is caused by an $n\pi^*$-transition or by absorption of the cis-isomer. Since the effect is similar to the effect observed with increasing acidity, is is concluded that the second band belongs to a strongly hydrogen-bonded species [136].
Figure 5.3 shows a decomposition of the absorption spectra of Methyl Orange and Metanil Yellow in water solution into two bands, analogous to ref. [136]. Although Gaussian functions were used instead of the skewed functions used by Reeves and coworkers [136], the position and relative intensity of the bands agree well with the fitted curves for pure water shown in the publication. From the overlap with the 400 nm pump pulse spectrum it can be concluded, that the band at higher energy will be predominantly excited. This band is associated with the species with weaker hydration, which is found in ethanol.
Apart from protonation [134] and hydration [136], also aggregation has to be considered as an influence on the molecular structure of the investigated sample. In UV-vis absorption measurements of both dyes with various concentrations up to 1 mM, no strong changes in the absorption spectrum with concentration are observed. However the absorption spectra of the Methyl Orange monomer and dimer are also very similar [138].
The literature on the aggregation is somewhat inconsistent. While some publications prepare dilute solutions in the μM regime to avoid aggregation [139], aggregation is claimed to be negligible in transient absorption measurements with a 0.3 mM solution of Methyl Orange in water [22]. It is assumed that the non-protonated/hydrogen-bonded form has a strong tendency to dimerize [139]. Measurements of the aggregation constant in room temperature water however yield values of 9200 (extrapolation to room temperature) [140] and 97 [138]. The dimer concentrations for Methyl Orange at the concentration used in the time-resolved photoelectron experiments, i.e. 2 mM, can be estimated to be approximately 10%, using the newer aggregation constant from ŗef. [138]. Assuming the same aggregation constant for Metanil Yellow, but factoring in the higher concentration of 5 mM used in the experiment, one would expect dimer concentrations of up to 20%. Dimerization is expected to result in an increase of the isomerization timescale [21].
An overview of the various effects of solvation of Methyl Orange and their impact on the photochemistry is shown in table 5.1.

Table 5.1: Overview of the expected solvation effects for Methyl Orange. In the photoelectron experiments a 2 mM solution at neutral pH is used.

Environment	Effect	Observed changes
Acidic solution	Protonation on the azo-group	Shift of the Absorption Spectrum to higher wavelengths
Hydrogen bonding solvent	Hydrogen bonding to nitrogen atoms (azo-group or amino-group)	Second absorption band at higher wavelengths
Concentration over 0.3 mM	Aggregation, estimated 10% dimers at 2 mM	small changes in absorption, slower isomerization

Due to the changes of the absorption spectrum with hydration and the strong overlap of the transitions, assigning isomerization timescales and quantum yields to either the $\pi\pi^*$ or the $n\pi^*$ transition is difficult. Even the ordering of excited states in unclear. Due to the higher cross-section, all publications on Methyl Orange or DMAAB assume an initial $\pi\pi^*$ excitation. But some attribute this to excitation of S_2 [141, 142] and others to the excitation of S_1 [125]. Another difficulty stems from the extremely rapid thermal cis-trans isomerization. For Methyl Orange in ethanol a rate of 0.1-0.5 s^{-1} was measured, increasing with concentration [143] and solvent polarity [144].

In irradiation experiments on the similar dye 4-(diethylamino)Azobenzene in cyclohexane trans-cis isomerization quantum yields of 0.2-0.3 are measured for wavelengths of 366 nm and lower, while irradiation with 400 nm light was observed to yield values close to 1 and 436 nm light gives a quantum yield of approximately 0.7 [144]. In contrast, a quantum yield of 0.17 was reported for irradiation of the similar DMAAB in n-hexane with 405 nm light [145].

If the $\pi\pi^*$-state is the lowest-lying excited state, the decrease of quantum yield at lower wavelengths could be related to the onset of the $n\pi^*$ transition, in analogy to the lower $n\pi^*$ isomerization quantum yield observed for pure azobenzene. On the other hand the involvement of higher lying $\pi\pi^*$ transitions beyond 400 nm is also plausible. In a low temperature absorption spectroscopy experiment thermal isomerization is sufficiently inhibited. Using this technique two new absorption bands are identified upon irradiation, which can be attributed to the cis-isomer [146]. The new absorption features are centered around wavelengths of 365 nm and 458 nm. If the $n\pi^*$ absorption increases upon isomerization, as in pure azobenzene, the feature at 458 nm could belong to the $n\pi^*$ absorption. This would support the hypothesis that the lowest transition is the $n\pi^*$ transition also for Methyl Orange, and yield an energy difference between the excited states of approximately 0.3 eV.

The timescale of light-induced trans-cis isomerization of Methyl Orange in water solution is addressed in a study employing transient spectroscopy [141]. Upon excitation with 400 nm light the authors find timescales of 0.7 ps and 10 ps which they assign

to isomerization and vibrational cooling respectively [141]. In transient absorption experiments on DMAAB in various solvents Mayer and coworkers [125] find similar timescales of 0.6-1.2 ps for the isomerization, depending on the solvent.
The isomerization pathway of DMAAB was investigated using chirp controlled ultrashort laser pulses to investigate the coupling of vibrational modes [142]. The authors find that in the excited state the N=N and C-N stretching modes are coupled through at least two modes, of which one is identified as the torsion mode around the nitrogen double bond. Thus the simplified view of either pure inversion or pure rotation is found to be insufficient for amino-azobenzenes [142]. Similar to the isomerization of azobenzene, the isomerization of amino-azobenzenes in solution most probably follows a mixed torsional-inversion mechanism.
To summarize, the absorption spectrum of Methyl Orange in aqueous solution is dominated by the overlapping $\pi\pi^*$ transitions of two different hydration species. The $\pi\pi^*$ excitation with 400 nm light leads to efficient isomerization on a timescale of approximately 1 ps. The ordering of the much weaker $n\pi^*$ transition with respect to the $\pi\pi^*$ transition is unclear due to the overlap of the two transitions. The evidence for an $n\pi^*$ state below the excited $\pi\pi^*$ state is more pronounced, meaning that 400 nm light would excite Methyl Orange into S_2. But a timescale belonging to internal conversion from S_2 to S_1 has not been observed for Methyl Orange or DMAAB [125, 141].

5.1.3 Molecular Structure of Methyl Orange and Metanil Yellow

To obtain information on how much the molecular structure of the azobenzene base is influenced by the amino-substituents, DFT geometry optimization calculations are performed in vacuum and in aqueous solution. As for Quinoline Yellow (sec. 4.2) the TPSS functional [37] is used together with the def2-TZVP basis set [38]. The CPCM model [35] is used to simulate the influence of the solvent. Table 5.2 shows the results of the geometry optimization and compares them to the known geometry of azobenzene from ref. [127].
The trans-isomer of Methyl Orange is almost perfectly planar and there are no drastic changes in geometry compared to trans-azobenzene. In cis Methyl Orange however the amino-substituted phenyl-ring has a significantly smaller out-of-plane twist angle (NNCC) of approximately 30° instead of 60°.
For Metanil Yellow the changes relative to the molecular structure of azobenzene are already obvious in the trans-form. The molecule is no longer planar and both phenyl-rings are twisted out of plane. This is likely caused by the substituted third phenyl-ring, which is also twisted out of plane by around 30° relative to the plane of its neighboring phenyl group (CNCC angle). The structure of cis Metanil Yellow is similar to the cis-form of Methyl Orange, with the amino-substituted ring twisted out of plane. The geometry of the amino-substituent remains similar in the cis- and trans-isomer, indicating that it does not change during isomerization.

Table 5.2: DFT-optimized geometries (TPSS/def2-TZVP) for Methyl Orange and Metanil Yellow compared to the Azobenzene geometry from ref. [127]. The bond lengths are averaged values in Ångstrom, all angles are in degrees. Since the substituted azobenzenes are no longer completely symmetric, two values are given for the NNC angle and the NNCC angle (out of plane twist of the phenyl-rings). The first value always belongs to the sulfonated phenyl-ring. The single point energy difference ΔE is given relative to the trans-isomer in vacuum and relative to the vacuum calculation of the same isomer for water solution.

Azobenzene (from ref. [127])

isomer	solvent	bond-lengths			angles							
		NN	CN	CC	NNC	$CNNC$	$NNCC$					
trans	vac.	1.26	1.44	1.39	114.2	180.0	0.0					
cis	vac.	1.24	1.47	1.39	121.9	0.0	60.8					

Methyl Orange

		azobenzene-part						amino-substituent					ΔE [eV]
		bond-lengths			angles			bond-lengths		angles			
		NN	CN	CC	NNC	$CNNC$	$NNCC$	CN	NC	CCN	CNC	$CCNC$	
trans	vac.	1.27	1.40	1.40	114.1	177.8	3.3	1.37	1.46	120.9	120.2	178.9	
					115.2		0.0						
trans	H_2O	1.29	1.40	1.40	114.1	178.5	3.8	1.36	1.47	120.9	120.4	179.5	-0.74
					116.1		0.1						
cis	vac.	1.26	1.42	1.40	123.8	11.8	61.4	1.37	1.46	120.9	120.3	174.4	+0.63
					123.7		30.4						
cis	H_2O	1.27	1.41	1.40	124.1	14.4	59.0	1.36	1.47	121.0	120.5	176.0	-0.82
					124.6		24.9						

Metanil Yellow

		NN	CN	CC	NNC	$CNNC$	$NNCC$	CN	CC	CNC	$CCNC$	$CNCC$	
trans	vac.	1.27	1.41	1.40	114.2	175.2	21.4	1.40	1.40	129.4	24.5	27.1	
					115.0		9.0						
trans	H_2O	1.28	1.40	1.40	114.1	173.3	24.7	1.39	1.40	129.9	18.8	28.4	-0.78
					116.1		9.9						
cis	vac.	1.26	1.42	1.40	123.8	11.1	59.4	1.40	1.40	129.9	11.7	36.5	+0.60
					123.6		32.0						
cis	H_2O	1.27	1.42	1.40	124.0	12.6	59.6	1.39	1.40	130.4	8.8	35.0	-0.87
					124.4		27.1						

5.2 XUV Photoelectron Spectroscopy Results

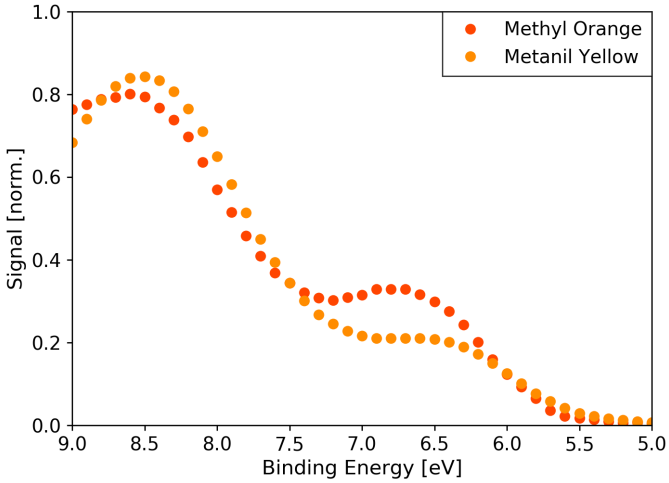

Fig. 5.4: Photoelectron spectra of Methyl Orange and Metanil Yellow in aqueous solution acquired with the 17th harmonic (26.5 eV). The Methyl Orange spectrum was recorded at a concentration of 2 mM, that of Metanil Yellow at a concentration of 5 mM. Both spectra are normalized to the concentration as well as the signal of the liquid water $1b_1$ peak, which is proportional to the XUV intensity.

Figure 5.4 shows photoelectron spectra of Methyl Orange and Metanil Yellow in aqueous solution acquired with harmonic 17. The solutions are prepared from a 60 mM NaCl buffer solution. The photoelectron signal of the buffer solution is subtracted to obtain the spectrum of the dye, as discussed in section 4.2. The sample solution is kept in the dark prior to the experiment. Due to the fast thermal cis-trans isomerization, it can be assumed that the samples contain only the trans-isomer of the dyes.
Due to the lower solubilities of the dyes, lower concentrations than for Quinoline Yellow are used in the photoelectron experiment. For Methyl Orange a 2 mM solution is prepared, for Metanil Yellow a 5 mM solution. The concentration dependence measurement, which was presented for Quinoline Yellow (see section 4.2), is repeated for Methyl Orange and Metanil Yellow. The photoelectron spectrum is measured with dye concentrations ranging from 0.25 mM to 2 mM or 5 mM respectively. Up to the concentrations used in the experiment there is no evidence of a saturation effect, as it is observed in the case of Quinoline Yellow (see fig. 4.5). The spectrum is reproduced at all concentrations in the case of both dyes.
The photoelectron spectra of the two dyes are similar, which is expected since the spectrum is likely dominated by ionization from molecular orbitals on the azobenzene part of the molecules. Overall the ionization energies of Metanil Yellow appear to be 0.1-0.2 eV lower. With the signal normalized to the dye concentration and the liquid

water signal, the photoelectron yield is also similar. The normalization to the liquid water photoelectron yield removes the influence of fluctuations in XUV intensity. Thus the similar yield of the molecular photoelectron signal indicates similar photoionization cross-sections of the two molecules.

5.2.1 DFT Ionization Energies

As discussed in section 4.2, computational ionization energies can aid in the interpretation of the measured photoelectron spectra. The DFT calculations are performed using the M06-2x functional [39], the def2-TZVP basis set [38], and the conductor-like polarizable continuum model [35], as discussed in detail in section 2.2. The calculated HOMO vertical ionization energies in water solution are 5.55 eV and 5.68 eV for trans Methyl Orange and trans Metanil Yellow respectively. For the cis-isomer the calculation yields 5.57 eV for Methyl Orange and 5.73 eV for Metanil Yellow.
In figure 5.5 the calculated ionization energies are shown together with the measured photoelectron spectra. It is apparent that the agreement of the calculated values and the measured spectra is not nearly as good as for Quinoline Yellow (section 4.2). The calculation appears to underestimate the vertical binding energies by almost 1 eV. Typically errors of 0.3-0.5 eV would be expected for a calculation of this type [36]. A possible explanation for the large deviation of the calculated values is the hydrogen bonding of the molecules in water. The CPCM only accounts for polarization and does not include the hydrogen bonding to the nitrogen atoms. The hydrogen bonding can affect the energy levels substantially as evident from the absorption spectra of differently hydrated species [136]. Additionally, the photoelectron spectrum contains signal from the two hydrogen-bonded species, whose absorption maxima are spaced by approximately 0.5 eV as discussed in the previous section.
Figure 5.5 also shows the shapes of the two highest-lying molecular orbitals of both amino-azobenzene molecules, as obtained from the ground state DFT calculations. They are compared to the molecular orbitals of azobenzene. The molecular orbitals of Methyl Orange are very similar to those of Azobenzene, and evidently the designation as n- and π-orbital still applies. The calculation yields the π-orbital as the highest occupied molecular orbital, supporting the assumption of ref. [125] that the $\pi\pi^*$ transition lies below the $n\pi^*$ transition in energy. The DFT calculation for Methyl Orange returns a gap of almost 2 eV between the HOMO and the HOMO-1. This is clearly incompatible with the overlap of the $n\pi^*$ and $\pi\pi^*$ transitions. Also here a likely reason for the discrepancy is hydrogen bonding to the azo-nitrogens.
For Metanil Yellow the assignment of n and π to the two highest occupied molecular orbitals is not as straightforward. While the HOMO is still relatively similar to the HOMO of Methyl Orange, the HOMO-1 appears to be a mix of the nitrogen lone pair orbital and a more π-like orbital extending over all three phenyl-rings. The reason for this mixing is probably the stronger out-of-plane twist of the phenyl-rings in trans-

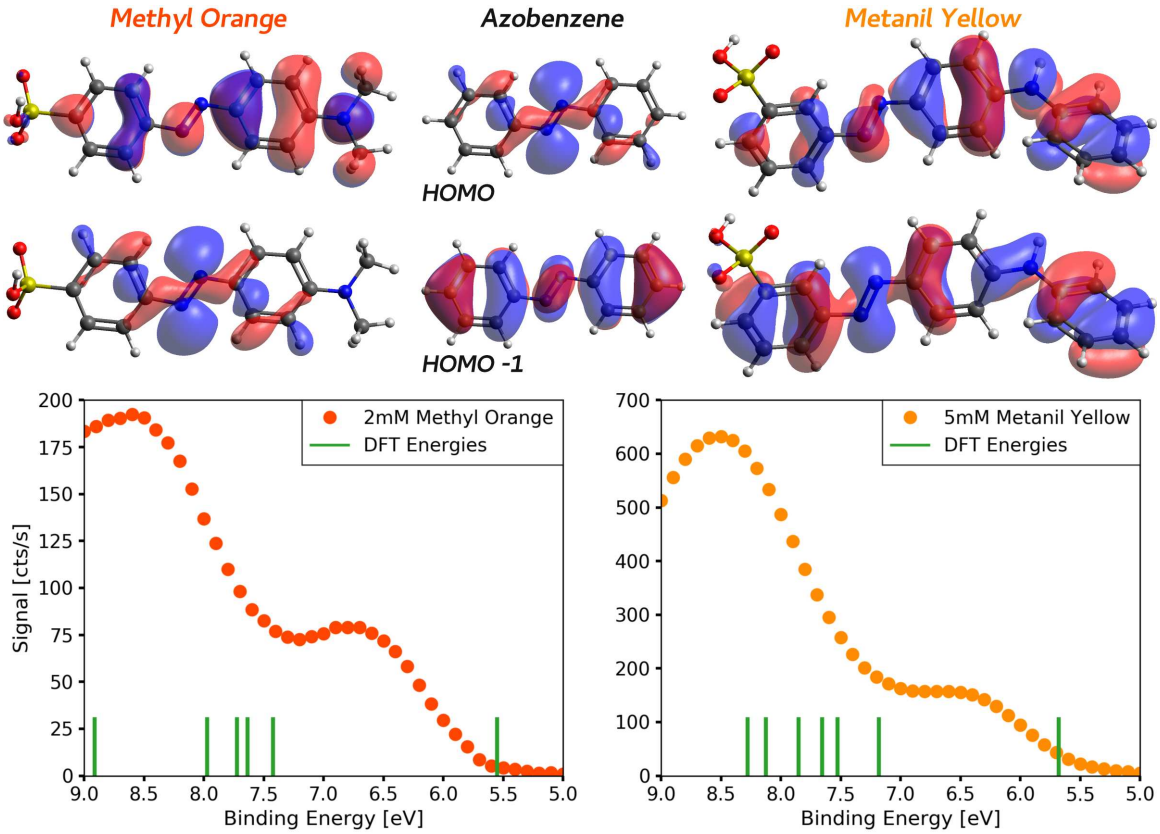

Fig. 5.5: Photoelectron Spectra of Methyl Orange and Metanil Yellow together with the ionization energies from the DFT calculation (M06-2x/def2-TZVP). The shapes of the HOMO and HOMO-1 from the DFT calculation of Azobenzene and the two dye-molecules are also shown.

Metanil Yellow. The gap between the HOMO and HOMO-1 obtained from the DFT calculation for Metanil Yellow is similarly large as for Methyl Orange, but also for Metanil Yellow the influence of hydrogen bonding is probably not accurately modeled in the calculation.

The DFT calculations for both molecules supports the assignment of the $\pi\pi^*$-state as the lowest-lying excited state. However the spacing of the occupied molecular orbitals clearly disagrees with the close spacing of the excited states, which is well-established [21]. Therefore it is unclear, if the ordering of molecular orbitals is modeled correctly. Additionally the visualization of the orbitals shows that the concept of a $\pi\pi^*$-transition and a $n\pi^*$ transition may only be applicable to Methyl Orange, but not to Metanil Yellow.

5.3 Time-Resolved Photoelectron Spectroscopy Results

To access the isomerization dynamics of the amino-azobenzene molecules upon 400 nm excitation, time-resolved photoelectron measurements of both Methyl Orange and Metanil Yellow are performed with 400 nm pump pulses and 17th harmonic (26.5 eV) probe pulses. As discussed in section 5.1.2 the 400 nm pump pulse will excite predominantly the strong $\pi\pi^*$ transition of one of the hydrogen bonded species present in the solution.
Comparable to the measurement with Quinoline Yellow, a strong increase in the 400 nm only photoelectron signal is observed upon switching from a reference NaCl solution to the dye solution. Associated with this, also the expected shift of the photoelectron spectrum to lower kinetic energy with positive delays is seen. The correction for this light-induced space charge effect is applied, as discussed in section 4.3, and succeeds in removing the shift.

5.3.1 Methyl Orange

Figure 5.6a shows the counting mode pump-probe photoelectron signal after the space charge correction, acquired with a 2 mM aqueous solution of Methyl Orange. The map in figure 5.6 is obtained by averaging over 27 delay scans, in which the spectrum at each delay point is averaged over 10 s per scan. This means that each delay point is obtained by averaging over a total measurement time of 4.5 minutes or 270000 laser shots. The difference map is obtained by subtracting the signal at negative delays, which is equivalent to subtracting the sum of the single-color signals since no pump-probe signal is observed in this energy range at negative delays.
There are two distinct regions with a positive difference signal. As discussed before the cross-correlation signal centered around 8 eV binding energy can be attributed to the first positive sideband of liquid water. The decaying positive signal at lower binding energy is associated with the Methyl Orange excited state signal. Additionally there are areas with a negative difference signal for example around binding energies of 6.5 eV and 8 eV and areas with a positive difference signal around binding energies of 7.5 eV and 9 eV.
The photoelectron spectrum of the excited state at different delays is shown in figure 5.6b. The spectrum at long delays (purple, 0.3-10 ps) matches the spectrum at shorter positive delays (turquoise, 0.15-0.25 ps), if it is scaled appropriately (dashed line). This shows that after approximately 200 fs the excited state photoelectron spectrum remains the same. The spectrum around time overlap and for short delays (green, -0.05-0.1 ps) however extends to higher kinetic energies, i.e. lower binding energies. This indicates dynamics on a fast femtosecond timescale.
The delay dependence of the excited state signal, integrated for binding energies between 2.5 eV and 5.5 eV, is shown in figure 5.7a. The errorbars are given by the statistical

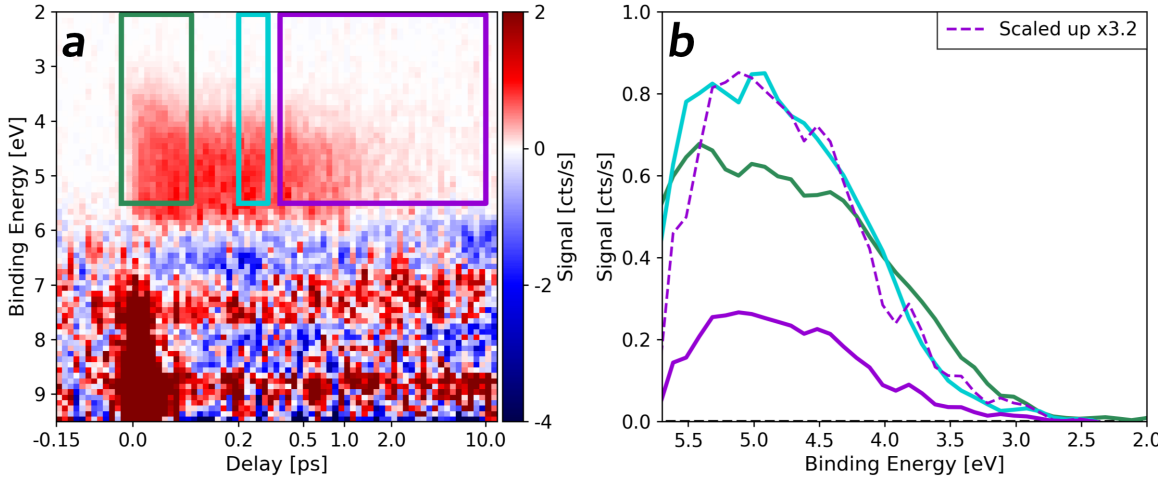

Fig. 5.6: Pump-probe photoelectron data of 2 mM Methyl Orange Solution obtained with a 400 nm pump pulse and a 17th harmonic probe pulse. **a)** Difference Map after space charge correction, obtained by subtracting the signal at negative delays. **b)** Averaged difference photoelectron spectra in the delay ranges highlighted in the difference map.

standard error of the signal at the individual delay points over the 27 scans. To further reduce the noise, caused mainly by fluctuations in the XUV intensity, the number of delay points is additionally reduced by a factor of 2 by binning the delay points.

The total excited state decay can be modeled well with a single exponential decay of approximately 1 ps, which matches the expected isomerization timescale for Methyl Orange [22, 141]. The residuals of the fit are consistently above zero at delays longer than 3 ps, which could indicate a second, longer decay constant. Given the low signal in this delay range, which did not allow retrieval of an excited state photoelectron spectrum, it is however also possible that the effect is caused by a slight decrease of the signal at negative delays, which is subtracted from the map. Therefore no attempt was made to extract a second timescale from the data.

The single decay time of 1 ps cannot, however, explain the spectral change which is evident in the first 200 fs. To extract the dynamics of the spectral change the "center of mass" of the excited state spectrum at every delay point is calculated by taking the average binding energy of the spectrum between binding energies of 2.5 eV and 5.5 eV. This mean energy of the excited state spectrum is plotted over the delay for the first picosecond in figure 5.7b. As expected from the excited state spectra shown in figure 5.6b, there is no evidence of significant spectral changes after a delay of approximately 200 fs.

The exponential fit of the "center of mass" dynamics yields an amplitude of the spectral shift of 0.24 eV, matching the difference of the high kinetic energy edge of the spectrum

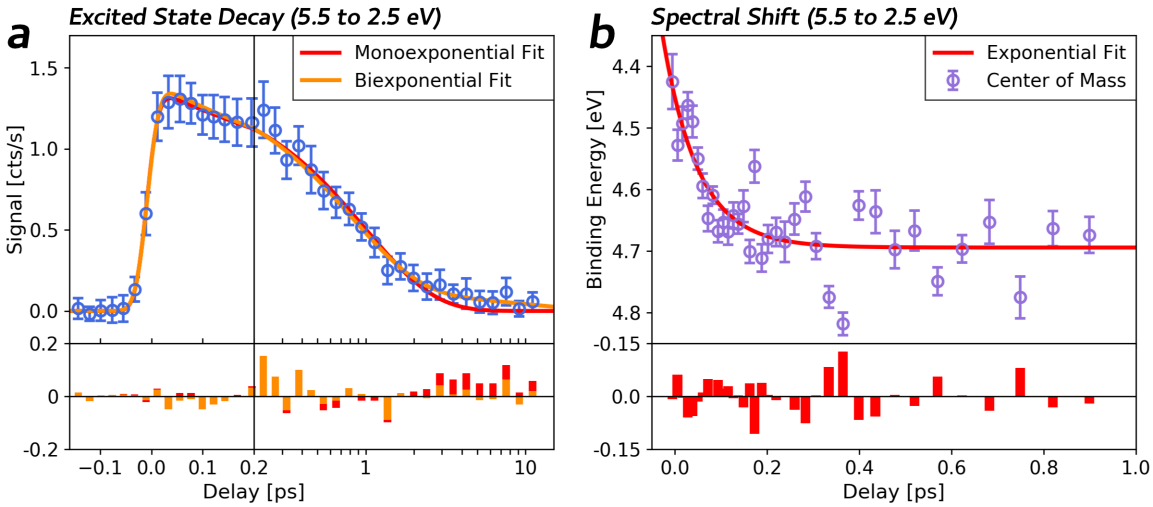

Fig. 5.7: **a)** Integrated excited state decay signal modeled with an exponential decay. The fit yields a decay constant of 0.96±0.05 ps. **b)** The Delay dependent "center of mass" of the excited state spectrum can be modeled with a single exponential decay with an amplitude of 0.24±0.03 eV and a decay constant of 80±20 fs.

between time-overlap and longer positive delays. The time constant associated with the spectral shift is approximately 80 fs. As discussed for Quinoline Yellow in section 4.3, this fast loss of excited state photoelectron energy could be associated to the initial solvent rearrangement, reacting to the changes in dipole moment upon excitation of the molecule.

To check whether the signal of the ground state recovery can also be observed, the full difference spectra at short (turquoise, 0.03-1.0 ps) and long (purple, 1.5-10 ps) delays are compared in figure 5.8a. The features with a positive difference signal at 9 eV and around 7 eV binding energy, as well as the depletion feature around 8 eV binding energy, do not show any time-dependence and are therefore probably artifacts of the subtraction of the spectrum at negative delays. The depletion feature at lower binding energy, however, appears weaker and shifted towards lower binding energies at long delays.

Since it coincides with the flank of the XUV-only spectrum, the dip in the purple curve at approximately 6 eV is likely an artifact from the space charge correction procedure. This can however not explain the stronger dip at shorter delays (turquoise curve), which is likely attributed to the pump-probe signal on the electronic ground state. This depletion feature is centered at a binding energy of approximately 6.5 eV, which matches the binding energy of the lower photoelectron band in the XUV only photoelectron spectrum. Additionally the depletion appears immediately after the zero time delay, where the space charge correction has no effect.

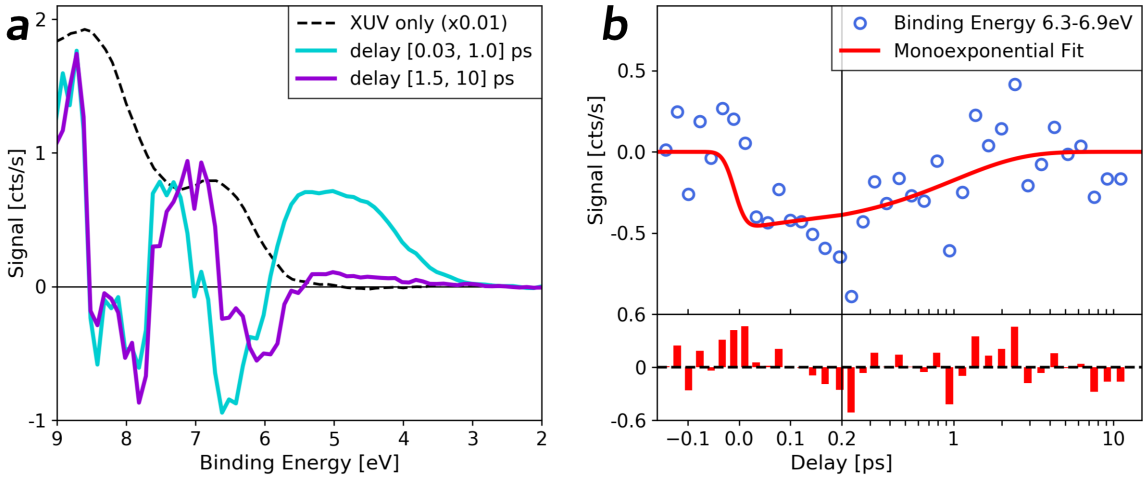

Fig. 5.8: **a)** Methyl Orange difference photoelectron spectra at short and long positive delays together with the single-color XUV photoelectron spectrum. **b)** Integrated signal in the binding energy range of the ground state recovery signal (6.3-6.9 eV). The exponential fit yields a timescale of 0.9±0.4 ps

The time-dependent signal of the depletion feature, integrated in the binding energy range from 6.3 eV to 6.9 eV, is shown in figure 5.8b. Since the signal is measured against a 100 times stronger XUV-only background signal the fluctuations are large. Nevertheless the integrated signal shows a depletion at zero time-delay and recovers towards longer delays. The ground state recovery can be modeled with an exponential decay, yielding a decay time of 0.9±0.4 ps. This agrees well with the timescale of the excited state decay.

If the depletion signal is associated to the ground state recovery, there are however some inconsistencies. The integrated signal of the depletion is almost three times weaker than the integrated signal of the excited state decay. Additionally the depletion signal in the spectrum is far narrower than the excited state photoelectron spectrum. The energy gap between the high kinetic energy edge of the depletion feature and the high kinetic energy edge of the excited state spectrum is approximately 3 eV and therefore matches the energy of one 400 nm photon. However there is also excited state photoelectron signal at a binding energy of 5.5 eV but no corresponding depletion signal at a binding energy of 8.5 eV.

A possible explanation for both effects would be that the dynamic range for the detection of pump-probe signal decreases as the XUV-only signal increases at a binding energy of approximately 7 eV. As discussed in section 3.2, the counting signal can already exhibit a small saturation effect even at low count rates. This would also explain the steep edge of the depletion feature at high binding energy. Another explanation for

the broader excited state spectrum extending to lower kinetic energy would be the stabilization of the excited state by solvent rearrangement, which could occur on a timescale of a few femtoseconds and therefore not be resolved in the experiment [112]. Additionally the homogeneous broadening, i.e. broadening by changes in solvation structure of molecules, can affect the excited state stronger than the ground state.

Methyl Orange reportedly has a high isomerization quantum yield [144], therefore one would expect that a large fraction of excited molecules relaxes to the ground state of the cis-isomer. However a change in the XUV photoelectron spectrum after the isomerization is not observed. From the ratio of pump-probe signal to XUV-only signal it can be estimated that approximately one percent of Methyl Orange molecules are excited. This means that even after a delay time of over 1 ps, less than 1% of molecules are isomerized. It is questionable if a change of that magnitude would be detectable in the pump-probe photoelectron spectrum. Additionally the ionization energy of cis- Methyl Orange from the DFT calculation (section 5.2) is the same as for the trans-isomer. It is therefore plausible that the photoelectron spectrum changes only marginally upon isomerization, making it an insensitive probe for information on isomerization quantum yields.

5.3.2 Metanil Yellow

The pump-probe photoelectron data of the 5 mM Metanil Yellow solution is shown as a difference map in figure 5.9a. The map is obtained by averaging over 10 delay scans, i.e. an average over approximately 1.5 minutes or 100000 laser shots per delay point. The excited state decay is clearly visible as a broad decaying band at low binding energy. The sideband signal however is not observed as clearly as in the measurement with Methyl Orange. This is related to the lower 400 nm photon flux used in this measurement. The total excited state signal is similar in magnitude to that in the Methyl Orange measurement. But the Metanil Yellow measurement was performed at a higher concentration, so a similar pump-probe signal yield is consistent with a lower 400 nm intensity.

The map shown in figure 5.9a is corrected for the light-induced space charge effect. There is, however, a residual depletion visible at a binding energy of 6 eV, which is likely an artifact of the space charge correction. Overall the fluctuations of the ground state signal are more pronounced in the case of Metanil Yellow, as expected from a stronger XUV-only signal. This is probably the reason that the signal associated to the ground state recovery is not visible in the difference map. What is immediately evident from the difference map is the slower overall timescale of the excited state decay compared with the Methyl Orange data. While the Methyl Orange excited state signal decays almost completely within the first two picoseconds (fig. 5.6a), there is still considerable excited state signal left after 10 ps in the case of Metanil Yellow.

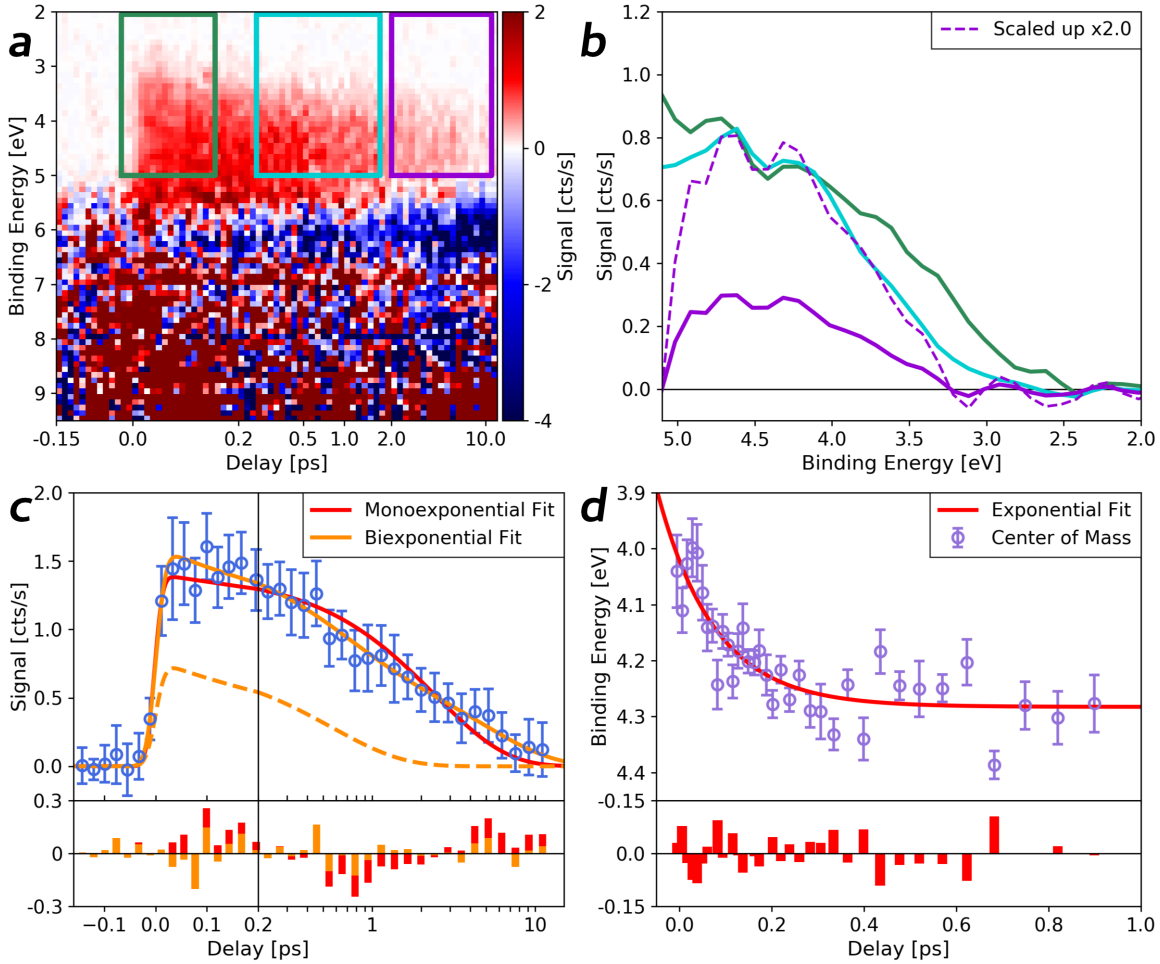

Fig. 5.9: Pump-probe photoelectron data of 5 mM Metanil Yellow solution. **a)** Difference map after space charge correction, obtained by subtracting the signal at negative delays. **b)** Averaged difference photoelectron spectra in the delay ranges highlighted in the difference map. **c)** Excited state decay signal of Metanil Yellow, integrated in the binding energy range from 2.0 eV to 5.0 eV. The monoexponential decay curve yields a decay constant of 2.5±0.5 ps, but clearly misrepresents the data. The excited state decay has to be modeled with a biexponential function with decay constants of 0.6±0.2 ps and 4.8±0.9 ps. **d)** The delay-dependent "center of mass" of the excited state spectrum can be modeled with a single exponential with an amplitude of 0.26±0.03 eV and a decay constant of 120±30 fs.

The integrated excited state decay signal is shown in figure 5.9c and is modeled with an exponential decay function. It is evident that a single decay constant is not sufficient to model the data accurately and a biexponential decay is necessary to model the

excited state decay of Metanil Yellow. The biexponential decay yields decay constants of approximately 0.6 ps and 5 ps with similar amplitudes of 0.8 cts/s for both decay constants. The dashed line in figure 5.9c shows the contribution of the 0.6 ps decay, indicating that this component is completely decayed after approximately 2 ps.
Accordingly figure 5.9b shows the excited state photoelectron spectra at time-overlap (green, -0.05-0.15 ps), short positive delays (turquoise, 0.25-1.8 ps), and long positive delays (purple, 2-10 ps). The spectrum at long delays (purple) matches the spectrum at shorter positive delays (turquoise) if it is scaled up appropriately, indicating that the 0.6 ps timescale is not associated with a change in the excited state photoelectron spectrum. As for Methyl Orange, the spectrum around time-overlap and for short positive delays (green) however extends to higher kinetic energies, indicating spectral change on a timescale faster than 0.6 ps.
To access that timescale once again the "center of mass" of the excited state spectrum is extracted. The delay-dependent average binding energy is shown in figure 5.9d and modeled with an exponential decay with a decay constant of 120 fs. The spectral change therefore appears to be associated to a third, faster timescale not found in the fit of the integrated total excited state decay signal. This timescale can probably be attributed to the solvent rearrangement, since both the energy shift and the timescale are similar to what is observed for Methyl Orange.

5.3.3 Discussion

In the time-resolved photoelectron spectroscopy both azo dyes exhibit a femtosecond change in the photoelectron spectrum, shifting the center of the spectrum by approximately 0.25 eV on a timescale of around 100 fs. Analogous to the fast behavior observed in the Quinoline Yellow measurement this can be linked to the initial solvent rearrangement. The other possible explanation is, that this timescale is associated to the internal conversion from $\pi\pi^*$ to $n\pi^*$, which was recently observed on a 70 fs timescale in the related molecule 4-(amino)azobenzene [147]. In that case the state ordering would be the same as in azobenzene, i.e. the lowest transition having the $n\pi^*$ character. However internal conversion would be expected to lead to a decrease in photoelectron signal, which is not observed on the 100 fs timescale. Therefore the solvent rearrangement is the most probable explanation for the fast spectral shift.
In the case of Methyl Orange the interpretation of the time-resolved data is quite straightforward. After solvent rearrangement, a single timescale of approximately 1 ps is found both for the excited state decay and for the ground state recovery, which was successfully identified in this measurement. This timescale is in good agreement with results from all-optical transient experiments [22, 141] and can be attributed to the trans-cis isomerization. Although this isomerization occurs with a high quantum yield [144], the signal of the cis-isomer cannot be identified because photoelectron spectroscopy is probably not a sensitive probe for isomerism. There is a weak excited

state photoelectron signal after isomerization, which could originate from a triplet state. Intersystem crossing was recently reported to occur in 4-(amino)azobenzene on a timescale of 180 ps from S_1 and 480 ps from S_2 [147].

In the case of Metanil Yellow two timescales of 600 fs and 5 ps after the initial solvent rearrangement are found in the excited state decay signal. Since isomerization is likely the last process on the potential energy surfaces of the excited states, the decay constant of 5 ps can be attributed to the trans-cis isomerization. This means that isomerization of Metanil Yellow is five times slower than isomerization of Methyl Orange.

One possible explanation for this effect would be the larger moment of inertia of the third phenyl-ring of Metanil Yellow. From the optimized geometries of Methyl Orange and Metanil Yellow (sec. 5.1) the moments of inertia for rotation around the N=N bond can be calculated. The calculation assumes rotation of the side with the amino-group attached. This assumption is justified since the sulfonic acid group is likely much stronger bound to water and would therefore resist rotation through the solvent. The calculation yields a moment of inertia of 1800 u/Å^2 for Methyl Orange and 5400 u/Å^2 for Metanil Yellow. Since the rotational constant is inversely proportional to the moment of inertia, this would only explain a three times slower isomerization of Metanil Yellow. An additional effect could be the larger fraction of dimers of approximately 20%, which was estimated to be present in the Metanil Yellow solution.

The interpretation of the intermediate timescale of 0.6 ps in Metanil Yellow remains speculative without the possibility to compare with excited state quantum chemistry calculations or transient absorption spectroscopy results. If the 100 fs timescale is associated to solvent rearrangement, one option would be internal conversion to a lower-lying excited state. Another explanation would be an internal conversion to the ground state of the trans-isomer, competing with isomerization. This process was found to occur on a timescale of 0.7 ps in 4-(amino)azobenzene [147]. This can however be excluded, since a competing process would lead to a monoexponential decay with a decay time close to that of the faster process. Another possibility would be the vibrational relaxation out of the Franck-Condon region, which is however usually considered to occur on faster femtosecond timescales. Thus the internal conversion to a lower-lying excited state is the most probable explanation for the 0.6 ps timescale.

In conclusion the internal conversion process is most probably observed in Metanil Yellow, but not observed in Methyl Orange. This points to a difference in state ordering between the two molecules. While the $\pi\pi^*$-state appears to be the lowest-lying excited state in Methyl Orange, there probably is a lower-lying excited state in Metanil Yellow. It is however unclear if the model of a $\pi\pi^*$- and an $n\pi^*$-state, as introduced for azobenzene, is still valid for Metanil Yellow. As discussed in section 5.2, the molecular orbitals of Metanil Yellow are dissimilar to those of azobenzene. Thus the lower-lying excited state is not necessarily comparable to the $n\pi^*$-state in azobenzene.

5.4 Summary

In this chapter the static and time-resolved photoelectron spectroscopy of two amino-azobenzene derivatives in aqueous solution are presented. One of the open questions in this type of molecules is whether amino-azobenzenes indeed offer the possibility to study isomerization of azobenzene from the $\pi\pi^*$-state without the influence of the $n\pi^*$-state. This would only be the case if the ordering of the excited states is reversed with respect to azobenzene [125, 141].
The measured static photoelectron spectra of the two amino-azobenzene molecules Methyl Orange and Metanil Yellow are similar. As opposed to the XUV-only measurements for Quinoline Yellow (sec. 4.2), the photoelectron spectra of the azo dyes do not compare well with ionization energies obtained from DFT calculations. A possible reason is the complex hydrogen bonding on the azo- and amino-groups of the azo dyes, which is known to cause large changes for example in the UV-vis absorption spectrum [136]. This effect is not modeled in the DFT calculations employed here, using the conductor-like polarizable continuum model.
In the time-resolved experiments the time-dependent excited state photoelectron signals of both molecules are measured. Similar to the Quinoline Yellow experiment (section 4.3), a fast shift of the excited state photoelectron spectrum is observed. This effect can most likely be attributed to the initial solvent rearrangement after excitation. The decay of the excited state signals can be modeled to extract isomerization timescales for both molecules. The isomerization timescale for Methyl Orange is approximately 1 ps, in agreement with previous studies [22, 141]. For Metanil Yellow an isomerization timescale of approximately 5 ps is extracted. The slower isomerization can be explained by the larger moment of inertia for rotation around the nitrogen double bond and therefore supports the hypothesis of a mainly rotational isomerization [23]. This could be confirmed by experiments in other solvents, investigating the influence of solvent viscosity.
Regarding the ordering of excited states, the two molecules appear to be different. Internal conversion is not observed in the Methyl Orange experiment, which supports the assignment of the $\pi\pi^*$-state as the lowest exciting state [125]. In Metanil Yellow a 600 fs decay is observed before isomerization, which can most likely be assigned to internal conversion. Thus the $\pi\pi^*$-state is probably not the lowest excited state.
Therefore the inverted ordering of the excited states appears probable for Methyl Orange, but not for Metanil Yellow. This can be another reason for the slower isomerization of Metanil Yellow, since isomerization occurs after internal conversion to the lower-lying state. The results show that the substituents on amino-azobenzene have a strong influence on the ordering of excited states. The study of amino-azobenzenes can however not necessarily provide insight on the parent molecule azobenzene, since the model of a $\pi\pi^*$- and a $n\pi^*$-state may not be valid for Metanil Yellow.

6 Ionization of Tryptophan in Aqueous Solution

The generation of charged species in aqueous solutions is an important topic in biochemistry, since charged species are highly reactive and the oxidation of proteins is a precursor for cell damage. Proteins are major targets for photoionization in cells, mainly due to their high abundance in the cells. An important pathway to protein oxidation is light absorption by bound chromophore groups, for example amino acids. L-Tryptophan is the most photoactive among the common amino acids, which makes its photochemistry highly relevant for studies on the oxidation of proteins [24]. Since L-Tryptophan is the biologically relevant enantiomer of the chiral molecule, Tryptophan will always refer to the L-enantiomer in the following.

In the context of photodamage, knowledge of the threshold for direct photoionization in the gas-phase and in aqueous solution is essential to quantify the energy necessary for direct ionization [148]. This way the photon energy necessary for direct ionization of aqueous Tryptophan can be quantified and compared to the photon energy necessary for indirect ionization, e.g. by charge transfer from an excited state. As discussed in section 2.1, the ionization energy for direct ionization in aqueous solution is often significantly lower than in the gas-phase. This phase transition shift can be accurately estimated by comparing results from gas-phase photoelectron spectroscopy [149] and results from photoelectron spectroscopy in aqueous solution.

In addition to the importance of the steady-state energetics of aqueous Tryptophan, there is also great interest for its excited state dynamics. Its strong fluorescence already indicates that Tryptophan remains in the excited state long enough for excited state charge transfer processes to play a role. Excited state proton transfer, electron transfer, and intersystem crossing are considered as mechanisms for fluorescence quenching [25]. Additionally the photophysics of Tryptophan depend sensitively on its environment [25].

In this chapter first the ionization energy of isolated Tryptophan molecules and the effects of aqueous solution on Tryptophan are discussed. Then the results from XUV-only photoelectron spectroscopy in solution are presented. The photoelectron spectrum of Tryptophan in aqueous solution is measured, investigating also the influence of the photon energy and the Tryptophan concentration. Based on the results, accurate estimates for the phase transition shift and for the threshold energy for direct ionization in aqueous solution can be calculated. The XUV-only experiments also provide the basis for a possible time-resolved experiment on Tryptophan in aqueous solution.

6.1 Ionization Energy of Tryptophan

Photoelectron spectroscopy of Tryptophan in the gas-phase is challenging since the molecules often decompose in the inlet system [150]. Thus only few direct measure-

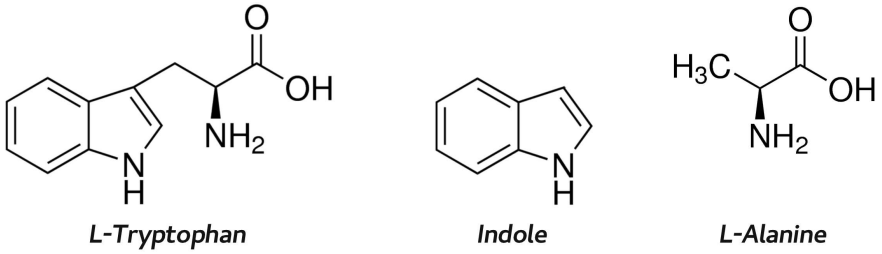

Fig. 6.1: Molecular Structures of Tryptophan, Indole and Alanine.

ments of the gas-phase spectrum of Tryptophan have been reported [149, 151]. The photoelectron spectrum has two distinct bands at binding energies of 8.1 eV and 9.8 eV [149]. The photoionization threshold in the gas-phase has been reported at 7.2-7.3 eV. The Tryptophan molecule consist of an Indole part and an Alanine part (see figure 6.1), and photoelectron spectra of these compounds can be recorded more easily. This, together with quantum chemistry calculations, can be used to assign the photoelectron bands of Tryptophan to specific orbitals [152]. The first band at 8.1 eV is attributed to ionization from the π_1 and π_2 orbitals of Indole and will hereafter be referred to as the $\pi_1\pi_2$ band. The band at 9.8 eV is attributed to ionization from the π_3 orbital of Indole and from non-bonding Alanine orbitals. While the early assignment considered only the n_N orbital of the Alanine amino-group [149], a more recent computational study considers the n_O of the C=O group and the n_{Oh} of the C-OH group as well [153]. For simplicity the composed photoelectron band will be labeled as the $\pi_3 n$-band.

Recent computational studies [153, 154] give values for the vertical binding energies of gas-phase Tryptophan, depending on the conformation. In both studies it was concluded that the lowest energy conformation is one, in which there is an additional hydrogen bonding interaction between the amino group of Alanine and the Indole group. For this conformer the calculated ionization energies also agree best with the experimental values. The DFT calculation of Dehareng and coworkers [153] yields ionization energies approximately 0.5 eV lower than the experimental values for the π-orbitals, but reproduces the experimental values for the non-bonding orbitals quite well. Using a wavefunction-based *ab initio* method, Close [154] calculated a vertical ionization energy of 7.8 eV for the π_1-orbital, in excellent agreement with the experimental value.

In solution amino acids can form iso-electric dipolar ions, also known as zwitterions. This means that, although the entire molecule has no net charge, groups in the molecule carry opposite charges. In the case of Tryptophan both charged groups are on the Alanine part of the molecule. The amino-group on the Alanine is positively charged (NH_3^+) and the carboxyl-group carries the negative charge (COO^-) in the zwitterion form of Tryptophan (fig. 6.2a). In the gas phase the zwitterion form is not stable, but in studies with Tryptophan water clusters it has been found that few water molecules can stabilize the zwitterion form [155].

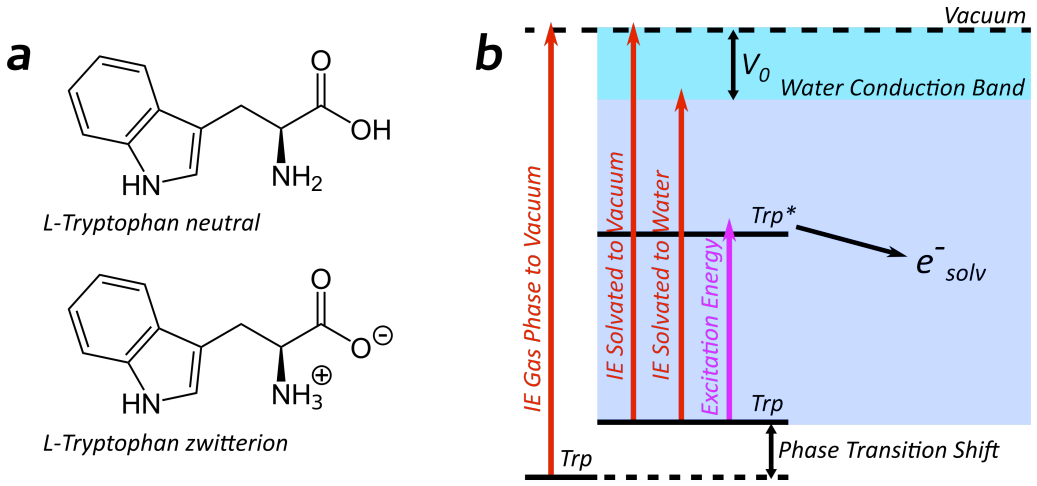

Fig. 6.2: **a)** Molecular structure of L-Tryptophan in the neutral and in the zwitterion form. **b)** Illustration of the different ionization processes. They are, in order of descending necessary energy: direct ionization of gas-phase molecules referenced to vacuum, direct ionization of solvated molecules referenced to vacuum, direct ionization of solvated molecules referenced to the water conduction band, and ionization by charge transfer after excitation.

For amino acids in aqueous solution the equilibrium content of neutrals, anions, cations and zwitterions is governed by the logarithmic apparent acid dissociation constants of the amino and carboxyl groups. These constants quantify the pH-values, at which the concentrations of dissociated and bound groups are equal. For the amino acid Glycin values of $pK'_{COOH} = 2.3$ and $pK'_{NH_2} = 9.6$ were measured [156]. For Glycin the content of anions or cations is found to be below 1% at all pH-values between 4.3 and 7.7. Additionally the zwitterion form is favored in aqueous solution at neutral pH, with a ratio of neutral Glycin to zwitterions of approximately 10^{-5} [156]. For Tryptophan the measured acid dissociation constants are $pK'_{COOH} = 3.4$ and $pK'_{NH_2} = 9.4$ [156]. Since these values are similar to the values measured for Glycin, it can be safely assumed, that the zwitterion form also dominates for Tryptophan in aqueous solution at neutral pH.

The difference in orbital energies in the neutral and in the zwitterion form was evaluated in quantum chemistry calculations in ref. [149]. Seki and coworkers reported only a small shift for the Indole orbitals. For the orbitals associated to the Alanine part of the molecule they predicted a 2-3 eV lower binding energy in the zwitterion form in the gas phase. In a more recent DFT study [154], the vertical ionization energies of various amino acids in aqueous solution were calculated using a polarization cavity model (see section 2.2), resulting in a much smaller phase transition shift of 0.8 eV for Tryptophan.

To discuss the photoionization potential of Tryptophan in aqueous solution, the definition of the ionization energies for solvated molecules has to be expanded as illustrated in figure 6.2b. Photoelectron spectroscopy measures the ionization potential of the gas phase or solvated molecules referenced to vacuum. The difference between these values is defined as the phase transition shift. The energy relevant for the generation of charged species in aqueous solution is the ionization energy referenced to water. This important quantity is the photon energy necessary to generate electrons in the conduction band of liquid water. The energy of the liquid water conduction band relative to vacuum V_0 is -1.2 eV [148]. Using this, the ionization threshold referenced to the conduction band was estimated as 5.5 eV [148].
Ionization threshold measurements using absorption detection of solvated electrons [148], photoconductivity [157], or detection by scavenging the generated electron [158], yield much lower values for Tryptophan and Indole in aqueous solution. An ionization threshold of approximately 4.5 eV is reported. This is due to the fact that Tryptophan can be ionized by electron transfer to the solvent after electronic excitation. This process needs less energy than direct ionization, because the solvated electrons have a higher binding energy than electrons in the conduction band of water. Therefore generation of solvated electrons can be observed with photon energies below the threshold for direct ionization [148]. This property has also sparked major interest in the relaxation pathways of Tryptophan after UV excitation, leading to recent studies employing time-resolved techniques [25, 159].

6.2 XUV Photoelectron Spectroscopy Results

For this thesis XUV-only photoelectron spectroscopy experiments on Tryptophan in aqueous solution are performed. In the experiments the vertical ionization energies of aqueous Tryptophan, referenced to vacuum, can be directly measured. In comparison with the gas phase photoelectron spectrum this yields a direct measurement of the phase transition shift. Therefore also the ionization energy referenced to the water conduction band can be calculated more accurately.
As discussed before, the intense water contributions in the spectrum have to be subtracted to isolate the solute photoelectron spectrum. For this purpose a reference 60mM NaCl solution in demineralized water is prepared. Tryptophan is then added to a part of the reference solution, thus ensuring that both contain the same concentration of NaCl. L-Tryptophan was purchased from *Sigma Aldrich* and used as received.
A recurring problem in the subtraction of the water signal are XUV intensity fluctuations. Since the switch from the reference solution to the sample solution takes approximately 15 minutes, slow drifts in the XUV intensity cannot be averaged out. In the counting mode measurements, which were presented in the previous chapters, the maximum accessible binding energy was approximately 9 eV. Since the water signal for binding energies below 9 eV is small, the error introduced by the background subtraction can

be neglected. To access the photoelectron spectrum of Tryptophan at binding energies beyond 9 eV, the background subtraction procedure needs to be revisited.
The photoelectron spectrum of the Tryptophan solution is the sum of the water spectrum and the Tryptophan spectrum, i.e. $W(E) + T(E)$. The reference spectrum is the spectrum of water measured at a different XUV intensity, i.e. $W'(E) = \text{const.} \cdot W(E)$. To correct for the intensity difference, the reference spectrum is normalized to the maximum intensity of the liquid water $1b_1$ band

$$W_{norm}(E) = W'(E)\frac{W(1b_1) + T(1b_1)}{W'(1b_1)} = W(E)\left(1 + \frac{T(1b_1)}{W(1b_1)}\right) \tag{6.1}$$

Subtracting the normalized reference spectrum from the spectrum of the Tryptophan yields the difference spectrum

$$D(E) = T(E) - W(E)\frac{T(1b_1)}{W(1b_1)} \tag{6.2}$$

meaning that the true Tryptophan spectrum is

$$T(E) = D(E) + W(E)\frac{T(1b_1)}{W(1b_1)} \tag{6.3}$$

which contains the ratio of Tryptophan signal to water signal at the liquid water peak. This parameter is unknown. It can, however, be estimated to correct the Tryptophan spectrum with the measured spectrum of water. To quantify how important the correction term is for the extracted binding energies, the estimated Tryptophan signal at the liquid water peak will be varied.
Figure 6.3a shows the photoelectron spectra of the 10 mM Tryptophan solution and the reference NaCl solution (buffer). In the difference spectrum two photoelectron bands from Tryptophan are visible. The difference spectrum is corrected according to equation (6.3). Figure 6.3a shows the Tryptophan photoelectron spectra obtained with estimated ratios of the Tryptophan to liquid water signal of 0.005 (lower dashed line), 0.01 (red line), and 0.02 (upper dashed line). As discussed above, the correction term has no effect for binding energies below 9 eV, where the water signal is negligible. With increasing water signal the correction term becomes more important. Up to a binding energy of 10 eV the corrected spectra are similar, so the error introduced by the correction is small.
Figure 6.3b shows the photoelectron spectra of aqueous Tryptophan acquired with the harmonics 15, 17, and 19. The photoelectron spectra measured with the harmonics 15 and 17 are corrected with an estimated Tryptophan to water signal ratio of 0.01. The XUV yield with harmonic 19 is considerably lower, so the Tryptophan signal could only be distinguished using the counting mode. Therefore the spectrum acquired with harmonic 19 is only shown up to a binding energy of 9 eV.

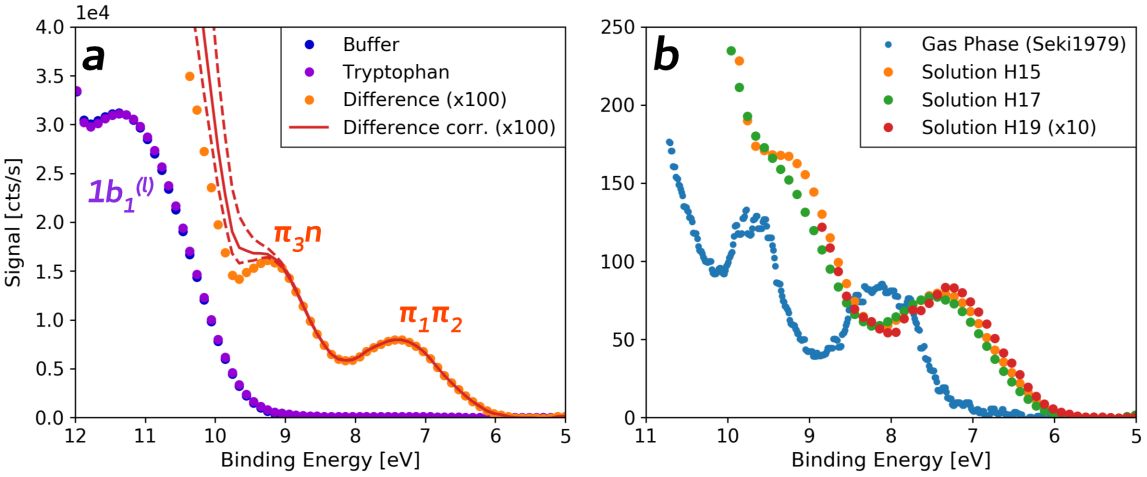

Fig. 6.3: **a)** Photoelectron spectra (averaging mode) of a 10 mM Tryptophan solution and a reference NaCl solution (buffer), averaged over an acquisition time of approximately 5 min. The difference spectrum is corrected as discussed in the text (red lines). **b)** Tryptophan spectra obtained with the harmonics 15, 17 and 19 compared to the gas-phase photoelectron spectrum, digitized from ref. [149].

The solubility of Tryptophan in water at room temperature is approximately 60 mM, but drops to circa 1 mM at 0°C [160]. Due to evaporative cooling the water temperature in the liquid jet is significantly below room temperature, therefore a 10 mM concentration can be close to the solubility limit or already cause aggregation.

To check if the photoelectron spectrum is affected by a saturation of the surface concentration or a possible aggregation, measurements with different concentrations are conducted. The spectra for concentrations from 0.5mM to 10 mM are shown in figure 6.4. For the low concentrations the Tryptophan signal could only be distinguished from the noise in the counting mode, therefore only the $\pi_1\pi_2$ band is shown. The spectra are scaled according to the concentration to highlight that the observed signal is linear with concentration. No significant spectral changes are observed with changing concentration. Therefore there appears to be no significant aggregation of the sample, meaning that the measured spectrum can be interpreted as the unaltered spectrum of solvated Tryptophan.

To compare gas phase and aqueous Tryptophan, the gas phase spectrum from ref. [149] is plotted together with the solution spectra in figure 6.3b. To extract the peak position, width and total signal, the photoelectron spectra are modeled with three Gaussian peaks, two for the assigned bands and one for the onset of the next band at higher binding energies. The extracted fit parameters are listed in table 6.1.

Averaging of the values in table 6.1 yields a vertical binding energy of 7.35±0.1 eV

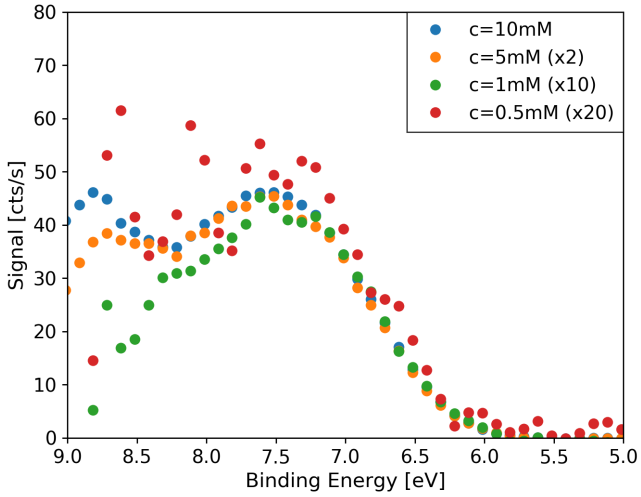

Fig. 6.4: Photoelectron spectra (counting mode) of solvated Tryptophan for different concentration, the reference water spectrum is subtracted. The spectra are scaled according to the Tryptophan concentration to highlight that no spectral changes are observed with changes in the concentration.

and a FWHM of 1.35±0.09 eV for the $\pi_1\pi_2$-band, with the errors estimated from the variance of the extracted values and the systematical error of the calibration procedure. For the $n\pi_3$-band a vertical binding energy of 9.3±0.2 and a FWHM of 1.4±0.2 eV is obtained. The errors for the $n\pi_3$-band are larger due to the influence of the overlapping liquid water peak. Thus the measured phase transition shift for the $\pi_1\pi_2$-band is 0.8 eV, while it is only approximately 0.4 eV for the $n\pi_3$-band. The retrieved vertical ionization energy of 7.35 eV also agrees reasonably well with the value of 6.67 eV, obtained by Close and coworkers in DFT calculations [154].
Evidently, the phase transition shift for the $\pi_1\pi_2$-band is larger while the broadening is larger for the $n\pi_3$-band. This can be intuitively understood, since the lower band consists of overlapping peaks from two π-orbitals that should respond similarly to the phase transition. The $\pi_3 n$ band consists of a π-orbital and an n-orbital. The phase transition shift of the n-orbital is expected to be smaller than that of the π-orbital resulting in a stronger broadening and a weaker shift of the combined peak (see section 2.1).
For the zwitterion Seki and coworkers predicted a 2 eV decrease in the binding energy of the nitrogen lone pair orbital on the Alanine [149]. It is clear that this is not reproduced in this measurement, in the accessible spectral range only sub-eV shifts from gas-phase to solution are observed. In fact the retrieved phase transition shift of the first ionization energy agrees with the shift obtained from CPCM DFT calculations (see section 2.2) in ref. [154]. This shows that evidently the polarization model is sufficient to treat the ionization of aqueous Tryptophan and a treatment describing the

Table 6.1: Binding energies, peak widths, and total signal of the Tryptophan photoelectron bands. The total signal of the $1b_1$ peak of liquid water is given for comparison. The values in brackets are extracted from the corrected difference spectra shown in figure 6.3b. [a] *obtained from a fit of the re-plotted spectrum from ref.* [149].

	Tryptophan $\pi_1\pi_2$			Tryptophan $\pi_3 n$			Water $1b_1^{(l)}$
	E [eV]	FWHM [eV]	cts/s	E [eV]	FWHM [eV]	cts/s	cts/s
Solution H15	7.40	1.44	124	9.21 (9.21)	1.24 (1.25)	209 (214)	66500
Solution H17	7.42	1.36	112	9.46 (9.48)	1.61 (1.62)	262 (272)	66200
Solution H19	7.22	1.26	10	-	-	-	13600
Gas Phase[a]	8.15	1.11	-	9.66	0.85	-	-

first solvation shell with discrete water molecules, as it is suggested in ref. [154], is not necessary in this case.
A value for the ionization threshold cannot be extracted from the photoelectron spectra as reliably as the vertical binding energy, due to the limited energy resolution caused by the bandwidth of the XUV pulse. The broadening of the $\pi_1\pi_2$-band approximately corresponds to the broadening of photoelectron peaks expected from the XUV-bandwidth. Therefore the shift of the ionization threshold due to solvation can be assumed to be similar to the shift of the vertical ionization energy, i.e. 0.8 eV.
Adding the binding energy of the water conduction band threshold of 1.2 eV [148], the total difference between the gas phase ionization energy and the ionization energy in solution is 2.0 eV. Taking the measured gas phase ionization threshold of 7.3 eV [149], the ionization threshold of aqueous Tryptophan referenced to the water conduction band is 5.3 eV. Katoh and coworkers [148] came to an estimate of 5.5 eV for this value, but using a overestimated phase transition shift of 1.1 eV and an overestimated gas-phase ionization threshold of 7.8 eV. Liquid-phase XUV photoelectron spectroscopy can improve this estimate with a much more reliable method, since it contains a directly measured liquid-phase ionization potential. The value for the phase transition shift of 0.8 eV is more accurate than previous estimates, since it is based completely on photoelectron experiments from this thesis and from Seki and coworkers [149].

6.3 Summary

In this chapter results from XUV photoelectron spectroscopy of Tryptophan in aqueous solution were presented. The vertical binding energies of two photoelectron bands of aqueous Tryptophan are obtained. The photoelectron bands can be assigned to molecular orbitals by comparison with gas phase photoelectron and computational studies on Tryptophan [149, 154]. The vertical binding energies of the $\pi_1\pi_2$-band

and the $n\pi_3$-band are 7.4 eV and 9.3 eV respectively. Comparison with a literature photoelectron spectrum of gas-phase Tryptophan [149], yields a phase transition shift of 0.8 eV. This value for the phase transition shift is in excellent agreement with a recent computational study [154].
Using the retrieved phase transition shift the threshold for direct ionization referenced to water can be calculated. The extracted value is 5.3 eV, which compares well to the value of 5.5 eV estimated in ref. [148]. However, the value using a directly measured photoelectron spectrum is much more reliable, since the uncertain estimate of the phase transition shift is not necessary.
The XUV-only measurement will serve as a basis for a 266 nm pump, XUV-probe photoelectron experiment, which could prove highly beneficial to understand the complicated relaxation dynamics of Tryptophan. Possible relaxation pathways are fluorescence, electron transfer, intramolecular proton transfer and intersystem crossing. According to a recent study the primary photoreaction at neutral pH is an intramolecular proton transfer leading to a zwitterionic form where the nitrogen on the Indole carries the charge [25]. It is however unclear, if the intersystem crossing to a triplet state is competing with the proton transfer mechanism or if proton transfer is followed by intersystem crossing.
The open questions in the relaxation dynamics of Tryptophan could be addressed with time-resolved photoelectron spectroscopy. Advantages of photoelectron spectroscopy would be the unambiguous detection of solvated electron signals [46], and the observation of a possible triplet state which has been proposed to play a role in the charge transfer process [25].

7 Summary and Outlook

This thesis presents the experimental implementation of time-resolved XUV photoelectron spectroscopy of organic molecules in solution and the application of this novel method to the investigation of electronic structure and excited state dynamics of several functional organic chromophores of biological and industrial importance. Due to the large variety of topics covered in the thesis, the summary is divided into three parts. The first part discusses the technical aspects of liquid-phase photoelectron spectroscopy, with a special focus on the detection of solute signals and possible technical improvements. In section 7.2 the results on Quinoline Yellow and Tryptophan are summarized. The results show the potential of the developed technique for the investigation of charge transfer processes, since excited state proton transfer is proposed as a major relaxation pathway in both molecules. In section 7.3 the results on the light-induced isomerization of amino-azobenzene derivatives are summarized and possible future experiments on molecular switches are discussed.

7.1 Time-Resolved XUV Photoelectron Spectroscopy in Solution

The implementation of liquid-phase photoelectron spectroscopy is discussed in chapter 3 of the thesis. This includes the integration of a liquid jet target [11] into the vacuum system of the existing XUV monochromator setup [17]. A thin liquid filament is injected into the vacuum system under high pressure and collected by a catcher after a travel distance of a few millimeters. With this technique the necessary vacuum conditions for photoelectron detection and for the propagation of XUV pulses are achieved. The redesign of the liquid jet assembly, which was carried out as part of this thesis, successfully improved the stability and flexibility of the liquid jet system. Photoelectron detection from the liquid-phase is accomplished with a magnetic bottle time-of-flight electron spectrometer in a design similar to the one described in ref. [66], which offers a significantly higher collection efficiency than field-free electron spectrometers.
As a first step of evaluating the performance of the liquid jet endstation, XUV photoelectron spectra of water, ethanol, and acetonitrile are acquired. The obtained photoelectron spectra are in good agreement with photoelectron spectra from the literature [12]. With the magnetic bottle photoelectron spectrometer high quality photoelectron spectra of liquid samples can be collected in acquisition times of a few seconds. To demonstrate the sensitivity of the detection scheme, pump-probe experiments on liquid water are performed. The laser-assisted photoelectric effect is observed with 400 nm pump pulses (see chapter 3), although it is significantly weaker than with an 800 nm dressing field as it was used in a previous study [19].

Regarding the XUV-only photoelectron spectroscopy of solvated molecules, the solute photoelectron signals are successfully separated from the photoelectron signals of water for all molecules covered in this thesis. High quality photoelectron spectra of solvated molecules can be acquired in acquisition times of a few minutes, making detailed investigations on the influence of XUV photon energy and solute concentration possible. Solute photoelectron spectra are measured at solute concentrations below 1 mM, which is three orders of magnitude below the concentration used in high harmonic photoelectron spectroscopy of solvated molecules before [101]. The sample concentrations used in the XUV-only experiments are even lower than those used in liquid jet photoelectron experiments at synchrotron facilities [16], which once more demonstrates the sensitivity of the implemented setup.
An interesting discovery in this context is that the solute photoelectron signals do not necessarily increase linearly with the concentration. Overall the experiments in this thesis suggest a negative correlation between solubility and photoelectron yield (see chapter 4), which can be intuitively explained by the tendency of low solubility samples to accumulate closer to the surface of the liquid jet. If this correlation proves to be robust, it means that low sample solubility is not as limiting for photoelectron spectroscopy of solvated molecules as expected. More data to investigate the universality of the suspected correlation will be automatically collected in future experiments on other organic molecules.
In the time-resolved experiments discussed in this thesis the excited state decay signals of three organic dye molecules in aqueous solution are successfully measured using millimolar sample concentrations. The pump-probe experiments however also show a strong photoelectron signal from ionization of the sample molecules by the 400 nm pump pulse. This causes a light-induced space charge effect, as previously observed in time-resolved photoelectron spectroscopy of water [49]. For this thesis a correction procedure is devised, which corrects the resulting delay-dependent shift based on the liquid water photoelectron spectrum (see chapter 4).
The main challenge in the time-resolved experiments is the low yield of excited state electrons, which was on the order of 1-2 electrons per 1000 laser shots in the presented experiments. Due to the low electron yield the experiments require long measurement times. This in turn causes a high consumption of sample solution of approximately 500 ml for a complete time-resolved experiment. This limits the technique to the investigation of sample molecules which can be obtained in large quantities.
Increasing the pump-probe signal yield is challenging in the present configuration. A higher pump pulse intensity causes a higher 400 nm only photoelectron signal, which increases the influence of the light-induced space charge effect. Additionally, it is crucial that the pump-probe signals can be measured background-free. Therefore the pump pulse intensity has to be limited, such that no electrons in the kinetic energy range of the pump-probe signal are generated. Increasing the photon flux of the XUV pulse is also problematic. The correction procedure for the space charge effect (chapter 4)

relies on the detection of the liquid water photoelectron peak. Therefore the dynamic range in the photoelectron detection needs to be high enough to allow unsaturated detection of the liquid water peak, while also distinguishing the single electron peaks of the molecular pump-probe signal. To accomplish this with a much higher XUV photon flux is impossible with the current digitizer card.
Thus the most promising approach to shorter acquisition times and lower sample consumption is an increase in repetition rate. The setup currently operates at a repetition rate of 1 kHz, but the laser system offers a 10 kHz output. Operation at 10 kHz, while also challenging due to the higher average power in both laser beams, would be a promising technical improvement. To further decrease sample consumption, the automatic recycling of the sample solution should be implemented. While collecting the sample after the liquid jet is already possible with water solutions, recycling more volatile solvents was not successful with the current collection system. Cooling of the collection bottle to lower temperatures and a smaller diameter of the catcher orifice are necessary to recycle solvents like ethanol.

7.2 Investigation of Charge Transfer Processes

In chapter 4 steady-state and time-resolved photoelectron experiments of the sulfonated dye molecule Quinoline Yellow in aqueous solution are presented. Additionally, ionization energies from DFT calculations performed within the scope of this thesis are presented. The calculations include the aqueous solution via the conductor-like polarizable continuum model. The agreement between the DFT calculations and the photoelectron spectrum is excellent, leading to the conclusion that one band in the photoelectron spectrum can clearly be assigned to a delocalized π-orbital of the planar tautomer of the molecule.
In the time-resolved photoelectron experiment in water, three timescales are extracted from the excited state signal. The fastest timescale of approximately 250 fs is related to a spectral change rather than a change in excited state signal, and can therefore be attributed to the initial solvent rearrangement. The excited state decay then proceeds with timescales of approximately 1.3 ps and 90 ps. Evidence was found recently, that Quinoline Yellow in cyclohexane solution undergoes excites state intramolecular proton transfer (ESIPT) after excitation [20]. The 1.3 ps timescale is consistent with an excited state proton transfer process over a barrier, as it is suggested in ref. [20]. The long timescale could be explained by a rotational relaxation to the ground state or a tautomerization pathway.
To confirm that the ESIPT occurs also in aqueous solution, further theoretical and experimental work is necessary. The ground state DFT calculations, which are performed in this thesis, suggest that the CPCM treatment is sufficient to model the influence of the solvent on Quinoline Yellow. Therefore time-dependent DFT (TDDFT) calculations, as they were performed by Han and coworkers [20], but including various

solvents could provide insight into the dynamics of the ESIPT in various solvents. Additionally, future TDDFT calculations should not only include the proton transfer coordinate. Since rotational stability is likely decreased by the proton transfer, the coordinate associated to rotation around the bridge bond should also be considered in future TDDFT calculations.
Further insight into the plausibility of intramolecular proton transfer in aqueous solution could come from measurements with the deuterated form of Quinoline Yellow. Since the molecule deuterates easily [20], measurements with deuterated Quinoline Yellow should be performed in a solution of deuterated water. Additionally, a time-resolved photoelectron experiment with Quinoline Yellow in an aprotic solvent, for example acetonitrile, could provide insight into how the 90 ps timescale changes in an aprotic environment. Since the tautomerization pathway likely includes a proton transfer through the solvent, it would be expected to be inhibited in an aprotic environment.
In chapter 6, the amino acid Tryptophan in aqueous solution is investigated. Also for Tryptophan an excited state proton transfer is reported as the most likely relaxation pathway after excitation [25]. Tryptophan is only studied with steady-state XUV photoelectron spectroscopy in this thesis. In comparison with gas-phase photoelectron spectroscopy the photoelectron spectra of Tryptophan in aqueous solution can be used to determine an accurate experimental value for the phase transition shift, i.e. the decrease of the ionization energy due to solvation. The determined value of 0.8 eV is in excellent agreement with recent computational results [154].
Additionally the steady-state experiment on Tryptophan can be seen as the first step towards a time-resolved photoelectron spectroscopy experiment using 266 nm pump pulses. Such an experiment could aid in disentangling the complicated excited state dynamics of Tryptophan [25], including possible electron or proton transfer processes to the solvent. Advantages of photoelectron spectroscopy in this context would be the possibility of the unambiguous detection of both triplet states and solvated electrons.
The experiments on Quinoline Yellow and Tryptophan show that time-resolved photoelectron spectroscopy is a promising technique for the investigation of both intramolecular and intermolecular charge transfer processes. In the future the experiments could be extended to other photoactive amino acids or photoacids.

7.3 Isomerization of Functional Molecules

Results from steady-state and time-resolved photoelectron spectroscopy of the two amino-azobenzene derivatives Methyl Orange and Metanil Yellow are presented in chapter 5. Amino-azobenzene derivatives are studied mainly for their light-induced isomerization, which is why they are used as molecular switches. An open question in these molecules is the ordering of the excited states [22, 125], which are labeled as the $\pi\pi^*$ and the $n\pi^*$ states, in analogy to azobenzene. Since the $\pi\pi^*$-state has a much higher absorption cross-section, time-resolved experiments can be helpful to resolve

this question. If the internal conversion from $\pi\pi^*$ to $n\pi^*$ is observed, the $n\pi^*$ state is clearly lower in energy.
XUV-only photoelectron spectra of both dyes in aqueous solution are collected at concentrations of a few millimolar. DFT calculations of ionization energies in solution are performed, to support the interpretation of the photoelectron spectra. However, the agreement between the calculated ionization energies and the measured photoelectron spectrum is not nearly as good as for Quinoline Yellow. This is likely due to the hydrogen bonding between the solvent and the nitrogen atoms, both on the azo-group and the amino-substituent. Expectedly the polarization cavity model is insufficient for the modeling of this interaction. Probably an explicit solvation model (see section 2.2) is needed to accurately predict the ionization energies of the amino-azobenzene dyes.
Time-resolved photoelectron experiments of both dyes in aqueous solution are performed to investigate the isomerization dynamics. In the time-resolved photoelectron experiments of both dyes a spectral change on a timescale of approximately 100 fs is observed, which can again be associated with the solvent rearrangement after excitation. For the dye Methyl Orange a single timescale of approximately 1 ps is extracted from both the excited state decay and the ground state recovery signals. This timescale can clearly be assigned to the trans to cis isomerization of the dye, in good agreement with the timescale found in transient absorption measurements [22, 141]. In Methyl Orange the internal conversion from $\pi\pi^*$ to $n\pi^*$ is not observed. This, however, does not exclude it entirely, since this decay could occur on a similar timescale as the initial solvent rearrangement.
The second amino-azobenzene derivatives, Metanil Yellow, exhibits a biexponential decay of the excited state signal with decay constants of approximately 0.6 ps and 5 ps. The 5 ps decay is assigned to the isomerization of Metanil Yellow, which is significantly slower than the isomerization of Methyl Orange. This can probably be explained by the larger moment of inertia of the heavier substituent and the larger fraction of dimers in the Metanil Yellow solution. The most likely explanation for the 600 fs timescale is the internal conversion from $\pi\pi^*$ to $n\pi^*$. This would support the assignment of the $n\pi^*$-state as the lowest-lying excited state in Metanil Yellow.
To conclusively answer the question of the ordering of excited states in amino-azobenzene molecules, support from computational chemistry, e.g. TDDFT, is needed. It is, however, unlikely that the influence of the solvent can be ignored in a computational investigation. Unfortunately the implicit treatment of the solvent proved insufficient for the calculation of ionization energies of the amino-azobenzene dyes. Explicit solvation on the other hand would make a TDDFT calculation extremely costly. Probably the most promising approach would be QM/MM, which treats the solute with TDDFT and the solvent with molecular mechanics.
Altogether the study of molecular switches is another promising direction for future experiments with time-resolved XUV photoelectron spectroscopy in solution. A large variety of differently substituted azobenzene dyes are available, and the technique could

be used to investigate substituent effects on ordering of excited states and isomerization dynamics. Additionally, solvent mixtures or pH-variation could provide insight into the effect of protonation or hydration of amino-azobenzene derivatives on the isomerization. Furthermore, the technique could be extended to study the isomerization of biologically relevant functional molecules, for example the chromophore of human vision, retinal.

A Appendices

A.1 Molecular Structures

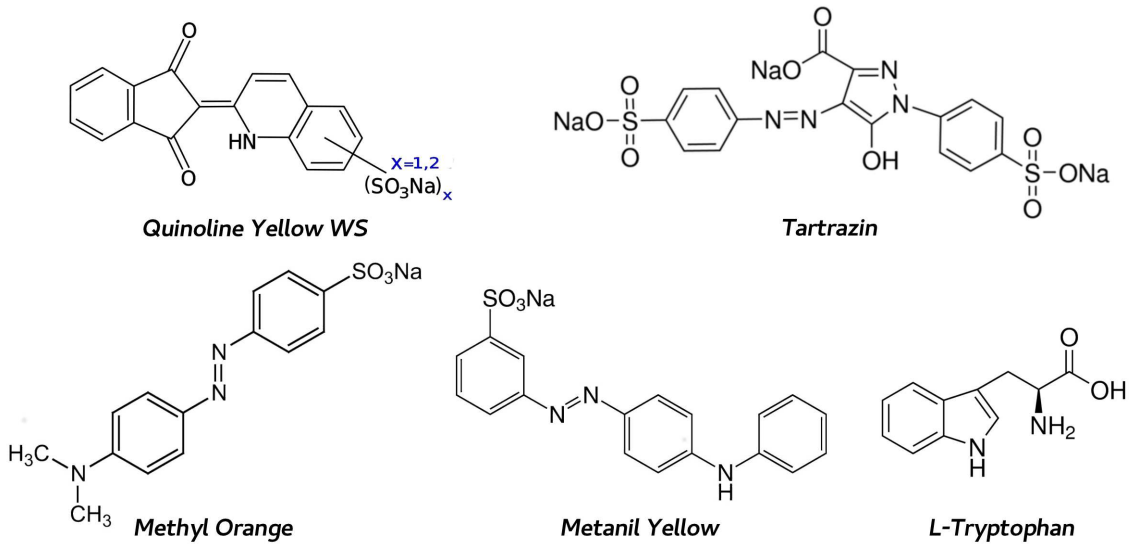

Fig. A.1: Molecular Structures of all sample molecules used in the experiments for this thesis

A.2 Optimized Geometries of Quinoline Yellow and Azo Dyes

Quinoline Yellow SS

enamino $E = -24443.064\,\text{eV}$				ketoenol $E = -24442.769\,\text{eV}$				keto $E = -24442.276\,\text{eV}$			
H	-6.5460	0.3522	0.0174	H	-6.5355	0.4263	0.0127	H	-5.1705	1.5198	-1.6859
C	-5.4609	0.3814	0.0103	C	-5.4495	0.4271	0.0071	H	-5.1534	2.1629	0.6951
H	-5.3699	2.5415	-0.0012	H	-5.3081	2.5875	-0.0046	C	-4.4620	1.0437	-1.0133
H	-5.2370	-1.7576	0.0178	H	-5.2826	-1.7141	0.0154	C	-4.4518	1.4105	0.3444
C	-4.7941	1.6204	0.0003	C	-4.7537	-0.7639	0.0089	H	-3.5811	-0.2105	-2.5490
C	-4.7322	-0.7951	0.0110	C	-4.7503	1.6550	-0.0021	C	-3.5805	0.0830	-1.5034
C	-3.4109	1.6837	-0.0075	C	-3.3712	1.6831	-0.0080	C	-3.5598	0.8249	1.2399
C	-3.3224	-0.7695	0.0025	C	-3.3388	-0.7717	0.0022	H	-3.5454	1.0983	2.2907
H	-2.9988	-2.9162	0.0071	H	-3.0759	-2.9243	0.0083	C	-2.6802	-0.4956	-0.6064
H	-2.8945	2.6394	-0.0153	H	-2.8278	2.6234	-0.0154	C	-2.6697	-0.1298	0.7457
C	-2.6657	0.4907	-0.0057	C	-2.6345	0.4737	-0.0052	C	-1.6562	-1.5398	-0.8703
C	-2.5070	-1.9463	0.0019	C	-2.5648	-1.9641	0.0030	C	-1.6376	-0.9049	1.4843
N	-1.2927	0.5150	-0.0122	N	-1.2703	0.5159	-0.0098	O	-1.4706	-2.1310	-1.9168
C	-1.1448	-1.8723	-0.0046	C	-1.1969	-1.9051	-0.0024	O	-1.4552	-0.9070	2.6861
H	-0.7559	1.4065	-0.0153	H	-0.5743	-2.7932	-0.0015	H	-0.8851	-2.8115	0.7249
H	-0.5086	-2.7501	-0.0045	C	-0.5582	-0.6293	-0.0075	C	-0.8644	-1.7524	0.4469
C	-0.4946	-0.5962	-0.0097	H	-0.1832	1.6324	-0.0059	C	0.5680	-1.2840	0.2865
C	0.8950	-0.3978	-0.0099	O	0.8349	1.9369	-0.0024	N	0.7541	0.0267	0.2712
O	0.9167	2.0208	-0.0079	C	0.8738	-0.4670	-0.0079	H	1.3665	2.5453	0.2173
C	1.5036	0.9171	-0.0067	C	1.4741	0.7918	-0.0036	H	1.3980	-3.2879	0.1413
O	1.8329	-2.6483	-0.0105	O	1.8457	-2.7043	-0.0100	C	1.6180	-2.2249	0.1256
C	1.9428	-1.4206	-0.0082	C	1.9419	-1.4802	-0.0080	C	2.0233	0.4996	0.0986
C	2.9836	0.7141	-0.0005	C	2.9413	0.6723	0.0006	C	2.2315	1.9017	0.0864
C	3.2457	-0.6640	-0.0037	C	3.2412	-0.7012	-0.0035	C	2.9003	-1.7652	-0.0519
H	3.8034	2.7096	0.0111	H	3.7081	2.6920	0.0112	C	3.1486	-0.3711	-0.0706
C	4.0157	1.6442	0.0079	C	3.9434	1.6318	0.0076	C	3.4979	2.4161	-0.0861
C	4.5475	-1.1452	-0.0011	C	4.5507	-1.1435	-0.0025	H	3.6496	3.4919	-0.0929
H	4.7414	-2.2141	-0.0038	H	4.7765	-2.2061	-0.0056	H	3.7289	-2.4589	-0.1776
C	5.3305	1.1627	0.0111	C	5.2744	1.1842	0.0090	C	4.4387	0.1899	-0.2460
C	5.5926	-0.2121	0.0058	C	5.5739	-0.1785	0.0033	C	4.6099	1.5565	-0.2535
H	6.1611	1.8633	0.0169	H	6.0830	1.9097	0.0135	H	5.2894	-0.4764	-0.3736
H	6.6233	-0.5574	0.0073	H	6.6129	-0.4967	0.0033	H	5.6011	1.9801	-0.3877

Quinoline Yellow WS Q4

enol vac.				enol H_2O				keto vac.				keto H_2O			
$E = -41423.365\,eV$				$E = -41424.193\,eV$				$E = -41422.231\,eV$				$E = -41423.520\,eV$			
H	-7.5004	0.4629	0.0500	H	-7.5000	0.4977	0.0507	H	-6.3872	1.9904	-1.0267	H	-6.4877	1.4861	-1.5320
H	-6.9932	-1.9486	0.0779	H	-7.0150	-1.9203	0.0830	H	-6.3692	1.7658	1.4661	H	-6.4601	2.0248	0.8742
C	-6.4639	0.1368	0.0250	C	-6.4674	0.1604	0.0268	C	-5.6113	1.3916	-0.5495	C	-5.6887	1.0934	-0.9099
C	-6.1761	-1.2335	0.0409	C	-6.1924	-1.2121	0.0452	C	-5.6003	1.2635	0.8794	C	-5.6718	1.4024	0.4622
H	-5.6520	2.1538	-0.0303	H	-5.6436	2.1689	-0.0321	H	-4.6434	0.8521	-2.4019	H	-4.7072	0.0567	-2.5392
C	-5.4379	1.0889	-0.0204	C	-5.4302	1.1037	-0.0201	C	-4.6397	0.7694	-1.3159	C	-4.6984	0.2947	-1.4800
C	-4.8538	-1.6913	0.0112	C	-4.8717	-1.6826	0.0163	C	-4.6159	0.5228	1.5105	C	-4.6608	0.9253	1.2955
H	-4.6219	-2.7523	0.0244	H	-4.6580	-2.7476	0.0314	H	-4.6047	0.4141	2.5943	H	-4.6455	1.1649	2.3541
C	-4.1274	0.6315	-0.0482	C	-4.1243	0.6329	-0.0466	C	-3.6188	0.0273	-0.6902	C	-3.6898	-0.1883	-0.6437
C	-3.8395	-0.7421	-0.0332	C	-3.8493	-0.7430	-0.0293	C	-3.6010	-0.0929	0.7491	C	-3.6681	0.1263	0.7248
C	-2.8420	1.4133	-0.0847	C	-2.8295	1.3945	-0.0849	C	-2.5696	-0.7625	-1.2913	C	-2.5381	-1.0496	-0.9905
O	-2.7520	2.6410	-0.1070	O	-2.7377	2.6306	-0.1112	C	-2.5417	-0.9704	1.1852	C	-2.4905	-0.4942	1.3732
C	-2.3584	-0.9197	-0.0592	C	-2.3680	-0.9282	-0.0560	O	-2.2975	-0.8878	-2.5029	O	-2.2180	-1.4326	-2.1046
C	-1.7720	0.4086	-0.0828	O	-1.7731	-2.0292	-0.0517	O	-2.2464	-1.3055	2.3520	O	-2.1242	-0.3379	2.5278
O	-1.7489	-2.0098	-0.0533	C	-1.7685	0.3920	-0.0808	H	-2.0457	-2.5516	-0.2022	H	-2.0617	-2.4326	0.5713
H	-0.4185	2.7874	-0.0690	H	-0.3988	2.7740	-0.0637	C	-1.8279	-1.4772	-0.1153	C	-1.7984	-1.3934	0.3264
C	-0.3916	0.6326	-0.0652	C	-0.3777	0.6162	-0.0636	C	-0.3377	-1.2911	-0.1174	C	-0.3009	-1.2506	0.2432
H	-0.0928	-1.3679	-0.0597	H	-0.0538	-1.3843	-0.0645	H	0.1009	-3.4022	-0.0816	H	0.0818	-3.3875	0.2976
C	0.2345	1.9223	-0.0431	C	0.2453	1.9041	-0.0391	N	0.1543	-0.0237	-0.1391	N	0.1655	-0.0092	0.1637
N	0.4294	-0.4670	-0.0508	N	0.4428	-0.4767	-0.0511	C	0.5284	-2.4001	-0.1025	C	0.5282	-2.4012	0.2186
C	1.5914	2.0241	0.0220	C	1.6039	2.0130	0.0264	H	1.2615	2.3168	-0.1956	H	1.3175	2.3175	-0.0033
C	1.7960	-0.4163	0.0154	C	1.8097	-0.4247	0.0136	C	1.4814	0.1624	-0.1560	C	1.5131	0.1657	0.0420
H	2.0665	3.0012	0.0488	H	2.0746	2.9914	0.0547	C	1.9031	-2.2312	-0.1177	C	1.8880	-2.2440	0.0955
H	2.0672	-2.5620	0.0151	H	2.0796	-2.5724	-0.0053	C	1.9922	1.5123	-0.1921	C	2.0192	1.4902	-0.0520
C	2.4265	0.8586	0.0634	C	2.4364	0.8505	0.0657	C	2.4537	-0.9144	-0.1517	C	2.4251	-0.9372	-0.0038
C	2.5632	-1.5966	0.0489	C	2.5736	-1.6073	0.0395	H	2.5715	-3.0919	-0.1117	H	2.5531	-3.1030	0.0716
C	3.8262	0.9166	0.1638	C	3.8371	0.9131	0.1664	C	3.3375	1.7778	-0.2375	C	3.3656	1.7157	-0.2096
C	3.9406	-1.5156	0.1405	C	3.9495	-1.5258	0.1324	H	3.7011	2.8018	-0.2686	H	3.7505	2.7269	-0.2908
H	4.3240	1.8793	0.2271	H	4.3253	1.8804	0.2243	C	3.8275	-0.6324	-0.1958	C	3.8114	-0.6897	-0.1573
H	4.5462	-2.4147	0.1881	H	4.5498	-2.4283	0.1628	C	4.2880	0.7199	-0.2658	C	4.2546	0.6108	-0.2640
C	4.5662	-0.2568	0.2012	C	4.5715	-0.2629	0.2038	H	4.5491	-1.4448	-0.2299	H	4.5083	-1.5210	-0.1970
S	6.3327	-0.1623	0.3681	S	6.3330	-0.1672	0.3691	S	5.9498	1.0861	-0.1801	S	5.9824	0.9185	-0.5145
O	6.6590	1.0027	1.1455	O	6.6762	0.9873	1.1691	H	6.0840	0.4578	1.8933	O	6.1501	1.9129	-1.5522
O	6.8228	0.2068	-1.1416	O	6.8463	-1.4790	0.7083	O	6.2663	2.4171	-0.6803	O	6.4314	1.7012	0.8190
O	6.8382	-1.4817	0.6785	H	6.8515	-0.5524	-1.6874	O	6.3517	1.2961	1.4744	H	6.4744	1.0816	1.5770
H	7.0117	-0.6300	-1.6073	O	6.8528	0.2332	-1.1020	O	6.7560	-0.0653	-0.5853	O	6.6895	-0.3435	-0.5935

Quinoline Yellow WS Q4I3

enol vac.				enol H_2O				keto vac.				keto H_2O			
$E = -58403.632\,eV$				$E = -58404.804\,eV$				$E = -58402.738\,eV$				$E = -58404.003\,eV$			
O	-7.9438	0.0608	-0.9265	O	-8.0053	0.1037	0.8594	H	-6.2786	2.3730	-1.1882	H	-6.8306	1.5782	-1.0381
H	-7.9025	0.8997	-1.4241	O	-7.8273	0.3990	-1.5154	O	-5.7369	2.7798	1.1856	O	-6.0735	2.1544	-1.2753
O	-7.8430	-0.6802	1.3854	H	-7.8181	-0.4972	1.6105	O	-5.3519	2.6691	-1.2731	O	-6.0227	2.6633	1.1731
O	-7.3063	1.7261	0.8034	O	-7.3008	-1.8500	-0.5262	S	-4.6827	2.6642	0.2038	S	-5.1765	2.4571	0.0178
S	-7.2483	0.3084	0.5261	S	-7.2437	-0.4038	-0.4634	H	-4.6002	0.8254	2.3582	H	-4.8883	0.7454	2.2913
H	-6.0157	-2.2487	0.2862	H	-6.0564	2.1948	-0.2792	C	-4.0447	0.3653	1.5470	O	-4.2748	3.4968	-0.4238
C	-5.5492	-0.1493	0.2261	C	-5.5565	0.0954	-0.2084	C	-3.9855	1.0196	0.3042	C	-4.2662	0.3321	1.5049
C	-5.2278	-1.5124	0.1678	C	-5.2601	1.4647	-0.1788	O	-3.5968	3.6030	0.1251	C	-4.2466	0.9478	0.2432
H	-4.8467	1.9058	0.1709	H	-4.8236	-1.9474	-0.1167	H	-3.4070	-1.3631	2.6818	H	-3.4877	0.9426	-1.7939
C	-4.5808	0.8557	0.1044	C	-4.5703	-0.8932	-0.0888	C	-3.3864	-0.8482	1.7263	C	-3.4855	0.4621	-0.8210
C	-3.9007	-1.9086	-0.0145	C	-3.9345	1.8852	-0.0312	C	-3.3214	0.4765	-0.7960	C	-3.4793	-0.7936	1.7410
H	-3.6297	-2.9593	-0.0513	H	-3.6913	2.9429	-0.0115	H	-3.2964	0.9815	-1.7560	H	-3.4768	-1.2735	2.7140
C	-3.2664	0.4436	-0.0660	C	-3.2621	-0.4541	0.0426	C	-2.6757	-1.3754	0.6471	C	-2.7032	-0.6618	-0.5688
C	-2.9320	-0.9165	-0.1187	C	-2.9489	0.9101	0.0673	C	-2.6654	-0.7360	-0.6004	C	-2.6865	-1.2685	0.6965
C	-2.0104	1.2737	-0.1634	C	-1.9922	-1.2581	0.1334	O	-1.8868	-1.4374	-2.7865	C	-1.7960	-1.3871	-1.4957
O	-1.9685	2.5025	-0.1598	O	-1.9466	-2.4947	0.1449	C	-1.8703	-1.5357	-1.5784	C	-1.7289	-2.4052	0.7044
C	-1.4458	-1.0383	-0.2336	C	-1.4599	1.0485	0.1651	C	-1.8252	-2.5976	0.6061	O	-1.7218	-1.2416	-2.7037
C	-0.9105	0.3079	-0.2411	C	-0.9068	-0.2880	0.1853	O	-1.7123	-3.4441	1.4701	O	-1.5388	-3.1937	1.6141
O	-0.8058	-2.1085	-0.2848	O	-0.8392	2.1322	0.2011	C	-1.0729	-2.5672	-0.7499	H	-0.9953	-3.3955	-1.0995
H	0.3686	2.7326	-0.1761	H	0.3852	-2.7131	0.1525	H	-1.0451	-3.5576	-1.2110	C	-0.9910	-2.3960	-0.6555
C	0.4651	0.5800	-0.2185	C	0.4796	-0.5582	0.1690	C	0.3328	-2.0336	-0.5158	C	0.4343	-1.9015	-0.4669
H	0.8284	-1.4093	-0.2616	H	0.8673	1.4308	0.1895	N	0.4835	-0.7288	-0.6752	N	0.6000	-0.5876	-0.5253
C	1.0467	1.8873	-0.1541	C	1.0565	-1.8645	0.1254	H	1.0133	1.7895	-0.9870	H	1.1751	1.9472	-0.6354
N	1.3189	-0.4915	-0.2206	N	1.3318	0.5071	0.1602	H	1.1932	-3.9596	0.0165	H	1.2845	-3.8825	-0.1816
C	2.3984	2.0298	-0.0464	C	2.4103	-2.0168	0.0332	C	1.3840	-2.8992	-0.1148	C	1.4884	-2.8174	-0.2185
C	2.6799	-0.4006	-0.0967	C	2.6945	0.4118	0.0600	C	1.7153	-0.1825	-0.4725	C	1.8574	-0.0847	-0.3606
H	2.8403	3.0209	0.0161	H	2.8479	-3.0100	-0.0122	C	1.8799	1.2117	-0.6810	C	2.0423	1.3201	-0.4525
H	3.0140	-2.5379	-0.1149	H	3.0323	2.5502	0.0786	C	2.6299	-2.3640	0.1076	C	2.7602	-2.3278	-0.0387
C	3.2667	0.8912	0.0046	C	3.2769	-0.8823	-0.0186	C	2.8388	-0.9734	-0.0729	C	2.9853	-0.9300	-0.1140
C	3.4790	-1.5589	-0.0442	C	3.4942	1.5700	0.0154	C	3.1102	1.8002	-0.5156	C	3.2962	1.8676	-0.3274
C	4.6589	0.9889	0.1747	C	4.6723	-0.9892	-0.1632	H	3.2489	2.8614	-0.6944	H	3.4415	2.9397	-0.4119
C	4.8452	-1.4387	0.1255	C	4.8615	1.4450	-0.1289	H	3.4601	-2.9952	0.4155	H	3.5950	-2.9975	0.1494
H	5.1250	1.9639	0.2805	H	5.1279	-1.9710	-0.2413	C	4.0953	-0.3455	0.1139	C	4.2701	-0.3499	0.0267
C	5.4288	-0.1621	0.2362	C	5.4403	0.1620	-0.2245	C	4.2143	1.0085	-0.1096	C	4.4060	1.0169	-0.0886
H	5.4721	-2.3209	0.2005	H	5.4873	2.3288	-0.1829	H	4.9615	-0.9265	0.4177	H	5.1329	-0.9826	0.2106
S	7.1810	-0.0207	0.5041	S	7.1922	0.0119	-0.4509	O	5.5451	2.8599	1.2487	O	5.9224	2.7114	1.2955
O	7.4373	1.2134	1.1960	O	7.4815	-1.2475	-1.0986	H	5.7125	2.4152	2.1016	H	5.9537	2.1830	2.1204
O	7.6812	-1.2995	0.9596	O	7.7043	1.2564	-0.9884	S	5.8098	1.7801	0.0590	S	6.0209	1.7425	0.0142
O	7.7559	0.2174	-1.0009	O	7.7703	-0.1877	1.0390	O	6.0594	2.5867	-1.1051	O	6.2026	2.6635	-1.0871
H	8.0425	-0.6479	-1.3502	H	7.8296	0.6764	1.4967	O	6.7545	0.7999	0.5473	O	7.0012	0.7063	0.2668

Quinoline Yellow WS Q6I3

enol vac.				enol H_2O				keto vac.				keto H_2O			
$E = -58403.363$ eV				$E = -58404.554$ eV				$E = -58402.937$ eV				$E = -58404.491$ eV			
O	-7.4200	-0.9465	1.1766	O	-7.5114	-0.3947	-0.9358	O	-6.5387	0.4161	-1.2702	O	-7.3093	0.7268	-0.1133
O	-7.4034	-0.1606	-1.1222	H	-7.3626	0.2202	-1.6842	O	-6.4984	1.1959	1.1355	O	-6.6966	-1.5497	-0.9877
H	-7.3828	0.6894	-1.6017	O	-7.3606	-0.6718	1.4432	S	-5.8582	0.9948	-0.1444	S	-6.4039	-0.1444	-0.8301
O	-7.0318	1.5069	0.6824	O	-7.0262	1.6169	0.4614	O	-5.3054	2.4196	-0.6789	H	-6.2512	1.3644	-2.3544
S	-6.8399	0.1049	0.3842	S	-6.8315	0.1825	0.4028	H	-5.1464	3.0001	0.0907	O	-6.2222	0.3849	-2.3326
H	-5.3888	-2.3422	0.2330	H	-5.4122	-2.2930	0.2167	H	-5.0164	-0.6021	2.0477	H	-5.3746	1.5910	1.2107
C	-5.0938	-0.2108	0.2017	C	-5.1000	-0.1565	0.1881	C	-4.3413	0.0788	0.1226	C	-4.7653	0.0188	-0.1318
C	-4.6588	-1.5429	0.1603	C	-4.6818	-1.4933	0.1506	C	-4.2215	-0.6616	1.3109	C	-4.5542	0.9613	0.8862
H	-4.5629	1.8955	0.1874	H	-4.5531	1.9451	0.1385	H	-3.4514	0.6545	-1.7750	H	-3.9369	-1.5521	-1.3848
C	-4.2072	0.8717	0.1347	C	-4.2041	0.9187	0.1076	C	-3.3547	0.0732	-0.8637	C	-3.7562	-0.8250	-0.5999
C	-3.2959	-1.8268	0.0480	C	-3.3205	-1.7912	0.0381	C	-3.0973	-1.4536	1.5304	C	-3.2980	1.0739	1.4807
H	-2.9350	-2.8504	0.0226	H	-2.9815	-2.8221	0.0118	H	-2.9894	-2.0398	2.4372	H	-3.1224	1.7921	2.2749
C	-2.8563	0.5708	0.0286	C	-2.8584	0.6009	0.0080	C	-2.2264	-0.7081	-0.6219	C	-2.5078	-0.7013	0.0046
C	-2.4101	-0.7568	-0.0094	C	-2.4250	-0.7300	-0.0202	C	-2.1058	-1.4690	0.5492	C	-2.2849	0.2281	1.0330
O	-1.7347	2.7317	-0.0268	O	-1.7244	2.7510	-0.0533	C	-1.0218	-0.8751	-1.4813	C	-1.2720	-1.4702	-0.2821
C	-1.6708	1.5029	-0.0286	C	-1.6615	1.5150	-0.0507	C	-0.8319	-2.2352	0.5437	O	-1.0631	-2.2260	-1.2080
C	-0.9161	-0.7555	-0.0739	C	-0.9296	-0.7338	-0.0811	O	-0.8069	-0.3224	-2.5410	C	-0.8809	0.1407	1.5038
C	-0.4938	0.6322	-0.0758	C	-0.4950	0.6438	-0.0891	O	-0.4340	-2.9930	1.4039	H	-0.4628	-1.9333	1.6073
O	-0.1879	-1.7628	-0.1063	O	-0.2113	-1.7560	-0.1051	C	-0.0976	-1.9021	-0.7903	O	-0.3007	0.9139	2.2435
H	0.5539	3.1499	-0.0773	H	0.5948	3.1664	-0.0979	H	-0.0921	-2.8180	-1.3965	C	-0.2778	-1.1332	0.8730
C	0.8531	1.0174	-0.0722	C	0.8652	1.0279	-0.0823	H	0.7510	1.3830	-0.9767	C	1.1780	-1.1551	0.5440
C	1.3100	2.3734	-0.0648	C	1.3324	2.3745	-0.0782	O	0.8689	2.3787	-1.0763	H	1.3039	0.9034	0.1681
H	1.3846	-0.9331	-0.0785	H	1.3848	-0.9221	-0.0766	O	0.9108	2.5163	1.4088	H	1.4049	-3.2779	0.7923
N	1.8016	0.0246	-0.0617	N	1.8003	0.0307	-0.0624	C	1.3237	-1.4555	-0.5514	O	1.4194	2.5329	-0.4064
C	2.6448	2.6406	-0.0392	C	2.6728	2.6320	-0.0472	N	1.5419	-0.1596	-0.3690	N	1.8019	-0.0124	0.2320
O	2.8631	-2.7819	-1.1757	O	2.8187	-2.7882	-1.1564	S	1.6878	2.8079	0.2237	C	1.9091	-2.3545	0.5333
O	2.8676	-2.7163	1.3444	O	2.8302	-2.7342	1.3455	H	2.1145	-3.4742	-0.6060	S	2.8492	2.8951	-0.2035
H	2.9974	3.6689	-0.0345	H	3.0333	3.6566	-0.0445	O	2.1932	4.1363	-0.0136	O	3.1303	3.3565	1.1630
C	3.1537	0.2471	-0.0115	C	3.1556	0.2374	-0.0113	C	2.3522	-2.4259	-0.4570	C	3.1367	0.0766	-0.0817
S	3.5172	-2.4921	0.0817	S	3.5066	-2.5053	0.0879	C	2.8059	0.2614	-0.0604	C	3.2446	-2.3396	0.1919
C	3.6198	1.5920	-0.0057	C	3.6337	1.5766	-0.0077	C	3.0497	1.6453	0.1746	O	3.3803	3.7658	-1.2568
C	4.1030	-0.8060	0.0455	C	4.0935	-0.8254	0.0510	C	3.6342	-2.0187	-0.1822	C	3.7409	1.3286	-0.3567
O	4.9010	-3.3368	0.1186	O	4.8447	-3.3727	0.1683	C	3.9078	-0.6457	0.0274	H	3.8116	-3.2663	0.1682
C	5.0039	1.8463	0.0440	C	5.0223	1.8200	0.0435	C	4.3230	2.1006	0.4412	C	3.9013	-1.1259	-0.1194
H	5.0474	-3.6842	-0.7824	H	5.1697	-3.5816	-0.7326	H	4.4452	-2.7400	-0.1181	C	5.0848	1.3489	-0.6847
H	5.3420	2.8791	0.0457	H	5.3687	2.8492	0.0437	H	4.4800	3.1635	0.5966	C	5.2756	-1.0549	-0.4544
C	5.4607	-0.5189	0.1044	C	5.4537	-0.5527	0.1073	C	5.2040	-0.1497	0.3166	H	5.5578	2.3008	-0.9047
C	5.9153	0.8077	0.0972	C	5.9205	0.7718	0.0979	C	5.4079	1.1976	0.5109	C	5.8514	0.1639	-0.7369
H	6.1692	-1.3364	0.1664	H	6.1610	-1.3713	0.1650	H	6.0319	-0.8515	0.3770	H	5.8560	-1.9724	-0.4826
H	6.9806	1.0084	0.1408	H	6.9880	0.9589	0.1396	H	6.4021	1.5769	0.7250	H	6.9031	0.2258	-0.9977

Quinoline Yellow WS Q4Q6

enol vac.				enol H_2O				keto vac.				keto H_2O			
$E = -58403.329$ eV				$E = -58404.472$ eV				$E = -58402.694$ eV				$E = -58403.925$ eV			
H	-7.7440	0.4539	0.1801	H	-7.7464	0.4737	0.1187	H	-5.1716	2.1680	-1.7622	H	-5.4965	2.0045	-1.7429
H	-7.1174	-1.9291	0.2234	H	-7.1263	-1.9118	0.2005	H	-5.1468	2.6742	0.6507	H	-5.4881	2.5170	0.6693
C	-6.6942	0.1791	0.1201	C	-6.6971	0.1943	0.0808	C	-4.6823	1.4774	-1.0809	C	-4.9335	1.3666	-1.0678
C	-6.3385	-1.1759	0.1443	C	-6.3454	-1.1605	0.1265	C	-4.6675	1.7658	0.2950	C	-4.9277	1.6592	0.3082
H	-5.9868	2.2323	0.0095	H	-5.9900	2.2434	-0.0408	H	-4.0724	0.1006	-2.6418	H	-4.2301	0.0482	-2.6355
C	-5.7200	1.1794	0.0242	C	-5.7165	1.1924	-0.0094	C	-4.0723	0.3297	-1.5805	C	-4.2279	0.2763	-1.5741
C	-4.9983	-1.5693	0.0694	C	-5.0026	-1.5578	0.0788	C	-4.0422	0.9140	1.2022	C	-4.2134	0.8710	1.2092
H	-4.7122	-2.6170	0.0888	H	-4.7285	-2.6084	0.1150	H	-4.0179	1.1321	2.2653	H	-4.2065	1.0971	2.2710
C	-4.3896	0.7863	-0.0461	C	-4.3863	0.7949	-0.0517	C	-3.4332	-0.5160	-0.6724	C	-3.5050	-0.5072	-0.6720
C	-4.0348	-0.5717	-0.0267	C	-4.0354	-0.5637	-0.0117	C	-3.4181	-0.2280	0.6994	C	-3.4958	-0.2131	0.7006
C	-3.1489	1.6313	-0.1281	C	-3.1385	1.6274	-0.1247	C	-2.7031	-1.7755	-0.9488	C	-2.6765	-1.6999	-0.9476
O	-3.1204	2.8614	-0.1610	O	-3.1115	2.8639	-0.1761	C	-2.6748	-1.2750	1.4417	C	-2.6502	-1.1848	1.4270
C	-2.5504	-0.6796	-0.1051	C	-2.5504	-0.6692	-0.0683	O	-2.6304	-2.3758	-2.0024	O	-2.5245	-2.2593	-2.0221
C	-2.0285	0.6797	-0.1499	C	-2.0217	0.6821	-0.1185	O	-2.5935	-1.4104	2.6457	O	-2.4830	-1.2537	2.6349
O	-1.8842	-1.7293	-0.1170	O	-1.8896	-1.7299	-0.0653	H	-2.2361	-3.2648	0.6011	H	-2.2341	-3.1707	0.6061
H	-0.8285	3.1195	-0.1396	H	-0.7813	3.1291	-0.0995	C	-2.0259	-2.2132	0.3866	C	-2.0022	-2.1243	0.3839
C	-0.6670	0.9717	-0.1463	C	-0.6499	0.9755	-0.1073	O	-0.5878	2.1509	-1.0014	C	-0.5085	-1.9138	0.2932
H	-0.2624	-1.0119	-0.1684	H	-0.2530	-1.0061	-0.1199	C	-0.5415	-1.9713	0.2879	O	-0.4612	2.2355	-1.0269
C	-0.1223	2.2971	-0.1116	C	-0.0946	2.2923	-0.0718	O	-0.3023	2.1595	1.5123	O	-0.2190	2.1934	1.4768
N	0.2205	-0.0851	-0.1479	N	0.2266	-0.0830	-0.1038	N	-0.1680	-0.6985	0.2472	N	-0.1181	-0.6451	0.2373
O	1.0691	-3.0434	0.9942	O	1.0434	-3.0567	0.9988	H	0.0243	-4.0697	0.2406	H	0.0146	-4.0226	0.2842
O	1.1875	-2.8171	-1.5141	O	1.1257	-2.8081	-1.4917	S	0.2397	2.1921	0.1723	S	0.3684	2.2417	0.1550
C	1.2213	2.4786	-0.0218	C	1.2530	2.4653	0.0184	C	0.3821	-3.0461	0.1957	C	0.3913	-3.0069	0.2250
C	1.5771	0.0496	-0.0655	C	1.5852	0.0372	-0.0295	O	1.1094	3.5646	0.0515	C	1.2010	-0.3827	0.0879
H	1.6415	3.4796	0.0235	H	1.6791	3.4627	0.0650	C	1.1430	-0.4082	0.0904	O	1.2316	3.5929	0.0307
S	1.7907	-2.7125	-0.2136	S	1.7772	-2.7247	-0.2047	H	1.2105	3.9166	0.9564	H	1.5422	3.8711	0.9173
C	2.1243	1.3636	0.0246	C	2.1435	1.3443	0.0595	C	1.5371	0.9625	0.0171	C	1.6260	0.9779	0.0059
C	2.4618	-1.0632	-0.0518	C	2.4568	-1.0846	-0.0336	C	1.7178	-2.7671	0.0398	C	1.7349	-2.7542	0.0748
O	3.1318	-3.6203	-0.2522	O	3.0717	-3.6488	-0.3178	C	2.1488	-1.4180	-0.0286	C	2.1864	-1.4132	-0.0105
H	3.2214	-4.0453	0.6229	H	3.3209	-3.9986	0.5636	H	2.4504	-3.5661	-0.0416	H	2.4543	-3.5655	0.0125
C	3.5080	1.5329	0.1729	C	3.5313	1.5009	0.1948	C	2.8491	1.3138	-0.1978	C	2.9453	1.3030	-0.2050
C	3.8279	-0.8706	0.0904	C	3.8259	-0.9104	0.0916	H	3.1392	2.3530	-0.2965	H	3.2575	2.3365	-0.2956
H	3.9200	2.5320	0.2738	H	3.9444	2.5002	0.2850	C	3.4992	-1.0420	-0.2244	C	3.5457	-1.0687	-0.2045
C	4.3429	0.4263	0.2154	C	4.3513	0.3828	0.2221	C	3.8258	0.2937	-0.3101	C	3.8973	0.2591	-0.3127
H	4.4985	-1.7209	0.1180	H	4.4898	-1.7661	0.0944	H	4.2715	-1.7990	-0.3276	H	4.2953	-1.8497	-0.2850
S	6.0856	0.6494	0.4811	S	6.1006	0.5849	0.4509	S	5.5139	0.7640	-0.6285	S	5.5892	0.6929	-0.6413
O	6.2756	1.8697	1.2173	O	6.3292	1.6820	1.3625	O	5.5145	1.8495	-1.5708	O	5.6175	1.7195	-1.6588
O	6.6473	0.9732	-1.0112	O	6.6184	1.1516	-0.9602	O	5.9582	1.4473	0.7815	O	6.0511	1.4669	0.6892
O	6.6476	-0.6183	0.8926	O	6.6896	-0.7159	0.6904	O	6.3010	-0.4359	-0.8058	H	6.2873	0.8255	1.3920
H	6.9477	0.1335	-1.4086	H	6.7013	0.4234	-1.6109	H	6.3521	0.7513	1.3417	O	6.3648	-0.5202	-0.7895

Methyl Orange

trans vac. $E = -36221.967\,\text{eV}$				trans H_2O $E = -36222.710\,\text{eV}$				cis vac. $E = -36221.334\,\text{eV}$				cis H_2O $E = -36222.152\,\text{eV}$			
H	-7.6392	0.5303	1.5877	O	-7.6262	-0.2615	1.0544	H	-5.5618	-0.0477	-0.0416	H	-5.6334	1.5688	-0.6163
O	-7.6098	-0.2791	1.0433	O	-7.5305	-0.8513	-1.2689	H	-5.5386	1.6199	-0.6595	H	-5.6197	-0.0982	0.0065
O	-7.4812	-0.9096	-1.2956	H	-7.4886	0.4566	1.7063	C	-4.9756	0.6872	-0.6118	C	-5.0614	0.6429	-0.5792
O	-7.3298	1.5301	-0.6354	O	-7.3312	1.5668	-0.6139	H	-4.8487	0.3117	-1.6342	H	-4.9387	0.2645	-1.5999
S	-7.0147	0.1339	-0.4208	S	-7.0191	0.1702	-0.3792	H	-4.2929	2.9014	0.4226	H	-4.3888	2.8783	0.4021
H	-5.3269	-2.1850	-0.2686	H	-5.3544	-2.1747	-0.2614	H	-3.8894	-1.5512	-0.9659	H	-3.9593	-1.5853	-0.9133
C	-5.2622	-0.0306	-0.2035	C	-5.2729	-0.0127	-0.1999	N	-3.6822	0.9542	0.0071	N	-3.7582	0.9286	0.0260
H	-4.9382	2.0965	-0.1355	H	-4.9149	2.1148	-0.1079	C	-3.4740	2.2308	0.6847	C	-3.5456	2.2364	0.6535
C	-4.6945	-1.3082	-0.1743	C	-4.7184	-1.2990	-0.1822	H	-3.4509	2.1189	1.7780	H	-3.4784	2.1502	1.7454
C	-4.4683	1.1189	-0.0991	C	-4.4643	1.1280	-0.0972	C	-2.9546	-1.3239	-0.4655	C	-3.0131	-1.3370	-0.4461
C	-3.3180	-1.4295	-0.0430	C	-3.3421	-1.4360	-0.0732	C	-2.7431	-0.0441	0.1082	C	-2.8050	-0.0397	0.1034
C	-3.0919	0.9910	0.0209	C	-3.0884	0.9828	0.0030	H	-2.5340	2.6941	0.3626	H	-2.6263	2.6997	0.2791
H	-2.8409	-2.4045	-0.0241	H	-2.8859	-2.4213	-0.0640	H	-2.1601	-3.2906	-0.8014	H	-2.1989	-3.2872	-0.7868
C	-2.5042	-0.2873	0.0396	C	-2.5092	-0.3029	0.0043	C	-1.9839	-2.3059	-0.3781	C	-2.0239	-2.2965	-0.3760
H	-2.4523	1.8644	0.0854	H	-2.4496	1.8563	0.0712	C	-1.5276	0.1645	0.8112	C	-1.5643	0.2010	0.7653
N	-1.1149	-0.5379	0.1085	N	-1.1273	-0.5698	0.0634	H	-1.3529	1.0986	1.3323	H	-1.3956	1.1442	1.2715
N	-0.3954	0.5143	0.0872	N	-0.3885	0.4814	0.0400	C	-0.7398	-2.0580	0.2280	C	-0.7590	-2.0204	0.1891
H	0.9742	-1.8599	0.1910	C	0.9792	0.2663	0.0632	C	-0.5479	-0.8091	0.8524	C	-0.5693	-0.7523	0.7893
C	0.9831	0.2923	0.1060	H	1.0017	-1.8972	0.1479	N	0.1508	-3.1600	0.2545	N	0.1388	-3.0983	0.1915
H	1.3201	2.4083	0.0231	H	1.3121	2.3919	-0.0151	H	0.3598	-0.6073	1.4086	H	0.3472	-0.5274	1.3219
C	1.6013	-0.9755	0.1460	C	1.6128	-1.0013	0.1083	H	1.3663	-1.4487	-1.8156	H	1.3739	-1.3284	-1.7891
C	1.8005	1.4345	0.0509	C	1.7952	1.4190	0.0157	N	1.4040	-3.0442	0.3416	N	1.3991	-2.9875	0.3246
C	2.9745	-1.0908	0.1177	C	2.9838	-1.1058	0.0944	C	2.0327	-1.1049	-1.0309	C	2.0528	-1.0246	-0.9988
C	3.1797	1.3322	0.0212	C	3.1715	1.3296	0.0017	C	2.0986	-1.8107	0.1822	C	2.1099	-1.7629	0.1985
H	3.4202	-2.0790	0.1444	H	3.4392	-2.0889	0.1251	H	2.7483	0.6018	-2.1396	H	2.8100	0.6703	-2.0840
H	3.7761	2.2361	-0.0265	H	3.7627	2.2368	-0.0384	C	2.8031	0.0362	-1.2152	C	2.8582	0.0927	-1.1672
C	3.8079	0.0610	0.0448	C	3.8134	0.0579	0.0330	C	2.9963	-1.3985	1.1815	C	3.0260	-1.3989	1.2009
N	5.1746	-0.0607	-0.0060	N	5.1677	-0.0524	0.0016	H	3.0730	-1.9784	2.0964	H	3.0886	-1.9912	2.1086
H	5.4768	-1.9827	-0.8560	H	5.5013	-1.9729	-0.8363	C	3.6312	0.4826	-0.1810	C	3.7175	0.4827	-0.1323
H	5.5673	-1.9291	0.9221	H	5.5670	-1.9114	0.9437	C	3.7371	-0.2364	1.0160	C	3.8124	-0.2645	1.0489
H	5.7885	1.7033	-1.0125	H	5.7971	1.7168	-0.9835	O	4.1828	2.5777	-1.6578	O	4.1958	2.6964	-1.4567
C	5.8015	-1.3790	0.0013	C	5.8130	-1.3693	0.0234	H	4.3898	0.1194	1.8068	H	4.4870	0.0428	1.8415
H	5.8796	1.7861	0.7642	H	5.8412	1.7947	0.7963	O	4.4149	2.7609	0.8544	S	4.6802	1.9487	-0.3120
C	6.0143	1.1285	-0.1045	C	6.0086	1.1463	-0.0715	S	4.5112	2.0073	-0.3683	O	4.8268	2.5981	0.9732
H	6.8830	-1.2508	-0.0570	H	6.8914	-1.2226	-0.0215	O	6.0724	1.5377	-0.4184	O	6.1765	1.4293	-0.6272
H	7.0592	0.8179	-0.1431	H	7.0526	0.8352	-0.0831	H	6.2862	1.3148	-1.3443	H	6.2384	1.1247	-1.5558

Metanil Yellow

trans vac. $E = -40372.155\,\text{eV}$				trans H_2O $E = -40372.931\,\text{eV}$				cis vac. $E = -40371.559\,\text{eV}$				cis H_2O $E = -40372.428\,\text{eV}$			
O	-7.7043	0.3012	1.9897	O	-7.5076	1.7931	0.4376	H	-7.7751	0.9447	-0.5330	H	-7.8258	0.9476	-0.5363
O	-7.3868	1.8753	0.1688	O	-7.4277	0.3038	2.3171	H	-6.7618	-1.2669	-0.0108	H	-6.8090	-1.2717	-0.0446
H	-7.3293	-1.4376	0.0361	H	-7.3521	-1.3425	0.0661	C	-6.7198	0.8695	-0.2887	C	-6.7697	0.8701	-0.2949
H	-6.8104	2.6291	-0.0598	H	-7.0109	2.4598	-0.0809	H	-6.3519	2.9885	-0.4611	H	-6.4031	2.9939	-0.4359
S	-6.6399	1.0192	1.3393	S	-6.5194	1.0378	1.4622	C	-6.1479	-0.3707	-0.0034	C	-6.1963	-0.3748	-0.0267
C	-6.2687	-1.2746	-0.1221	C	-6.2910	-1.2006	-0.1088	C	-5.9219	2.0141	-0.2465	C	-5.9717	2.0165	-0.2381
H	-5.9496	-3.0923	-1.2241	H	-6.0614	-2.9831	-1.2875	C	-4.7964	-0.4784	0.3175	C	-4.8421	-0.4864	0.2880
O	-5.7641	1.9250	2.0499	C	-5.6172	-0.0988	0.4359	C	-4.5674	1.9177	0.0564	C	-4.6160	1.9175	0.0624
C	-5.6510	-0.1332	0.4046	O	-5.5982	2.0010	2.0323	H	-4.3761	-1.4420	0.5846	H	-4.4263	-1.4557	0.5397
C	-5.4887	-2.1981	-0.8149	C	-5.5599	-2.1209	-0.8586	C	-3.9895	0.6695	0.3382	C	-4.0365	0.6632	0.3205
C	-4.2906	0.1067	0.2510	C	-4.2565	0.1090	0.2432	H	-3.9449	2.8093	0.0697	H	-3.9935	2.8079	0.0970
C	-4.1187	-1.9907	-0.9607	C	-4.1877	-1.9521	-1.0393	H	-2.7887	-1.5113	-0.9993	H	-2.8432	-1.6057	-0.9203
H	-3.8203	0.9818	0.6854	H	-3.7496	0.9569	0.6889	N	-2.6295	0.6282	0.6973	N	-2.6731	0.6306	0.6686
C	-3.5136	-0.8367	-0.4437	H	-3.6087	-2.6816	-1.5988	H	-2.2733	1.4765	1.1208	H	-2.3232	1.4859	1.0880
H	-3.4918	-2.7140	-1.4744	C	-3.5290	-0.8339	-0.5048	C	-1.8536	-1.4060	-0.4613	C	-1.8975	-1.4444	-0.4174
N	-2.1111	-0.7382	-0.5971	N	-2.1288	-0.7655	-0.6781	C	-1.6713	-0.3405	0.4431	C	-1.7126	-0.3253	0.4253
N	-1.6513	0.4379	-0.4477	N	-1.6456	0.4110	-0.5561	H	-0.9631	-3.1357	-1.3752	H	-0.9997	-3.1919	-1.2737
H	-0.4099	2.6791	-0.4875	H	-0.4037	2.6540	-0.6674	C	-0.8249	-2.3079	-0.6859	C	-0.8552	-2.3314	-0.6268
C	-0.2527	0.5385	-0.4907	C	-0.2540	0.5068	-0.5750	C	-0.4331	-0.2367	1.1178	C	-0.4515	-0.1570	1.0541
H	0.2207	-1.5617	-0.5238	H	0.2360	-1.5981	-0.5077	H	-0.2982	0.5482	1.8588	H	-0.3160	0.6712	1.7450
C	0.2787	1.8394	-0.4931	C	0.2804	1.8116	-0.6151	C	0.4331	-2.1542	-0.0795	C	0.4198	-2.1222	-0.0643
C	0.6330	-0.5583	-0.5014	C	0.6359	-0.5894	-0.5162	C	0.6024	-1.1110	0.8540	C	0.5925	-1.0220	0.8084
C	1.6476	2.0445	-0.4914	C	1.6453	2.0201	-0.5810	N	1.3889	-3.1546	-0.4000	N	1.3766	-3.1118	-0.3679
C	2.0002	-0.3608	-0.4832	C	2.0003	-0.3889	-0.4567	H	1.5328	-1.0046	1.3985	H	1.5301	-0.8689	1.3283
H	2.0481	3.0560	-0.4835	H	2.0481	3.0294	-0.6099	H	2.2567	-0.8342	-1.9802	H	2.3163	-0.8380	-1.9787
C	2.5356	0.9486	-0.4639	C	2.5359	0.9250	-0.4705	N	2.6339	-2.9619	-0.3752	N	2.6312	-2.9329	-0.3200
H	2.6706	-1.2132	-0.5100	H	2.6653	-1.2444	-0.4220	C	2.9894	-0.6668	-1.1967	C	3.0346	-0.6658	-1.1832
H	3.8177	-0.7495	1.4279	H	3.8217	-0.8314	1.4147	C	3.2358	-1.6748	-0.2489	C	3.2490	-1.6538	-0.2052
N	3.9008	1.1941	-0.4630	N	3.8873	1.1862	-0.4163	H	3.4594	1.3420	-1.8214	H	3.5580	1.3050	-1.8658
H	4.1734	2.1269	-0.7476	H	4.1578	2.1235	-0.6956	C	3.6633	0.5446	-1.1139	C	3.7316	0.5333	-1.1235
C	4.7884	-0.6058	0.9665	C	4.7909	-0.6490	0.9645	C	4.2181	-1.4834	0.7361	C	4.2185	-1.4571	0.7919
C	4.9561	0.3710	-0.0275	C	4.9492	0.3645	0.0051	H	4.4320	-2.2868	1.4345	H	4.4042	-2.2395	1.5212
H	5.7348	-2.1099	2.1634	H	5.7580	-2.1738	2.1198	C	4.5799	0.7538	-0.0781	C	4.6387	0.7476	-0.0785
C	5.8792	-1.3623	1.3883	C	5.8947	-1.3969	1.3726	O	4.6531	3.2922	-0.7363	O	4.7698	3.2756	-0.7763
C	6.2347	0.5828	-0.5686	C	6.2294	0.6277	-0.5122	C	4.8686	-0.2608	0.8417	C	4.8966	-0.2476	0.8725
H	6.3697	1.3356	-1.3420	H	6.3538	1.4177	-1.2485	S	5.3478	2.3401	0.1049	S	5.4500	2.3091	0.0641
C	7.1485	-1.1532	0.8477	C	7.1653	-1.1420	0.8514	H	5.5866	-0.0814	1.6356	H	5.6102	-0.0728	1.6711
C	7.3193	-0.1689	-0.1272	C	7.3255	-0.1183	-0.0868	O	5.5928	2.5776	1.5032	O	5.6957	2.6003	1.4604
H	7.9945	-1.7435	1.1869	H	8.0205	-1.7261	1.1790	H	6.7796	2.3308	-1.4845	H	6.9054	2.0371	-1.5035
H	8.3010	0.0095	-0.5566	H	8.3080	0.0984	-0.4965	O	6.8340	2.1232	-0.5325	O	6.9333	2.0642	-0.5249

Bibliography

1. Ferri, V., Elbing, M., Pace, G., Dickey, M. D., Zharnikov, M., Samorì, P., Mayor, M. & Rampi, M. A. Light-Powered Electrical Switch Based on Cargo-Lifting Azobenzene Monolayers. *Angewandte Chemie International Edition* **47,** 3407–3409 (2008).
2. Diguet, A., Yanagisawa, M., Liu, Y.-J., Brun, E., Abadie, S., Rudiuk, S. & Baigl, D. UV-Induced Bursting of Cell-Sized Multicomponent Lipid Vesicles in a Photosensitive Surfactant Solution. *Journal of the American Chemical Society* **134,** 4898–4904 (2012).
3. Emmott, C. J. M., Röhr, J. A., Campoy-Quiles, M., Kirchartz, T., Urbina, A., Ekins-Daukes, N. J. & Nelson, J. Organic photovoltaic greenhouses: a unique application for semi-transparent PV? *Energy & Environmental Science* **8,** 1317–1328 (2015).
4. Schoenlein, R. W., Peteanu, L. A., Mathies, R. A. & Shank, C. V. The first step in vision: femtosecond isomerization of rhodopsin. *Science* **254,** 412–415 (1991).
5. Zewail, A. H. Laser Femtochemistry. *Science* **242,** 1645–1653 (1988).
6. Sundström, V. Femtobiology. *Annual Review of Physical Chemistry* **59,** 53–77 (2008).
7. Stolow, A., Bragg, A. E. & Neumark, D. M. Femtosecond Time-Resolved Photoelectron Spectroscopy. *Chemical Reviews* **104,** 1719–1758 (2004).
8. Ferray, M., L'Huillier, A., Li, X. F., Lompre, L. A., Mainfray, G. & Manus, C. Multiple-harmonic conversion of 1064 nm radiation in rare gases. *Journal of Physics B: Atomic, Molecular and Optical Physics* **21,** L31 (1988).
9. Birge, R. R. Photophysics of light transduction in rhodopsin and bacteriorhodopsin. *Annual review of biophysics and bioengineering* **10,** 315–354 (1981).
10. Faubel, M., Siefermann, K. R., Liu, Y. & Abel, B. Ultrafast Soft X-ray Photoelectron Spectroscopy at Liquid Water Microjets. *Accounts of Chemical Research* **45,** 120–130 (2012).
11. Faubel, M., Steiner, B. & Toennies, J. P. Photoelectron spectroscopy of liquid water, some alcohols, and pure nonane in free micro jets. *The Journal of Chemical Physics* **106,** 9013–9031 (1997).
12. Winter, B., Weber, R., Widdra, W., Dittmar, M., Faubel, M. & Hertel, I. V. Full Valence Band Photoemission from Liquid Water Using EUV Synchrotron Radiation. *The Journal of Physical Chemistry A* **108,** 2625–2632 (2004).

13. Nordlund, D., Odelius, M., Bluhm, H., Ogasawara, H., Pettersson, L. G. M. & Nilsson, A. Electronic structure effects in liquid water studied by photoelectron spectroscopy and density functional theory. *Chemical Physics Letters* **460,** 86–92 (2008).

14. Kurahashi, N., Karashima, S., Tang, Y., Horio, T., Abulimiti, B., Suzuki, Y.-I., Ogi, Y., Oura, M. & Suzuki, T. Photoelectron spectroscopy of aqueous solutions: Streaming potentials of NaX (X = Cl, Br, and I) solutions and electron binding energies of liquid water and X-. *The Journal of Chemical Physics* **140,** 174506 (2014).

15. Buchner, F., Nakayama, A., Yamazaki, S., Ritze, H.-H. & Lübcke, A. Excited-State Relaxation of Hydrated Thymine and Thymidine Measured by Liquid-Jet Photoelectron Spectroscopy: Experiment and Simulation. *Journal of the American Chemical Society* **137,** 2931–2938 (2015).

16. Tentscher, P. R., Seidel, R., Winter, B., Guerard, J. J. & Arey, J. S. Exploring the Aqueous Vertical Ionization of Organic Molecules by Molecular Simulation and Liquid Microjet Photoelectron Spectroscopy. *The Journal of Physical Chemistry B* **119,** 238–256 (2015).

17. Eckstein, M. *Investigation of Ultrafast Electronic and Nuclear Dynamics in Molecular Nitrogen using an XUV Time Delay Compensating Monochromator* Dissertation (Freie Universität Berlin, 2015).

18. Kruit, P. & Read, F. H. Magnetic field paralleliser for 2π electron-spectrometer and electron-image magnifier. *Journal of Physics E: Scientific Instruments* **16,** 313 (1983).

19. Arrell, C. A., Ojeda, J., Mewes, L., Grilj, J., Frassetto, F., Poletto, L., van Mourik, F. & Chergui, M. Laser-Assisted Photoelectric Effect from Liquids. *Physical Review Letters* **117,** 143001 (2016).

20. Han, G. R., Hwang, D., Lee, S., Lee, J. W., Lim, E., Heo, J. & Kim, S. K. Shedding new light on an old molecule: quinophthalone displays uncommon N-to-O excited state intramolecular proton transfer (ESIPT) between photobases. *Scientific Reports* **7.** (2017).

21. Bandara, H. M. D. & Burdette, S. C. Photoisomerization in different classes of azobenzene. *Chemical Society Reviews* **41,** 1809–1825 (2012).

22. Takei, M., Yui, H., Hirose, Y. & Sawada, T. Femtosecond Time-Resolved Spectroscopy of Photoisomerization of Methyl Orange in Cyclodextrins. *The Journal of Physical Chemistry A* **105,** 11395–11399 (2001).

23. Wang, L., Xu, J., Zhou, H., Yi, C. & Xu, W. Cis–trans isomerization mechanism of 4-aminoazobenzene in the S0 and S1 states: A CASSCF and DFT study. *Journal of Photochemistry and Photobiology A: Chemistry* **205,** 104–108 (2009).

24. Davies, M. J. & Truscott, R. J. W. Photo-oxidation of proteins and its role in cataractogenesis. *Journal of Photochemistry and Photobiology B: Biology* **63,** 114–125 (2001).
25. Léonard, J., Sharma, D., Szafarowicz, B., Torgasin, K. & Haacke, S. Formation dynamics and nature of tryptophan's primary photoproduct in aqueous solution. *Physical Chemistry Chemical Physics* **12,** 15744 (2010).
26. Nordling, C., Sokolowski, E. & Siegbahn, K. Precision method for obtaining absolute values of atomic binding energies. *Physical Review* **105,** 1676 (1957).
27. Carlson, T. A. Photoelectron spectroscopy. *Annual Review of Physical Chemistry* **26,** 211–234 (1975).
28. Demtröder, W. *Molekülphysik: Theoretische Grundlagen und experimentelle Methoden* 2., überarb. und erw. Aufl. (De Gruyter Oldenbourg, Berlin/Boston, 2013).
29. Lewars, E. G. . *Computational chemistry: introduction to the theory and applications of molecular and quantum mechanics* 3. edition (Springer, Cham, Switzerland, 2016).
30. Brundle, C. R. & Turner, D. W. High Resolution Molecular Photoelectron Spectroscopy. II. Water and Deuterium Oxide. *Proceedings of the Royal Society of London A: Mathematical, Physical and Engineering Sciences* **307,** 27–36 (1968).
31. Ågren, H. & Carravetta, V. Origin of phase transition shifts of ionization energies in water. *Molecular Physics* **55,** 901–922 (1985).
32. Lundholm, M., Siegbahn, H., Holmberg, S. & Arbman, M. Core electron spectroscopy of water solutions. *Journal of Electron Spectroscopy and Related Phenomena* **40,** 163–180 (1986).
33. Hohenberg, P. & Kohn, W. Inhomogeneous electron gas. *Physical review* **136,** B864 (1964).
34. Stowasser, R. & Hoffmann, R. What Do the Kohn-Sham Orbitals and Eigenvalues Mean? *Journal of the American Chemical Society* **121,** 3414–3420 (1999).
35. Barone, V. & Cossi, M. Quantum Calculation of Molecular Energies and Energy Gradients in Solution by a Conductor Solvent Model. *The Journal of Physical Chemistry A* **102,** 1995–2001 (1998).
36. Isegawa, M., Neese, F. & Pantazis, D. A. Ionization Energies and Aqueous Redox Potentials of Organic Molecules: Comparison of DFT, Correlated ab Initio Theory and Pair Natural Orbital Approaches. *Journal of Chemical Theory and Computation* **12,** 2272–2284 (2016).

37. Tao, J., Perdew, J. P., Staroverov, V. N. & Scuseria, G. E. Climbing the Density Functional Ladder: Nonempirical Meta-Generalized Gradient Approximation Designed for Molecules and Solids. *Physical Review Letters* **91,** 146401 (2003).

38. Weigend, F. & Ahlrichs, R. Balanced basis sets of split valence, triple zeta valence and quadruple zeta valence quality for H to Rn: Design and assessment of accuracy. *Physical Chemistry Chemical Physics* **7,** 3297–3305 (2005).

39. Zhao, Y. & Truhlar, D. G. The M06 suite of density functionals for main group thermochemistry, thermochemical kinetics, noncovalent interactions, excited states, and transition elements: two new functionals and systematic testing of four M06-class functionals and 12 other functionals. *Theoretical Chemistry Accounts* **120,** 215–241 (2008).

40. Neese, F. The ORCA program system. *Wiley Interdisciplinary Reviews: Computational Molecular Science* **2,** 73–78 (2012).

41. Banna, M. S., McQuaide, B. H., Malutzki, R. & Schmidt, V. The photoelectron spectrum of water in the 30 to 140 eV photon energy range. *The Journal of Chemical Physics* **84,** 4739–4744 (1986).

42. Pedersen, S. & Zewail, A. Femtosecond real-time probing of reactions XXII. Kinetic description of probe absorption, fluorescence, depletion and mass spectrometry. *Molecular Physics* **89,** 1455–1502 (1996).

43. Siegbahn, H. & Siegbahn, K. ESCA applied to liquids. *Journal of Electron Spectroscopy and Related Phenomena* **2,** 319–325 (1973).

44. Lübcke, A., Buchner, F., Heine, N., Hertel, I. V. & Schultz, T. Time-resolved photoelectron spectroscopy of solvated electrons in aqueous NaI solution. *Physical Chemistry Chemical Physics* **12,** 14629–14634 (2010).

45. Tang, Y., Shen, H., Sekiguchi, K., Kurahashi, N., Mizuno, T., Suzuki, Y.-I. & Suzuki, T. Direct measurement of vertical binding energy of a hydrated electron. *Physical Chemistry Chemical Physics* **12,** 3653–3655 (2010).

46. Siefermann, K. R., Liu, Y., Lugovoy, E., Link, O., Faubel, M., Buck, U., Winter, B. & Abel, B. Binding energies, lifetimes and implications of bulk and interface solvated electrons in water. *Nature Chemistry* **2,** 274–279 (2010).

47. Elkins, M. H., Williams, H. L., Shreve, A. T. & Neumark, D. M. Relaxation Mechanism of the Hydrated Electron. *Science* **342,** 1496–1499 (2013).

48. Ojeda, J., Arrell, C. A., Grilj, J., Frassetto, F., Mewes, L., Zhang, H., van Mourik, F., Poletto, L. & Chergui, M. Harmonium: A pulse preserving source of monochromatic extreme ultraviolet (30–110 eV) radiation for ultrafast photoelectron spectroscopy of liquids. *Structural Dynamics* **3,** 023602 (2016).

49. Al-Obaidi, R., Wilke, M., Borgwardt, M., Metje, J., Moguilevski, A., Engel, N., Tolksdorf, D., Raheem, A., Kampen, T., Mähl, S., Kiyan, I. Y. & Aziz, E. F. Ultrafast photoelectron spectroscopy of solutions: space-charge effect. *New Journal of Physics* **17,** 093016 (2015).

50. Link, O., Lugovoy, E., Siefermann, K., Liu, Y., Faubel, M. & Abel, B. Ultrafast electronic spectroscopy for chemical analysis near liquid water interfaces: concepts and applications. *Applied Physics A* **96,** 117–135 (2009).

51. Franken, P. A., Hill, A. E., Peters, C. W. & Weinreich, G. Generation of Optical Harmonics. *Physical Review Letters* **7,** 118–119 (1961).

52. Corkum, P. B. Plasma perspective on strong field multiphoton ionization. *Physical Review Letters* **71,** 1994–1997 (1993).

53. Kulander, K. C., Schafer, K. J. & Krause, J. L. *Dynamics of short-pulse excitation, ionization and harmonic conversion* in. Presented at the NATO Workshop, Han-Sur-Lesse, Belgium (1993).

54. Goulielmakis, E., Loh, Z.-H., Wirth, A., Santra, R., Rohringer, N., Yakovlev, V. S., Zherebtsov, S., Pfeifer, T., Azzeer, A. M., Kling, M. F., Leone, S. R. & Krausz, F. Real-time observation of valence electron motion. *Nature* **466,** 739–743 (2010).

55. Sansone, G., Benedetti, E., Calegari, F., Vozzi, C., Avaldi, L., Flammini, R., Poletto, L., Villoresi, P., Altucci, C., Velotta, R., Stagira, S., Silvestri, S. D. & Nisoli, M. Isolated Single-Cycle Attosecond Pulses. *Science* **314,** 443–446 (2006).

56. Poletto, L. & Villoresi, P. Time-delay compensated monochromator in the off-plane mount for extreme-ultraviolet ultrashort pulses. *Applied Optics* **45,** 8577 (2006).

57. Constant, E., Garzella, D., Breger, P., Mével, E., Dorrer, C., Le Blanc, C., Salin, F. & Agostini, P. Optimizing High Harmonic Generation in Absorbing Gases: Model and Experiment. *Physical Review Letters* **82,** 1668–1671 (1999).

58. Werner, W. X-ray efficiencies of blazed gratings in extreme off-plane mountings. *Applied Optics* **16,** 2078–2080 (1977).

59. Siffalovic, P., Drescher, M., Spieweck, M., Wiesenthal, T., Lim, Y. C., Weidner, R., Elizarov, A. & Heinzmann, U. Laser-based apparatus for extended ultraviolet femtosecond time-resolved photoemission spectroscopy. *Review of Scientific Instruments* **72,** 30–35 (2001).

60. Gaudin, J., Rehbein, S., Guttmann, P., Godé, S., Schneider, G., Wernet, P. & Eberhardt, W. Selection of a single femtosecond high-order harmonic using a zone plate based monochromator. *Journal of Applied Physics* **104,** 033112 (2008).

61. Metje, J., Borgwardt, M., Moguilevski, A., Kothe, A., Engel, N., Wilke, M., Al-Obaidi, R., Tolksdorf, D., Firsov, A., Brzhezinskaya, M., Erko, A., Kiyan, I. Y. & Aziz, E. F. Monochromatization of femtosecond XUV light pulses with the use of reflection zone plates. *Optics Express* **22,** 10747–10760 (2014).

62. Eckstein, M., Yang, C.-H., Kubin, M., Frassetto, F., Poletto, L., Ritze, H.-H., Vrakking, M. J. J. & Kornilov, O. Dynamics of N2 Dissociation upon Inner-Valence Ionization by Wavelength-Selected XUV Pulses. *The Journal of Physical Chemistry Letters* **6,** 419–425 (2015).

63. Microliquids GmbH. *Microjet System Manual* 2012.

64. Buchner, F., Lübcke, A., Heine, N. & Schultz, T. Time-resolved photoelectron spectroscopy of liquids. *Review of Scientific Instruments* **81,** 113107 (2010).

65. Link, O. *Femtosekunden-Photoelektronenspektroskopie mit extrem ultravioletter Strahlung an Flüssigkeitsgrenzflächen* Dissertation (Georg-August-Universität zu Göttingen, Göttingen, 2007).

66. Kothe, A., Metje, J., Wilke, M., Moguilevski, A., Engel, N., Al-Obaidi, R., Richter, C., Golnak, R., Kiyan, I. Y. & Aziz, E. F. Time-of-flight electron spectrometer for a broad range of kinetic energies. *Review of Scientific Instruments* **84,** 023106 (2013).

67. Baltzer, P., Larsson, M., Karlsson, L., Wannberg, B. & Carlsson Göthe, M. Inner-valence states of N2+ studied by uv photoelectron spectroscopy and configuration-interaction calculations. *Physical Review A* **46,** 5545–5553 (1992).

68. Clauberg, R. & Blacha, A. High electron density effects in electron spectroscopies: Consequences for picosecond photoemission and electron-beam sampling. *Journal of Applied Physics* **65,** 4095–4106 (1989).

69. Passlack, S., Mathias, S., Andreyev, O., Mittnacht, D., Aeschlimann, M. & Bauer, M. Space charge effects in photoemission with a low repetition, high intensity femtosecond laser source. *Journal of Applied Physics* **100,** 024912 (2006).

70. Ong, S., Zhao, X. & Eisenthal, K. B. Polarization of water molecules at a charged interface: second harmonic studies of the silica/water interface. *Chemical Physics Letters* **191,** 327–335 (1992).

71. Behrens, S. H. & Grier, D. G. The charge of glass and silica surfaces. *The Journal of Chemical Physics* **115,** 6716–6721 (2001).

72. Preissler, N., Buchner, F., Schultz, T. & Lübcke, A. Electrokinetic Charging and Evidence for Charge Evaporation in Liquid Microjets of Aqueous Salt Solution. *The Journal of Physical Chemistry B* **117,** 2422–2428 (2013).

73. Anderson, J. H. J. & Parks, G. A. Electrical conductivity of silica gel in the presence of adsorbed water. *The Journal of Physical Chemistry* **72,** 3662–3668 (1968).

74. Van der Heyden, F. H. J., Derek Stein & Dekker, C. Streaming Currents in a Single Nanofluidic Channel. *Physical Review Letters* **95.** (2005).

75. Faubel, M. & Steiner, B. Strong Bipolar Electrokinetic Charging of Thin Liquid Jets Emerging from 10 MUm PtIr Nozzles. *Berichte der Bunsengesellschaft für physikalische Chemie* **96,** 1167–1172 (1992).

76. Seah, M. P. & Dench, W. A. Quantitative electron spectroscopy of surfaces: a standard data base for electron inelastic mean free paths in solids. *Surface and interface analysis* **1,** 2–11 (1979).

77. Powell, C. J. & Jablonski, A. Evaluation of Calculated and Measured Electron Inelastic Mean Free Paths Near Solid Surfaces. *Journal of Physical and Chemical Reference Data* **28,** 19–62 (1999).

78. Ottosson, N., Faubel, M., Bradforth, S. E., Jungwirth, P. & Winter, B. Photoelectron spectroscopy of liquid water and aqueous solution: Electron effective attenuation lengths and emission-angle anisotropy. *Journal of Electron Spectroscopy and Related Phenomena. Water and Hydrogen Bonds* **177,** 60–70 (2010).

79. Thürmer, S., Seidel, R., Faubel, M., Eberhardt, W., Hemminger, J. C., Bradforth, S. E. & Winter, B. Photoelectron Angular Distributions from Liquid Water: Effects of Electron Scattering. *Physical Review Letters* **111.** (2013).

80. Suzuki, Y.-I., Nishizawa, K., Kurahashi, N. & Suzuki, T. Effective attenuation length of an electron in liquid water between 10 and 600 eV. *Physical Review E* **90.** (2014).

81. Olivieri, G., Parry, K. M., Powell, C. J., Tobias, D. J. & Brown, M. A. Quantitative interpretation of molecular dynamics simulations for X-ray photoelectron spectroscopy of aqueous solutions. *The Journal of Chemical Physics* **144,** 154704 (2016).

82. Watanabe, K. & Jursa, A. S. Absorption and Photoionization Cross Sections of H2O and H2S. *The Journal of Chemical Physics* **41,** 1650 (1964).

83. Haddad, G. N. & Samson, J. A. R. Total absorption and photoionization cross sections of water vapor between 100 and 1000 Å. *The Journal of Chemical Physics* **84,** 6623 (1986).

84. Hayashi, H., Watanabe, N., Udagawa, Y. & Kao, C.-C. The complete optical spectrum of liquid water measured by inelastic x-ray scattering. *Proceedings of the National Academy of Sciences* **97,** 6264–6266 (2000).

85. *Solvent Polarity Table - Miller's Home* https://sites.google.com/site/miller00828/in/solvent-polarity-table (2017).

86. *Viscosity, Surface Tension, Specific Density and Molecular Weight of Selected Liquids* https://www.accudynetest.com/visc_table.html (2017).

87. *NIST Chemistry WebBook* http://webbook.nist.gov/chemistry/ (2017).

88. Ohno, K., Imai, K. & Harada, Y. Variations in reactivity of lone-pair electrons due to intramolecular hydrogen bonding as observed by Penning ionization electron spectroscopy. *Journal of the American Chemical Society* **107,** 8078–8082 (1985).

89. Gochel-Dupuis, M., Delwiche, J., Hubin-Franskin, M. J. & Collin, J. E. High-resolution HeI photoelectron spectrum of acetonitrile. *Chemical Physics Letters* **193,** 41–48 (1992).

90. Schins, J. M., Breger, P., Agostini, P., Constantinescu, R. C., Muller, H. G., Grillon, G., Antonetti, A. & Mysyrowicz, A. Observation of Laser-Assisted Auger Decay in Argon. *Physical Review Letters* **73,** 2180–2183 (1994).

91. Glover, T. E., Schoenlein, R. W., Chin, A. H. & Shank, C. V. Observation of laser assisted photoelectric effect and femtosecond high order harmonic radiation. *Physical Review Letters* **76,** 2468 (1996).

92. Saathoff, G., Miaja-Avila, L., Aeschlimann, M., Murnane, M. M. & Kapteyn, H. C. Laser-assisted photoemission from surfaces. *Physical Review A* **77.** (2008).

93. Kroll, N. M. & Watson, K. M. Charged-particle scattering in the presence of a strong electromagnetic wave. *Physical Review A* **8,** 804 (1973).

94. Maquet, A. & TaÏeb, R. Two-colour IR + XUV spectroscopies: the "soft-photon approximation". *Journal of Modern Optics* **54,** 1847–1857 (2007).

95. Cooper, J. & Zare, R. N. Angular Distribution of Photoelectrons. *The Journal of Chemical Physics* **48,** 942–943 (1968).

96. Nishitani, J., West, C. W. & Suzuki, T. Angle-resolved photoemission spectroscopy of liquid water at 29.5eV. *Structural Dynamics* **4,** 044014 (2017).

97. Truscott, T. O., Land, E. J. & Sykes, A. The in vitro photochemistry of biological molecules-III. Absorption spectra, lifetimes and rates of oxygen quenching of the triplet states of BETA-carotene, retinal and related polyenes. *Photochemistry and Photobiology* **17,** 43–51 (1973).

98. Pope, R. M. & Fry, E. S. Absorption spectrum (380–700 nm) of pure water II Integrating cavity measurements. *Applied Optics* **36,** 8710 (1997).

99. Quickenden, T. I. & Irvin, J. A. The ultraviolet absorption spectrum of liquid water. *The Journal of Chemical Physics* **72,** 4416–4428 (1980).

100. Buchner, F., Ritze, H.-H., Lahl, J. & Lübcke, A. Time-resolved photoelectron spectroscopy of adenine and adenosine in aqueous solution. *Physical Chemistry Chemical Physics* **15,** 11402 (2013).

101. Engel, N., Bokarev, S. I., Moguilevski, A., Raheem, A. A., Al-Obaidi, R., Möhle, T., Grell, G., Siefermann, K. R., Abel, B., Aziz, S. G., Kühn, O., Borgwardt, M., Kiyan, I. Y. & Aziz, E. F. Light-induced relaxation dynamics of the ferricyanide ion revisited by ultrafast XUV photoelectron spectroscopy. *Physical Chemistry Chemical Physics* **19,** 14248–14255 (2017).

102. European Food Safety Authority. Refined exposure assessment for Quinoline Yellow (E 104). *EFSA Journal* **13,** n/a–n/a (2015).

103. Kutsuna, H., Komatsu, K., Matsuoka, M., Namba, R., Morikawa, Y. & Tanaka, M. Analyses and Purification of Quinoline Yellow WS. *Journal of Society of Cosmetic Chemists of Japan* **16,** 50–56 (1982).

104. *ChemicalBook Chemical Search Engine* `https://www.chemicalbook.com/` (2017).

105. Kehrer, F., Niklaus, P. & Manukian, B. K. IR.-spektroskopische Untersuchungen in der Chinophtalon-Reihe. *Helvetica Chimica Acta* **50,** 2200–2211 (1967).

106. Blakemore, W. M., Rushing, L. G., Thompson, H. C., Freeman, J. P., Levine, R. A. & Nony, C. R. Characterization, purification, and analysis of solvent yellow 33 and solvent green 3 dyes. *Journal of Chromatography A* **391,** 219–231 (1987).

107. Dobosz, R., Ośmiałowski, B. & Gawinecki, R. DFT studies on tautomeric preferences. Part 3: Proton transfer in 2-(8-acylquinolin-2-yl)-1,3-diones. *Structural Chemistry* **21,** 1037–1041 (2010).

108. Abbott, L. C., Batchelor, S. N., Oakes, J., Gilbert, B. C., Whitwood, A. C., Lindsay Smith, J. R. & Moore, J. N. Experimental and Computational Studies of Structure and Bonding in Parent and Reduced Forms of the Azo Dye Orange II. *The Journal of Physical Chemistry A* **109,** 2894–2905 (2005).

109. Hanwell, M. D., Curtis, D. E., Lonie, D. C., Vandermeersch, T., Zurek, E. & Hutchison, G. R. Avogadro: an advanced semantic chemical editor, visualization, and analysis platform. *Journal of Cheminformatics* **4,** 17 (2012).

110. With, G. d. *Liquid-state physical chemistry: fundamentals, modeling, and applications* (Wiley-VCH, Weinheim, 2013).

111. Glasbeek, M. & Zhang, H. Femtosecond Studies of Solvation and Intramolecular Configurational Dynamics of Fluorophores in Liquid Solution. *Chemical Reviews* **104,** 1929–1954 (2004).

112. Maroncelli, M. & Fleming, G. R. Computer simulation of the dynamics of aqueous solvation. *The Journal of Chemical Physics* **89,** 5044–5069 (1988).

113. Jimenez, R., Fleming, G. R., Kumar, P. V. & Maroncelli, M. Femtosecond solvation dynamics of water. *Nature* **369,** 471–473 (1994).

114. Kropman, M. F. & Bakker, H. J. Dynamics of Water Molecules in Aqueous Solvation Shells. *Science* **291,** 2118–2120 (2001).

115. Wait, S. C. & McNerney, J. C. Vibrational spectra and assignments for quinoline and isoquinoline. *Journal of Molecular Spectroscopy* **34,** 56–77 (1970).

116. Pathak, J., Narayan, V., Sinha, L. & Prasad, O. Theoretical Raman and FTIR vibrational analysis of 2-phenyl-1H-indene-1,3(2H)-dione by ab initio method. *Journal of Atomic and Molecular Sciences* **3,** 95–105 (2012).

117. Takeuchi, S. & Tahara, T. Coherent Nuclear Wavepacket Motions in Ultrafast Excited-State Intramolecular Proton Transfer: Sub-30-fs Resolved Pump-Probe Absorption Spectroscopy of 10-Hydroxybenzo-[h]quinoline in Solution. *The Journal of Physical Chemistry A* **109,** 10199–10207 (2005).

118. Yamazaki, S., Sobolewski, A. L. & Domcke, W. Molecular mechanisms of the photostability of indigo. *Physical Chemistry Chemical Physics* **13,** 1618–1628 (2011).

119. Driscoll, E. W., Hunt, J. R. & Dawlaty, J. M. Photobasicity in Quinolines: Origin and Tunability via the Substituents' Hammett Parameters. *The Journal of Physical Chemistry Letters* **7,** 2093–2099 (2016).

120. Mohammed, O. F., Pines, D., Dreyer, J., Pines, E. & Nibbering, E. T. J. Sequential Proton Transfer Through Water Bridges in Acid-Base Reactions. *Science* **310,** 83–86 (2005).

121. Yan, S., Zhang, L., Cukier, R. I. & Bu, Y. Exploration on Regulating Factors for Proton Transfer along Hydrogen-Bonded Water Chains. *ChemPhysChem* **8,** 944–954 (2007).

122. Park, S.-Y., Kim, B., Lee, Y.-S., Kwon, O.-H. & Jang, D.-J. Triple proton transfer of excited 7-hydroxyquinoline along a hydrogen-bonded water chain in ethers: secondary solvent effect on the reaction rate. *Photochemical & Photobiological Sciences* **8,** 1611 (2009).

123. Quick, M., Dobryakov, A. L., Gerecke, M., Richter, C., Berndt, F., Ioffe, I. N., Granovsky, A. A., Mahrwald, R., Ernsting, N. P. & Kovalenko, S. A. Photoisomerization Dynamics and Pathways of trans- and cis-Azobenzene in Solution from Broadband Femtosecond Spectroscopies and Calculations. *The Journal of Physical Chemistry B* **118,** 8756–8771 (2014).

124. Tan, E. M. M., Amirjalayer, S., Smolarek, S., Vdovin, A., Zerbetto, F. & Buma, W. J. Fast photodynamics of azobenzene probed by scanning excited-state potential energy surfaces using slow spectroscopy. *Nature Communications* **6,** 5860 (2015).

125. Mayer, S. G., Thomsen, C. L., Philpott, M. P. & Reid, P. J. The solvent-dependent isomerization dynamics of 4-(dimethylamino) azobenzene (DMAAB) studied by subpicosecond pump–probe spectroscopy. *Chemical physics letters* **314,** 246–254 (1999).

126. Bafana, A., Devi, S. S. & Chakrabarti, T. Azo dyes: past, present and the future. *Environmental Reviews* **19,** 350–371 (NA 2011).

127. Cattaneo, P. & Persico, M. An ab initio study of the photochemistry of azobenzene. *Physical Chemistry Chemical Physics* **1,** 4739–4743 (1999).

128. Andersson, J.-Å., Petterson, R. & Tegnér, L. Flash photolysis experiments in the vapour phase at elevated temperatures I: spectra of azobenzene and the kinetics of its thermal cis-trans isomerization. *Journal of Photochemistry* **20,** 17–32 (1982).

129. Rau, H. Photoisomerization of azobenzenes. *Photochemistry and photophysics* **2,** 119–141 (1990).

130. Harabuchi, Y., Ishii, M., Nakayama, A., Noro, T. & Taketsugu, T. A multireference perturbation study of the NN stretching frequency of trans-azobenzene in nπ^* excitation and an implication for the photoisomerization mechanism. *The Journal of Chemical Physics* **138,** 064305 (2013).

131. Schultz, T., Quenneville, J., Levine, B., Toniolo, A., Martínez, T. J., Lochbrunner, S., Schmitt, M., Shaffer, J. P., Zgierski, M. Z. & Stolow, A. Mechanism and Dynamics of Azobenzene Photoisomerization. *Journal of the American Chemical Society* **125,** 8098–8099 (2003).

132. Tiberio, G., Muccioli, L., Berardi, R. & Zannoni, C. How Does the Trans–Cis Photoisomerization of Azobenzene Take Place in Organic Solvents? *ChemPhysChem* **11,** 1018–1028 (2010).

133. Cilento, G., Miller, E. C. & Miller, J. A. On the Addition of Protons to Derivatives of 4-Aminoazobenzene. *Journal of the American Chemical Society* **78,** 1718–1722 (1956).

134. De Meyer, T., Hemelsoet, K., Van der Schueren, L., Pauwels, E., De Clerck, K. & Van Speybroeck, V. Investigating the Halochromic Properties of Azo Dyes in an Aqueous Environment by Using a Combined Experimental and Theoretical Approach. *Chemistry - A European Journal* **18,** 8120–8129 (2012).

135. Fan, J., Shen, X. & Wang, J. Dissociation constants of methyl orange in aqueous alcohol solvents. *Analytica chimica acta* **364,** 275–280 (1998).

136. Reeves, R. L., Kaiser, R. S., Maggio, M. S., Sylvestre, E. A. & Lawton, W. H. Analysis of the visual spectrum of methyl orange in solvents and in hydrophobic binding sites. *Canadian Journal of Chemistry* **51,** 628–635 (1973).

137. Brode, W. R., Seldin, I. L., Spoerri, P. E. & Wyman, G. M. The relation between the absorption spectra and the chemical constitution of dyes. XXVIII. The hydration of azo dyes in organic solvents. *Journal of the American Chemical Society* **77,** 2762–2765 (1955).

138. Alberghina, G., Bianchini, R., Fichera, M. & Fisichella, S. Dimerization of Cibacron Blue F3GA and other dyes: influence of salts and temperature. *Dyes and Pigments* **46,** 129–137 (2000).

139. Boily, J.-F. & Seward, T. M. On the Dissociation of Methyl Orange: Spectrophotometric Investigation in Aqueous Solutions from 10 to 90 DEG C and Theoretical Evidence for Intramolecular Dihydrogen Bonding. *Journal of Solution Chemistry* **34,** 1387–1406 (2005).

140. Kendrick, K. L. & Gilkerson, W. R. The state of aggregation of methyl orange in water. *Journal of Solution Chemistry* **16,** 257–267 (1987).

141. Yui, H., Takei, M., Hirose, Y. & Sawada, T. Ultrafast transient lens spectroscopy of photoisomerization dynamics of azocompounds in confined nanospace of cyclodextrins. *Review of Scientific Instruments* **74,** 907–909 (2003).

142. Saito, T. & Kobayashi, T. Conformational Change in Azobenzene in Photoisomerization Process Studied with Chirp-Controlled sub-10-fs Pulses. *The Journal of Physical Chemistry A* **106,** 9436–9441 (2002).

143. Yano, A., Konno, Y., Kinoshita, E. & Yano, R. Concentration dependence of thermal isomerization process of methyl orange in ethanol. *Journal of Photochemistry and Photobiology A: Chemistry* **346,** 411–415 (2017).

144. Albini, A., Fasani, E. & Pietra, S. The photochemistry of azo dyes. Photoisomerisation versus photoreduction from 4-diethylaminoazobenzene and 4-diethylamino-4-methoxyazobenzene. *Journal of the Chemical Society, Perkin Transactions 2,* 1021–1024 (1983).

145. Rau, H., Greiner, G., Gauglitz, G. & Meier, H. Photochemical quantum yields in the $A(h\nu) \rightleftarrows B(+h\nu, \Delta)$ system when only the spectrum of A is known. *Journal of physical chemistry* **94,** 6523–6524 (1990).

146. Fischer, E. & Frei, Y. Photoisomerization Equilibria in Azodyes. *The Journal of Chemical Physics* **27,** 328–330 (1957).

147. Wang, Y., Zhang, S., Sun, S., Liu, K. & Zhang, B. Ultrafast Excited State Dynamics of *trans*-4-Aminoazobenzene Studied by Femtosecond Transient Absorption Spectroscopy. *Chinese Journal of Chemical Physics* **26,** 651–655 (2013).

148. Katoh, R. Dependence of photoionization quantum yield of indole and tryptophan in water on excitation wavelength. *Journal of Photochemistry and Photobiology A: Chemistry* **189,** 211–217 (2007).

149. Seki, K. & Inokuchi, H. Photoelectron spectrum of l-tryptophan in the gas phase. *Chemical Physics Letters* **65,** 158–160 (1979).

150. Klasinc, L. Application of photoelectron spectroscopy to biologically active molecules and their constituent parts. *Journal of Electron Spectroscopy and Related Phenomena* **8,** 161–164 (1976).

151. Campbell, S., Beauchamp, J. L., Rempe, M. & Lichtenberger, D. L. Correlations of lone pair ionization energies with proton affinities of amino acids and related compounds. Site specificity of protonation. *International journal of mass spectrometry and ion processes* **117,** 83–99 (1992).

152. Cannington, P. H. & Ham, N. S. The photoelectron spectra of amino-acids: A survey. *Journal of Electron Spectroscopy and Related Phenomena* **15,** 79–82 (1979).

153. Dehareng, D. & Dive, G. Vertical Ionization Energies of a-L-Amino Acids as a Function of Their Conformation: an Ab Initio Study. *International Journal of Molecular Sciences* **5,** 301–332 (2004).

154. Close, D. M. Calculated Vertical Ionization Energies of the Common a-Amino Acids in the Gas Phase and in Solution. *The Journal of Physical Chemistry A* **115,** 2900–2912 (2011).

155. Xu, S., Nilles, J. M. & Bowen, K. H. Zwitterion formation in hydrated amino acid, dipole bound anions: How many water molecules are required? *The Journal of Chemical Physics* **119,** 10696–10701 (2003).

156. Cohn, E. J. & Edsall, J. T. *Proteins, Amino Acids And Peptides As Ions And Dipolar Ions* (Reinhold Publishing Corporation ; New York, 1943).

157. Grand, D., Bernas, A. & Amouyal, E. Photoionization of aqueous indole: Conduction band edge and energy gap in liquid water. *Chemical Physics* **44,** 73–79 (1979).

158. Amouyal, E., Bernas, A. & Grand, D. On the Photoionization Energy Threshold of Tryptophan in Aqueous Solutions. *Photochemistry and Photobiology* **29,** 1071–1077 (1979).

159. Bräm, O., Oskouei, A. A., Tortschanoff, A., van Mourik, F., Madrid, M., Echave, J., Cannizzo, A. & Chergui, M. Relaxation Dynamics of Tryptophan in Water: A UV Fluorescence Up-Conversion and Molecular Dynamics Study. *The Journal of Physical Chemistry A* **114,** 9034–9042 (2010).

160. *U.S. National Library of Medicine, TOXNET HSDB Database* `https://toxnet.nlm.nih.gov/newtoxnet/hsdb.htm` (2017).

Acknowledgments

First of all my I want to express my gratitude to my direct supervisor Oleg Kornilov. Without his resourcefulness and unwavering optimism this work would not have been possible. In many cases he was the direly needed opposing force to my skepticism. I also want to thank him for the fun we had outside the institute, for example on the basketball court or on one of his bike rallies through Berlin.
I am also deeply grateful to Marc J.J. Vrakking for giving me the opportunity to conduct the research for my PhD at the Max Born Institute. With his vast knowledge of, as I perceived it, everything ever published he kept this project on track (or as close to the track as possible).
Further I want to thank Karsten Heyne for co-refereeing this thesis.
Special thanks also to Martin Eckstein, who not only built the XUV monochromator setup but also taught me all the tricks necessary to keep it running. It is a great machine, which did not cause any major difficulties during my time at the Max Born Institute. At the monochromator setup I mainly worked with Geert Reitsma, whom I want to thank for sharing both the successful and the frustrating lab days with me. I also want to thank Judith Dura for the many hours she invested into rewiring the monochromator entrails with me.
Next I want to express my gratitude to all those involved in making the liquid jet setup work: Katrin Aziz-Lange, Reinhard Grosser, Nicola Mayer, Andrea Lübcke, Boris Peev, and Evgenii Ikonnikov. I wish Evgenii all the best for his PhD and hope the project continues successfully.
Many thanks to Roman Peslin, for his support with all kinds of technical issues. His creativity and precision were essential for implementing the new version of the liquid jet. I am also grateful to Katrin Herrmann and Regina Lendt, for their help with the sample preparation and with the absorption and fluorescence measurements.
I also want to express my gratitude to the extended kHz lab team consisting of Lorenz Drescher, Jochen Mikosch, Martin Galbreith, Felix Schell, Claus-Peter Schulz and Ahmed Akin Ünal. Especially Ahmed was invaluable for making the laser work reproducibly every single day.
I also want to generally thank my colleagues at the Max Born Institute for providing a good work atmosphere and for countless cakes at various opportunities. Special thanks go to my fellow PhD students Katrin Reininger, Lorenz Drescher, and Peter Jürgens for forming the "Festkomitee" and organizing the PhD Barbecue and other activities.
I also want to thank my family and friends for their moral support during the more stressful phases of the PhD. I am especially grateful to Rebecca for putting up with me during the most frustrating experimental campaigns.

List of Publications

Hummert J., Reitsma G., Mayer N., Ikonnikov E., Eckstein M., and Kornilov O. **Femtosecond XUV photoelectron spectroscopy of organic dye molecules in solution** *Nature Communications (submitted)*

Hummert J., Reitsma G., Mayer N., Ikonnikov E., Eckstein M., and Kornilov O. **Direct measurement of the ionization potential of aqueous tryptophan** *(In preparation)*

Hummert J., Reitsma G., Mayer N., Ikonnikov E., Eckstein M., and Kornilov O. **Isomerization of amino-azobenzen dyes investigated with liquid phase time-resolved photoelectron spectroscopy** *(In preparation)*

Short Summary

The ultrafast electronic relaxation dynamics of photoactive organic molecules is a fundamental research topic in physical chemistry. Understanding the role of transient states in the relaxation is essential to further the understanding of biological processes such as vision, but also for improving molecular switches. Molecular processes on femtosecond timescales are routinely studied in solution with all-optical techniques. However, time-resolved photoelectron spectroscopy meets with considerable challenges when it comes to the investigation of molecules in solution. This thesis deals with the implementation of liquid phase time-resolved XUV photoelectron spectroscopy and its application to investigate functional photoactive molecules in aqueous solution.
Part of the thesis is dedicated to the implementation of liquid phase photoelectron spectroscopy at an existing XUV monochromator setup, which provides wavelength selected XUV light. The two main challenges are the stable operation of a liquid jet in vacuum and the detection of the extremely weak solute photoelectron signals against a strong background originating from the solvent. To allow for stable operation over long measurement times, the initial commercial liquid jet setup is substantially modified to improve its stability and precision of alignment. The crucial step to detect the weak solute signals is the implementation of a new acquisition software, allowing for averaging and single-count detection simultaneously. The proof-of-principle experiment for the technique is carried out with an organic dye, Quinoline Yellow WS, in aqueous solution. The ground state photoelectron spectrum of the dye molecule is obtained and is in excellent agreement with DFT calculations performed for this thesis. In a UV-pump, XUV-probe experiment the photoelectron signal of the excited state decay of Quinoline Yellow is observed. The relaxation is found to occur with timescales of 1.3 ps and 90 ps, which are attributed to an excited state intramolecular proton transfer process and the subsequent internal conversion to the ground state.
As synthetic functional molecules two azobenzene derivatives, Methyl Orange and Metanil Yellow, are investigated. Azobenzene derivatives are promising candidates for application as molecular switches due to their light-induced isomerization. In a time-resolved experiment ground and excited state photoelectron spectra are obtained and isomerization timescales are measured for both molecules. The measured isomerization timescale for Methyl Orange agrees with previous all-optical studies. The isomerization of Metanil Yellow is found to be significantly slower, which is explained by the larger rotational moment of inertia, indicating a mainly rotational isomerization.
As a biologically relevant molecule the amino acid Tryptophan in aqueous solution is investigated with XUV-only photoelectron spectroscopy. From the photoelectron spectrum the ionization energy of aqueous Tryptophan referenced to water, which is relevant for the oxidation of proteins, is estimated at 5.5 eV. Additionally, this experiment is a prerequisite for a 266 nm-pump, XUV-probe photoelectron experiment to disentangle the complex relaxation dynamics of Tryptophan.

Kurzfassung

Ein wichtiges Teilgebiet der physikalischen Chemie ist die Erforschung ultraschneller Prozesse in photoaktiven organischen Molekülen, deren Verständnis essentiell für die Erforschung biologisch relevanter Prozesse sowie für die Entwicklung funktioneller Moleküle ist. Die Relaxation von Molekülen in Lösung wird in der Ultrakurzzeitspektroskopie mit optischen Methoden untersucht. Die Untersuchung von Molekülen in Lösung mit zeitaufgelöster Photoelektronenspektroskopie stößt hingegen auf beachtliche technische Hindernisse. Diese Dissertation behandelt die Umsetzung der zeitaufgelösten EUV Photoelektronenspektroskopie an Flüssigkeiten und deren Anwendung zur Untersuchung funktioneller photoaktiver Moleküle in wässriger Lösung.
Zunächst wird die Umsetzung von Photoelektronenspektroskopie an Flüssigkeiten an einem existierenden EUV Monochromator beschrieben. Der, zunächst kommerzielle, Liquid Jet Aufbau wurde im Zuge der Dissertation erheblich umgebaut um die Stabilität des Aufbaus zu verbessern und längere Messzeiten zu ermöglichen. Außerdem wurde eine neue Software zur Datenaufnahme implementiert, mit der Flugzeitdaten simultan sowohl als gemittelte Spannung als auch als einzeln gezählte Elektronen aufgenommen werden können. Dies ist notwendig um die schwachen Signale der gelösten Moleküle gegen den starken Hintergrund des Lösungsmittels zu messen. Der Grundsatzbeweis für die Methode wird mit einem Experiment an dem organischen Farbstoff Chinolingelb in wässriger Lösung erbracht. Das gemessene EUV Photoelektronenspektrum des Moleküls stimmt mit DFT Berechnungen überein, die im Zuge der Dissertation ausgeführt wurden. In einem zeitaufgelösten Experiment mit 400 nm Anregungspulsen kann die Relaxation des angeregten Zustands von Chinolingelb beobachtet werden. Die Zeitkonstanten der Relaxation sind ca. 1,3 ps und 90 ps, wobei die kürzere einem Protonentransfer im angeregten Zustand und die längere einem strahlungslosen Übergang zum Grundzustand zugeordnet werden können.
Als Beispiel für synthetische funktionelle Moleküle werden die zwei Azobenzolderivate Methylorange und Metanilgelb in wässriger Lösung untersucht. Azobenzolderivate werden aufgrund ihrer effizienten Photoisomerisierung als molekulare Schalter eingesetzt. Im zeitaufgelösten Experiment werden die Photoelektronenspektren der angeregten Zustände sowie die Zeitkonstanten der Isomerisierung beider Moleküle gemessen. Für Methylorange stimmt die gemessene Zeitkonstante mit vorhergehenden rein optischen Messungen überein. Die langsamere Isomerisierung von Metanilgelb mit einer Zeitkonstante von 5 ps kann mit einem größeren Trägheitsmoment begründet werden, was für Rotation als Mechanismus der Isomerisierung spricht. Als Beispiel für ein biologisch relevantes Molekül wird die Aminosäure Tryptophan mit EUV Photoelektronenspektroskopie untersucht. Mithilfe der Messung wird ein Ionisationspotential von Tryptophan in wässriger Lösung von 5,5 eV bestimmt. Zusätzlich ist die Messung eine Voraussetzung für ein zeitaufgelöstes Experiment, in dem die komplexe Relaxation von Tryptophan nach Anregung mit 266 nm Pulsen untersucht werden könnte.

Selbstständigkeitserklärung

Hiermit versichere ich, die vorliegende Arbeit selbstständig verfasst und keine anderen als die angegebenen Quellen und Hilfsmittel benutzt sowie die Zitate deutlich kenntlich gemacht zu haben. Die Arbeit ist weder in einem früheren Promotionsverfahren angenommen noch als ungenügend beurteilt worden.

Berlin, June 1, 2018 Johan Hummert